Title

Surface Acoustic Waves Integrated with Solid-State Single Photon Sources and Superconducting Electronics

Permalink

https://escholarship.org/uc/item/8dk2p1cm

Author

Choquer, Michael

Publication Date

2024

Peer reviewed|Thesis/dissertation

University of California
Santa Barbara

PhD Thesis - Surface Acoustic Waves Integrated with Solid-State Single Photon Sources and Superconducting Electronics

A dissertation submitted in partial satisfaction
of the requirements for the degree

Doctor of Philosophy

in

Electrical and Computer Engineering

by

Michael Choquer

Committee in charge:

Professor Galan Moody, Chair
Prof. John Bowers
Prof. Jon Schuller
Dr. Garrett Cole, Technical Manager

September 2024

The dissertation of Michael Choquer is approved.

Approved: _____

Dr. Garrett Cole, Technical Manager

Approved: _____

Prof. Jon Schuller

Approved: _____

Prof. John Bowers

Approved: _____

Prof. Galan Moody, Committee Chair

June 2024

To Molly and our dog, Sammie

Acknowledgements

First, I want to express my heartfelt appreciation for my advisor, Galan Moody, who both mentored me the last 5 years and helped me manage a difficult project. With the pandemic and starting a new group, it was challenging journey for both of us, and I really appreciated him keeping a cool head and setting us on a clear path towards achieving the milestones of this project.

I also want to thank my group mates for creating a fun, inspiring and uplifting work culture. Josh, Trevor and I were the first three PhD students to join Galan's group in his first year at UCSB. It was great working with the other PhD students, Sahil, Kamyar, Hae, Lilli, Nick, Yiming, Sean; the undergraduate students, Yiming, Wei-Wei, Eaman, and Mitchell, and postdocs Corey and Shaimaa these last four years. My heartfelt appreciation goes to Sahil and Kamyar for leading the experimental characterization of the SAW devices I designed and fabricated in our work with 2D materials.

I deeply appreciated my group's collaboration with Professor Hubert Krenner at the University of Meunster. Working together allowed me to learn from the experts in surface acoustic waves coupled to self-assembled quantum dots. I am indebted to Dr. Emeline Nysten, Dr. Matthias Weiss, and Michelle Lienhart for leading the characterization of the first generation of SAW devices integrated with quantum dots and collaborating on the review article "Quantum Control of Optically Active Artificial Atoms With Surface Acoustic Waves." It has been a pleasure working with all of you, and I hope to see you again at conferences in Europe!

Many hours were spent working with the UCSB Nanofabrication Facility staff. I had several long discussions with the processing engineers Dr. Demis John and Bill Mitchell to build working processes. My thanks to tool engineers and facility staff Tony Bosch, Lee Sawyer, Dr. Brian Thiabeault, Dr. Dan Read, Dr. Biljana Stamenic, Don Freeborn,

To the above and all of the friends I made over the last several years, thank you!

Curriculum Vitæ
Michael Choquer

Education

2024	Ph.D. in Electrical and Computer Engineering, University of California, Santa Barbara.
2021	M.Sc. in Electrical and Computer Engineering, University of California, Santa Barbara.
2018	B.Sc. in Electrical and Computer Engineering, University of Washington, Seattle.

Publications

1. M. Choquer et al., "Quantum Control of Optically Active Artificial Atoms With Surface Acoustic Waves," in IEEE Transactions on Quantum Engineering, vol. 3, pp. 1-17, 2022, Art no. 5100217, doi: 10.1109/TQE.2022.3204928.

2. M. Lienhart et al., "Heterogeneous integration of superconducting thin films and epitaxial semiconductor heterostructures with lithium niobate," J. Phys. D: Appl. Phys., vol. 56, no. 36, p. 365105, Sep. 2023, doi: 10.1088/1361-6463/acd7f9.

3. S. D. Patel et al., "Surface Acoustic Wave Cavity Optomechanics with Atomically Thin h -BN and WSe 2 Single-Photon Emitters," PRX Quantum, vol. 5, no. 1, p. 010330, Feb. 2024, doi: 10.1103/PRXQuantum.5.010330.

Presentations

1. S. D. Patel, K. Parto, M. Choquer, S. Umezawa, L. Hellman, D. Polishchuk, and G. Moody, "Cavity optomechanics with WSe2 single photon emitters," CLEO (2023).

2. S. D. Patel, K. Parto, M. Choquer, S. Umezawa, L. Hellman, D. Polishchuk, and G. Moody, "Quantum emitter optomechanics in a hybrid WSe2-LiNbO3 surface acoustic wave resonator," APS March Meeting (2023).

3. M. Choquer, M. Lienhart, E. D. Nysten, M. Weiss, K. Muller, J. Finley, H. Krenner, and G. Moody, "Time-resolved optomechanical dynamics of In(Ga)As quantum dots modulated by surface acoustic waves," APS March Meeting (2022).

4. Y. You, M. Choquer, and G. Moody, "Numerical modeling of surface acoustic wave resonators for quantum transduction," UCSB Undergraduate Physics Research Symposium (2020).

5. M. Choquer, S. Patel, K. Parto, S. Umezawa, L. Hellman, D. Polishchuk, K. Müller, H. Krenner, and G. Moody, "Cavity Optomechanics with Surface Acoustic Waves and Solid-State Quantum Emitters," UCSB Quantum Foundry Industry Showcase (2023).

6. M. Choquer, H. Wang, B. Liu, and G. Moody, "Microwave-to-optical single-photon transduction using co-designed surface-acoustic-wave and quantum emitter nanocavities," QED-C Workshop (2020).

Abstract

PhD Thesis - Surface Acoustic Waves Integrated with Solid-State Single Photon
Sources and Superconducting Electronics

by

Michael Choquer

One of the outstanding issues of many stationary qubit platforms is their limited
ability to connect qubits across long distances, necessary for scaling quantum computers
to sizes where they can be useful for solving difficult problems. This thesis investi-
gates the design and development of novel SAW devices combining strong piezoelectric
and superconducting alloy materials with semiconductors hosting two classes of quan-
tum emitters–self-assembled In(Ga)As quantum dots, and quantum emitters in h-BN and
WSe$_2$ layered materials. The aims of this research are to both understand the mechanism
of the optomechanical coupling and engineer high-quality devices which push forward the
state of the art of SAWs coupled to optically active quantum emitters. Two studies were
performed with these hybrid quantum systems, wherein the electromechanical and op-
tomechanical performance of the devices were independently verified through microwave
reflection and photoluminescence spectroscopy. These studies prompted an extensive
design and fabrication effort to create a next generation of optimized SAW devices, of
which their characterization is just beginning at the writing of this thesis.

Contents

Chapter 1

Introduction

Now deeply in the "second quantum revolution," technologies exploiting the unique properties of quantum superposition and entanglement are intensely investigated, both in academic labs and in industry [64, 224, 282, 276]. Indeed, currently 27 countries around the world are investing billions of dollars in the development of quantum technologies [317]. One of the principle aims of these efforts is developing quantum computers which can directly simulate complex quantum systems, opening a new door into materials discovery, system optimizations, and pharmaceutical drug development and discovery. This is an enormous challenge, requiring sustained collaboration over several decades between applied physicists, materials scientists and engineers to push forward the performance of many qubit technologies.

One of the predominant issues the stationary qubit platforms experience as the system sizes scale is the limitation in connecting larger numbers of qubits across long distances. Kimble proposed a "quantum internet" to address this problem [143], whereby the stationary qubit nodes are entangled with optical photons, which can propagate across distances of several kilometers without incurring significant losses, with the added benefits of operating at room temperature and being compatible with existing classi-

cal telecommunications optical fiber networks. Such a quantum internet will allow many quantum nodes to exchange quantum information with each other, functioning as a modular system and enabling a wide array of new device architectures. Figure 1.1 shows a prototypical example architecture for a quantum network. Here, quantum switches (QS) and quantum repeaters (QR) route quantum information between the stationary quantum nodes, which can include quantum sensors, quantum-certified random number generators (RNGs), quantum memories (QMemory), modular quantum computing units (QMod), and even end users–for example, those supplying or receiving parts of a multipartite quantum state for distributed quantum information processing.

Moving towards the realization of a distributed quantum network, many research efforts are investigating hybrid quantum systems, particularly those which can transfer quantum information between distinct physical degrees of freedom. Essential for the development of quantum networks is a device which can couple quantum systems operating at gigahertz frequencies, including many quantum processors and memories, to optical photons operating at frequencies of 100s of terahertz. Such a quantum frequency converter (QFC) is the ultimate goal of the current effort in microwave to optical quantum transduction.

Microwave-to-optical quantum frequency conversion is a difficult process because of the large difference in operating frequencies–from $\approx$ GHz frequencies for superconducting qubits and other solid-state microwave quantum systems, to several hundred THz for optical photons, a difference of $\approx 10^5$ Hz. A single optical photon incident on a transducer device can be absorbed and generate quasiparticles which break superconductivity and limit the performance of superconducting qubits [199].

Many approaches are being taken for quantum transduction: only the three most common classes of methods will be briefly discussed here. The first is direct transduction using the electro-optic effect [80, 215, 186, 119], which is broadband and more straight-

2
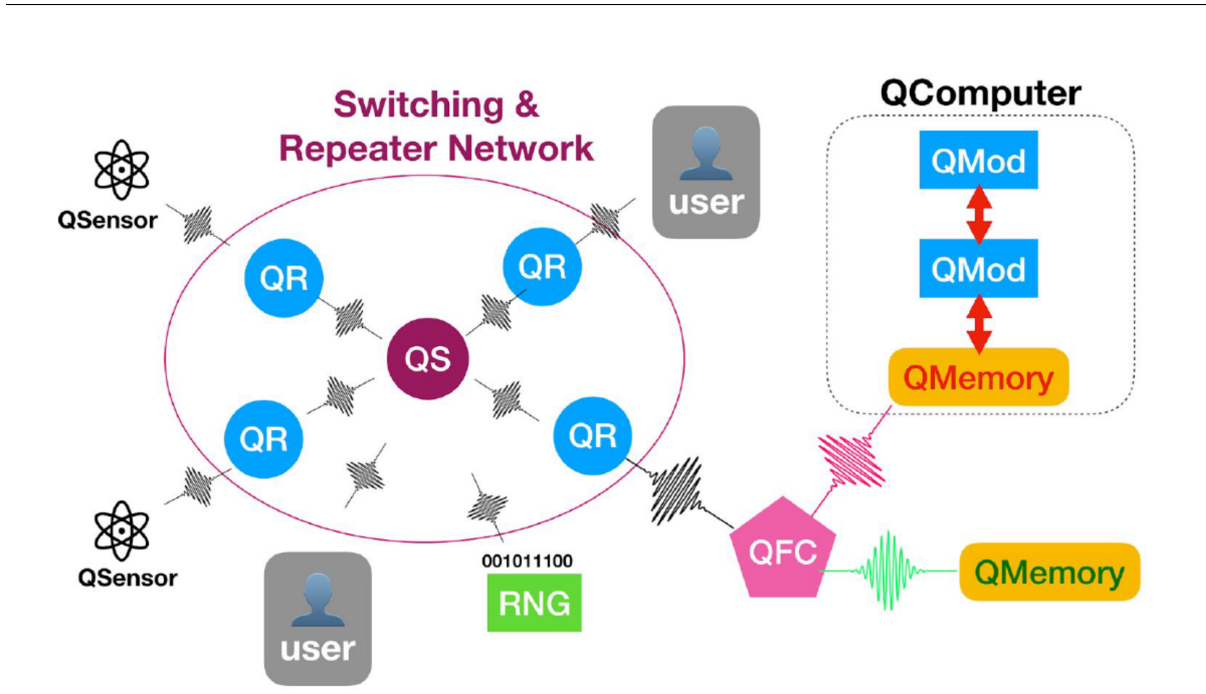
Figure 1.1: Example quantum network. Reprinted from Ref. [12].

forward to scale; however, the intrinsically weak nonlinearity of the electro-optic effect has been a serious obstacle in this direction. One viable alternative is manipulating either three-level, Λ-type systems or Rydberg systems in ensembles of cold neutral atoms, which can possess narrow optical transitions with accessible hyperfine transitions in the microwave frequency range [151, 56, 77]. However, these cold-atom systems are difficult to integrate with superconducting quantum systems; similarly, three-level systems in solid-state ion ensembles implanted in a host crystal often possess deleterious inhomogeneous broadening, which limits the achievable microwave-to-optical coupling strength [157].

The third and most widely studied approach to transduction is to introduce a mechanical resonator as an intermediary between the microwave quantum system and optical photons, the latter resonantly enhanced in an optical resonator. Efforts using the optomechanical approach have recently entered the quantum regime, with optomechanical

efficiencies as high as 93 % [266], even demonstrating nonclassical correlations between optical and microwave fields [190].

Up until very recently [266], attempts at quantum transduction with mechanical resonators have struggled to overcome the thermal decoherence from heating due to optical absorption [235]. One modification to the optomechanical approach which may reduce device heating is using solid-state optically active artificial atoms in lieu of optical resonators, the primary examples include self-assembled quantum dots, defects in wide-bandgap materials, and quantum emitters in layered materials. The optical pumping powers required to drive these systems can be lower than nanowatts [73, 284], compared to microwatts to milliwatts for the state of the art in suspended optomechanical crystals [235] and suspended membranes integrated within Fabry-Perot optical cavities [7].

These quantum emitters are also especially sensitive to strain fields, motivating exploration into coupling their single-photon emission to elastic mechanical waves. Mechanical resonators in the form of suspended cantilevers or antennas have demonstrated coupling to embedded artificial atom systems through strain generated from elastic mechanical motion[323, 281, 40, 314]. In parallel, mechanical resonators hosting surface acoustic waves (SAWs) have gained increasing interest in recent years [61], owing to their relaxed planar fabrication methods and high strain concentration at the surface. SAW resonators hosting a piezoactive material can couple to a wide variety of quantum systems sensitive to strain, electric, and even magnetic fields; SAWs have been demonstrated to couple to many forms of individual artificial atoms, including optically-active semiconductor quantum dots (QDs)[90, 194, 252, 311], electrostatically-defined quantum dots[112, 187, 125], defect centers in wide-bandgap materials [95, 313, 116], superconducting qubits [102, 202, 264], and van der Waals materials[123, 159]. This flexibility in coupling modalities opens up possibilities go beyond coupling to individual quantum systems by using SAW resonators and propagating SAWs as a universal quantum bus to connect dissimilar,

spatially separated quantum systems [251, 52].

This thesis investigates the design and development of novel SAW devices combining strong piezoelectric and superconducting alloy materials with semiconductors hosting two classes of quantum emitters–self-assembled In(Ga)As quantum dots, and quantum emitters in h-BN and WSe$_2$ layered materials. The aims of this research are to both understand the mechanism of the optomechanical coupling and engineer high-quality devices which push forward the state of the art of SAWs coupled to optically active quantum emitters. Two studies were performed with these hybrid quantum systems, wherein I led the design and fabrication and supported the electromechanical characterization work. I also led an extensive design and fabrication effort to create a next generation of optimized SAW devices, of which their characterization is just beginning at the writing of this thesis. **Chapter 2** introduces the theoretical background behind surface acoustic waves, including their governing equations, computer simulation with finite element method solvers, SAW resonators and acoustic Bragg reflectors, generation of SAWs, SAW materials, and selected advanced design methods. **Chapter 3** is both a tutorial on theoretical SAW-quantum emitter and SAW-spin coupling, as well as a survey of the state of the art of SAWs and optically active solid-state artificial atoms. **Chapter 4** discusses the design of the SAW devices shown in this thesis, with device engineering, device parameters, and simulations explained. **Chapter 5** shows the fabrication methods and process development for these same SAW devices. **Chapter 6** and **Chapter 7** show the experimental characterization of the first-generation SAW devices coupled to quantum dots and emitters in layered materials, respectively. Finally, **Chapter 8** discusses future directions and outlook on the field of quantum control of quantum emitters with SAWs.

Chapter 2

Surface Acoustic Waves

Surface acoustic waves (SAWs) are elastic waves which are confined to the surface of a solid. These waves were first theoretically predicted by Lord Rayleigh in 1885 [233] and later measured in recordings of seismic activity. SAWs are used in a variety of applications, including radio-frequency (RF) signal processing, acousto-fluidic devices, and biological and chemical sensors [61].

As mentioned in Chapter 1, both the exceptionally small acoustic wavelength and the surface-confined nature of SAWs make them appealing for classical and quantum technologies. The speed of sound is about five orders of magnitude less than the speed of light in most materials, with a corresponding difference in the wavelength of RF SAWs and electromagnetic waves. The much smaller wavelength scale enables RF bandpass filters, resonators, and delay lines with frequencies $\approx$ 10 MHz-10 GHz to occupy less than a few centimeters, at most, on a planar circuit. Recent work has pushed SAW operating frequencies above 30 GHz [302], extending the range of applications. SAWs are also easily generated on the surface of a piezoelectric material with metallic electrodes patterned onto the surface. These μm to sub-μm scale electrodes can be fabricated using photolithography or electron-beam lithography, leveraging the decades of research and

development and economies of scale of the semiconductor industry to produce SAW devices.

This chapter addresses the fundamental principles of SAWs and their generation and manipulation using periodic structures. First, the governing equations of SAWs are introduced, followed by the boundary conditions and modelling techniques for Rayleigh SAWs. Next, a basic discussion of SAW resonators and integrated transducers is presented as well as a brief survey of materials for SAW devices and quantum control. Finally, bandstructure engineering and focusing SAW structures are shown as advanced techniques for manipulating SAWs. Much of the theoretical background for this work is sourced from the books by David Morgan [203] and Daniel Royer and Eugène Dieulesaint [243].

2.1   Basic Properties

SAWs are mathematically described using linear elastic wave theory, which omits the higher-order terms for the solid displacement, which for the rigid materials used in this thesis are completely negligible [11]. In this theory, a change in the position, $\vec{r}$, of a point due to a deformation of the solid is quantified using a displacement vector, $\vec{u}$. Unlike the displacement vector, however, the linearized strain tensor, S, is invariant under any rotations or rigid translation of the solid, therefore providing a measure of the internal deformation of the solid. The linearized relation between the strain, S_{ij}, and displacement, u_i, for the displacement direction $i \in x, y, z$ for the spatial coordinates r_x, r_y, r_z is then the following:

$$S_{ij} = \frac{1}{2}\left(\frac{\partial u_i}{\partial r_j} + \frac{\partial u_j}{\partial r_i}\right), \quad i, j = x, y, z \tag{2.1}$$

Equation 2.1 shows that the strain tensor is symmetric, $S_{ij} = S_{ji}$, and so contains 6 independent elements: $\{S_{xx}, S_{yy}, S_{zz}, S_{xz}, S_{yz}, S_{xy}\}$. As the strain tensor has two indices,
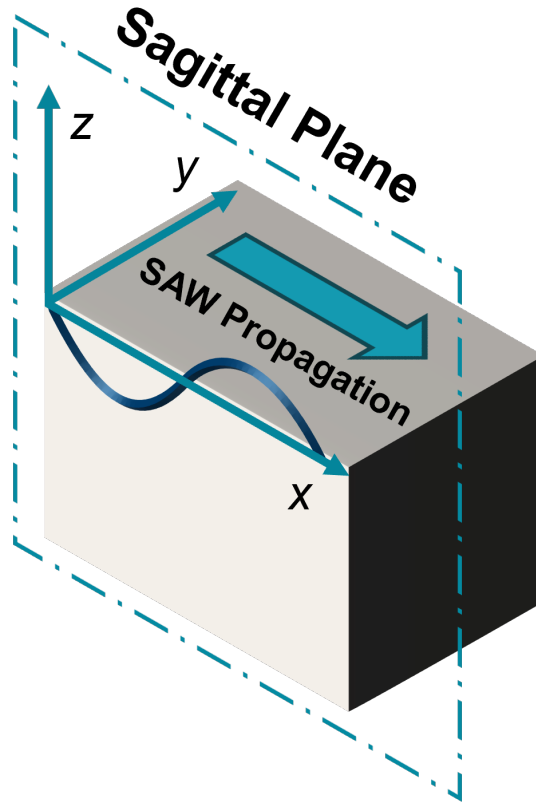
Figure 2.1: Coordinate System

it is a second-rank tensor, and therefore transforms under coordinate rotations with two rotation matrices a_{ij} shown in B. In a generalization of Hooke's Law, strain is described as a scaled linear combination of the components of the stress tensor, T_{ij}:

$$T_{ij} = c_{ijkl}S_{kl}, \quad i, j, k, l = x, y, z \tag{2.2}$$

The tensor c_{ijkl} is known as the stiffness or elasticity tensor, and is a fourth-rank tensor with $3^4 = 81$ components. Fortunately, the stiffness tensor has several symmetries that significantly reduce the number of independent components, which are also called the elastic constants. The first symmetry, known as the minor symmetry, arises because both the strain and stress tensors are symmetric, $c_{ijkl} = c_{jikl}$ and $c_{ijkl} = c_{ijlk}$, which simplifies the stiffness tensor to 36 independent components. Secondly, thermodynamic

8

arguments are used to show that the two pairs of indices of the stiffness tensor can be interchanged, so that $c_{ijkl} = c_{klij}$. This is known as the major symmetry, and it further reduces the independent components of the stiffness tensor to 21 components. Lastly, the symmetry group of crystalline materials dramatically simplifies the stiffness tensor. For example, crystalline materials with cubic symmetry, including GaAs used in this thesis, have stiffness tensors with only three elastic constants: C_{11}, C_{12}, and C_{44}. The substrate used in this work, LiNbO$_3$, has trigonal symmetry and therefore has 6 elastic constants: $C_{11}, C_{12}, C_{13}, C_{14}, C_{44}$, and C_{66}, with $C_{66} = \frac{1}{2}(C_{11} - C_{12})$. These elastic constants are observed to change with temperature [280]. Rotations of the coordinate system will transform the stiffness tensor as shown in B for the crystalline materials used in this thesis.

2.1.1 Governing Equations

In the following, a generalization of Newton's second law of motion is used to derive a set of wave equations which are the governing equations for SAWs in a piezoelectric material. From linear elastic wave theory, the force per unit volume, $\frac{\partial T_{ij}}{r_j}$ is equivalent to the product of the density ρ of a solid and its acceleration, $\frac{\partial^2 u_i}{\partial t^2}$:

$$\frac{\partial T_{ij}}{\partial r_j} = \rho \frac{\partial^2 u_i}{\partial t^2}, \quad i, j = x, y, z \tag{2.3}$$

While Equation 2.3 is a wave equation for any anisotropic material, it does not take into account the piezoelectric effect, which is the mechanism for generating SAWs from RF waves, as will be discussed in Section 2.2. Piezoelectricity is the production of an electric field, $\vec{\mathcal{E}}$, from a strain inside a crystalline material lacking inversion symmetry. The piezoelectric effect couples the elastic field quantities of a solid, the stress and strain tensors, to the electric field and electric displacement. There are two ways of expressing these relationships; for brevity, only the "stress-charge" form of the equations are expressed

below:

$$T_{ij} = c_{ijkl}S_{kl} + e_{kij}\mathcal{E}_k, \quad i,j,k,l = x,y,z \tag{2.4}$$

$$D_i = \epsilon_{ij}\mathcal{E}_j + e_{ijk}S_{jk}, \quad i,j,k = x,y,z \tag{2.5}$$

where e_{ijk} is the piezoelectric coupling tensor, $\vec{D}$ is the electric displacement and ϵ_{ij} is the permittivity tensor of the material. The piezoelectric coupling tensor has the symmetry $e_{ijk} = e_{ikj}$ from the corresponding symmetry of the strain tensor. Solving Equations 2.4 and 2.5 simultaneously along with the Maxwell equations for the electric and magnetic fields yields two solutions for the coupled mechanical and electromagnetic fields. The first solution is a predominantly electromagnetic wave with some mechanical strain, which has a wave velocity greater than the speed of light due to the piezoelectric coupling. This quasi-electromagnetic wave therefore has a velocity much greater than the speed of sound in the solid. The speed of sound, in turn, takes different values depending on whether a pressure wave or shear wave is excited; in general, it is proportional to $\sqrt{E/\rho}$, where E is Young's elastic modulus and ρ is the density of the material. These two constants limit the speed of sound to approximately 1000-6000 m/s, approximately five orders of magnitude below the speed of light in vacuum, 2.998 $\times 10^8$ m/s. Because the wave velocity of the quasi-electromagnetic solution has a large mismatch from the speed of sound, it is not an elastic wave solution and can be neglected. The other solution is the quasi-acoustic wave, with a propagation velocity around the speed of sound. Because the velocity of the quasi-acoustic wave is so low compared to that of an electromagnetic wave, the magnetic field generated from the spatially-varying electric field is minimal and can be neglected: $\nabla \times \mathcal{E} = -\frac{\partial B}{\partial t} \approx 0$. This approximation allows the electric field to be expressed as the gradient of a scalar potential:

$$\mathcal{E}_i = -\frac{\partial \Phi}{\partial r_i}, \quad i = x,y,z \tag{2.6}$$

Equation 2.6 greatly simplifies the governing equations for SAWs. Inserting this equation into 2.4, then inserting the resulting equation into Equation 2.3 along with Equation 2.1, the equation of motion for the SAW wave can be found for a piezoelectric solid:

$$\rho\frac{\partial^2 u_i}{\partial t^2} = e_{kij}\frac{\partial^2 \Phi}{\partial r_j \partial r_k} + c_{ijkl}\frac{\partial^2 u_k}{\partial r_j \partial r_l}, \quad i,j,k,l = x,y,z \tag{2.7}$$

By assuming the SAW substrate is an insulating material, $\nabla \cdot \vec{D} = 0$ because there are no free charges, which simplifies Equation 2.5 to the following:

$$e_{jkl}\frac{\partial^2 u_l}{\partial r_j \partial r_k} - \epsilon_{jk}\frac{\partial^2 \Phi}{\partial r_j \partial r_k} = 0, \quad i,j,k,l = x,y,z \tag{2.8}$$

Equation 2.7 and Equation 2.8 result in four equations for the three components of the displacement $\vec{u}$ and the scalar potential Φ. To solve these equations for SAWs, the boundary conditions for SAWs propagating in a piezoelectric solid material will be applied.

2.1.2   Boundary Conditions

Figure 2.1 shows the coordinate system used for the following. The solid SAW substrate is assumed to be infinite for $z < 0$. At the surface $z = 0$, the force normal to the surface and therefore the corresponding stress components must vanish, which implies the following, known as a free boundary condition:

$$T_{31} = T_{32} = T_{33} = 0|_z = 0 \tag{2.9}$$

To find acoustic wave solutions which are localized to the surface of the material, a constraint that the displacement drops to zero is used:

$$u_i|_{z \to -\infty} = 0 \tag{2.10}$$

For piezoelectric solid materials, the electric boundary conditions also need to be applied. The first such condition is that the electric potential must be continuous across the surface

11
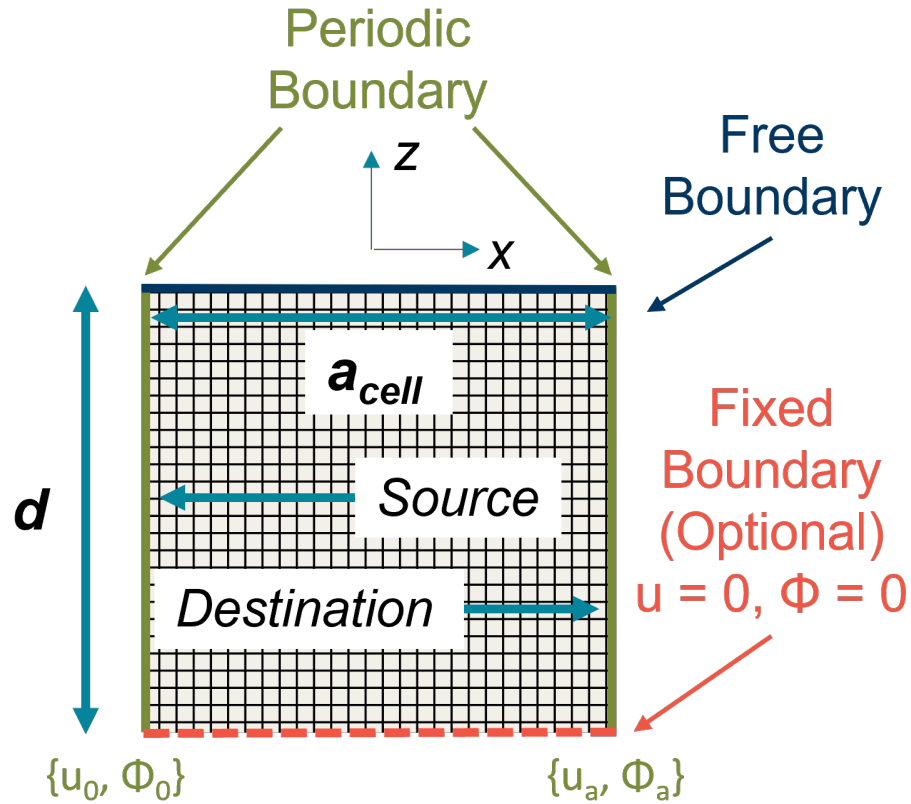
Figure 2.2: Modelling Unit Cell

boundary:

$$\Phi|_{z\to 0, z<0} = \Phi|_{z\to 0, z>0} \tag{2.11}$$

Like the displacement, the electric potential decays to zero far away from the surface:

$$\Phi|_{z\to\pm\infty} = 0 \tag{2.12}$$

The electrical boundary condition applied to the surface $z = 0$ can be used to determine the purely electromechanical behavior of Rayleigh SAWs in a piezoelectric material, decoupled from mechanical effects. In the first case, a hypothetical dielectric material with permittivity $\epsilon_d = 0$ is placed on the surface of the SAW substrate, which by being infinitely thin, the dielectric modifies the electrical boundary conditions without affecting

the mechanical properties of the solid, also known as mechanical loading. Because the surface permittivity is zero, the free charge at the surface is zero, and therefore the electric displacement field component vanishes $D_z|_{z=0} = 0$, and the tangential electric field components $\mathcal{E}_{x,y}$ are continuous. This boundary condition is known as the "open circuit" condition. In the second case, an infinitely thin film of a perfect electrical conductor with $\epsilon_d = \infty$ is placed on the surface, also with no mechanical loading effect. Such a "short circuit" condition causes the electric potential Φ as well as the tangential electric field and electric displacement $\mathcal{E}_{x,y}$ and $D_{x,y}$ to vanish. These boundary conditions influence the SAW wave velocity from v_f for the open-circuit or "free surface" condition to v_m for the short-circuit or "metallized" condition. The metallized SAW velocity is lower than the free surface velocity because the condition of zero tangential electric field for the metallized surface reduces the piezoelectric contribution to the wave velocity. If instead, the solid is exposed to vacuum with $\epsilon_d = \epsilon_0$, then the wave velocity falls somewhere between the two extremes, such that $v_m < v_{vac} < v_f$. The relative change in the wave velocity between the free and metallized surfaces is quantified using the electromechanical coupling coefficient, defined as follows:

$$K_S^2 = \frac{v_f^2 - v_m^2}{v_f^2 + \frac{\epsilon_d}{\epsilon_p} v_m^2} \tag{2.13}$$

where ϵ_p is the permittivity of the piezoelectric substrate, and ϵ_d is the permittivity of medium above the piezoelectric solid, such as vacuum or air with $\epsilon \approx \epsilon_0$. This square of the electromechanical coupling coefficient is equivalent to the portion of energy converted from electrical energy applied to the surface into mechanical energy. The coefficient is therefore bounded $0 \leq K_S^2 \leq 1$, and it measures how strongly a particular material can excite SAWs from applied electrical RF signals, which depends on both the orientation of the crystal cut of the material as well as the SAW propagation direction. In the literature, a simplified definition of the electromechanical coupling coefficient is commonly used,

which is very similar to K_S^2 for materials where $v_f \approx v_m$ and $\epsilon_p \gg \epsilon_d$:

$$K_S^2 = \frac{(v_f - v_m)(v_f + v_m)}{v_f^2 + \frac{\epsilon_d}{\epsilon_p}v_m^2} \xrightarrow{v_m \approx v_f} K^2 = \frac{2(v_f - v_m)}{v_f(1 + \frac{\epsilon_d}{\epsilon_p})} \xrightarrow{\epsilon_p \gg \epsilon_d} \frac{2\Delta v}{v_f} \qquad (2.14)$$

For convenience in calculating K^2, the "free surface" velocity condition $\epsilon_d = 0$ can be simplified to SAWs propagating in vacuum $\epsilon_d = \epsilon_0$ [203].

2.1.3 Finite Element Modelling of SAWs

For acoustically anisotropic materials, which includes all crystalline materials, there is often no analytical solution to solving Equation 2.7 and Equation 2.8. Instead, finite-element modelling (FEM) is used to find the solution to the wave equation. The SAWs studied in this thesis are the Rayleigh SAWs, which have displacement components in the x, z plane, known as the saggital plane; a diagram of the coordinate system used in this work is shown in Figure 2.1. Because Rayleigh waves are polarized in the saggital plane, they can be simulated using a 2D model, which is much less computationally intensive to solve than an FEM in three dimensions.

Figure 2.2 shows the simulation geometry and boundary conditions used to model SAWs. A 2D unit cell of width a_{cell} is created, with a dimension chosen based on the requirements of the structure. For SAWs propagating in free space–hereafter defined as propagation in an unpatterned substrate in vacuum–the translational symmetry in the x direction means a_{cell} can be made much smaller than the SAW wavelength Λ_{SAW}, since periodic conditions are applied and which specify the phase difference between the source and destination boundaries. Setting $a_{cell} \ll \Lambda_{SAW}$ reduces the number of spurious bulk modes matching the approximate SAW frequency which can be returned from an FEM mode solver: $a_{cell} = \Lambda_{SAW}/10$ was used to produce the SAW mode profile in Figure 4.10c. A Floquet periodic boundary condition is applied to the left and right faces at $x = \{0, a_{cell}\}$, such that $u_a = u_0 \exp(-ik_{SAW}a_{cell})$ and $\Phi_a = \Phi_0 \exp(-ik_{SAW}a_{cell})$. This

Floquet relationship between the dependent variables applies for phasor quantities in the frequency domain. Setting the phase u_0 to zero as a reference and taking the real part of the phasor quantities extracts the values in the time domain at time $t = 0$. As discussed previously in 2.1.2, a free boundary is applied to the surface of the SAW substrate, and the substrate is assumed to be infinitely long in the -z direction. While the depth, d has to be set to some finite value to simulate SAWs in an FEM solver, if d is set to too low relative to Λ_{SAW}, then the modes returned by an FEM solver would be Lamb waves due to coupling between the wave solutions localized at the top and bottom boundaries. Empirically, $d \gtrapprox 3.5 \ \Lambda_{SAW}$ isolates the bottom boundary sufficiently well for simulating SAWs, and meshing dimensions of $\Lambda_{SAW}/20$ or finer are ideal for sufficiently resolving the SAW strain distribution in the unit cell.

2.2 SAW Resonators and IDTs

Using classical wave theory, SAW resonators and IDTs are analyzed and designed through either the coupling-of-modes (COM) or the reflective array method. Finite-element methods[205] are commonly employed to extract coupling-of-modes parameters of periodic unit cells[132] and to match SAW mode profiles to the reflection spectra of IDTs[84] and SAW resonators[262]. The unit cell response can then be cascaded with other grating and IDT unit cells to determine the SAW device's scattering properties, characterized by the P-matrix[243, 108]. SAW resonators and IDTs are also modelled through equivalent circuit representations[265, 8], including the Butterworth Van Dyke circuit [155], which can be characterized empirically through measurements of the S_{11} scattering parameter[203, 294] and has been extended to the quantum regime[325].

2.2.1   Bragg Reflection of SAW Electrodes

High-quality SAW resonators cannot be constructed from localized reflectors[24], which strongly scatter SAWs to bulk acoustic waves. Instead, SAW resonators are created using distributed Bragg reflectors (DBRs). Analogous to optical Bragg grating mirrors, for SAWs small periodic perturbations to the surface-wave velocity result in an appreciable reflection coefficient when distributed over many acoustic wavelengths. These reflectors suppress surface-to-bulk mode scattering because SAWs have a lower acoustic velocity than bulk waves, shifting the coherent coupling to bulk modes to above the SAW grating's upper stopband edge (Figure 2.4). SAW gratings are commonly realized either through metallic strips deposited on a piezoelectric substrate surface, or by etching grooves in the substrate to couple propagating SAWs from the left and right[262]; grooves typically produce resonators with higher quality factors for materials with lower piezoelectric coupling, such as GaAs[203, 38]. A unit cell of such a SAW DBR is schematically represented in Figure 2.8a with the characteristic design parameters being the etched groove depth h and pitch p.

Before discussing the SAW devices used in this work, this subsection analyzes the behavior of SAW distributed Bragg reflectors (DBRs). The relationships and trends discussed herein will provide the theoretical background for the subsequent subsection on SAW resonators. DBRs for SAW waves are formed using periodic arrays of either deposited metal electrodes or etched grooves; the below analysis does not distinguish between these two types of reflectors. The electrode reflectors may be either shorted by connecting them using bus bars on either end of the electrodes or left disconnected in an open-circuit or floating configuration, which modifies the reflection coefficient as shown below. The below analysis is based on the reflective array method (RAM); alternatively, the coupling-of-modes (COM) method gives similar results and is commonly used in
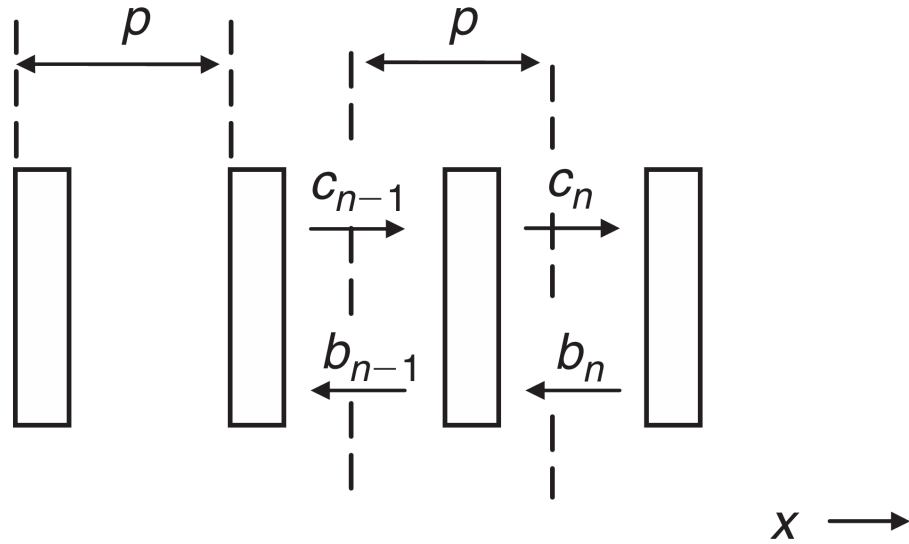
Figure 2.3: RAM analysis of an infinite-length grating. Reproduced from Ref. [203].

optics and microwave electrics. The RAM is used here because it includes expressions for the reflection and transduction parameters of a single-electrode transducer or grating, unlike the COM, which requires input from other methods. In practice, the COM method is commonly used in the SAW literature [132, 25, 203], especially since finite-element methods discussed above allow the coupling parameters to be more accurately modelled and for more complicated SAW devices than using analytical methods such as the RAM.

Infinite-Length Grating

This analysis will use the RAM to obtain a theoretical expression for the width of the reflection stop band. Figure 2.3 shows a simplified schematic for the reflection parameters from an array of individual reflecting strips with a pitch p, which is assumed to be infinite along the x direction. Each strip is symbolized by a rectangle, and they produce pairs of respective left and right-scattered waves $\{c_n, b_n\}$ and $\{c_{n-1}, b_{n-1}\}$ from SAWs interacting with neighboring strips to the right and to the left, respectively. The vertical dotted lines

17

indicate the port positions, where the scattered SAW amplitudes are evaluated; port 1 is on the left and port 2 on the right side. The strips are identical, and therefore all have a transmission coefficient t_s and reflection coefficients $\{r_{s1}, r_{s2}\}$ for the respective waves coming from the left and from the right. This analysis assumes energy conservation from strip to strip, which will be relaxed later when losses will be considered.

The reflection and transmission coefficients only denote the scattered wave amplitudes with respect to the center of the strip. To also consider the accumulated phase in moving from one port to the next, the P-matrix is used, as defined in Appendix D of Ref. [203], which is a type of scattering matrix used for SAW gratings and transducers. The P-matrix components are below:

$$p_{11} = r_{s1} \exp(-jk_e p) \tag{2.15}$$

$$p_{12} = p_{21} = t_s \exp(-jk_e p) \tag{2.16}$$

$$p_{22} = r_{s2} \exp(-jk_e p) \tag{2.17}$$

Here, k_e is the effective SAW wavenumber corresponding to an effective velocity $v_e = \omega/k_e$ which accounts for the change in phase velocity due to the reflecting strips. It is real because of energy conservation. The reciprocity between the uniform strips in the array implies $p_{21} = p_{12}$, which means that transmission is equal in both directions. The transmission coefficient t_s can be taken to be real, since any additional phase accumulation in transmission between strips can be transferred to k_e. By taking t_s to be positive, energy conservation leads to the following:

$$t_s = \sqrt{1 - |r_{s1}|^2} = \sqrt{1 - |r_{s1}|^2} > 0 \tag{2.18}$$

so that $|r_{s1}| = |r_{s2}|$. Power conservation for the P-matrix components leads to the conclusion

$$r_{s2} = -r_{s1}^*. \tag{2.19}$$

If the strips are symmetrical about the center, then $r_{s2} = r_{s1}$, and therefore the reflection coefficients are imaginary.

Now the scattering from one strip will be written in terms of the wave amplitudes from its neighbors:

$$b_{n-1} = (r_{s1}c_{n-1} + t_s b_n)\exp(-jk_e p) \tag{2.20}$$

$$c_n = (r_{s2}b_n + t_s c_{n-1})\exp(-jk_e p). \tag{2.21}$$

Rearranging to express the waves on the right side in terms of those on the left:

$$c_n = (1/t_s)c_{n-1}\exp(-jk_e p) + (r_{s2}/t_s)b_{n-1}, \tag{2.22}$$

$$b_n = -(r_{s1}/t_s)c_{n-1} + (1/t_s)b_{n-1}\exp(jk_e p). \tag{2.23}$$

which uses Equation 2.18 and 2.19. The scattering amplitudes $\{c_n, b_n\}$ can now be set equal to those of a *grating-mode* solution, such that

$$c_n = c_{n-1}\exp(-j\gamma p) \qquad b_n = b_{n-1}\exp(-j\gamma p). \tag{2.24}$$

Substituting these expressions into Equation 2.23 yields

$$\cos(\gamma p) = \frac{\cos(k_e p)}{t_s}. \tag{2.25}$$

Again assuming no losses, k_e is real, so $\cos(\gamma p)$ is real. For most frequencies $\omega = v_e/k_e$, γ is real, and Equation 2.25 has a solution with $\gamma \approx k_e$. Because $t_s < 1$, however, the right side has a magnitude greater than unity when $k_e p$ is near an integer number M of π, when $p \approx M\Lambda/2$. This results in γ becoming complex, with an imaginary component which attenuates the SAW, forming a stop band. Figure 2.4 shows the real and imaginary components of γ, a dispersion relation with multiple smooth curves punctuated by discontinuities in the normalized frequency $k_e p/\pi$. These discontinuities represent frequency bands where the propagation constant k_e becomes imaginary, which causes SAWs propagating within the solid to become attenuated and reflected backwards. Therefore no
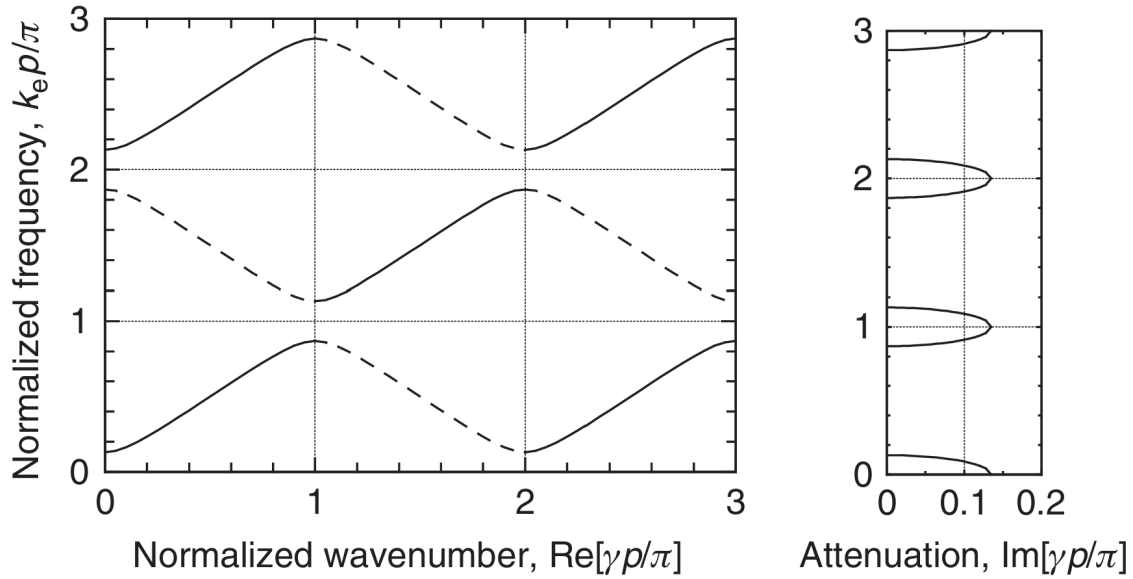
Figure 2.4: Dispersion diagram for the grating mode, Equation 2.25. Reproduced from Ref. [203].

SAWs can propagate indefinitely within these reflection bands or acoustic "band gaps". The imaginary propagation constant of k_e increases to a maximum around the middle within these reflection bands; therefore, stronger reflection of SAWs is expected close to the middle of the band gap [130].

If both v_e and the reflection coefficients r_{s1} and r_{s2} are assumed to be independent of frequency, the stop bands have the same width:

$$\Delta f / f_{c1} = (2/\pi) \arcsin |r_{s1}| \approx 2 |r_{s1}| / \pi \tag{2.26}$$

where $f_{c1} = v_e / (2p)$ is the center frequency of the first stop band where $M = 1$. The approximation is valid when $r_{s1} \ll 1$, which is valid in practice. Within each stop band, γ can be expressed in the form $\gamma = M\pi/p + j\alpha$, where α is the attenuation coefficient. The attenuation is maximum at the center of the stop band, where $\cosh(\alpha p) = 1/t_s$, resulting in $\alpha \approx |r_{s1}|/p$ for $r_{s1} \ll 1$.

Equations 2.24 and 2.25 are the solution for a Bloch wave. For a given frequency, there are an infinite number of solutions for γ in Equation 2.25, which repeat on an interval of $2\pi/p$ and have two solutions within each interval. These solutions differing by $2\pi/p$ are actually the same solution because of the discrete translational symmetry of the ports. For a mathematical justification, Floquet's theorem states that waves in a periodic material are of the form

$$\psi(x) = \sum_{n=-\infty}^{\infty} a_n \exp[-j(k + 2\pi n/p)]$$

where $(k + 2\pi n/p)$ corresponds to one of the bands of γ. The amplitude coefficients a_n are determined by the boundary conditions. If $2\pi/p$ is added to k, the series is fundamentally unchanged, with a_n being replaced by a_{n+1}. Therefore, the domain $-1 < \gamma p/\pi < 1$ contains all of the information of the solution, what is known as the first Brillouin zone. For the passbands where γ is real, the group velocity of the SAW wave is given by the slope of the solution curves for $\text{Re}[\gamma p/\pi]$. The group of solid lines in Figure 2.4 all have the same group velocity because they belong to the same solution of Equation 2.25. The group of dotted lines are the second solution, which propagate in the opposite direction.

This analysis assumed the reflection coefficients r_{s1}, r_{s2} were completely localized, which is an idealisation. In reality, the electric fields generated in scattering from a reflecting strip will couple to neighboring strips, causing the reflection to depend on the environment around each strip. Instead, effective reflection coefficients can be used with magnitudes compensated to give accurate scattering behavior of the array, which preserves the results from the above analysis.

Finite-Length Grating

A real grating can be modelled as a finite array of N reflecting strips, which are indexed with $\{c_0, b_0\}$ being the wave amplitudes on the left side, and $\{c_N, b_N\}$ those on
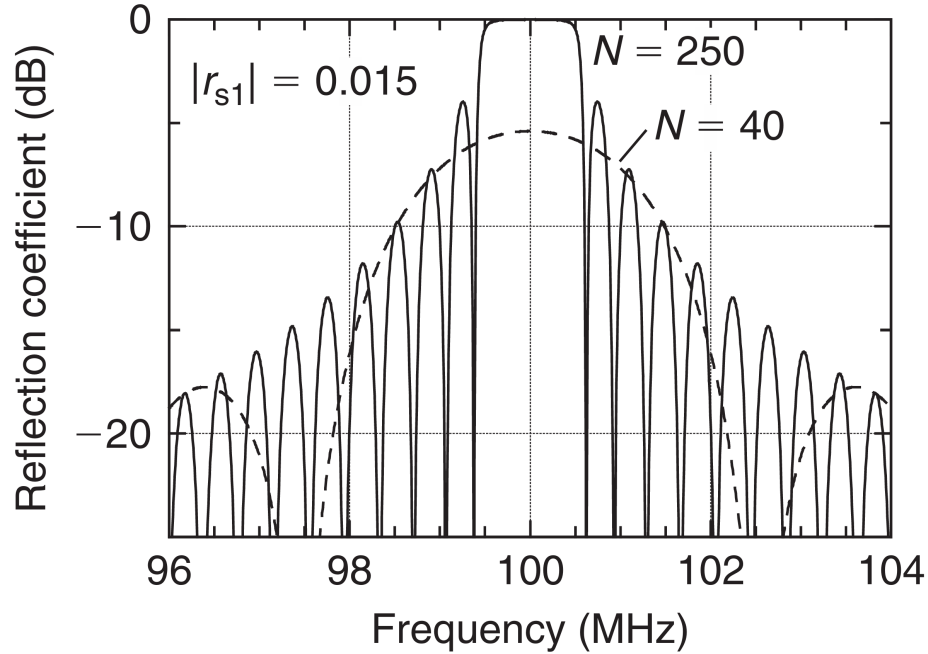
Figure 2.5: Reflection coefficient of a periodic grating with center frequency 100 MHz. Reprinted from Ref. [203].

the right side. Setting the input amplitudes to zero and solving the resulting equations yields the P-matrix of an individual strip, according to Appendix D of David Morgan's book, Ref. [203]. With $b_N = 0$, meaning no input from the right side, $P_{11} = b_0/c_0$ and $P_{21} = c_N/c_0$. With $c_0 = 0$, $P_{22} = c_N/b_N$ and $P_{12} = b_0/b_N$. The P-matrix of the entire grating can then be found by diagonalizing the P-matrix of the strip, yielding the following:

$$P_{11} = \frac{p_{11} \sin N\gamma p}{\sin N\gamma p - p_{12} \sin (N-1)\gamma p}, \tag{2.27}$$

$$P_{12} = P_{21} = \frac{p_{12} \sin \gamma p}{\sin N\gamma p - p_{12} \sin (N-1)\gamma p}, \tag{2.28}$$

$$P_{22} = \frac{p_{22} \sin N\gamma p}{\sin N\gamma p - p_{12} \sin (N-1)\gamma p} \tag{2.29}$$

where the p_{ij} are given by Equations 2.17. As with the infinite grating case, the P-matrix elements are relative to the ports, which are offset a distance $p/2$ outwards from

the centers of the end strips. By using power conservation, the magnitude of P_{11} can be shown to be given by

$$\frac{1}{|P_{11}|^2} = 1 + \left|\frac{t_s}{r_{s1}}\right|^2 \frac{\sin \gamma p^2}{\sin N\gamma p^2} \tag{2.30}$$

which shows that $|P_{11}|$ cannot exceed unity. The reflection coefficient for the center of the first stop band where $p = \Lambda/2$ is the following:

$$|P_{11}| = \tanh N \, \alpha \, p \approx \tanh(N|r_{s1}|) \tag{2.31}$$

which follows from manipulation of Equation 2.29. At the center frequency, the phase of P_{11} differs from the phase of r_{s1} by π; however, if the phase of P_{11} is instead referenced to the center of the first strip, then its phase is equal to that of r_{s1}.

For a weakly reflecting grating with $N|r_s| \ll 1$, Equation 2.30 yields the following, which is valid when multiple reflections within the grating are negligible. :

$$|P_{11}|^2 \approx |r_{s1}|^2 \left(\frac{\sin Nk_e \, p}{\sin k_e \, p}\right)^2 \tag{2.32}$$

Figure 2.5 shows the reflection coefficient P_{11} for two gratings of different lengths. A strong grating with $N = 250$ strips is shown in solid lines, with a shorter grating with $N = 40$ strips is shown with dotted lines. For the same unit reflection coefficient $|r_{s1}| = 0.015$, the shorter grating follows the same general envelope as the longer grating, except for in the mirror stopband given by Equation 2.26, where the longer grating achieves near-unity distributed reflection since $N|r_{s1}| = 3.75 \gg 1$. The reflection magnitude $|P_{11}|^2$ reaches unity in the limit $N \to \infty$. Further increasing the length of the longer grating will not increase the bandwidth of the stopband, which is instead set by the single-strip reflection $|r_{s1}|$ in Equation 2.26.

Even for strong gratings, an incident surface acoustic wave experiences a delay τ_g upon a complete reflection from a grating, which can also be characterized by an equivalent penetration depth L_p. The delay is given by $\tau_g = -\frac{d\phi}{d\omega}$, where ϕ is the phase of P_{11},

Equation 2.29. For a semi-infinite grating with $N \to \infty$, $\tau_g = p/(v_e|r_{s1}|)$. The resulting penetration depth is then

$$L_p = \frac{v_e \tau_g}{2} = \frac{p}{2|r_{s1}|}$$ (2.33)

which for a strip with a width a to pitch ratio of $1/2$ simplifies to $L_p = a/|r_{s1}|$.

2.2.2   Excitation of SAWs

SAWs are generated in piezoelectric materials via the inverse piezoelectric effect, where a strain is generated within a material when an electric voltage is applied to surface of the material. Using periodic metallic electrodes patterned onto a SAW substrate, SAWs can be generated when the electrode spacing creates constructive interference for either the fundamental SAW resonance or a higher-order resonance, which depends on the combination of substrate and electrode materials. These periodic electrode devices are called interdigital transducers (IDTs). By time-reversal symmetry, the reverse process using the direct piezoelectric effect allows IDTs to detect SAWs. IDTs can be designed to excite SAWs over a certain frequency band; the substrate material, cut and SAW orientation as well as the device geometry affect the IDT bandwidth and the maximal SAW amplitude.

(a) Split-1 IDT   (b) Split-2 IDT   (c) FEUDT
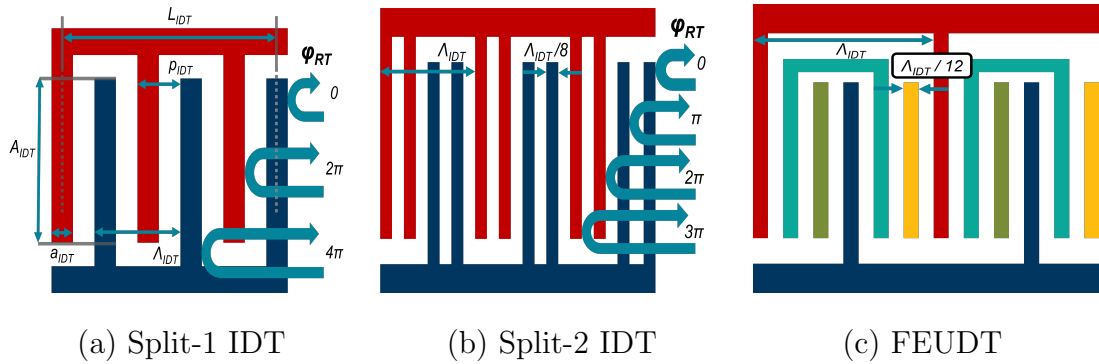
Figure 2.6: Electrode polarity diagrams of the IDT designs used in this work.

24
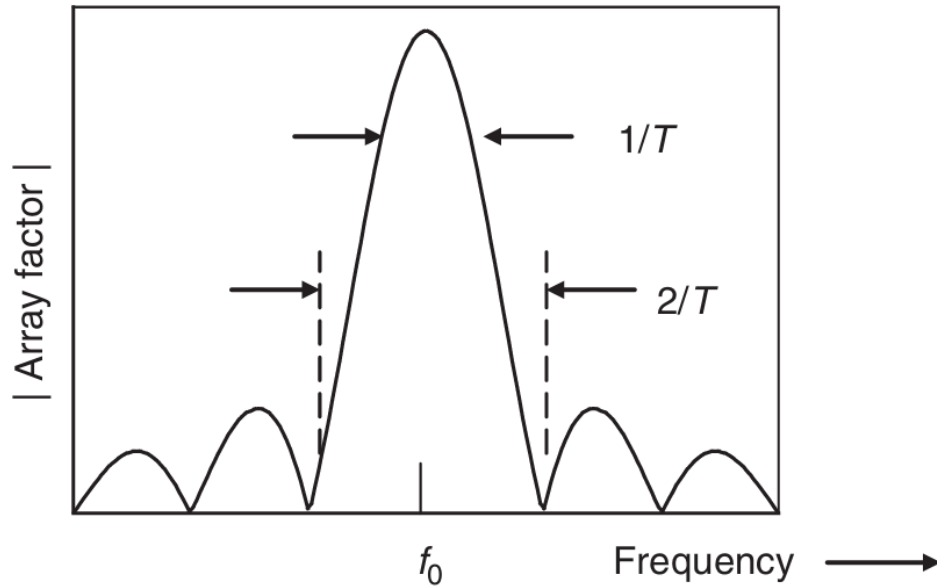
Figure 2.7: Array factor of a uniform transducer around the fundamental response.

Figure 2.6 shows schematic diagrams of the IDT designs used in this work, with electrodes with independent voltage polarities shown in separate colors. The Split-1 design is used for the Gen-1 devices, the Split-2 design is used for the Gen-2 SAW-2DM devices, and the FEUDT design is used for the test structures of the Gen-2 SAW-QD devices. The IDT aperture length A_{IDT} is the length of overlap between electrodes of opposite polarity, setting the width of the SAW wavefront. The metallisation ratio, $\eta = a_{IDT}/p_{IDT}$ is the ratio between the electrode "finger" width a_{IDT} and the electrode spacing p_{IDT}, which is commonly set to $a_{IDT}/p_{IDT} = 0.5$. The metallization ratio for the in Figure 2.6 is 0.5. The round-trip phase, φ_{RT} is shown for selected electrodes of the Split-1 and Split-2 designs. The phase φ_{RT} of adjacent electrodes in the Split-1 design are always mutually in-phase modulo 2π, which reinforces internal reflections from the IDT. By contrast, adjacent electrodes in the Split-2 design exhibit destructive interference, which reduces internal reflections from within the IDT. Avoiding internal reflections helps mitigate complex distortion of the IDT frequency response.

25

The length of the IDT or equivalently the number of IDT electrodes, N_p, affects the IDT bandwidth through the array factor, shown below for a non-reflective transducer. The magnitude of the IDT array factor is

$$|A(\omega)| \approx N_p \left| \frac{\sin(N_p\theta)}{N_p\theta} \right| \tag{2.34}$$

where $\theta = \pi(\omega - \omega_0)/\omega_0$, with $\omega_0 = \pi v_e/p$ the center frequency of the fundamental IDT response. This equation approximates the transducer response, because the element factor has been omitted because it is a slowly varying function of ω. The zeros of $|A(\omega)|$ nearest the center frequency f_0 occur at $f = f_0(1 \pm 1/N_p)$, and the points 4 dB in amplitude from the center at $f_0(1 \pm 1/2N_p$. Defining $T = N_p/f_0$ as the length of time to cross from one side of the transducer to the other, the 3 dB bandwidth is given approximately by $\Delta f \approx 1/T$, as shown in Figure 2.7. This relationship is valid for both Split-1 and Split-2 design transducers.

As a linear electrical device, IDTs can be modelled with equivalent electrical circuits, which help to predict the device admittance. Typically IDTs have a high admittance resulting from a large capacitance $C = N_pC_t$, where N_p is the number of IDT electrode periods, and C_t is the capacitance per period, which depends on the substrate material as shown in Table 2.3. The values for C_t are shown for single-electrode transducers: for the double-finger transducers, C_t must be multiplied by $\sqrt{2}$. Multiplying C_t by the aperture width A_{IDT} and the number of IDT electrode periods N_{IDT} yields the capacitance of the IDT, which is often the dominant component of its electrical admittance $Y(\omega)$ [203]. Electrical matching can maximize the power transfer from an electrical signal into the IDT and vice versa, from the device to a measurement device. The power transfer efficiency can be quantified by the insertion loss[203]. For quantum applications, improving the IDT power efficiency is highly desirable, motivating research in unidirectional SAW transducers[75, 322, 72] that break mirror symmetry in the IDT unit cell to
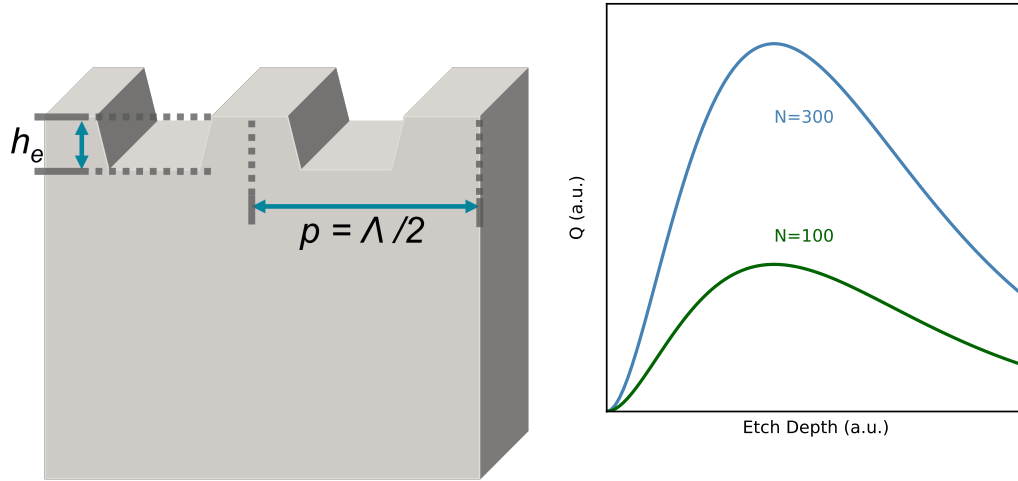
(a) Schematic of a SAW mirror unit cell.

(b) Quality factor of cavities using grooved mirrors.

launch SAWs predominantly in one direction, as opposed to regular IDTs where waves are produced in either direction, resulting in at least a 3 dB conversion loss. Alternatively, IDTs placed in the central cavity region of SAW resonators [8, 211, 247, 313, 6] eliminate insertion loss from reflection from outside of the cavity. Loss in IDTs can be reduced further by electrodes made from low-temperature superconductors, which show significant improvements below the superconducting critical temperature[322, 175].

2.2.3   SAW Resonators

The SAW resonator quality factor is a critical performance parameter for cavity quantum optomechanics. The quality factor is defined as $Q = \frac{f}{\Delta f}$, where f is the resonance frequency and Δf is the full width of the resonance at half-maximum (FWHM). For SAWs, it determines the acoustic energy density on resonance and the enhancement of the optomechanical interaction between SAWs and the quantum emitters in this work. The quality factor of SAW resonators is limited by several decay channels, including

27

propagation loss from the elastic SAW substrate material, diffraction causing SAW energy to escape from the resonator cross-section, SAW conversion to bulk modes, SAW leakage from the resonator mirrors, and SAW transduction to microwave photons via the IDTs. Q for SAWs can be divided into two components as $1/Q = 1/Q_\mathrm{i} + 1/Q_\mathrm{e}$, where the internal and external quality factors, Q_i and Q_e, respectively represent the limits from SAW decay and from dissipative coupling to IDTs. Also known as the unloaded quality factor, Q_i includes intrinsic material, diffraction, bulk scattering, and SAW mirror leakage decay channels, and it represents the ultimate achievable quality factor for a particular SAW resonator design in the limit of vanishing acoustic loss from IDTs[24]. Measurements of Q for state-of-the-art gigahertz SAW resonators at millikelvin temperatures show $Q_\mathrm{i} > 10^5$ for low-loss quartz [179], GaAs [6], and ZnO [175] substrates, and $Q \approx 10^4 - 10^5$ for gigahertz-frequency SAW resonators at cryogenic temperatures in LiNbO$_3$[262, 25] and AlN [129].

Figure 2.8b shows the relationship between the quality factor of a SAW resonator and the etched groove depth of the mirrors for two different total groove numbers $N = 300$ (blue) and $N = 100$ (green). For smaller etch depths, the reflection per groove is lower, requiring longer gratings with more grooves to achieve high SAW reflection. Consequently, the quality factor of a SAW resonator with finite mirror length will be limited by leakage losses for relatively small groove depths, typically on the order of 1% of the acoustic wavelength[203, 251]. Although increasing the etch depth will increase the mirror reflection, deeper grooves also increase SAW scattering to bulk modes, eventually limiting Q_i for larger groove depths. SAW-to-bulk mode conversion occurs predominantly near the boundaries of the SAW resonator mirrors[162], where SAWs propagating in the unpatterned free surface comprising the SAW cavity region experience a mode conversion process when entering the grating.

One approach to mitigate bulk mode conversion in SAW resonators is to add a tran-

sition region between the mirrors and the central cavity region, where the parameters of the SAW groove unit cell (Figure 2.8a) are varied adiabatically. This transition has been achieved by tapering the groove depth towards the ends of the gratings[162]. Alternatively, a localized SAW defect state can be engineered in the middle of the mirror bandgap by patterning the entire SAW resonator in a grating structure with an adiabatic transition from the groove period in the mirrors to a greater period in the central cavity region[262]. The latter approach is equivalent to creating a Wannier envelope function for the SAW mode in both real and reciprocal space [216], which confines the mode to near diffraction-limited volume, increasing the SAW amplitude interacting with artificial atoms while preserving a high Q_i. The design of such transition regions will be discussed in Chapter 4.

2.3 SAW Materials

Table 2.3 shows several low-loss piezoelectric SAW materials that are commonly used in quantum applications, each with trade-offs in SAW-specific properties and integration with artificial atoms. While piezomagnetic materials are currently being investigated for SAWs in the quantum regime [47], hereafter this thesis will focus on piezoelectric materials. Note that SAW resonators can consist of a single piezoelectric host material, such as lithium niobate (LiNbO$_3$) or gallium arsenide (GaAs), or incorporate a thin film of piezoelectric material such as aluminum nitride (AlN) or deposited zinc oxide (ZnO) to increase the electromechanical coupling efficiency on a non-piezoelectric or a weakly piezoelectric substrate, for instance silicon, zinc telluride, silicon carbide, and diamond. The row *Cut/Dir.* shows the particular crystal cut and SAW propagation direction that is common for these materials. As defined previously in Section 2.1.2, K^2 is the piezoelectric coupling coefficient and C_S is the effective capacitance of an IDT electrode

29

pair, shown here for the single-electrode polarity sequence [203]. These two parameters determine the IDT frequency bandwidth and the capacitance of the IDT, respectively, the latter being important for IDT impedance matching. The diffraction coefficient, γ determines the magnitude of diffraction, with the ideal case of zero diffraction at $\gamma = -1$. The two velocities listed, v_0 and v_{eff} are respectively the measured unpatterned SAW substrate velocity and the velocity including the electrical and mechanical loading from IDTs. The propagation loss, α_{mat} is the upper bound on the propagation loss from the elastic material loss at millikelvin temperatures, which can be estimated from known quality factors of SAW resonators[8] or by the insertion loss measurements of SAW delay lines[75]. The bottom row, $Q_{\mathrm{i}} \times f$ shows the highest demonstrated intrinsic quality factor-resonant frequency products in each platform for SAW resonators suitable for quantum applications with operation frequencies, $f \approx$ GHz. In the particular case†, the material propagation loss was extracted from the intrinsic quality factor, mirror separation, wave velocity and free spectral range according to the following formulas from Ref. [179] and [203]:

$$FSR = \frac{v}{2(L_p + d)} \rightarrow L_p = \frac{v}{2FSR} - d \tag{2.35a}$$

$$L_p = \frac{\Lambda}{4|r_s|} \rightarrow |r_s| = \frac{\Lambda}{4L_p} \tag{2.35b}$$

$$Q_g = \frac{\pi(d + 2L_p)}{\Lambda(1 - \tanh(|r_s|N_g)} \tag{2.35c}$$

$$\alpha = \frac{\pi f_0}{v} \times (1/Q_i - 1/Q_g) \tag{2.35d}$$

Here, the velocity, $v \approx 2864$ m/s; free spectral range, $FSR = 2.3$ MHz; and the mirror separation, $d = 600\,\mu m$ were known, which was used to calculate the penetration depth, $L_p = 22\,\mu m$ from Equation 2.35a. The value for L_p was then used to calculate the single-strip reflectivity, $|r_s| = 0.008$ using Equation 2.35b. Next, the grating loss-related quality factor, Q_g was calculated using Equation 2.35c with the number of grating strips,

$N_g = 500$. Finally, the propagation loss, $\alpha = 0.07$ dB/cm was calculated using the resonance frequency, f_0; the internal quality factor, Q_i; and v and Q_g. For case††, the intrinsic quality factor was estimated as $Q_i \approx Q$. For case‡, the $Q_i \times f$ product and propagation loss α_{mat} are quoted for a SAW device in thin-film AlN on sapphire. While this device does not have a substrate of pure AlN, the mode is heavily concentrated in the AlN layer, with close to 80 % of the total energy residing near the surface [129]. Therefore the quality factor of the characterized AlN-on-sapphire SAW resonator is indicative of what may be expected for SAWs on pure AlN substrates.

Material / Temp.		LiNbO$_3$	GaAs	Diamond	SiC	Quartz	ZnO	AlN
Cut/Dir.		128° Y-X	(001)-⟨110⟩	(111)	(0001)	ST-X	(002)	(0001)-[1$\bar{1}$00]
K^2 [%]	300 K	5.4 [203]	0.064 [222]	–	$< 10^{-4}$ [313]	0.12 [203]	1.07 [141]	0.25 [277]
C_S [pF/cm]	300 K	5.6 [203]	1.2 [74]	0.59 [329]	0.97 [329]	0.56 [203]	0.98 [8]	0.85 [50]
Diffraction γ	300 K	–0.35 [203]	–0.46 [164]	–	–	0.38 [203]	–	–
v_0 (m/s)	300 K	3979 [203]	2864 [74]	10934 [319]	6800 [277]	3159 [203]	–	5790 [277]
v_eff (m/s)	10 mK	3911 [26]	2880 [202]	–	–	3140.6 [180]	2680 [175]	–
α_mat (dB/cm)	10 mK	0.3 [25]	0.07 [6]†	–	–	0.065 [179]	–	5.24‡ [129]
Exp. $Q_\mathrm{i} \times f$ [Hz]	10 mK	1.13×10^{14} [25]††	1.0 × 10^{15} [6]	–	–	3.43×10^{14} [179]	2.50×10^{14} [175]	2.8×10^{14}‡ [129]

Two of the most common materials for classical SAW technologies are LiNbO$_3$ and quartz[203]. LiNbO$_3$ has exceptionally high electromechanical coupling K^2 compared to other SAW materials; however, materials with greater piezoelectricity also possess a greater susceptibility to stray electric fields, increasing environmental dissipation and decoherence. Using low-piezoelectricity substrates such as quartz[179] and GaAs[6] has yielded devices with high $Q_i \times f$ products for resonances in the range of several GHz, with the product in GaAs exceeding 10^{15} Hz. Despite the relatively low piezoelectricity, these substrates introduce deleterious dielectric loss to superconducting quantum circuits [255]. A recent work by Jiang *et al.* demonstrated the successful integration of AlN thin films on sapphire for high-quality SAW resonators exhibiting a $Q_i f$ product exceeding 10^{14} while preserving a high quality factor for coplanar waveguide resonators fabricated on the exposed sapphire substrate after AlN thin film wet etching [129].

In addition to single-crystal SAW substrates, numerous SAW material heterostructures consist of a thin film of piezoactive material deposited on a host substrate which has a higher Rayleigh SAW velocity than the film, facilitating efficient SAW generation in substrate materials without a strong intrinsic piezoelectric or piezomagnetic response. Such heterostructures are present in many of the works featured in this review[283, 95, 94, 177, 178, 113, 116, 313] and allow tailoring of the SAW properties, including velocity, diffraction and piezoelectricity [206, 142, 85, 84]. SAW material heterostructures can also support multimode acoustic waveguiding for "slow-on-fast" heterostructures [277, 222].

With the development of thin films of LiNbO$_3$ bonded to silicon or other substrates[246], new opportunities are available for hybrid and heterogeneously integrated SAW material heterostructures. Hybrid integration, including transfer printing and microprobe-based pick-and place and transfer methods[139], could allow prefabricated structures with embedded artificial atoms to be aligned precisely to SAW devices [114, 309, 312]. Heterogeneous integration involves epitaxial liftoff or wafer bonding of materials hosting artificial
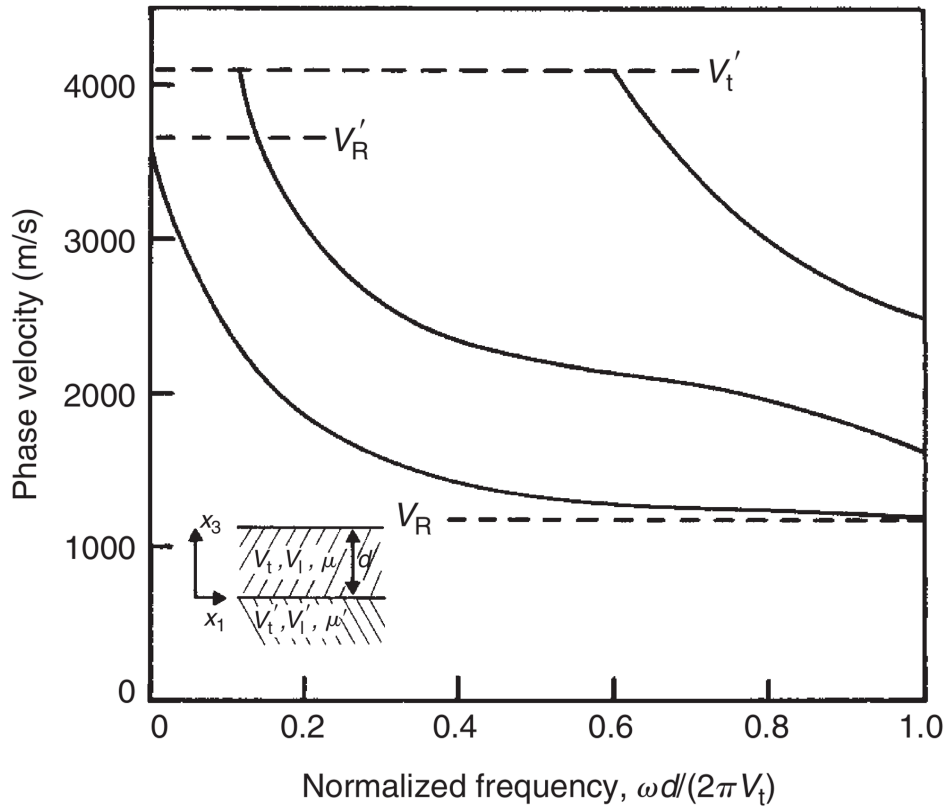
Figure 2.9: Layered Rayleigh wave dispersion diagram. Reprinted from Ref. [203].

atoms to a desired piezoelectric SAW substrate [212].

In contrast to Rayleigh SAWs in single-crystal substrates, which are dispersionless, the velocity of layered Rayleigh SAWs depends on the thickness of the top layer and the frequency. Figure 2.9 illustrates the dispersion curves for multiple SAW modes confined to a bilayer structure, where a semi-infinite substrate of acoustic material is covered by a finite layer of another material [203]. The phase velocity dispersion of the supported layered Rayleigh SAW modes are shown with respect to a normalized frequency axis, which is proportional to the layer thickness, d divided by the shear velocity of the top layer. Near zero frequency, there is only one Rayleigh SAW mode supported, with a velocity close to that of the substrate Rayleigh velocity V'_R. As either the frequency

or the layer thickness is increased, the velocity of the layered Rayleigh mode decreases monotonically towards that of the layer material. For larger normalized frequencies, multiple modes start to appear from the substrate shear velocity V_t', which show similar behavior to the fundamental layered Rayleigh mode. These modes are called Sezawa waves after their discoverer, seismologist Katsutada Sezawa [203]. This dispersion for layered Rayleigh waves can be minimized by choosing materials with minimal difference in wave velocity: ZnO is a common piezoelectric layer for GaAs SAW devices because it has a similar SAW velocity to that of GaAs: see Table 2.3.

Some piezoelectric overlayer materials also have favorable properties to function as standalone SAW substrates in the quantum regime. Bulk ZnO is readily available in wafer scale and becomes a low-loss SAW material at cryogenic temperatures, with SAW resonators exhibiting $Q_i \approx 1.5 \times 10^5$ [175]. A recent discovery of room-temperature quantum emission in crystalline AlN[27] could be a promising step towards a new monolithic artificial atom-SAW material platform, with a piezoelectric coupling comparable to that in ST-cut quartz and nearly an order of magnitude larger than in GaAs [277].

When cooled to their mechanical ground state at millikelvin temperatures (typically 10-50 mK: see Fig. 4.6), SAW resonators show a decrease in quality factor as the excitation power approaches single-phonon levels ($P_{RF} \ll -100$ dBm); this decrease is believed to be the result of SAW phonon coupling to a bath of two-level systems (TLSs). In a quartz resonator, Manenti et al. observed that the internal quality factor decreases for pump drives approaching the single-phonon level to approximately $Q_{i0} \approx 0.6 \times Q_i$ [179]. Similar single-phonon level measurements by Kandel et al. [133] and Jiang et al. [129] observe decreases of approximately 10 % and 17 % in Q_i for 128-Y-X LiNbO$_3$ and AlN on sapphire, respectively. Recent works have investigated the relative contribution of TLS loss to the reduction of the intrinsic quality factor at single-phonon power levels, showing TLS losses are not the dominant loss factor for bulk 128-Y LiNbO$_3$ SAW substrates but

are dominant for thin-film LiNbO$_3$ bonded to oxide-on-silicon or pure silicon substrates. These TLS losses in thin-film LiNbO$_3$ are attributed to surface oxides which form during the wafer bonding process [172]. Other SAW material platforms may have different TLS contributions to losses, including impurity ion ensembles[96]. An attempt to reduce the TLS density on the surface of SAW resonator substrates by independent acid cleaning, annealing, and ion sputtering processes was surprisingly found to increase the TLS density [101]. These results suggest that additional characterization techniques, such as transmission electron microscopy, may be needed to explain the relationship between the TLSs and the surface changes resulting from surface treatments.

2.4   Advanced Techniques

Realizing the quantum regime with artificial atoms is motivating further improvements in SAW resonator design. The following two subsections discuss recent developments in engineering resonators with improved quality factors and larger optomechanical interactions.

2.4.1   Bandstructure Engineering

Figure 2.10 shows the operating principle of SAW bandstructure engineering. Figure 2.10a shows the bulk (shaded) and SAW dispersion for an unpatterned surface, where the SAW bands intersect and do not show a bandgap at the edge of the Brillouin zone. Figure 2.10b shows a bandgap appears for a periodic SAW mirror unit cell. The intersecting curves from the bandstructure of the unpatterned surface are overlaid as dotted lines. The unpatterned SAW dispersion curves are observed to lie very close to the mirror upper stopband edge, which significantly reduces the mirror reflectivity compared to the reflectivity maximum in the center of the stopband (see Figure 2.4). To maximize the

36

(a) Free Surface
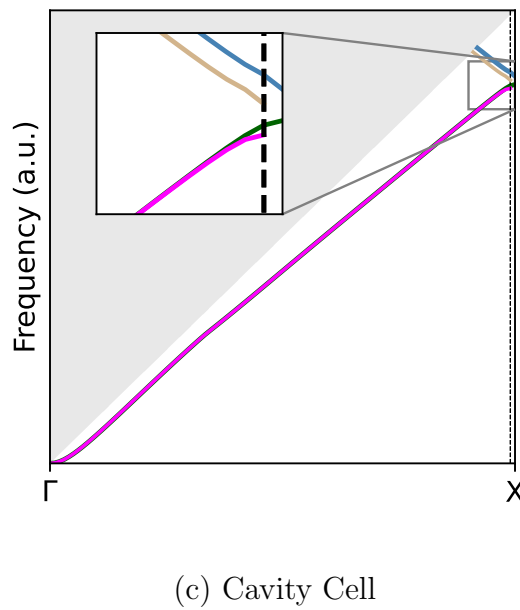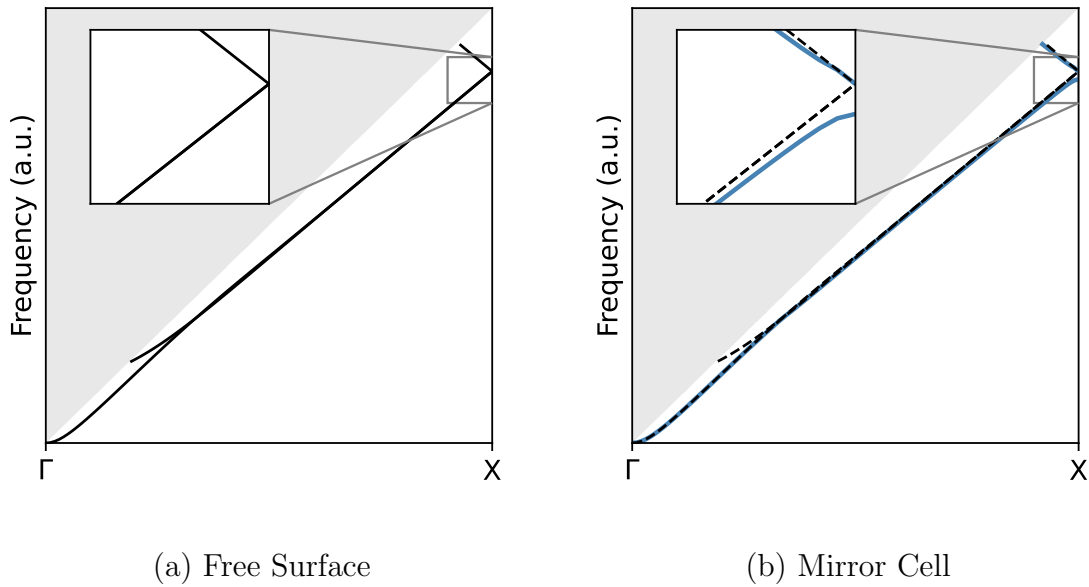
(b) Mirror Cell

(c) Cavity Cell

Figure 2.10: Acoustic bandstructure diagrams. (a) Unpatterned free surface, (b) SAW mirror supporting a Rayleigh-SAW bandgap below the sound cone, and (c) the periodic structure in (a) overlaid with that of a slightly elongated structure.

SAW reflectivity from the mirror stopband, an alternative dispersion curve from that of the unpatterned SAW is needed. One solution is to use a modified mirror or "cavity" unit cell, where the parameters are tuned such that one of the band edges coincides with the middle of the stopband of the unmodified mirror unit cell. If this cavity unit cell is inserted between two arrays of unmodified mirror unit cells, the structure will support a localized SAW mode with acoustic confinement to the cavity unit cell within some penetration depth $L_p = p/2|r_s|$ (see Equation 2.33). Figure 2.10c shows the result of shifting the upper band edge to coincide with the middle of the mirror stopband, attained by slightly elongating the mirror pitch p. In principle, either the lower or the upper band edges of the mirror unit cell could be modified in a cavity unit cell to coincide with the center of the reflection stopband; however, as shown in Chapter 4, the wave modal overlap between the unpatterned SAW and upper mirror band edge dispersion is much better than that of the lower band edge, motivating the use of the upper band edge to reduce the scattering from mode mismatch. In Chapter 4, the design of graded transition regions from a localized SAW cavity mode to the Bragg mirrors will be discused in detail.

2.4.2 Focusing SAW Devices

Focusing IDTs [156, 213] and SAW cavities [164, 214, 313, 204, 60] show focusing down to wavelength-scale beam waists, concentrating the SAW mode to near the diffraction limit. One of the main challenges of SAW focusing is acoustic diffraction, which occurs in any crystalline material and requires corrections to the IDT and mirror curvature to focus SAWs to a single focal point. Crystalline SAW materials are also acoustically anistropic, which causes significant variation in the phase velocity over the angular range of SAW propagation. Knowledge of the phase velocity as a function of the angular coordinate $v_p(\theta)$ is needed to engineer SAW structures to compensate for the anisotropy

and diffraction and focus to a common radial point in the center of the device [204, 124]. This involves designing the structures to mimic the angular profile of the Rayleigh SAW group velocity [204]. A detailed procedure for designing an anisotropy-corrected radial arc for arbitrary anisotropic SAW materials is given in Chapter 4, Section 4.2.4.

Chapter 3

Quantum Control of Optically Active Artificial Atoms with Surface Acoustic Waves

The following has been adapted from M. Choquer *et al.*, "Quantum Control of Optically Active Artificial Atoms With Surface Acoustic Waves," in IEEE Transactions on Quantum Engineering, vol. 3, pp. 1-17, 2022, Art no. 5100217.

3.1   Introduction

As discussed previously in 2, one of the primary approaches for quantum control with SAW resonators is coherent interactions with artificial atoms. Placing the optically active atom-like system at one of the anti-nodes of the SAW resonator's strain, electric or magnetic fields enables large interactions between the two subsystems, analogous to cavity and circuit quantum electrodynamics (QED) where the electromagnetic field is replaced by the acoustic field. Indeed, artificial atoms embedded within optomechanical cavities
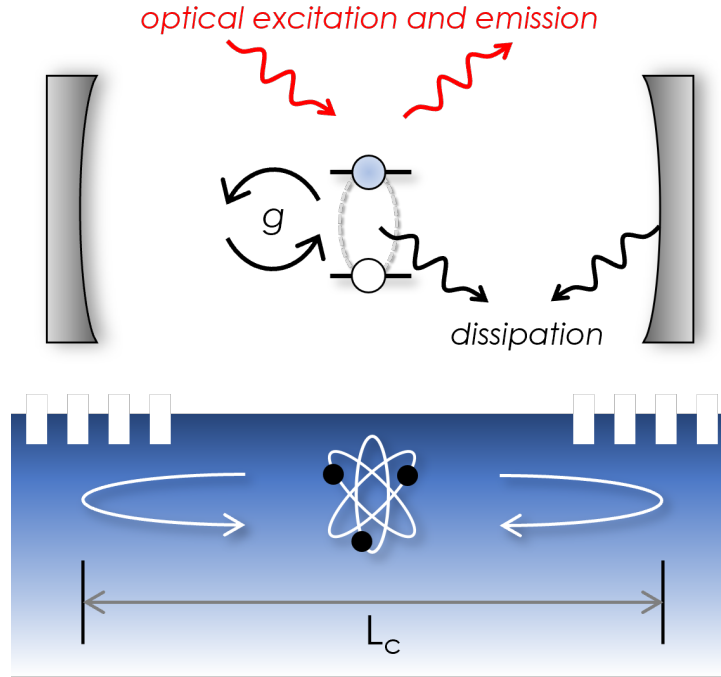
Figure 3.1: Schematic of a SAW resonator coupled to an artificial atom.

are remarkably sensitive to local strain, exhibiting frequency shifts nearly two orders-of-magnitude larger ($\sim$10 GHz/pm) than microscale optical resonators ($\sim$100 MHz/pm) [60]. The use of artificial atoms provides a strong optical nonlinearity that ensures only individual photons are emitted, typically with sub-nanowatt optical power requirements.

An abstracted representation of a SAW resonator interacting with an artificial atom is illustrated in Figure 3.1. Distributed Bragg reflectors form the acoustic resonator with an effective cavity length L_c; these reflectors are realized by either patterned metal electrodes or grooves etched into the substrate. The fundamental mode of the resonator is given by $f_c = v_s/2p$, where p is the pitch of the mirror corrugations and v_s is the phase velocity of the SAW in the material, typically on the order of 10^3 m/s. An artificial atom embedded within or near the surface of the resonator couples to surface-confined acoustic modes through strain, electric, or magnetic fields. The resonator and atom experience different dissipation mechanisms, which contribute to their respective uncoupled linewidths κ_M

and κ_A. In general, κ_M includes both damping and thermal decoherence channels, and κ_A includes both radiative and non-radiative decay as well as pure dephasing mechanisms. Because of the large frequency difference between mechanical resonators operating in the GHz range and optically active artificial atoms in the hundreds of THz range, typically $\kappa_A \gg \kappa_M$ and as such is the dominant dissipation rate in the optomechanical system.

The optomechanical interactions discussed in this thesis are quantified by a vacuum optomechanical coupling rate, g_0, as well as a quantum cooperativity, $C_{0,q}$. The vacuum coupling between a SAW resonator and an artificial atom with a transition modulated by the SAW strain field can be parameterized as $g_0 = \chi \epsilon_\mathrm{ZPM}$, where ϵ_ZPM is the dimensionless zero-point volumetric strain amplitude of the SAW ground state and χ is a mechanical strain susceptibility parameter [251]; an equivalent definition using the zero-point motion x_{ZPM} of the SAW field is commonly cited in the cavity optomechanics litterature [10, 62, 232]. The SAW zero-point strain amplitude is defined as $\epsilon_\mathrm{ZPM} = (2\pi/\lambda)\sqrt{\hbar/(2\rho v_\mathrm{s} A)}$, where ρ is the density of the SAW substrate, v_s is the SAW phase velocity, A is the SAW effective area in the plane of the substrate, and λ is the acoustic wavelength. For typical SAW materials in crystalline substrates, $\epsilon_\mathrm{ZPM} \approx 10^{-6}\,\%$ for a SAW confined to a planar area $A \approx 1\,\mu\mathrm{m}^2$ [251]. Characterizing SAW susceptibility parameters for various artificial atoms is still an active area of research, though values for some systems are available. For InAs self-assembled QDs[194, 134] as well as the SiV$^-$ center in diamond [191] and defects in hexagonal boron nitride [159], χ is on the order of 10 THz/%. The respective optical decoherence rates of these artificial atoms are $\kappa_\mathrm{A} < 1\,\mathrm{GHz}$ [183, 308], $\approx 1\,\mathrm{GHz}$ [238], and $\approx 50\,\mathrm{MHz}$, respectively [66].

A persistent challenge of cavity optomechanics is realizing large enough coupling rates to overcome the dominant intrinsic dissipation mechanisms: currently the state of the art is $g_0/\kappa \approx 10^{-2}$ [10], which by itself is insufficient for deterministic quantum transduction. One standard technique to increase the optomechanical coupling rate in
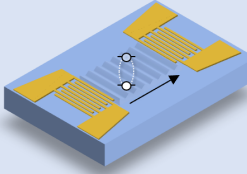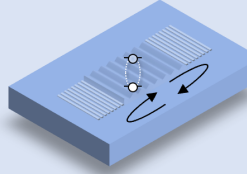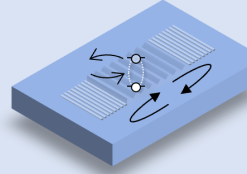
Artificial Atom-SAW System	Stage 1 Classical Control Propagating SAWs	Stage 2 Classical Control SAW Resonator	Stage 3 Quantum Control SAW Resonator
Quantum Dot Excitons	✓	✓	✗
Defect Center Spins	✓	✓	✗
Layered Materials	✓	✓	✗
Superconducting Circuits	✓	✓	✓

Table 3.1: A comparison of various SAW-artificial atom technologies and their stages of development, from classical control with propagating SAWs (Stage 1) and resonator-confined SAWs (Stage 2) to quantum acoustic control (Stage 3).

a canonical optomechanical system is to add cavity photons to the optical resonator, parametrically enhancing the coupling rate as $g = g_0\sqrt{n_c}$, where n_c is the intra-cavity average phonon number [199]. Parametric enhancement of the coupling rate allows optomechanical systems to enter the strong coupling regime $g/\kappa_A > 1$ [10]. Strong coupling can therefore occur even when the vacuum optomechanical coupling is relatively weak, $g_0 \ll \kappa_O$, where κ_O is the linewidth of an optical cavity for approaches that utilize optical cavities without artificial atoms for transduction. In this so-called "linearized regime," the system can be parameterized around a steady-state phonon amplitude $|\alpha_c|$, which corresponds to a phonon number $n_c = |\alpha_c|^2$. Here, several single-photon quantum operations, including phonon-phonon state swapping/"beam-splitter" and phonon-photon pair generation/"two-mode squeezing" operations [10], can be realized when the system is in the strong coupling and the resolved-sideband regimes, where in the latter the mechanical frequency exceeds the optical cavity linewidth, $\omega_M > \kappa_O$.

One complication with parametric enhancement of the coupling of a hybrid artificial atom-SAW optomechanical system is that populating the SAW resonator with cavity phonons means it becomes no longer possible to transduce single phonons to single photons and vice versa. When the SAW phonon population is large, $n_c \gg 1$, the system operates in the semiclassical regime, where the atom is still treated as a quantum mechanical object, but the SAW field can be treated as a classical acoustic field [106]. Instead, reaching the quantum regime with a large quantum optomechanical cooperativity can be used to perform some quantum operations, as discussed below.

The vacuum quantum optomechanical cooperativity $C_0, q = \frac{g_0^2}{\kappa_M \kappa_A n_b}$ is the ratio of the induced mechanical dissipation from optomechanical coupling, $4g_0^2/\kappa_A$, to the mechanical dissipation rate, $\kappa_M n_b$, where n_b is the Bose factor of the thermal bath coupled to the mechanical cavity [117, 54, 10, 235]. Also expressed as a rate, the cooperativity is directly proportional to the square of the optomechanical coupling and to the SAW quality factor, motivating improvements in both quantities for engineering coherent optomechanical interactions. The above data for the achievable SAW zero-point strain amplitude, quality factor, and the optomechanical susceptibility and homogeneous linewidths of several artificial atoms suggest that the vacuum quantum optomechanical cooperativity may approach or even exceed unity for SAW resonators cooled to their ground state ($\bar{n}_{\text{th}} \ll 1$), enabling quantum information processing with single photons, including quantum state transfer and generation of squeezed mechanical states [54], preparation of correlated photon-phonon pairs [236] and optomechanically induced transparency [306, 245].

Table 3.1 illustrates the state of the art of several coupled artificial atom-SAW platforms which have reached various levels of device and control complexity. Systems in Stage 1 demonstrate SAW-artificial atom coupling with propagating SAWs that are not in the quantum regime; this has been achieved for numerous artificial atom systems, including QDs [90], spins in defect centers [95], layered materials [159], and supercon-

ducting circuits [102]. Operation in Stage 1 is analogous to interactions between artificial atoms and open transmission lines in circuit quantum electrodynamics, whereby the large number of coherent propagating phonons can be described by classical wave theory and the artificial atom is treated quantum mechanically. Stage 2 is a transition towards the quantum regime as described by quantum acoustics, where SAW resonator modes couple to an artificial atom, yet the SAW-artificial atom system is not in the quantum regime and so can be described by semi-classical theory. Most technologies have reached this stage of complexity [212, 313, 180], with the exception of layered materials due to their relatively recent discovery. Stage 3 is reached when both the SAWs and artificial atoms are operating in the quantum regime. Stage 2 and 3 can qualitatively be distinguished by the quantum cooperativity. When the quantum cooperativity exceeds unity, the SAW-artificial atom system enters the quantum regime [235] (Stage 3), enabling a variety of quantum phenomena to be observed as discussed above. Currently Stage 3 has only been achieved with superconducting circuits [29, 202, 247, 6]. An even stronger condition is realizing the vacuum strong coupling regime, where the two subsystems can coherently exchange energy quanta [136]. Such a regime would enable deterministic entangling gates between single SAW phonons and artificial atoms [251].

Examining the different stages of development introduced in Table 3.1, the state-of-the-art SAW control is in Stage 2 – resonant classical control – for both semiconductor QD excitons and optically-addressable spins, with numerous demonstrations in Stage 1. Experiments with QDs show the SAW-QD optomechanical interaction in both the time and frequency domains, with observations of multiple phononic sidebands, including sum and difference frequency mixing[311], as well as resonant enhancement of the exciton SAW modulation amplitude[212]. Semiconductor defect centers have demonstrated control by SAWs not only in the orbital but also the electronic and nuclear spin degrees of freedom [95, 113, 178], with demonstrations of mode hybridization and Rabi

oscillations indicating that large couplings to SAWs can be achieved [313]. The recent integration of SAWs with defects in hBN [159] shows promising results for dynamic strain tuning of single-photon emitters operating at room temperature. For all SAW-artificial atom platforms, movement towards Stage 3 will be facilitated by acoustic cavities with greater quality factors[251], enhanced atom and spin-phonon interaction via localized SAW modes[262, 124], and impedance-matched SAW transducers for efficient acoustic excitation and detection [75].

In the following sections, an overview of SAW-artificial atom coupling in the various aforementioned platforms is presented, with a focus on optically active systems. In Section 3.2, a theoretical treatment is presented of artificial atom-SAW coupling and spin-SAW coupling. In Section 3.3, a brief survey of the literature is presented on the experimental implementations of SAW coupling to excitons in QDs, orbitals and spins in defect centers, and optically active defects in layered materials.

3.2   Theoretical Background

3.2.1   Artificial Atom-SAW Coupling

Artificial atoms with strong optical responses in the infrared to visible range are promising building blocks for quantum technologies that rely on controlled emission of photons [200]. Theoretically, artificial atoms are successfully described by few-level systems. Because these artificial atoms are hosted by solids, these systems naturally interact with the lattice vibrations, i.e., the phonons, of the host material; SAWs are acoustic phonons with a combination of longitudinal and transverse polarizations. A first estimate for the type of optomechanical coupling can be obtained by comparing the energy scales of the two systems: the artificial atoms have optically active transitions with energies in the range of electron-volts (eV) and inter-band transitions in the 10 meV range, while typical SAW frequencies span a few gigahertz, i.e., in the µeV, range. Already this enor-
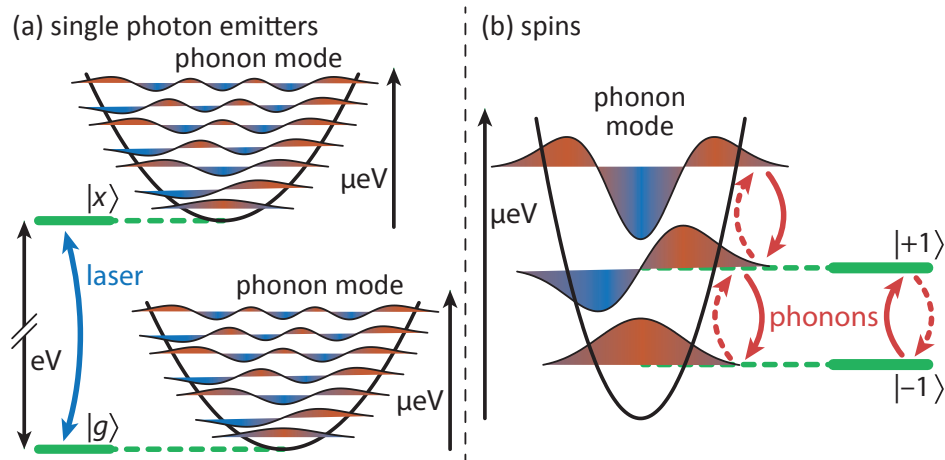

Figure 3.2: Schematic picture of the interaction between quantum systems and phonons. (a) For single-photon emitters, the typical Franck-Condon physics is found where the phonon energies are much smaller than optical transitions. (b) For spin systems the transitions can be in resonance with phonon energies.

47

mous mismatch shows that phonons cannot promote direct optical transitions between ground and excited states. The well-established Independent Boson (IB) model takes this fact into account and only couples phonons to the excited state via the Hamiltonian [176]

$$H_{\mathrm{IB}} = E_{\mathrm{g}} |g\rangle\langle g| + E_{\mathrm{x}} |x\rangle\langle x|$$
$$+ g_{\mathrm{IB}}(b + b^\dagger) |x\rangle\langle x| + \hbar\omega_{\mathrm{ph}} b^\dagger b\,, \tag{3.1}$$

where, $|g\rangle$ and $|x\rangle$ are the ground and excited states, respectively, with the transition energy $E_{\mathrm{x}} - E_{\mathrm{g}}$. $b^{(\dagger)}$ are phonon operators and g_{IB} is the coupling strength for this model, which is referred to as g_0 in the introduction. This model has the advantage that it can be diagonalized analytically by applying the so-called polaron transformation with $S = \frac{g_{\mathrm{IB}}}{\omega_{\mathrm{ph}}}(b^\dagger - b) |x\rangle\langle x|$ leading to

$$H_{\mathrm{IB}}^P = e^S H_{\mathrm{IB}} e^{-S} = \left(E_x - \frac{g_{\mathrm{IB}}^2}{\hbar\omega_{\mathrm{ph}}} \right) |x\rangle\langle x| + \hbar\omega_{\mathrm{ph}} b^\dagger b\,, \tag{3.2}$$

where $E_g = 0$ was set. The transformed excited state $e^S |x\rangle$ is called the polaron. This Hamiltonian describes the situation schematically visualized in Figure 3.2a usually associated with the Franck-Condon principle [223]. Each of the states of the two-level system defines a different equilibrium position upon which the phonon states are built. The displacement of the two phonon parabolas is determined by the relative phonon coupling strength $g_{\mathrm{IB}}/(\hbar\omega_{\mathrm{ph}})$. Here, optical excitations usually have to be treated in a perturbative way [39].

Another approach to treat the Independent Boson Hamiltonian is by introducing generating functions of the form [14, 291]

$$Y(\alpha) = \left\langle |g\rangle\langle x| e^{-\alpha^* b^\dagger} e^{\alpha b} \right\rangle\,, \tag{3.3a}$$

$$C(\alpha) = \left\langle |x\rangle\langle x| e^{-\alpha^* b^\dagger} e^{\alpha b} \right\rangle\,, \tag{3.3b}$$

$$F(\alpha) = \left\langle e^{-\alpha^* b^\dagger} e^{\alpha b} \right\rangle\,. \tag{3.3c}$$

This approach allows one to consider the optical driving without any approximations. The system can also be treated exactly in the framework of path integrals [292].

In the Independent Boson model, one can in principle consider an arbitrary initial phonon state. Several theoretical works have studied how specific optical excitations change the phonon state [234, 105]. It was for example shown that phonon squeezing can be reached when the phonons are initially in the vacuum state [315]. However, when interfacing an artificial atom with a traveling SAW field, the phonons are initially in a classical state. The limit of a classical state of a Boson field can be described by a coherent state fulfilling $b|\beta\rangle = \beta|\beta\rangle$ [92]. Then the IB coupling Hamiltonian can be replaced by [314]

$$g_{\mathrm{IB}}(b + b^{\dagger})|x\rangle\langle x|$$
$$\rightarrow 2g_{\mathrm{IB}}\mathrm{Re}(\beta)|x\rangle\langle x| = \Delta(t)|x\rangle\langle x| = H_{\mathrm{IB,SC}}, \tag{3.4}$$

which will hereafter be referred to as the semiclassical (SC) limit. Given that the coherent state has a harmonic time dependence with the frequency of the considered phonon mode ω_{ph}, this describes an energy modulation of the transition energy $E_1 + \Delta(t)$ in the full system.

Typically, for SAWs the dominant coupling mechanism is the deformation potential, which is proportional to the trace of the local strain tensor $\Delta \sim \mathrm{Tr}(\varepsilon)$. The transition regime between the full quantum treatment of the IB model and its semiclassical limit has recently been explored systematically, employing the generating functions introduced before [106]. It was shown how photon scattering spectra and the considered phonon state change when approaching the ultimate quantum limit of an initial vacuum state from a coherent state with a large initial coherent amplitude $\beta \gg 1$.

3.2.2   Spin-SAW Coupling

Here, atomic defect structures are considered, where a prototypical example is the nitrogen-vacancy (NV) center in diamond. The typical energy splittings among the spin states are a few µeV, which is automatically in the same range as the considered phonon energies. This shows that phonon-assisted transitions between the different spin states should in principle be possible. To find the coupling between the spin structure of such a defect and the lattice vibrations, one has to consider the specific symmetry of the system. The NV^- center will be considered in the following, as it is so far the most intensively investigated system.

The NV center possesses a spin-1 ground state manifold, with the basis states $|+1\rangle$, $|0\rangle$, and $|-1\rangle$. The transition energies between these states can for example be tuned by applying a magnetic field, which is routinely used in optically detected magnetic resonance (ODMR). The NV center has an additional excited state with a transition energy in the visible range. This state falls under the situation described in Sec. 3.2.1, as discussed in more detail later.

By applying group theoretical arguments, it was shown that the coupling between the NV ground state spin system with C_{3v} symmetry and a given strain field can be written in the form [289]

$$
\begin{aligned}
H_{\text{spin-strain}}^{\text{NV}} = {} & \gamma_0(\boldsymbol{\varepsilon})(|+1\rangle\langle+1| + |-1\rangle\langle-1|) \\
& + \gamma_{01}(\boldsymbol{\varepsilon})(|0\rangle\langle+1| - |0\rangle\langle-1|) + \text{h.c.} \\
& + \gamma_{11}(\boldsymbol{\varepsilon})\,|-1\rangle\langle+1| + \text{h.c.},
\end{aligned}
\tag{3.5}
$$

where γ_0 is a real and $\gamma_{0,1}$, $\gamma_{\pm 1}$ are complex functions of the strain tensor $\boldsymbol{\varepsilon}$. While the first term with γ_0 describes energy renormalizations of the states $|\pm 1\rangle$, the other two terms promote mixing between the different spin states. Note that, in case of SAWs, the components of the strain tensor carry harmonic time dependencies. In many cases

only the last term is considered, especially in cases where an additional microwave field resonantly drives the transitions between $|0\rangle$ and $|\pm 1\rangle$ [313, 177].

In direct analogy with the procedures carried out when deriving the Jaynes-Cummings model in quantum optics [257], here the strain field can be quantized and introduce the phonon operator $b^{(\dagger)}$. Then, the Hamiltonian describing state mixing and phonon-assisted transitions takes the general form

$$H_{\text{spin-phonon}}^{\text{NV}} = g_0(\boldsymbol{\varepsilon})(b^\dagger + b)(|{+}1\rangle\langle{+}1| + |{-}1\rangle\langle{-}1|)$$

$$+ g_{01}(\boldsymbol{\varepsilon})b^\dagger(|0\rangle\langle{+}1| - |0\rangle\langle{-}1|) + \text{h.c.}$$

$$+ g_{11}(\boldsymbol{\varepsilon})b^\dagger\,|{+}1\rangle\langle{+}1| - \text{h.c.}\,, \tag{3.6}$$

where it is assumed that the energetic ordering $E_{+1} > E_{-1} > E_0$, and the usual rotating wave approximation is applied. The situation described by the last term is schematically visualized in Fig. 3.2(b), where the decay within the spin states is associated with the creation of a phonon and vice versa. A model of this form has for example been applied to simulate the phonon-mediated coupling between distant spin systems [251, 161].

3.3   Experimental Implementation

3.3.1   Dynamic Control of Quantum Dot Excitons

QDs are an important building block for quantum technologies as they are an efficient source for both single and indistinguishable photons, as well as entangled photon pairs [3, 290]. Inside a QD, the motion of charge carriers is confined in all three spatial dimensions, resulting in their discrete energy spectrum; the solid-state nature of QDs makes them strongly susceptible to strain. Strong sensitivity to strain has traditionally been considered a drawback, since this can lead to, for example, appreciable phonon-induced dephasing of the QD [126, 98]. In recent years, however, several groups have
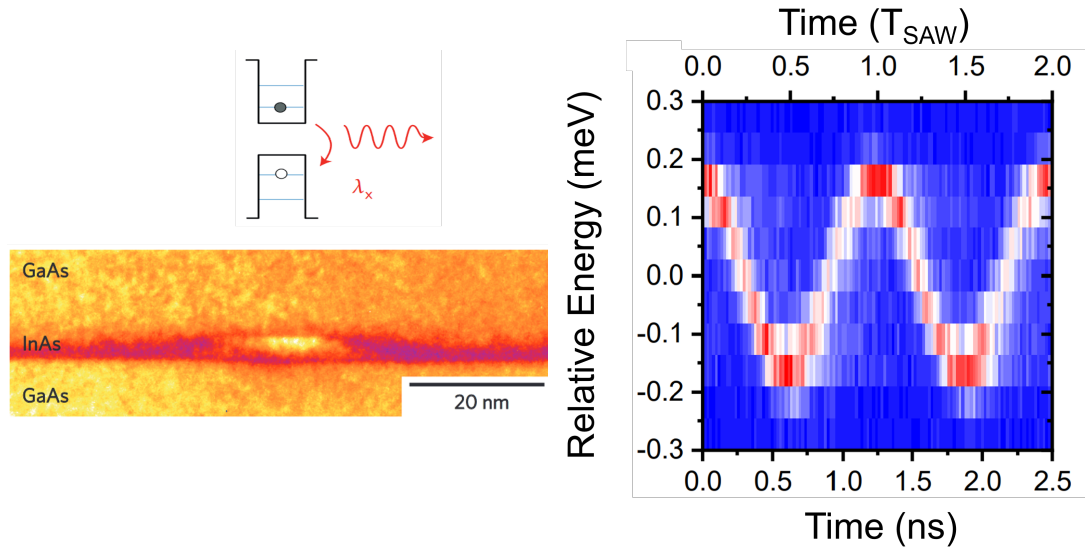
Figure 3.3: Left: TEM and band diagram of an InAs self-assembled quantum dot showing the single exciton transition. Reproduced from Ref. [261]. Right: Time-resolved PL of a SAW-modulated QD exciton line, showing pure sinusoidal oscillations with period equal to the SAW drive period. Figure panel provided by Dr. Matthias Weiß, University of Meunster.

leveraged this coupling to control QD excitonic emission via the strain field associated with a SAW, as long as the QD is located close to the surface of the substrate, typically within one acoustic wavelength. The interaction between a QD and a SAW is based on the deformation potential coupling that leads to a type-I band edge modulation and, therefore, to a dynamic modulation of the transition energy of a QD exciton as introduced in Sec. 3.2.1.

The most studied types of QDs are InAs QDs embedded in a GaAs matrix and GaAs QDs embedded in an (Al)GaAs matrix. These material systems have the advantage of being piezoelectric, albeit weakly compared to other materials such as $LiNbO_3$. Nonetheless, they enable a direct excitation of SAWs using IDTs on the host substrate. The dynamic modulation of QDs by SAWs was also recently expanded to CdTe QDs in a

ZnTe substrate using a ZnO layer to excite a SAW on the otherwise weakly-piezoelectric substrate [283]. This dynamic modulation can be observed by either time domain or stroboscopic-excitation spectroscopy. Figure 3.3 shows the time- and energy-dependent photoluminescence (PL) emission from a single acoustically modulated QD exciton over the course of two acoustic cycles. The QD was modulated at a frequency of $f_{\mathrm{SAW}} = 800$ MHz and was optically excited by a continuous wave (CW) laser. The collected emission from the QD transition was spectrally filtered and analyzed in the time domain by time-correlated single photon counting. The measured data nicely shows the sinusoidal modulation of the QD emission, where the modulation frequency corresponds to that of the driving acoustic field. The modulation amplitude, in this case $\Delta E = 0.156$ meV, is a measure of the hydrostatic pressure at the position of the QD which corresponds to ≈ 1 MPa. For more detailed information about stroboscopic-excitation spectroscopy and the other PL experiments in this section, the reader is referred to Ref. [316], [212].

The QD modulation amplitude ΔE can also be obtained from time-integrated spectra, as shown in Figure 3.4. Here, time-integrated spectra are shown for different radio-frequency (RF) powers P_{RF} that are applied to the IDT and thus for different SAW amplitudes u_z. The initial Lorentzian line shape of the unmodulated QD exciton emission is broadened under the influence of the SAW, and a characteristic split spectrum emerges once the modulation amplitude exceeds the spectral width of the emission line. For increasing P_{RF}, an increase in the broadening and the modulation amplitude ΔE is observed. The modulation amplitude's scaling with the applied RF-power P_{RF} is determined by the physics of the QD spectral modulation. For modulation mediated via the deformation potential of the QD, $\Delta E \propto \sqrt{P_{\mathrm{RF}}}$, because both the SAW amplitude u_z and the hydrostatic strain amplitude ϵ_{max} are proportional to $\sqrt{P_{\mathrm{RF}}}$. The QD modulation amplitude may also increase via the quantum confined Stark effect, where the electric field associated with a SAW propagating in a piezoelectric substrate modulates the QD:
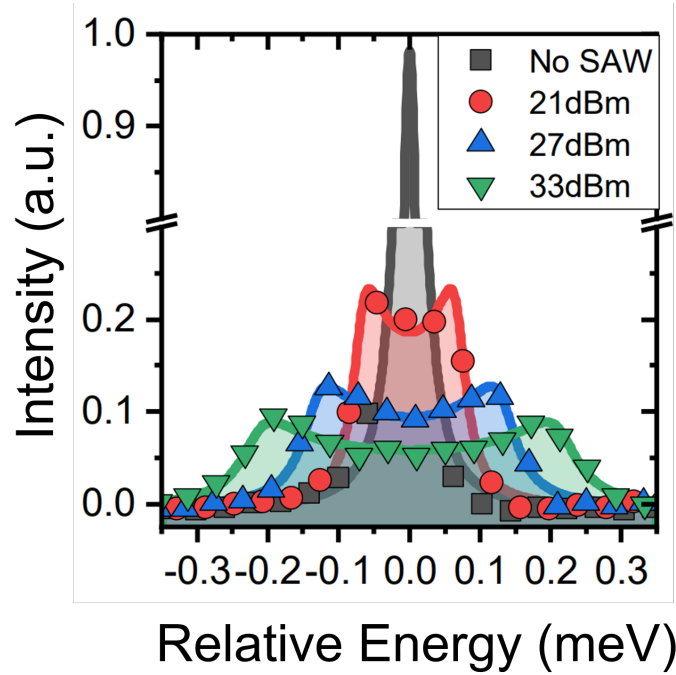
Figure 3.4: Time-integrated PL of a SAW-modulated QD exciton, showing clear modulation with increasing applied RF power, consistent with deformation-potential coupling. Figure provided by Dr. Matthias Weiß, University of Meunster.

$\Delta E \propto P_{\mathrm{RF}}$ [158, 309]. In Figure 3.4, the power dependence of the observed modulation agrees with $\Delta E \propto \sqrt{P_{\mathrm{RF}}}$, indicating deformation potential coupling is the dominant contribution to the QD spectral modulation.

Compared to non-resonant excitation used for PL spectroscopy, resonant excitation of a specific transition in a single semiconductor QD greatly enhances the quality of the emitted photons in terms of purity and indistinguishability, as they adapt to the coherence of the driving laser field while maintaining their single photon characteristics. Combined with a dynamic modulation by a SAW, this makes it possible to advance into the resolved-sideband regime, meaning the SAW-induced spectral modulation frequency exceeds the optical linewidth. Figure 3.5 shows the resonance fluorescence signal of a single QD
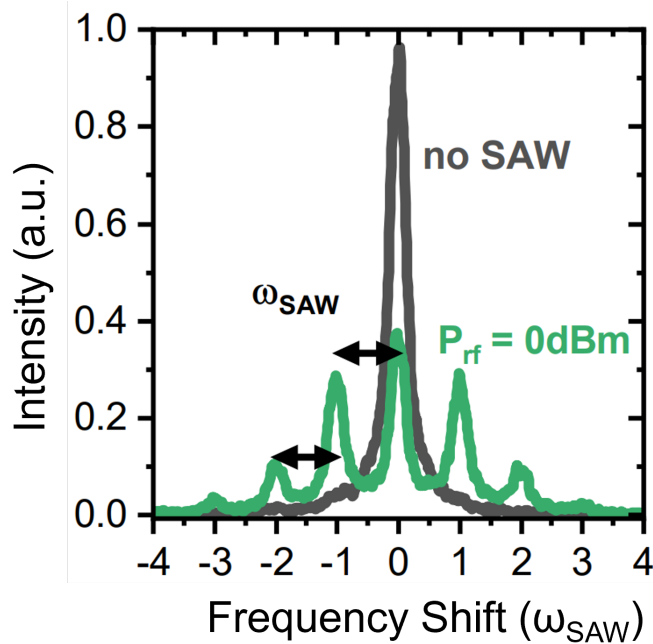
Figure 3.5: QD exciton resonance fluorescence showing several optomechanical sidebands at multiples of the SAW drive frequency. Figure provided by Dr. Matthias Weiß, University of Meunster.

transition with (green) and without (grey) dynamic modulation by a SAW. When the QD is not modulated by the SAW, the spectrum consists in a single emission line, the so-called zero phonon line (ZPL), with a linewidth limited by either the linewidth of the detection system or the driving resonant light field [183]. For the case of a dynamically modulated QD, the spectrum shows additional sidebands on either side of the ZPL. The splitting of the sidebands corresponds to the energy $\hbar\omega_{SAW}$ of a single SAW phonon. The formation of these phononic sidebands was first shown by Metcalfe *et al.* [194] for QDs in a planar Bragg cavity and by Villa *et al.* [295] for QDs in a pillar micro cavity.

Extending this excitation scheme to an additional SAW field with a different frequency, both sum and difference frequencies are observed in the emission spectra, probing optomechanical wave mixing of two SAW fields and the driving CW laser field by the

QD [311]. In the case of two mutually coherent SAW fields, the sum and difference SAW frequency generation processes depend on the phase between the two fields and a phase-matching scheme can be applied to control the relative intensity of specific sidebands. Furthermore, it could be shown that the different phononic sidebands show pronounced temporal dynamics that can be controlled by detuning the driving laser from resonance, paving the way towards precise temporal and spectral control of single photon emission [316]. The experiments presented so far are also compatible with a multitude of different photonic systems. For instance, the dynamic strain field of a SAW was used to control QDs in photonic cavities, enabling the realization of a triggered single photon source [307], or QDs located in the input waveguide of a dynamically tuned Mach-Zehnder interferometer, enabling wavelength division multiplexing of single photons [36].

In order to enhance the coupling of QDs to the acoustic strain field, the QDs can be placed in nanomechanical structures and cavities designed to focus the strain fields at the position of the QDs, for example nanophononic strings [296]. Focusing SAW cavities and IDT electrodes are also being investigated to enhance SAW interaction with QDs embedded in a GaAs substrate. Using focusing SAW cavities, Ref. [60] demonstrated resonance fluorescence of InAs QDs in the optomechanical resolved-sideband regime with a maximum vacuum coupling rate of $g_0 = 1.2\,2 \times 2\pi$ MHz, which is expected to increase to $2\pi \times 10$ MHz with improved device design.

Instead of patterning SAW cavities around QDs in a weakly-piezoelectric host substrate, a different approach is to transfer QDs onto a strongly-piezoelectric substrate, i.e., $LiNbO_3$, allowing for the generation of stronger SAW fields with lower RF drive power. A key requirement for such a transfer is robust mechanical coupling across the interface between the host substrate containing the QDs and the target substrate used to generate the SAW. This has been realized for QDs and QD-like emission centers that are located within semiconductor nanowires (NW) [114, 309, 312]. Due to the stronger
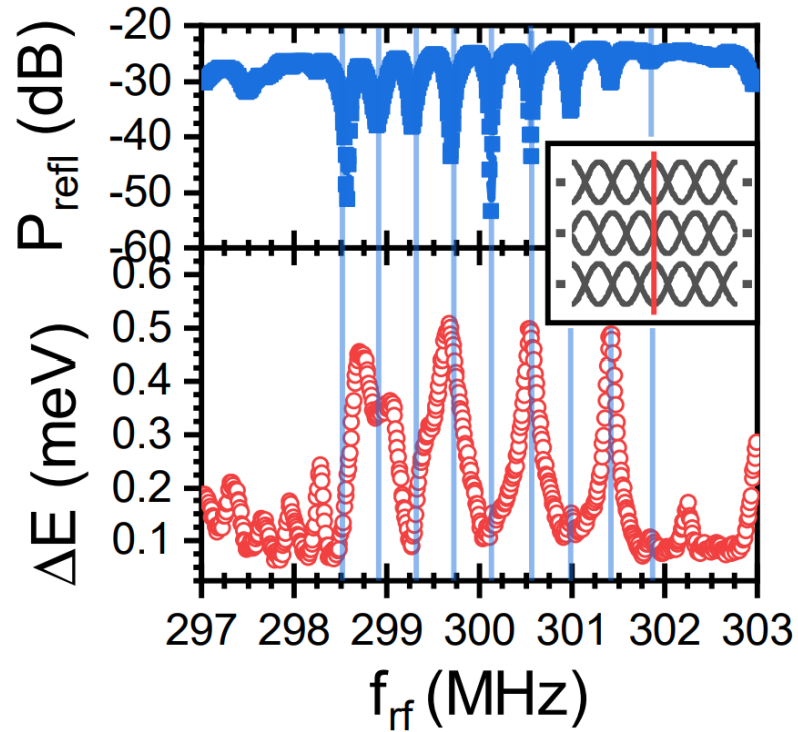
Figure 3.6: Top: reflected power spectrum of IDTs driving a SAW resonator with embedded QDs in a hybrid GaAs-LiNbO$_3$ system. Bottom: modulation amplitude as a function of the IDT frequency, showing pronounced enhancement at the SAW cavity resonances. Figure provided by Dr. Emeline Nysten, University of Meunster.

electromechanical coupling efficiency of LiNbO$_3$ and the associated stronger piezoelectric fields, spectral modulation of QD emission was observed due to both deformation potential coupling and the quantum confined Stark effect. Epitaxial lift-off and transfer of thin semiconductor membranes containing QDs has also been shown to be a successful technique for the fabrication of fused LiNbO$_3$–(Al)GaAs hybrid devices with enhanced acousto-optic coupling due to acoustic waveguiding and strong localization of the acoustic field within the transferred semiconductor membrane [211]. GaAs-based *p-i-n* photodiodes containing a single layer of QDs were successfully fabricated on LiNbO$_3$, enabling the combined dynamic and static tuning of the dot emission energy through the acoustic

field of a SAW and a static electric field applied at the diode [230]. This technique can also be used to transfer the (Al)GaAs-QD membrane inside a SAW resonator patterned on $LiNbO_3$ [212]. High acoustic quality factors $Q > 2500$ are demonstrated for an operation frequency of $f = 300$ MHz even after the heterointegration of the semiconductor QD membrane, which ensures the coherent behavior of the SAW field. The optomechanical response of the QD presented in Figure 3.6 with the simultaneously measured electrical spectrum of the resonator proves the efficient coupling of the QD to the resonator modes. The optomechanical coupling has an index-dependent character due to the position of the QD in the SAW cavity (see the inset of 3.6). The QD emission's frequency-dependent response shows complex behavior, with the presence of frequency-mixed peaks on the lower end of the frequency spectrum occurring between the phononic modes in the optomechanical response. To understand this possible nonlinear frequency conversion in the SAW resonator-QD coupling, resonators with higher resonant frequencies can be used to reach the resolved sideband regime [194]. In this regime, the contribution of each phonon interaction can be identified in the emission spectrum and the frequency mixing can be confirmed [311].

3.3.2 SAW-Spin Coupling in Defect Centers

Optically-addressable solid-state spins are widely investigated resources in quantum information science and technology [13, 69], with myriad applications in quantum communication, networking [304, 227], and sensing [111, 32]. Bound solid-state electronic spins may be realized either through local electrostatic potentials or via impurities in a host semiconductor crystal. A canonical example is a point defect in a wide-bandgap material such as diamond or silicon carbide (SiC), which is the focus in this section. Atomic-scale defects feature electronic localization as well as distinct spin and optical
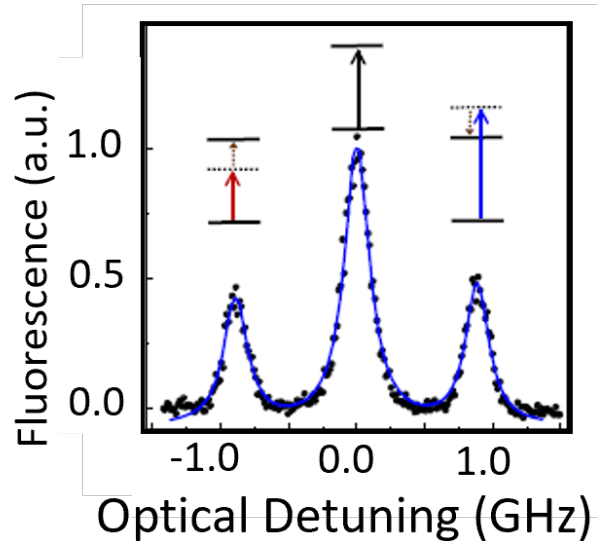
Figure 3.7: Resonance fluorescence of the NV$^-$ center in diamond showing red and blue-detuned optomechanical sidebands from SAW driving. Reproduced with permission from Ref. [95].

transitions that can be individually and coherently addressed. These defect-based spin centers can be integrated with photonic [209, 150, 169, 13] and phononic systems, including SAW transducers and resonators. SAWs can manipulate not only the defect's optical and charge degrees of freedom, but they can also directly manipulate spins through their resonant interaction with the fine-structure splitting as discussed in Section 3.2.2. Acoustic control offers an additional degree of freedom for both coherent sensing [174, 116] and accessing novel regimes of spin-phonon interaction [135]. Commonly used experimental tools of the field include ODMR, Ramsey interferometry, and spin-echo and dynamical decoupling microwave control, respectively used to read out spin states, probe spin coherence, and to not only isolate, but also coherently control interactions with neighboring systems [79, 160, 178].
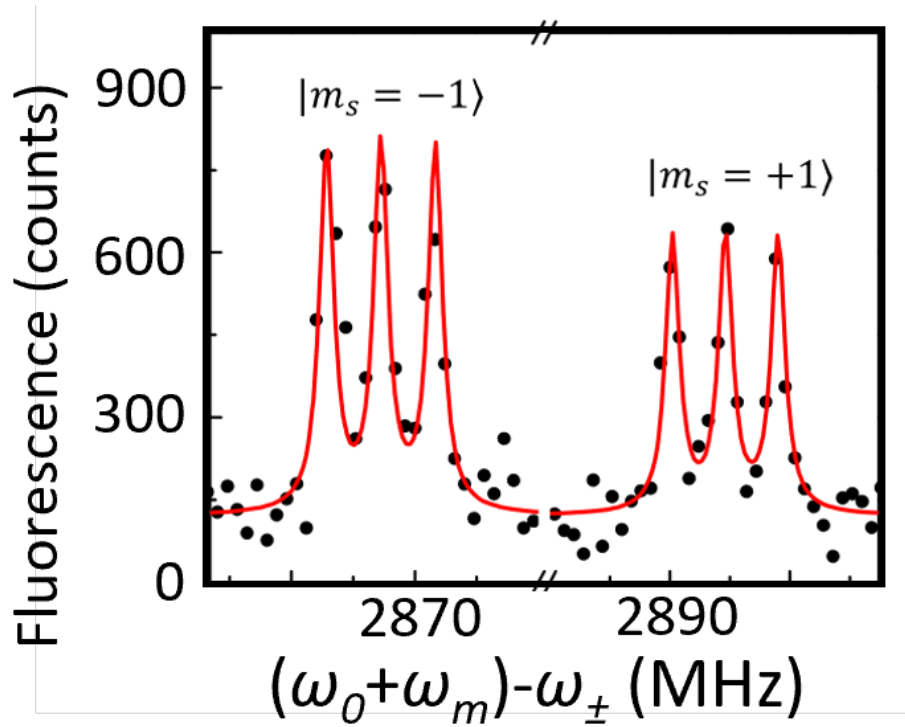
Figure 3.8: Effective spin-spin interactions between the $m_s = \pm 1$ and $m_s = 0$ states driven by optomechanical sideband transitions. Reproduced with permission from Ref. [94].

Nitrogen Vacancy Centers in Diamond

The NV center in diamond is an extremely sensitive probe of its local environment, motivating extensive research into using NV centers as a nanoscale magnetic field [17, 240, 318, 327], electric field [28, 196, 71, 70], temperature [263, 268], pressure [118], and stress and strain [19] sensor operable at room temperature [107, 135, 271, 160]. The NV center features high-coherence spin states and a bright optical transition coupled to a spin-selective nonradiative transition that enables high-fidelity optical spin initialization and readout.

Ref. [95] coupled single NV centers to propagating SAWs, demonstrating acoustic

control of the NV orbital state in the optomechanical resolved-sideband regime [95] – a step towards quantum control of hybrid atom-phonon systems. Figure 3.7 shows the NV$^-$ center driven by a SAW field at $\omega_m = 2\pi \times 900$ MHz as an optical pump is swept over the $|m_s\!=\!0\rangle$ to $|E_y\rangle$ optical transition at 637 nm, showing clear optomechanical sidebands detuned from the direct dipole-optical transition by ω_m. The authors also demonstrated optomechanically driven Rabi oscillations with Rabi frequencies exceeding 60 MHz, aided by the large strain susceptibility of the NV's excited states [95].

While the NV optical transition can be parametrically driven by SAWs, the NV ground state spin couples to strain with a susceptibility about six orders of magnitude weaker than the NV excited states [68, 185], necessitating alternative approaches to effectively couple the ground state spin to SAWs. By contrast, the excited states of the NV center have a relatively strong strain susceptibility facilitated by an orbital deformation potential of 6.1 THz/% [4], though they decay quickly to the ground state due to optical transitions. Instead, large spin-phonon interactions with the NV ground state can be engineered using a Raman scattering scheme where SAW phonons assist in driving transitions of a spectrally-isolated Λ-type three-level system comprising the $m_s = 0$ ground state, the $m_s = \pm 1$ ground state, and the E_y excited state. The excited-state population can be made negligible by either (1) tuning the resonant optical and acoustic drive amplitudes to realize a dark state, or (2) employing an off-resonant Raman transition, resulting in an effective spin-spin interaction. Using these techniques, Golter *et al.* realized coherent spin-SAW phonon interactions in both time-resolved and spectral-domain experiments [94].

Figure 3.8 shows a PL spectrum where SAW-assisted transitions from the $m_s = \pm 1$ states are selectively addressed using the $|m_s\!=\!0\rangle - |m_s\!=\!\pm 1\rangle$ NV$^-$ center zero-field splitting at 2.88 GHz. The three well-resolved peaks for each $m_s = \pm 1$ spin state correspond to hyperfine splittings of 2.2 MHz from the nitrogen $I\!=\!1$ nuclear spin. Such

nuclear spin-dependent transitions indicate the potential for accessing nuclear spins in SAW quantum acoustics. The transition resonance linewidths of 0.7 MHz agree with predictions from the spin dephasing rate dominated by the nuclear spin bath, suggesting no additional inhomogeneous broadening from the optical and SAW drives. An effective $|m_s = 0\rangle - |m_s = \pm1\rangle$ spin-spin interaction rate of $2\pi \times 0.3$ MHz was extracted by varying the duration of the optical drive pulse, and by analyzing the dependence of the interaction and decay rates on the detuning of the SAW and optical excitation, the authors show the potential for strong spin-phonon coupling with ultralow optical pump power and negligible added spin dephasing [94].

Silicon Vacancy Centers in Diamond

The negatively-charged silicon-vacancy (SiV$^-$) center in diamond has emerged as an attractive spin-photon interface for quantum networking applications, with a Debye-Waller factor of 0.75 and a ZPL transition compatible with downconversion to the telecommunications C-band [207, 99]. The SiV$^-$ center also features high mechanical susceptibilities for its spin transitions on the order of 10 THz/% [191], while still operating as a long-lived spin qubit with a coherence time greater than 10 ms at millikelvin temperatures [275]. This sensitive spin-phonon coupling could enable SAW-SiV$^-$ devices to reach the strong-coupling regime with feasible mechanical quality factors of $Q \approx 10^3$ [191].

Recently, the SiV$^-$ center has been coupled to SAWs in two works demonstrating SAW coherent control of both the SiV$^-$ center electronic spin [177] as well as a single ^{13}C nuclear spin neighboring an SiV center [178]. IDTs with a 3.43 GHz center frequency resonant with a single SiV$^-$ spin drove Rabi oscillations with a Rabi frequency of (34.0 ± 0.2) MHz (Figure 3.9). The SiV$^-$ was initialized and read out optically via optical pumping and fluorescence from a Λ-type three-level system, where the spin qubit levels were coupled to
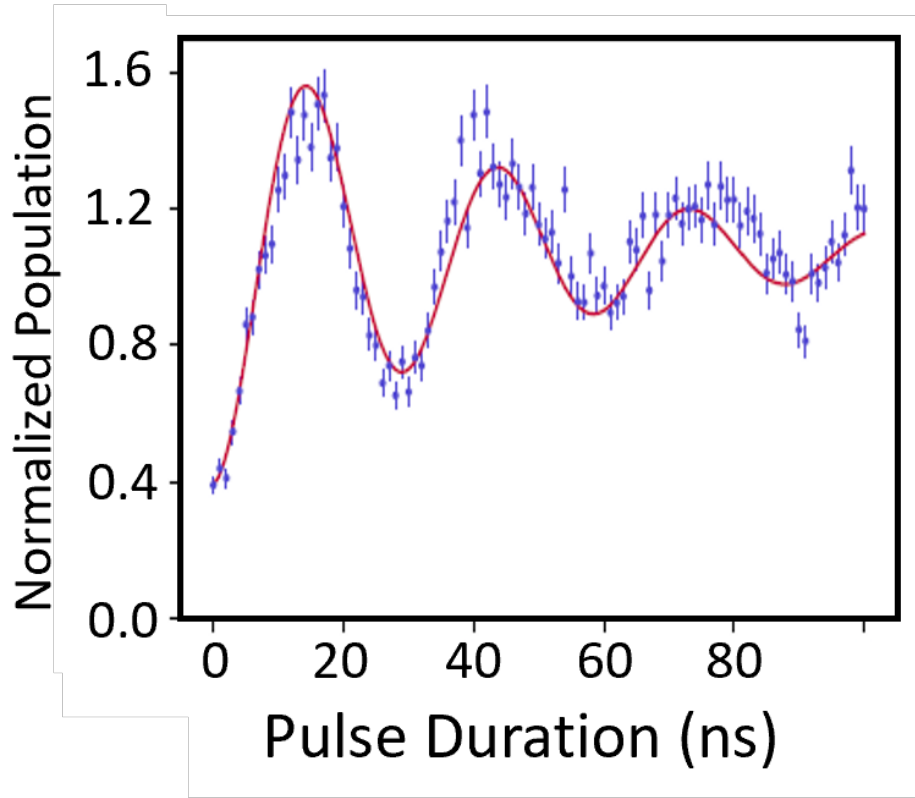
Figure 3.9: Diamond SiV$^-$ center spin Rabi rotations driven by SAWs. Reproduced with permission from Ref. [177].

an orbital excited state via one spin-preserving and one spin-flipping optical transition. Using focusing IDTs enhanced the SiV$^-$ driving efficiency, reducing the required SAW power to between 3 and 350 µW [177], which is promising for operation at millikelvin temperatures to preserve high spin coherence times. The mechanically-driven oscillations of the SiV electronic spin state were then used to control a ^{13}C nuclear spin [178]. The ^{13}C nuclear spin resonance was identified by applying a dynamical decoupling sequence to the IDTs, where periodic dips in the fluorescence from the SiV$^-$ for a pulse separation of 1.578 µs indicated a weakly-coupled spin interacting coherently with the SiV$^-$. The spin could also be selectively initialized, read out, and driven, with fidelities ≈ 0.9 limited
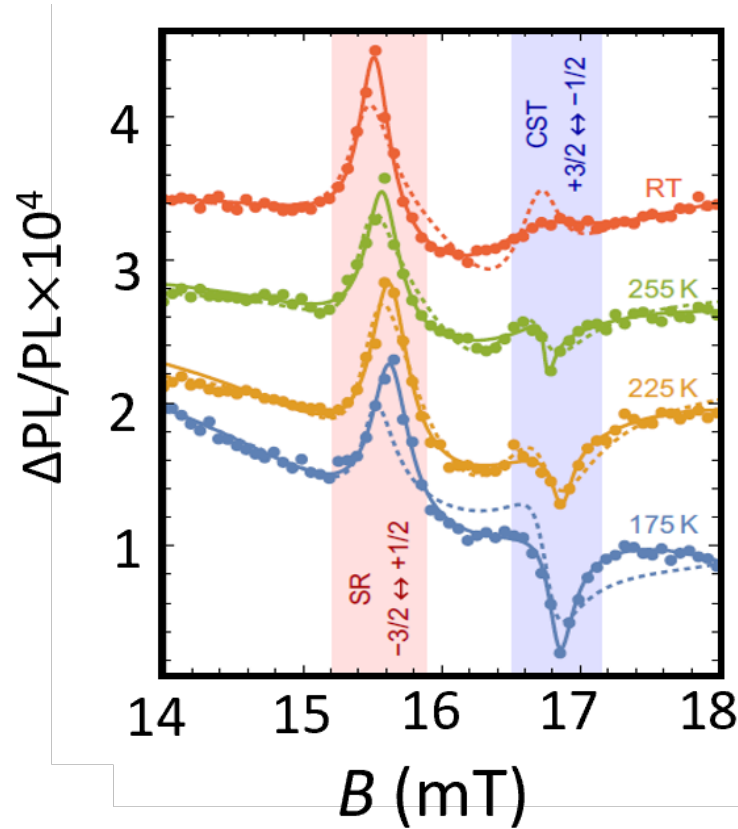
Figure 3.10: ODMR spectrum of V_{Si} centers in 4H-SiC with signatures of acoustic spin resonance (red banner) and coherent spin trapping (blue banner). Reproduced with permission from [116].

by the unintentional partial addressing of other ^{13}C nuclear spins, which may be reduced with longer pulse separation times [178]. These experiments demonstrate nuclear spin control similar to microwave-based experiments with the NV center in diamond [166, 33, 20] with orders of magnitude lower on-chip power.

Defect Centers in Silicon Carbide

Benefiting from a mature semiconductor processing industry, SiC is available in 4-inch wafers of isotopically-purified material, enabling long spin coherence times, and
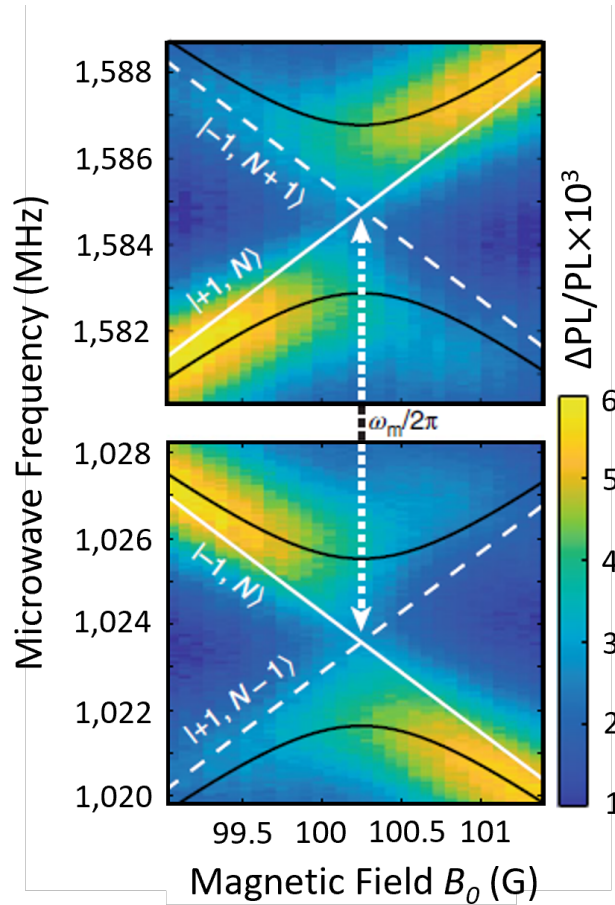
Figure 3.11: ODMR spectrum showing Autler-Townes splittings of VV^0 centers in 4H-SiC, the avoided crossings of hybridized spin-phonon modes as a magnetic field is tuned through the SAW resonator resonance. Reproduced with permission from Ref. [313].

it is commercially available in thin films with robust processing methods [13]. It is no surprise, then, that several optically addressable defect centers have been explored in SiC, including several vacancy, divacancy and antisite intrinsic defects of silicon and carbon, as well as many extrinsic defects [326]. While exploring novel candidates defect centers is an active research area, the silicon-vacancy (V_{Si}) and neutral divacancy ($V_{Si}V_C$) defects in the 4H-SiC polytype have demonstrated isolated single-photon emission and millisecond-long spin coherence times, critical milestones for practical quantum applications [13].

Shortly after their discovery, researchers began investigating these defects' susceptibilities to strain [79] and coupling them to SAWs. Leveraging the $S = 3/2$ spin manifolds of both ground and excited states of the V_{Si} center, Hernández-Mínguez *et al.* demonstrated spin acoustic resonance [113] with control over $\Delta m_s = \pm 1$ and $\Delta m_s = \pm 2$ transitions in both the ground and excited states with tuning provided by a static magnetic field. The same authors later showed that the V_{Si} center can be continuously optically driven while preserving the spin quantization along a predefined spin precession axis. A single SAW drive detuned from both the ground and excited state spin splittings is used to align the Rabi precession axes of the ground and excited-state spins, maintaining the spin projection along the precession axis for times limited only by intrinsic spin relaxation [116] (Figure 3.10).

Using a SAW resonator with focusing Bragg reflectors, Whiteley *et al.* demonstrated strong spin-SAW phonon coupling with spins in $V_{Si}V_C$ defects of 4H-SiC. The $V_{Si}V_C$ ensemble spin manifold with $S = 1$ was controlled by both an IDT, which drove the SAW cavity housing the spins, and a static magnetic field, which tuned the $|m_s = -1\rangle - |m_s = +1\rangle$ Zeeman splitting to selectively address both $\Delta m_s = \pm 1$ and $\Delta m_s = \pm 2$ transitions. Acoustic paramagnetic resonance for both the hh and kk configurations of the $V_{Si}V_C$ defects was measured over the profile of the SAW resonator, which confirmed the purely mechanical driving of the $\Delta m_s = \pm 1$ spin transitions. For the magnetic dipole-forbidden $\Delta m_s = \pm 2$ transition, the authors observed an acoustically-driven Rabi frequency of 1.1 MHz at 25 mW applied RF power to the SAW cavity. The Autler-Townes effect was also measured via the splitting of the $|m_s = -1\rangle$ state as the $\Delta m_s = \pm 2$ transition was tuned into resonance with the SAW cavity, showing hybridization of the spin state and SAW field (Figure 3.11) [313].
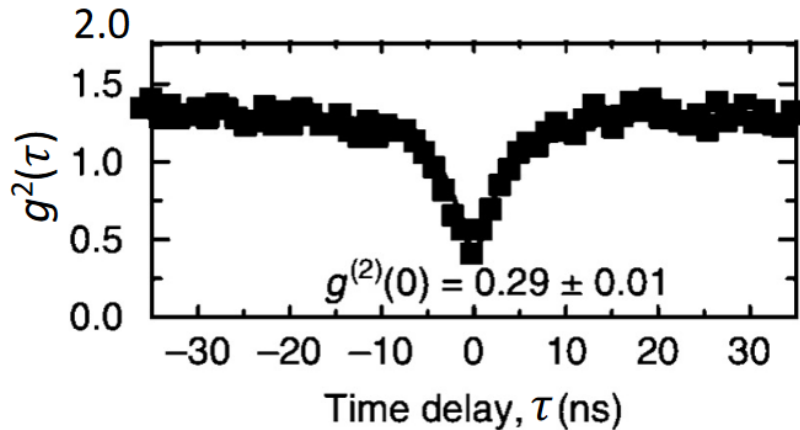
Figure 3.12: Normalized second-order correlation function $g^{(2)}(\tau)$ of an hBN spectral line illustrating photon anti-bunching. Figure reproduced with permission from Ref. [159].

3.3.3   Defects in Layered van der Waals Materials

Within the last decade, many two-dimensional van der Waals layered materials (2DM) such as insulating hexagonal boron nitride (hBN) [287, 182, 31] and semiconducting transition metal dichalcogenides (TMDCs) [285, 269, 148, 44, 110] have emerged as promising platforms for non-classical light emission [15, 195]. What is particularly appealing about quantum emitters in 2DMs is their high sensitivity to strain, motivating extensive research into mechanically controlled single-photon emission [225, 195]. In this section, the focus is on a set of experiments with defects in hBN due to the limited literature available for other 2DM coupled to SAWs. Although PL spectra of SPEs in TMDCs show acoustic phonon sidebands [146, 195] and exhibit spectral shifts when static strain is applied [122, 138], emitters in these materials have not yet been interfaced with SAWs; however, the experiments described below on hBN suggest an efficient coupling with SAWs should be possible for TMDCs and other 2DMs, and that comparable effects to those observed in QDs and color center systems can be expected.

The atomistic deep-level defects in hBN flakes [288, 100, 286], powder [229], and epitaxially grown films [115] have appeared as room-temperature single-photon emitters [168, 3, 31] with transform-limited linewidths as narrow as ≈ 50 MHz at cryogenic temperatures [66]. Various hBN defects exhibit photon anti-bunching when measuring the normalized second-order correlation function $g^{(2)}(\tau)$ at zero time delay, $\tau = 0$ (Figure 3.12 [159, 100], a characteristic signature of single-photon emission behavior [168]. In polarization-resolved micro-photoluminescence (µ-PL) measurements, the emission by hBN defects is highly linearly polarized, originating from the anisotropic structure of the emission center [147, 287, 159].

Recent experiments have demonstrated that defects in hBN are highly sensitive to strain, observed in both static and dynamic tuning of non-classical light emission. Initial studies tuned emission from defects in hBN using static electric [210] and strain fields [100, 288, 193], the latter producing shifts of roughly $1 - 13$ meV/%. SAWs were then investigated for dynamic, time-dependent strain tuning of defects in hBN. SAWs couple to defects in hBN primarily through the hBN deformation potential, with a mechanical susceptibility of 50 meV/% or approximately 10 THz/% [159]; on piezoelectric substrates, they may also couple via the electric field of piezoelectric SAWs, which induces a Stark effect [256]. Non-resonant PL spectroscopy of hBN defects modulated by travelling-wave SAWs exhibit lineshape broadening and split resonances with amplitudes up to 2.5 meV [123, 159]. Figure 3.13 shows an exemplary split resonance with time-binning of the emission windows labelled A, B, C exhibiting clear oscillations at either the SAW frequency (A, C) or twice the SAW frequency (B), consistent with a time-modulated Lorentzian lineshape. Lazić *et al.* showed that the contribution of the SAW's piezoelectric field is independent of its orientation with respect to the defect's symmetry axis and, therefore, can be neglected in comparison to the acousto-mechanical effect mediated through the defect deformation potential [159].
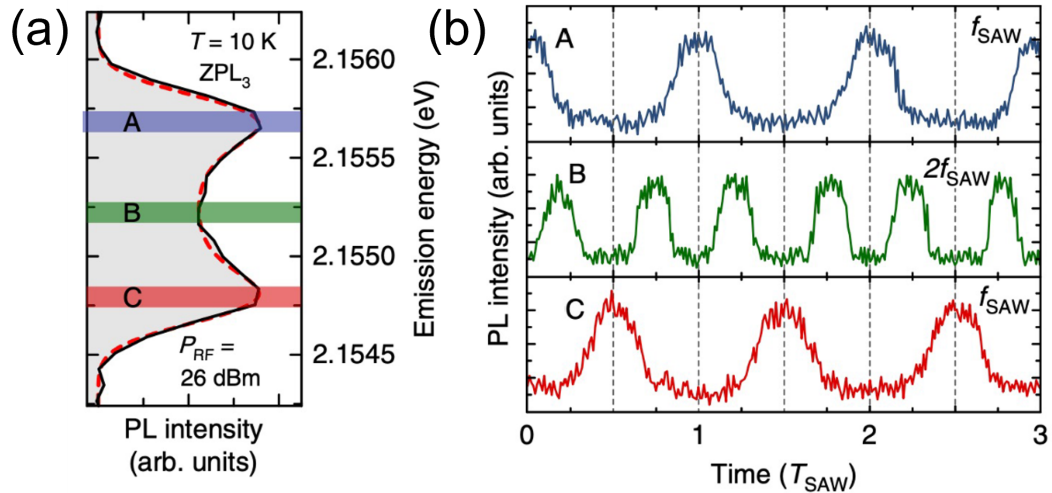
Figure 3.13: (a) Time-averaged photoluminescence spectrum. The dashed red line designates a fit, and the three color-coded rectangles (labelled A, B, C) mark the energy regions used for spectral filtering. (b) All three traces represent the time-dependent emission intensity spectrally filtered at the three color-coded energy regions indicated as A, B, and C. Figures reproduced with permission from Ref. [159].

The large strain susceptibility demonstrated in hBN defects motivates future work integrating hBN defects as well as other 2DM with SAWs. One promising direction is integrating hBN defects into SAW resonators, moving the field into Stage 2 (cf. Table 3.1) and potentially enabling studies of coherent SAW-artificial atom interactions at room temperature. The work detailed in Chapter 7 of this thesis shows PL results integrating both hBN and WSe$_2$ emitters with SAW resonators. These hBN defects must be placed into robust mechanical contact with the SAW substrate. Existing approaches have relied on transferred hBN flakes [123] or powder grains [159], which have non-uniform physical contact with the SAW substrate. Due to the weak interlayer van der Waals mechanical coupling, SAW strain is not efficiently transferred to defects at the top of a multilayer flake or other 2D structure [123], thus limiting yield of optically bright emitters coupled

69

to SAWs. Tackling this challenge opens new possibilities for room-temperature single photon emission, including frequency modulation and spectral stabilization of individual photons.

Chapter 4

Sample Design and Simulation

For the devices presented in this Thesis, 128° Y-X LiNbO$_3$ is used as a piezoelectric SAW substrate due to its high electromechanical coupling ($K^2 = 5.4\%$) along the crystalline X-axis direction [203], as shown in Table 2.3 in Chapter 2. The motivation for this choice of material is to leverage the strengths of LiNbO$_3$ while heterogeneously integrating quantum emitters as well as superconducting electronics into one multifunctional device platform.

While monolithic platforms are being explored for coupling SAWs to quantum dots (QDs) [308], the intrinsically weak piezoelectric effect in III-V materials housing QDs, such as GaAs or AlGaAs, limits the electromechanical coupling strength. Weak piezoelectricity limits the efficiency of converting microwave signals to SAWs through the IDTs, especially for small focusing IDTs which, despite demonstrating large optomechanical coupling rates, g_0, have low electromechanical coupling [60]. Ideally a SAW-QD platform will feature simultaneously large optomechanical and electromechanical couplings for efficient microwave-to-optical transduction. LiNbO$_3$ is one of the most common materials for high bandwidth RF filters, delay lines and correlators for pulse compression radar [[203]]. Indeed, 128° Y-X LiNbO$_3$ not only has the highest electromechanical coupling coeffi-

71
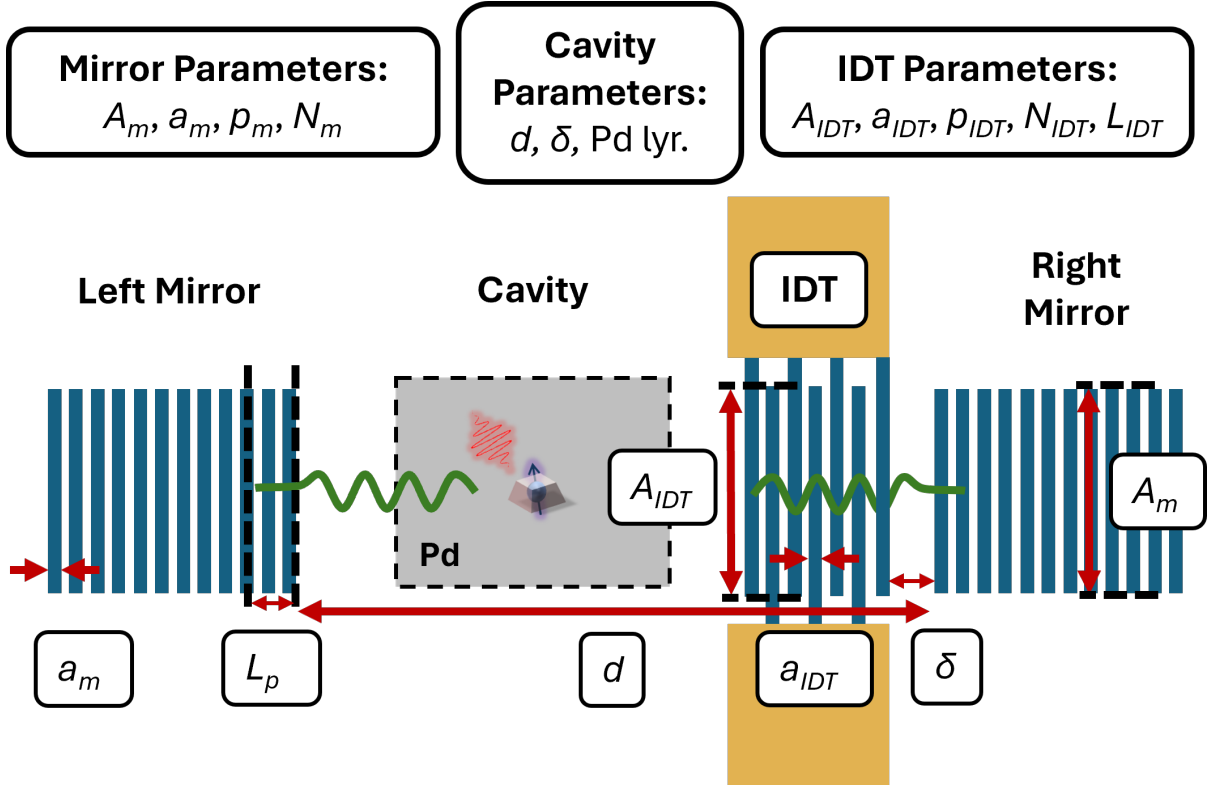
Figure 4.1: Cartoon of Gen-1 resonator with design parameters.

cient of all Rayleigh SAW substrate materials, but also a moderately high phase velocity $v_0 = 3979$ m/s at room temperature [203], useful for constructing high-frequency SAW devices with feasible device feature sizes. The main drawback of LiNbO$_3$ for classical room-temperature applications–the relatively large change in SAW resonance frequency with temperature–is not an issue for devices stabilized at cryogenic temperatures $\lesssim 10$ K, where thermal expansion and related effects are minimal [280]. For these advantages, and due to recent success integrating III/V thin films with LiNbO$_3$ [212], devices were designed with QD epilayers or 2D materials integrated with LiNbO$_3$.

4.1   Gen-1 Resonator Design

The fist generation of SAW resonator devices (Gen-1) were designed to accommodate QD epilayer and 2DM samples and facilitate optomechanical interactions with multiple SAW resonator modes. Shown schematically in Figure 4.1, the resonators are comprised of two Bragg mirrors separated by several hundred SAW wavelengths, allowing large QD epilayer and 2DM samples to be transferred and providing space for IDTs to launch SAWs directly into the resonator. For the Gen-1 SAW-QD devices, the large ($\gtrsim 100\,\mu m$) QD samples enabled many QDs to couple to the SAW field across several resonator modes, which enabled measurements of mode parity-dependent optomechanical coupling and oscillations in the time-domain QD optomechanical response corresponding to the SAW cavity round-trip time [212]. For the Gen-1 2DM devices, this large cavity region increased the number of quantum emitters which could couple to the SAW field, simplifying the process of identifying emitters which exhibited significant coupling to the SAW resonator modes.

Along with more area for sample transfer, the long cavity lengths of the Gen-1 devices also increase their internal quality factors. The internal quality factor of a one-port SAW resonator is directly proportional to the cavity length, L_c relative to the the SAW wavelength, Λ [203]:

$$Q_i = \frac{\omega_r T_c(\omega_r)}{2(1 - |\Gamma|)} = 2\pi \left(\frac{L_c(\omega_r)}{\Lambda} \right) \frac{1}{2(1 - |\Gamma|)}$$

where $T_c(\omega_r), L_c(\omega_r)$ are the cavity round-trip time and length, respectively at a cavity resonance frequency, ω_r; $(1 - |\Gamma|)$ is the fractional SAW energy loss per mirror reflection; and $\omega_r = 2\pi v_p/\Lambda$, where v_p is the SAW phase velocity. This equation shows that the larger the cavity round-trip time, the less frequently the mode energy is partially lost through the SAW mirrors, and therefore the higher the quality factor. While this equation favors larger SAW cavities for a constant mirror loss fraction $1 - |\Gamma|$, there are other

sources of loss which limit the maximum achievable Q in the limit of very large cavities. These loss mechanisms include elastic material propagation loss; acoustic diffraction, due to the finite aperture of the SAW mirrors and SAW material anisotropy; conversion of SAWs to bulk waves, particularly at the interfaces of the IDTs and reflectors; and finite Ohmic losses in the electrodes, which occur even for superconductors at microwave frequencies [293].

The upper limit of the SAW internal quality factor accounting for only propagation loss can be estimated for the 128° Y-X cut LiNbO$_3$ substrate, using the measured elastic material propagation loss measured in Ref. [25] of $\alpha_{visc} = 70$ Np/m in a SAW resonator with a resonance at 3.95 GHz. From Equation 3 in Ref. [179], $Q_i \approx 44{,}000$, which is likely a lower bound given the resonators in this work are operating at lower frequencies, and the propagation loss has a super-linear scaling with frequency [179]. As shown in Chapter 6 and Chapter 7, the typical internal quality factors of these Gen-1 devices is $\approx 10{,}000$, with a highest measured internal quality factor being 16,815. Therefore, propagation loss is likely not the dominant loss factor for these devices, and further device engineering will be discussed in Section 4.2 to reduce other sources of loss, including diffraction and mirror reflection loss, while simultaneously reducing the cavity length in order to improve the optomechanical coupling rate.

The first generation devices operated at relatively low frequencies ($f < 1$ GHz), which prevented the devices from reaching the ground state with cryogenic cooling alone in a dilution refrigerator. Part of the reasoning for designing devices at lower frequencies was to compare the quality factors of select devices with superconducting electrodes to those with normal metal electrodes and identical design parameters in Ref. [212]. Another factor in the decision was that the experimental setup for electromechanical and optomechanical testing in a dilution refrigerator was not going to be ready by the end of Gen-1 device design and fabrication, hence operating at lower frequencies was acceptable.

Tables with the design parameters of the devices under study are shown below for the data in Chapter 6 and Chapter 7 for the Gen-1 QD and the 2DM devices, respectively.

Device Name	IDT Geometry	f_0	λ_0	A_{IDT}	a_{IDT}	p_{IDT}	N_{IDT}	L_{IDT}
Res0	Split-1 IDT	300 MHz	13.3 μm	350 μm	$\lambda_0/4$	$\lambda_0/2$	41	$(2N_{IDT}-1)a_{IDT}$
Res1QdPd	Split-1 IDT	400 MHz	10.0 μm	350 μm	$\lambda_0/4$	$\lambda_0/2$	41	$(2N_{IDT}-1)a_{IDT}$
Res2QdPd	Split-1 IDT	400 MHz	10.0 μm	350 μm	$\lambda_0/4$	$\lambda_0/2$	41	$(2N_{IDT}-1)a_{IDT}$
Res2Qd	Split-1 IDT	400 MHz	10.0 μm	350 μm	$\lambda_0/4$	$\lambda_0/2$	41	$(2N_{IDT}-1)a_{IDT}$
Res3QD	Split-1 IDT	400 MHz	10.0 μm	350 μm	$\lambda_0/4$	$\lambda_0/2$	41	$(2N_{IDT}-1)a_{IDT}$
Res4QD	Split-1 IDT	400 MHz	10.0 μm	350 μm	$\lambda_0/4$	$\lambda_0/2$	41	$(2N_{IDT}-1)a_{IDT}$
Res1WSe	Split-1 IDT	300 MHz	13.3 μm	350 μm	$\lambda_0/4$	$\lambda_0/2$	41	$(2N_{IDT}-1)a_{IDT}$

Table 4.1: IDT parameters for the Gen-1 devices.

Device Name	f_0	λ_0	A_m	a_m	p_m	N_m	L_m
Res0	300 MHz	13.3 μm	350 μm	$\lambda_0/4$	$\lambda_0/2$	$\lambda_0/4$	200
Res1QdPd	400 MHz	10.0 μm	350 μm	$\lambda_0/4$	$\lambda_0/2$	$\lambda_0/4$	200
Res2QdPd	400 MHz	10.0 μm	350 μm	$\lambda_0/4$	$\lambda_0/2$	$\lambda_0/4$	200
Res2Qd	400 MHz	10.0 μm	350 μm	$\lambda_0/4$	$\lambda_0/2$	$\lambda_0/4$	200
Res3Qd	400 MHz	10.0 μm	350 μm	$\lambda_0/4$	$\lambda_0/2$	$\lambda_0/4$	200
Res4Qd	400 MHz	10.0 μm	350 μm	$\lambda_0/4$	$\lambda_0/2$	$\lambda_0/4$	200
Res1WSe	300 MHz	13.3 μm	350 μm	$\lambda_0/4$	$\lambda_0/2$	$\lambda_0/4$	200

Table 4.2: Mirror parameters for the Gen-1 devices.

Device Name	f_0	λ_0	d	δ	Emitter	Pd Layer
Res0	300 MHz	13.3 μm	85 λ_0	20 λ_0	No	No
Res1QDPd	400 MHz	10.0 μm	440 λ_0	30 λ_0	Yes	Yes
Res2QDPd	400 MHz	10.0 μm	220 λ_0	30 λ_0	Yes	Yes
Res2QD	400 MHz	10.0 μm	220 λ_0	30 λ_0	Yes	No
Res3QD	400 MHz	10.0 μm	110 λ_0	30 λ_0	Yes	No
Res4QD	400 MHz	10.0 μm	60 λ_0	30 λ_0	Yes	No
Res1WSe	300 MHz	13.3 μm	85 λ_0	20 λ_0	Yes	No

Table 4.3: Cavity parameters for the Gen-1 devices.

4.1.1   Verifying Gen-1 Strain Simulation

It is difficult to gauge the certainty of a finite-element simulation, especially for the behavior of SAW devices in this thesis. The piezoelectric effect complicates the relationship between input and output, requiring more physics interfaces and material constants to compute the device response. Resolving the small relative sizes of the IDT electrodes and the etched mirror corrugations significantly increases the computational cost of finite-element modelling because of the dense simulation mesh required. In addition, it is also not known how the material constants in the deposited NbN films, which are likely amorphous [57], compare to those in available literature on the elastic properties of crystalline NbN films.

To independently verify the simulation methodology used to produce the data shown in Figure 4.3 and the strain values used for the calculation of the WSe$_2$ and h-BN emitters, a simulation was developed to recreate the results of a one-port SAW device in Ref. [244]. Rummel *et al.* employed finite-element modelling for their simulation data, which shows excellent agreement with experimental measurements of fabricated SAW devices. Their one-port resonator has notable differences from the Gen-1 and Gen-2 devices in this work: it is composed of two IDTs, versus a single IDT for the Gen-1 devices, and it is composed of different materials, namely a GaAs SAW substrate and Al IDT and mirror electrodes. The physics and operating principle of the device remain the same, however, and the detailed description of the device simulation facilitates a convenient comparison to the simulation methods in this work.

Figure 4.2 shows a comparison of the microwave S_{21} parameter simulated and measured in a one-port SAW resonator in Figure 3 (b) of Ref. [244], versus a recreation of the simulated data using the same modelling techniques as those used for the Gen-1 devices. The S_{21} response shows good quantitative agreement over the simulated frequency
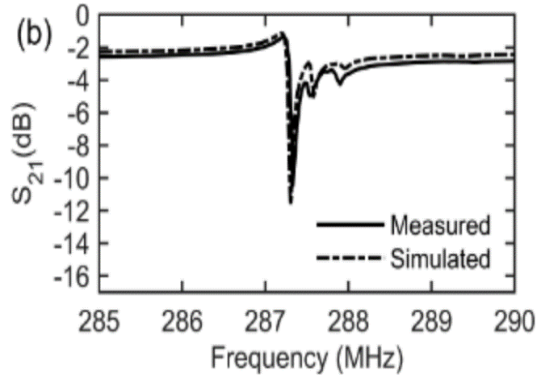
(a) Ref. [244] Data
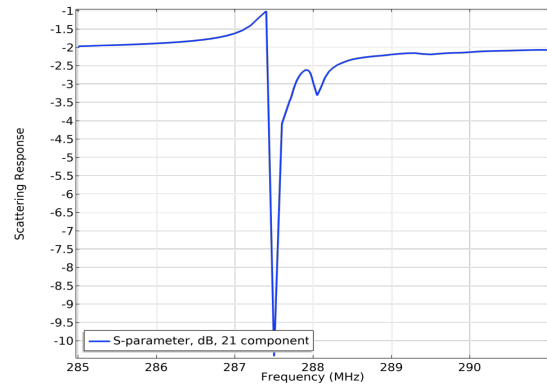
(b) Replicated Simulation Data
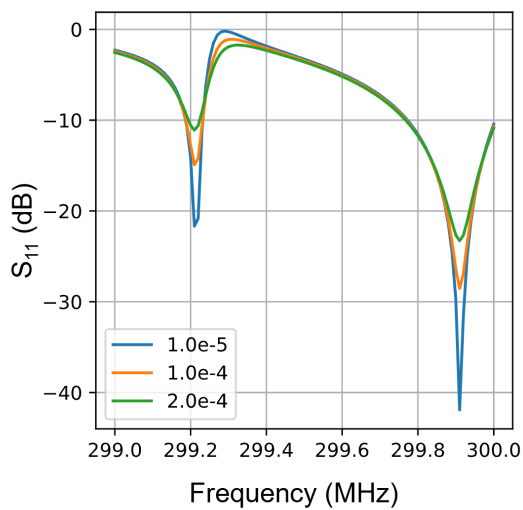
(c) Adjusting Loss Factor
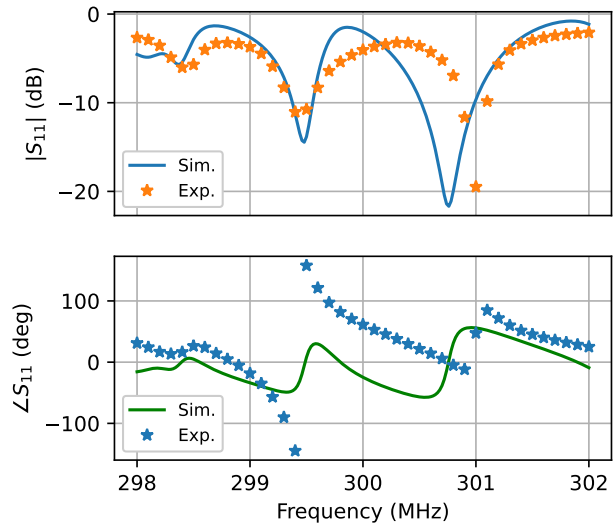
(d) Gen-1 S_{11} Parameter

Figure 4.2: a Reprinted data from Ref. [244]. b Replicating the S_{21} parameter simulation data in Ref. [244]. c Coarse sweep of the isotropic mechanical loss factor used for the strain simulation of the Gen-1 SAW-2DM devices. d Reproduction of the S_{11} parameter experimental data with a simulation from device (blue).

span. Recreating the S_{21} parameter simulation data required using the same SAW device geometry and material parameters, as well as meshing with a super-fine resolution ≈ 100 nm at the surface of a SAW resonator with a wavelength of 10.0 μm at its resonance frequency of 287.5 MHz. The S_{21} response is affected by the mechanical damping of the SAW substrate, which was quantified in Ref. [244] by introducing a material isotropic damping factor, η, which reduces the depth of the resonance peaks. This is shown in Figure 4.2c. Using the loss factor as a tuning parameter to adjust the depth of the S_{11} parameter resonance dips, a plot of S_{11} was created over the same frequency range as a scan of device **Res1WSe** in 4.3. The plots show qualitative agreement with the relative placement of the first two resonances at 298.4 and 299.5 MHz.

4.1.2 Strain and Zero-Point Motion Simulations

For the Gen-1 SAW-2DM devices, an FEM simulation was developed to help determine the strain susceptibilities of the WSe$_2$ and h-BN emitters by simulating the generated tensile in-plane strain for the specific SAW resonators with 2DM samples. With the tensile strain for a given applied power to the device, the strain susceptibility was calculated by taking the ratio of the observed optomechanical modulation ΔE to the simulated strain at the same applied power. Figure 4.3a shows an illustration of the simulation geometry, representing a 2D cross-section of the device along the propagation direction and the surface normal. The region in green is the LiNbO$_3$ substrate; the region in red is where the strain field was evaluated, coinciding with the location of sample transfer; and the regions in blue on the bottom and sides of the simulation geometry are PML boundaries. Figure 4.3b shows the extracted maximum value of the in-plane tensile strain in blue (S_{11} component, not to be confused with the microwave S_{11} parameter) as a function of the applied power to the IDT, assuming negligible loss in the cabling from the
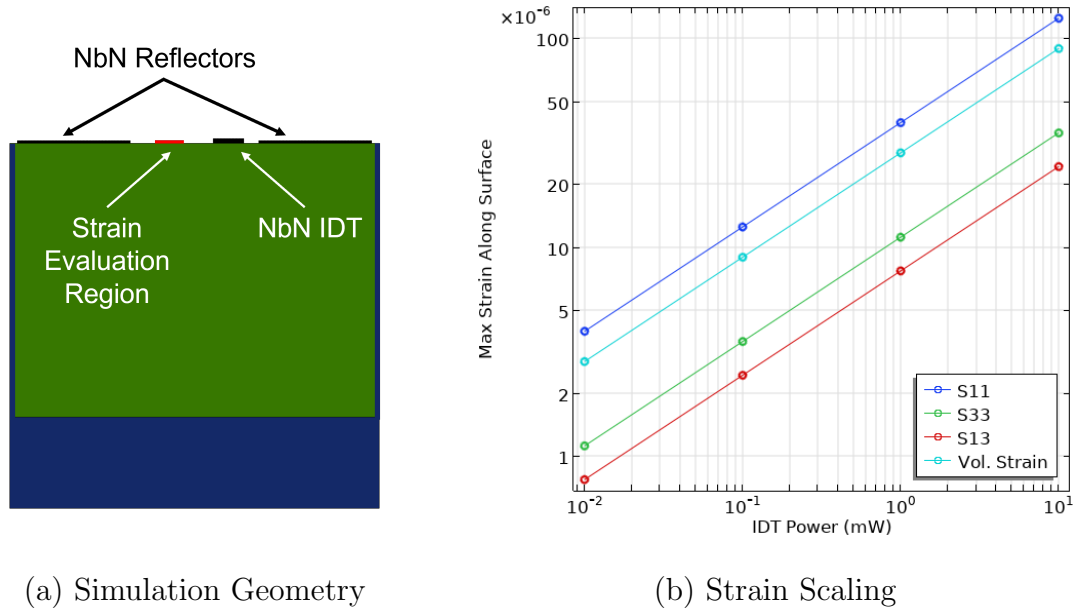
(a) Simulation Geometry   (b) Strain Scaling

Figure 4.3: Strain simulation for the Gen-1 device **Res1WSe** in 4.3

signal generator. The material parameters for LiNbO$_3$ were extracted from Ref. [280], and the elastic, piezoelectric, and permittivity tensors were then rotated 38° to simulate a 128° Y-X LiNbO3 substrate, as given in B. NbN reflectors and IDT electrodes were simulated with electrostatic floating-potential and terminal and ground boundary conditions, respectively. The coupled piezoelectric equations of motion were solved using a frequency-domain simulation with 0 dBm power applied to the IDT electrodes. Perfectly matched layers were applied to the boundaries of the simulation domain to absorb any scattered radiation. The strain amplitude was extracted by taking the maximum value of the tensile strain component oriented along the SAW propagation direction between the IDT and the NbN reflector placed further from the IDT. Over the frequency range of 299–301 MHz, a maximum tensile strain amplitude of 0.0119 % at 0-dBm applied IDT power coincided with a SAW cavity resonance at 299.665 MHz, in good agreement with the observed resonance at 299.425 MHz from the microwave S$_{11}$ parameter measurement compared to the simulated S$_{11}$ parameter, shown in Figure 4.2d.

The zero-point motion amplitude of a SAW resonator mode is the displacement magnitude caused by the zero-point energy of the mode, $\hbar\omega/2$. For a quantum harmonic oscillator in its ground state, the kinetic and potential energy terms are equal in magnitude. The zero-point motion amplitude u_{ZPM} can then be calculated:

$$\hbar\omega/4 = \frac{1}{2}m_{eff}\omega^2 u_{ZPM}^2 \rightarrow u_{ZPM} = \sqrt{\frac{\hbar}{2m_{eff}\omega}} = \sqrt{\frac{\hbar\omega}{2\rho\,\omega A_{eff}t_{eff}}} \tag{4.1}$$

Here, m_{eff} and A_{eff} are the effective mass and cross-sectional area of the SAW mode, respectively; ρ is the material density of the SAW substrate, and t_{eff} is the effective out-of-plane "thickness" of the SAW mode.

The zero-point motion of the Gen-1 devices was calculated in an FEM simulation by computing the effective mode area, A_{eff}, and using the length of the cavity mirror aperture, A_m for the thickness t_{eff} . First, the spatial mode profile was simulated with a similar setup to the strain simulation; then the effective mode area was calculated as the normalized sum of the modal strain energy, kinetic energy and electromagnetic energy densities integrated over the 2D simulation domain:

$$A_{eff} = \frac{\int d^3r(W_k + W_S + W_{EM})}{\text{Max}\{W_k + W_S + W_{EM}\}} \tag{4.2}$$

Equation 4.1 was then used to determine the zero-point motion of Device **Res1WSe** in 4.3, yielding 8.4×10^{-18} m, equating to a zero-point strain amplitude of 4.0×10^{-12} using the relation $\epsilon_{ZPM} = (2\pi/\Lambda)u_{ZPM}$ from Ref. [251]. This zero-point motion amplitude corresponds to a vacuum optomechanical coupling rate of ≈ 3 kHz, using the strain susceptibility of InAs QDs of $\approx 1\times 10^{15}$ [194]. This relatively low vacuum optomechanical coupling rate, which is much lower than the QD linewidth and the SAW cavity damping rate, prevents the Gen-1 resonators from entering the quantum regime, as was discussed in Chapter 3. However, the much smaller mode volumes and improved quality factors of the Gen-2 devices are promising to realize an optomechanical system with $C_{0,q} > 1$,

Taper parameters:
Taper period shift, Δp
Taper slope parameter, η
No. taper corr., N_{taper}

Cavity parameters:
Cavity length, L_{cav}
No. cavity corr., N_{cav}

Mirror parameters:
Etch width, w_{etch}
Etch depth, h_{etch}
No. mirror corr., N_{mirror}

$t_{epilayer}$

d_{QD}

Left Mirror

Left
Taper

Cavity

Right
Taper

Right Mirror

L_{cav}

z (001) (GaAs)

y x $\langle 110 \rangle$ (GaAs)
      X-axis (LiNbO$_3$)
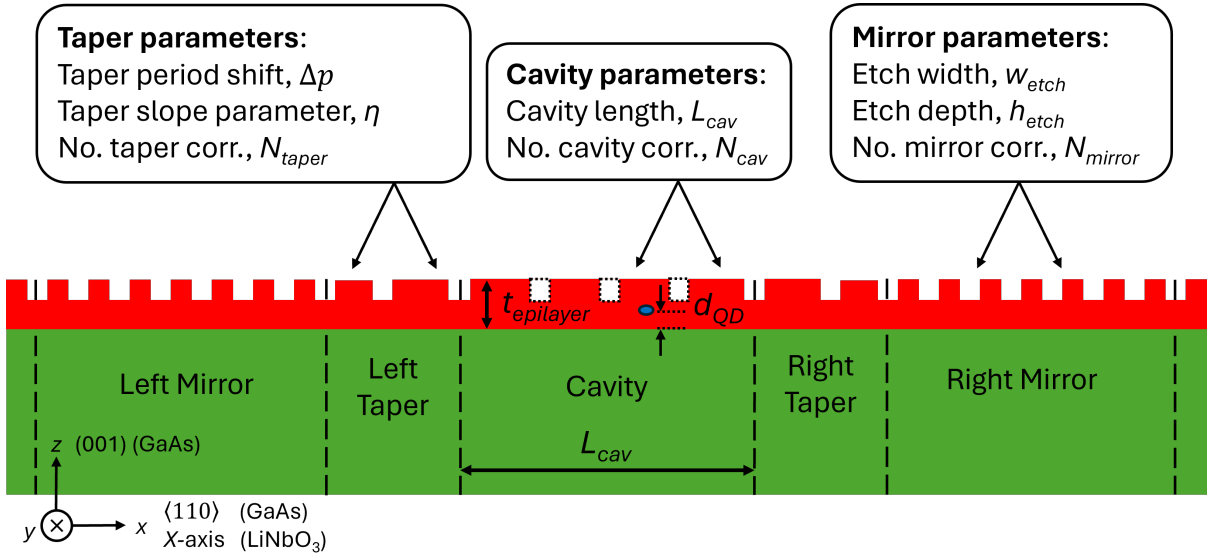
Figure 4.4: Design parameters of Gen-2 devices

which has not yet been demonstrated for SAWs, although it has been demonstrated with cavity optomechanics [235].

4.2   Gen-2 Resonator Design

The second generation of devices in this thesis (Gen-2) was designed to support ultralow mode volumes and improved quality factors compared to the Gen-1 devices. Figure 4.4 shows a representative SAW resonator for the Gen-2 devices, with design parameters labeled for the cavity, mirror and adiabatic taper regions. While the Gen-1 SAW-QD devices integrated QD epilayer onto the LiNbO$_3$ substrate after SAW device fabrication, the Gen-2 SAW-QD devices were designed with a QD epilayer bonded to the substrate at the start of device fabrication. This layer is shown in Figure 4.4 in red, with thickness $t_{overlayer}$ on top of the LiNbO$_3$ substrate, which is shown in green. The Gen-2 SAW-2DM devices do not include a bonded epilayer but otherwise have identical design parameters. Like with the Gen-1 devices, the 2DM flake is transferred onto the patterned
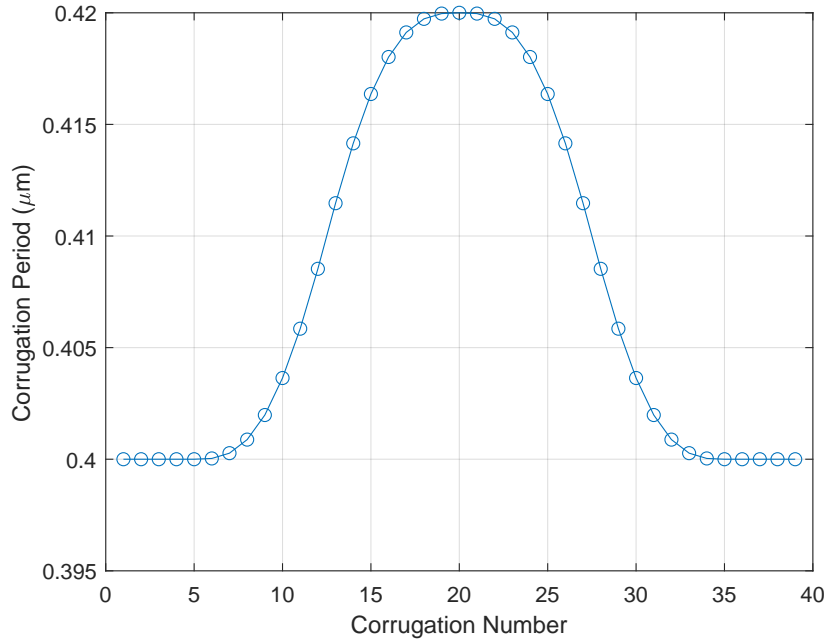
Figure 4.5: SAW taper corrugation profile in an example Gen-2 SAW device

Gen-2 SAW cavity after device fabrication, with some devices including a spacer region of unpatterned substrate over a length L_{cav} for facilitating 2DM flake transfer.

From a fabrication and device engineering perspective, one of the most important design decisions was whether to use deposited metallic electrodes or etched corrugations to form the mirrors comprising a SAW resonator. While deposited mirror electrodes can be integrated within the fabrication process of patterning the IDT electrodes, simplifying fabrication and device complexity, etched Bragg reflectors yield higher quality factors in one-port SAW resonators [203]. For this reason, in contrast to the Gen-1 devices, the Gen-2 devices in this thesis use etched corrugations for the mirrors.

These Bragg reflectors include an adiabatic transition or "taper" region to the center of the cavity to confine the fundamental Rayleigh SAW resonance. This taper design has been shown to realize SAW resonators with both low mode volumes $< 2\Lambda^2$ in cross-

sectional area and higher quality factors than those demonstrated in the Gen-1 devices at higher frequencies [262]. Figure 4.5 shows an example profile of the Gen-2 SAW-QD resonator mirror-to-cavity region taper with a periodicity shift of $\delta p = 0.05\Lambda$. The smooth curvature of the profile minimizes abrupt transitions in the SAW mode which could induce scattering to bulk waves. The taper also approximates a quadratic profile near the center of the cavity, which has been demonstrated in photonic crystals to be ideal for inducing the desired Gaussian envelope function [231].

Another important design choice was whether to intentionally extend the central SAW cavity region, either with an unpatterned spacer region, or with multiple periods N_{cav} of etched corrugations with a periodicity matching that of the ends of the adiabatic tapers $p_{cav} = p_{mirror} + \delta p$. An unpatterned spacer can facilitate integrating IDTs within the resonator, and it can provide a planar surface to which samples may be transferred via epitaxial liftoff[321] or Van der Waals transfer[15], such as with the Gen-1 devices. An extended cavity region increases the number of quantum emitters which may couple to the SAW cavity mode, which can be useful for lower-density emitter samples or those where the yield of emitters coupling to the SAW cavity modes is low, such as in the Gen-1 2DM devices with h-BN emitters, with a yield of 10 %. For the Gen-2 devices, however, the resonator mirror separation was made much smaller to reduce the SAW mode volume and enhance the optomechanical interaction strength. An unpatterned spacer region in the range between $\approx$ 20-40 μm long was added to some of the SAW-2DM devices to reduce the possibility that the patterning of the SAW cavity mirrors might interfere with the transfer of 2DM to the cavity.

The Gen-2 SAW devices have some designs with an IDT inside and some outside of the resonator mirrors, the former of which requires the mirrors to be separated by several acoustic wavelengths to accommodate the IDT. An IDT integrated within a one-port SAW resonator generates SAWs which are immediately coupled into the cavity. Devices
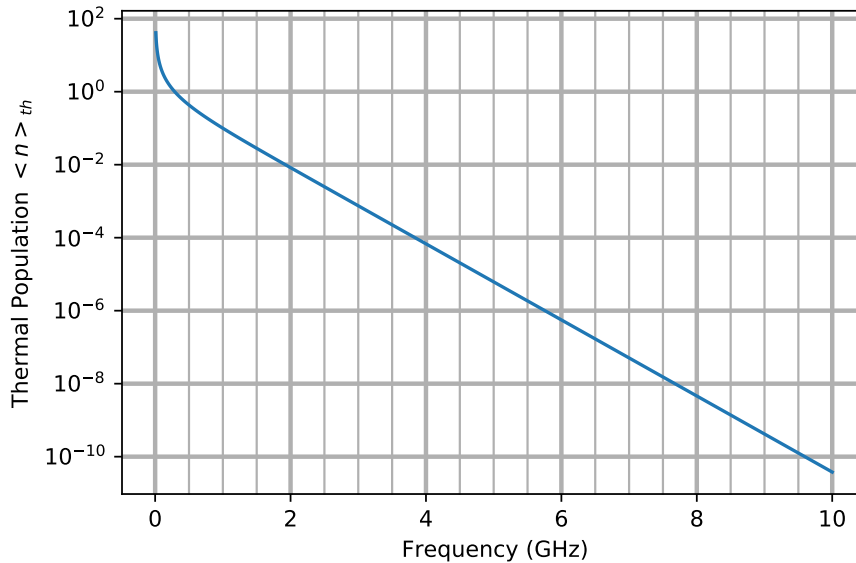
Figure 4.6: Thermal phonon population at T = 20 mK

with IDTs inside of the resonator can therefore generate larger SAW amplitudes per unit of applied IDT power; however, they also suffer from an additional loss channel of SAWs being converted back into electromagnetic microwave radiation by the IDTs through the direct piezoelectric effect. There may be additional loss channels introduced to the device from IDTs integrated within the cavity, such as conversion to bulk acoustic waves at the edges of the IDT electrodes and the mirrors [203]. On the other hand, devices with IDTs outside of the mirrors generate SAWs which must pass through the mirrors to be stored within the cavity region of the resonator. This is similar to optical free-space Fabry-Perot resonator filters, where a laser on resonance with one of the Fabry-Perot modes will couple a small amount of light into the cavity, which then builds in intensity in the steady-state and can become a large amount for cavities with sufficiently high mirror finesse. Likewise, for SAW cavities with strong mirrors, most of the SAW energy generated by an IDT outside of the cavity will be reflected; however, the SAW energy

transmitted into the SAW cavity will be greatly enhanced by the cavity buildup factor by potentially multiple orders of magnitude.

4.2.1 Operating Frequency, Wavelength, and QD Epilayer Thickness

After the general design choices, the next step of the Gen-2 design methodology was to determine the operation frequency and wavelength. The main constraint on the operation frequency of the Gen-2 devices was that the frequency is high enough to reach the quantum ground state of SAW mechanical motion when the device is cryogenically cooled to the base temperature of a dilution refrigerator: approximately 20 mK for the dilution refrigerator available for this work. Figure 4.6 shows the Bose-Einstein distribution for thermal phonons over the range of MHz-GHz frequencies at a dilution refrigerator base temperature of 20 mK. SAW resonator frequencies $f \approx \frac{k_b T}{h} \approx 2$ GHz are sufficient to reach the quantum ground state of motion in standard dilution refrigerator environments ($T \approx 10\text{-}30$ mK), using a heuristic definition for the ground state of requiring the average thermal phonon population, $\langle n \rangle_{th} < 10^{-2}$. However, there may be uncertainty in the true sample temperature, especially with thermally insulating samples such as LiNbO$_3$. Also, when driving an optomechanical device with applied optical and/or microwave power, there is often some absorption heating which limits the device from reaching the base temperature of the dilution refrigerator [189]. The Gen-2 SAW-2DM devices were designed to operate at 2.0 GHz, the lower limit to reach the ground state, to simplify photoluminescence measurements of the optomechanical sidebands of h-BN emitters. Other constraints on the SAW device operation frequency/wavelength include any technical limitations of the measurement electronics and optics, constraints on the minimum feature size and repeatable etch depth attainable with current nanofabrication

Epi GaAs (80 nm)

InGaAs QDs (5 nm)

Epi GaAs (185 nm)

$Al_{0.80}Ga_{0.20}As$ etch stop (250 nm)

Bulk GaAs
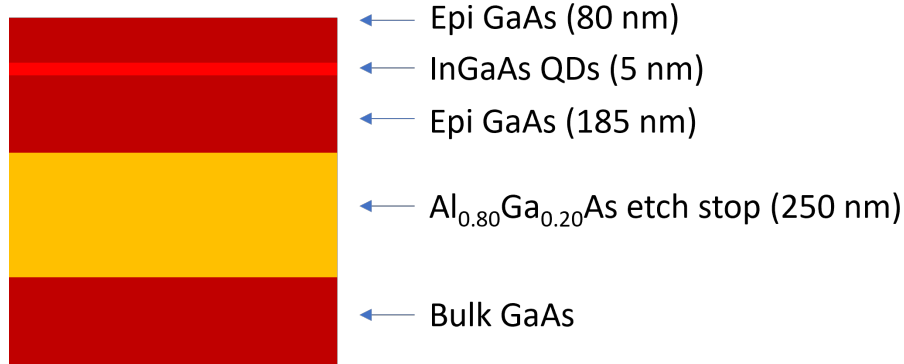
Figure 4.7: GaAs epilayer growth stack for the Gen-2 SAW-QD devices.

technology, limitations on the device footprint (below ≈ 100 MHz, device sizes reach several millimeters and can even exceed several centimeters), and compatibility with the operation frequencies of other atomic or solid-state microwave qubit platforms, such as superconducting qubits [202, 247, 5] and electrostatic quantum dots [204, 301, 133]. The Gen-2 SAW-QD devices were designed to operate at 4.0 GHz to further limit the thermal phonon population, as well as to operate closer to the typical frequencies of solid-state microwave qubit platforms.

For the Gen-2 QD-SAW devices, the thickness of the QD epilayer $t_{epilayer}$ and placement of the QDs within the epilayer d_{QD} needed to be decided. These parameters are shown in Figure 4.4. The epilayer thickness determines the optimal SAW wavelength for the SAW design frequency, and the placement of the QDs within the epilayer is an important factor in maximizing the volumetric strain at the position of the QDs. While QDs could be grown at or near the surface ($\lesssim 100$ nm), surface states can cause large amounts of spectral diffusion for QDs, motivating work into passivating the GaAs surface to reduce the surface state density [181]. Recent work on passivating GaAs surfaces with deposited AlO_x or AlN_x passivation layers and N_2H_4 chemical treatments showed that QDs grown at least 60 nm from the surface experience minimal broadening of the

86

homogeneous linewidth or spectral diffusion [46]. For this reason, to reduce the risk of proximity to the surface broadening the QD inhomogeneous linewidth or resulting in spectral diffusion, the QD epilayer was designed to be 80 nm from the surface (when bonded, 80 nm from the LiNbO$_3$ substrate) and 80 nm from the sacrificial AlGaAs layer.

A total thickness of $t_{epilayer} = 270$ nm for was determined to be a good tradeoff value for the QD epilayer, being thin enough to exploit the piezoelectric LiNbO$_3$ substrate and maximize the strain intensity near the QDs while also thick enough to protect the QDs from surface states, even accounting for etching into the GaAs epilayer to form the corrugations defining the SAW cavities. Hereafter, all figures shown in this thesis for the Gen-2 SAW-QD design use a GaAs thickness of 270 nm and SAW wavelength of 800 nm unless otherwise stated. Because the piezo-optomechanical coupling rate increases with the SAW frequency but decreases with the QD epilayer thickness [212], the QD epilayer needed to be acoustically thin for maximizing the optomechanical interaction. The GaAs epilayer was designed to work over multiple frequency values (≈ 4 GHz and ≈ 1 GHz), requiring an estimate of ≈ 110 nm of additional GaAs material to be added from the QD position on the sacrificial layer side, plus 80 nm to account for surface effects. The full GaAs epilayer stack is shown in Figure 4.7.

Determining the design wavelength from the design frequency requires knowledge of the Rayleigh SAW speed of sound in the substrate material, which was calculated separately for the Gen-2 SAW-QD and 2DM devices. For the SAW-2DM devices, the Rayleigh SAW mode is dispersionless because the SAW propagates only in LiNbO$_3$, and therefore the speed of sound only needed to be calculated once to convert between any SAW frequency and wavelength. For the QD-SAW devices, however, the QD epilayer causes considerable dispersion such that an iterative method is necessary to determine the effective speed of sound for the SAW material heterostructure, using the design
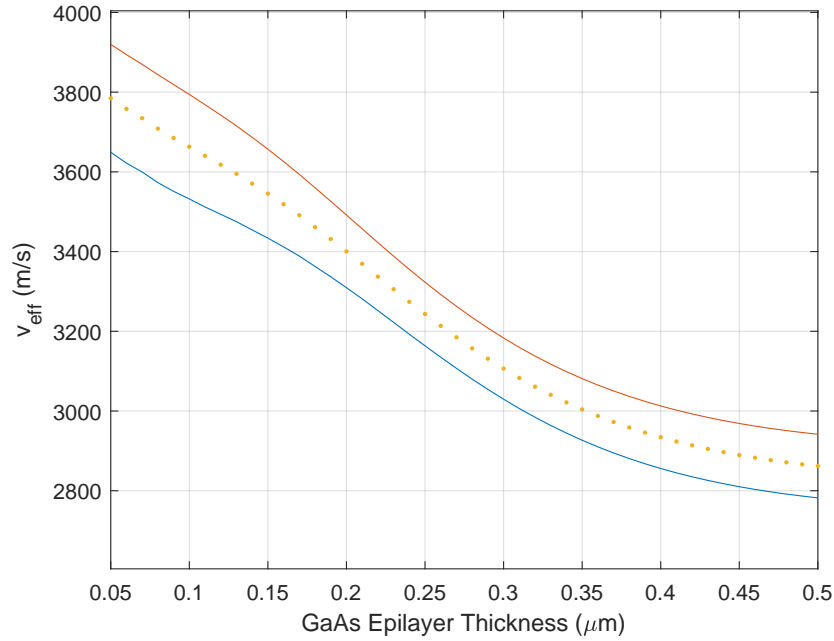
Figure 4.8: Effective velocity (dotted line) and upper and lower bands (solid lines) versus GaAs epilayer thickness in a GaAs-LiNbO$_3$ heterostructure for $\Lambda_{SAW} = 800$ nm.

frequency as input. In a simulation script developed to calculate this effective speed of sound, an initial guess on the design wavelength is used in a mode solver along with the design thicknesses of the epilayer and substrate, and then the mode solver returns the eigenfrequencies of SAW propagating modes with the design wavelength. The user must update the input design wavelength using the calculated Rayleigh SAW eigenfrequency and continue running the simulation, using the calculated effective velocity to update the SAW wavelength. For the simulations in this thesis, a typical estimate of the design wavelength within $\approx 10\%$ of the final design wavelength only required 2-3 rounds of iterative mode solving to converge to a constant value, which altogether takes less than one minute on a standard desktop computer.

Figure 4.8 shows the calculated effective velocity for a range of different GaAs epilayer
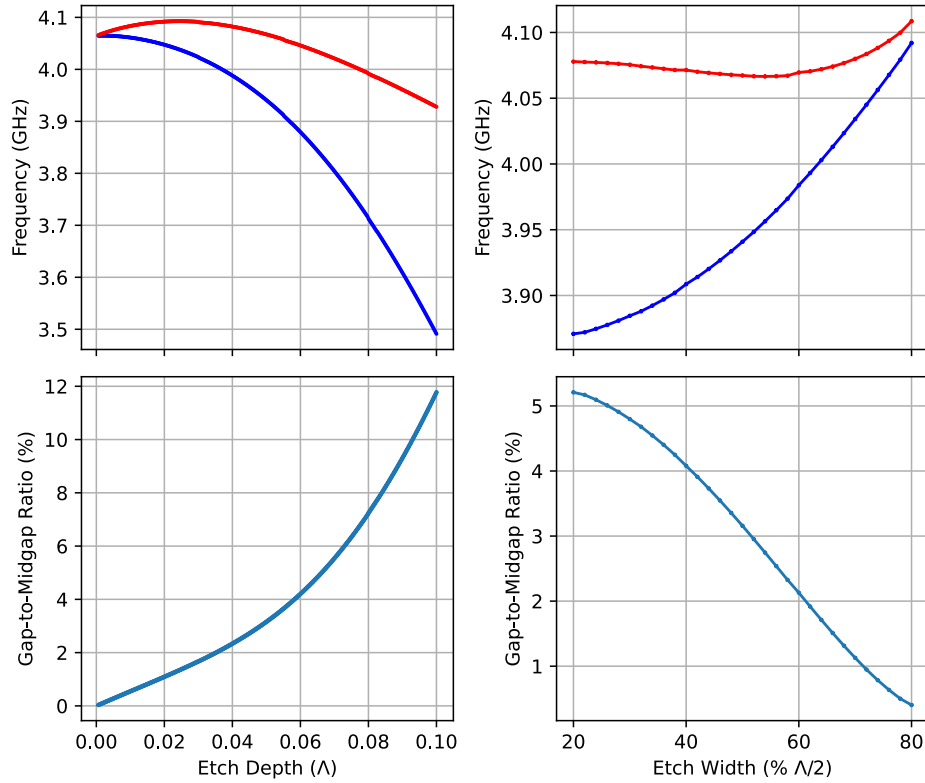
Figure 4.9: Sweeping the etch depth and width for a periodic array of etched corrugations forming a SAW mirror in the Gen-2 SAW-QD design.

thicknesses on $LiNbO_3$ from the the upper and lower SAW mirror band eigenfrequencies. This effective velocity, shown as a dotted line between the upper and lower mirror bands, decreases monotonically with the GaAs epilayer thickness, until eventually it begins to plateau at a GaAs epilayer thickness $\gtrsim \Lambda/2$. For the design epilayer thickness of $0.27\ \mu m$ used for the Gen-2 devices in this thesis, the effective velocity is 3185 m/s, which enables fabrication of SAW phononic crystal devices with a design frequency of approximately 4.0 GHz at a wavelength of 800 nm.

4.2.2   Cavity and Mirror Parameter Optimization

Using the effective velocity for the SAW-QD heterostructure above, another simulation was constructed with a single mirror corrugation etched into the GaAs/LiNbO$_3$ heterostructure to isolate the impact of changing the SAW corrugation etch parameters on the SAW resonator. By applying periodic boundary conditions to the left and right edges of the simulation domain, this model acts as an infinite array of mirror corrugations. A mode solver then computes the eigenfrequencies and mode profiles of the upper and lower SAW band edges for SAWs matching the reflection wavelength of the mirror corrugations. Figure 4.9 shows the extracted eigenfrequency data for the upper and lower SAW band edges, showing how the mirror reflection band changes as a function of the corrugation etch depth and etch width. The gap-midgap ratio increases for higher etch depths and narrower etch widths. These observations support the results of the optimization simulation shown below in Table 4.4.

The trends in the gap-midgap ratio seen in Figure 4.9 are predominantly driven by the lower band edge mode, which can be explained by the selected displacement mode profiles shown in Figure 4.10. These profiles show that the upper band edge mode more closely resembles the free-space Rayleigh SAW mode than the lower band edge mode, which has more of its displacement profile concentrated below the corrugations than the upper band edge mode. Therefore the lower band edge mode is more perturbed by changes to the corrugations than the upper edge mode.

Once these general design decisions were made, the Gen-2 devices were optimized for device parameters: corrugation etch depth, corrugation etch width, and number of mirror corrugations ($h_{etch}, w_{etch}, N_{mirror}$); taper period shift, taper slope steepness parameter, and number of taper corrugations ($\Delta p, \eta, N_{taper}$); and cavity spacer length/number of cavity corrugations (L_{cav}, N_{cav}). Any constraints on the cavity region length L_{cav} should

    (a) Lower Band Edge   (b) Upper Band Edge   (c) Free-Space
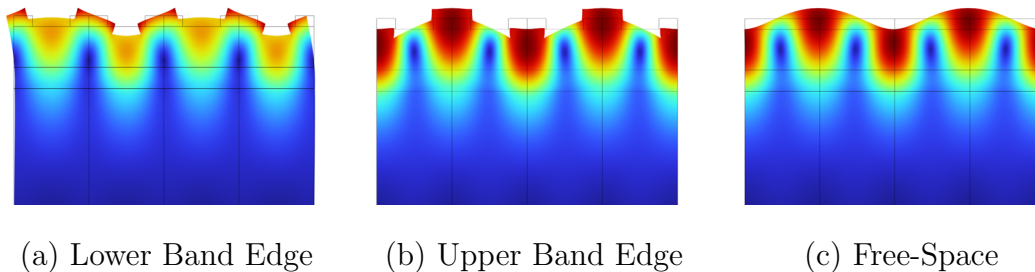
Figure 4.10: Mode displacement profiles of the mirror corrugation band edges and un-patterned material "Free-Space" of the Gen-2 SAW-QD design.

be taken into account. Before beginning optimization, however, a metric is needed to assess and compare a SAW cavity design's performance other designs. This is known as an objective function for optimization problems. Objective functions are typically minimized in optimization problems, and so the negative will be taken of the following for the true objective function. One potential objective function is the SAW quality factor; however, because Q typically scales directly with the mode volume [130], using Q alone for an objective function would rate larger SAW cavities higher in performance, which comes at the expense of the optomechanical coupling rate, g_0, which scales as the inverse square-root of the mode volume, $g_0 \sim \frac{1}{\sqrt{V}}$. Therefore, some correction to this prototype objective function is needed optimize for SAW cavities with small mode volumes. One alternative metric is the ratio of the quality factor to the effective mode area of the SAW mode cross section, A (Equation 4.2), which optimizes both the quality factor Q and the optomechanical coupling rate g_0. This ratio is a natural choice of objective function for optimizing the optomechanical cooperativity $C = \frac{4g_0^2}{\kappa\gamma} \sim Q/A$, though it is possible that there are other choices for the objective function to maximize the optomechanical cooperativity in this system: for example, one which includes a strain measurement at the location of the quantum emitter to determine the precise zero-point strain amplitude.
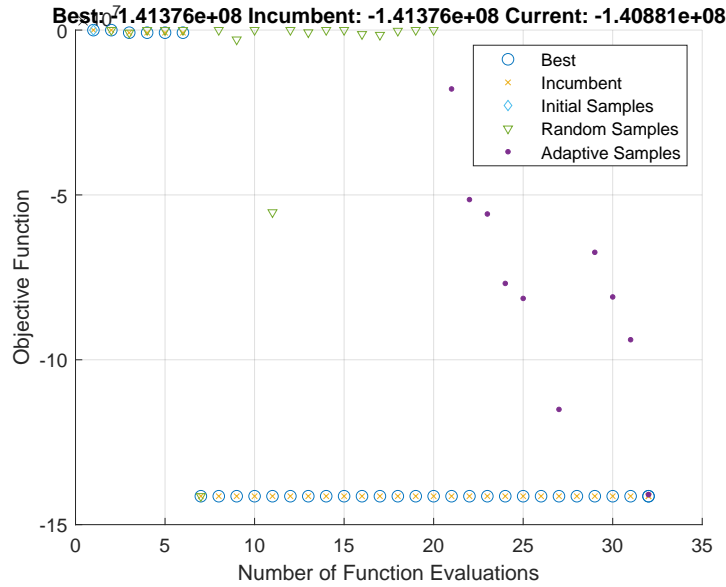
Figure 4.11: Example run of the `surrogateopt()` solver in MATLAB for the Gen-2 SAW-QD design using the objective function $f = -Q/A$.

h_{etch} (Λ)	w_{etch} ($\Lambda/2$)	δp (Λ)	η	N_{taper}	N_{cav}
0.0480	0.2375	0.0287	1.8125	29	0

Table 4.4: Optimization parameters for the Gen-2 SAW-QD design.

For simplicity, the Q/A ratio was used to optimize the Gen-2 devices in this thesis.

Because running design simulations for each permutation of the numerous design parameters above would take far too much time (roughly 30,000 years, estimating with a single simulation time of approximately 7 minutes for each of 6 parameters to sweep), this optimization is too expensive to perform with a brute force search. Instead, a multiparameter optimization solver was used, similar to `fmincon()` in MATLAB, which has been used in the optomechanics literature for similar optimization problems [45]. This solver, the `surrogateopt()` solver in MATLAB, is designed for objective functions

92
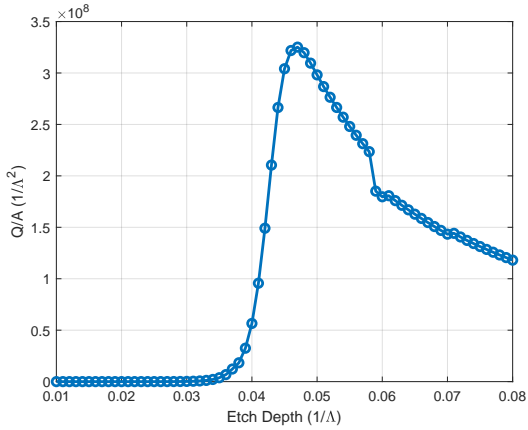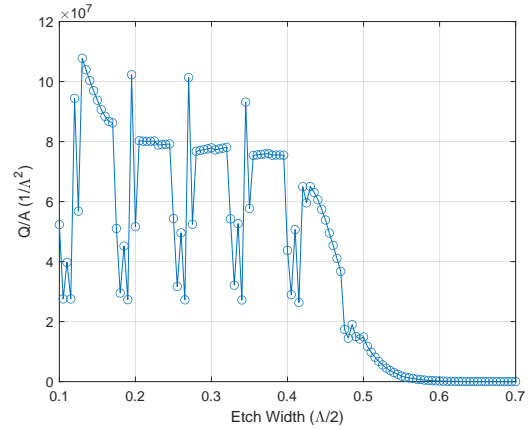
(a) Etch Depth

(b) Etch Width
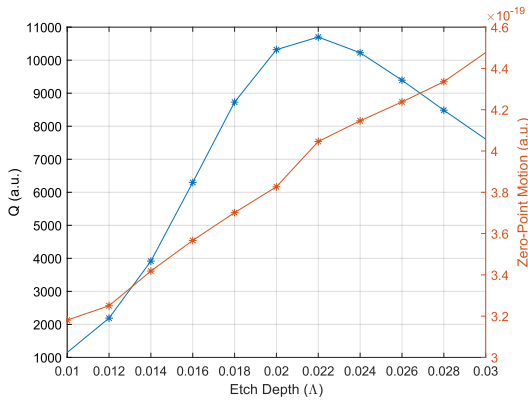
(c) Etch Depth
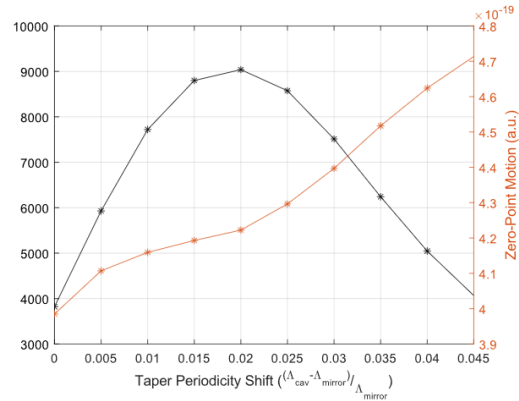
(d) Taper Periodicity Shift

Figure 4.12: a, b Example parameter sweeps for the Gen-2 SAW-QD design. c, d Example parameter sweeps for the Gen-2 SAW-2DM design with an unpatterned spacer region.

which are expensive to calculate, and it also allows both integer and floating-point value parameters to be optimized subject to upper and lower bound constraints. This allowed the number of taper and cavity corrugations to be inserted into the optimization. An example optimization plot is shown in Figure 4.11.

Once the optimized design is found, the sensitivity of the design to variations in design parameters from device fabrication. It is important during the device fabrication process

(a)

(b)
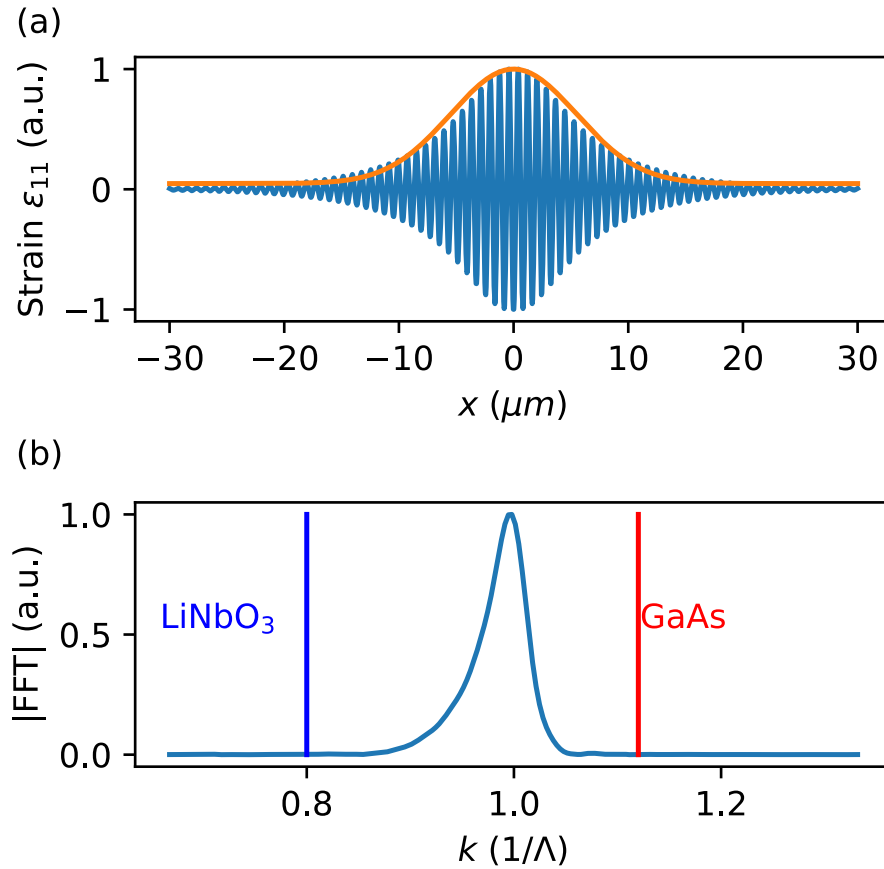
Figure 4.13: (a) Strain ϵ_{11} component along the SAW cavity axis. A fit to a Gaussian envelope function is shown in orange. (b) Fourier transform of the strain distribution in units of the inverse SAW wavelength, with lines indicated for the spatial frequencies corresponding to the edges of the sound cones for $LiNbO_3$ and GaAs.

to know how tolerant a design is to deviations from the ideal design; that is, how much of a difference in a design parameter is acceptable for a final device. For these SAW devices, there is no obvious criteria for what constitutes an "acceptable" final device, and so some heuristic measure is needed. One such possible heuristic is a threshold value of the objective function, such as 50 % of the objective function of the simulated ideal

94

device. This variation can be measured by running a simulation which sweeps the individual parameters across the desired range while monitoring the resulting Q/A objective function. Two exemplary parameter sweeps for the Gen-2 SAW-QD design are shown in Figure 4.12. An additional parameter sweep of the etch depth for the Gen-2 SAW-2DM design is shown in Figure 4.12c. Because of the relatively high quality factors simulated and the small depth of the etched corrugations compared to the SAW wavelength, small changes in the corrugation geometry cause changes to the simulation meshing which can have significant artificial effects on the simulated quality factor, leading to the appearance of discontinuities (sharp increases or decreases) in the objective function, Q/A at certain points in the sweep. Unfortunately these discontinuities can be difficult to avoid due to the computational expense of these simulations, requiring mesh spatial resolutions much less than a wavelength over areas $\approx 500\Lambda^2$, equating to several million degrees of freedom for the FEM simulation. The goal of these parameter sweeps is to identify the general trends of the objective function in response to the design parameters, and so the points of discontinuous change will be ignored in the following. Figure 4.12a shows a sweep of one of the corrugation etch depth over a wide enough range to see a significant variation in Q. The plot shows that an etch depth of $\approx 46\%$ is ideal, and an etching process with control to the precision of at least $\approx 1.0\%\Lambda = 8$ nm is needed to accurately reach the target etch depth. Similarly, 4.12b shows that an etch width of approximately 15-40 % of the corrugation period, $p = \Lambda/2$ is ideal for the Gen-2 SAW-QD devices. This observation that the quality factor improves for narrower etch corrugations is consistent with that observed in Figure 4.9, where the gap-midgap ratio and therefore the mirror reflectivity per corrugation improves with decreasing etch width. While it does appear in 4.12b that Q/A increases for etch widths smaller than 15 % of $\Lambda/2$, the feature sizes for these smaller etch widths become prohibitively small, particularly for using a wet etching method to fabricate the SAW-QD devices, detailed in Chapter 5. Interestingly,
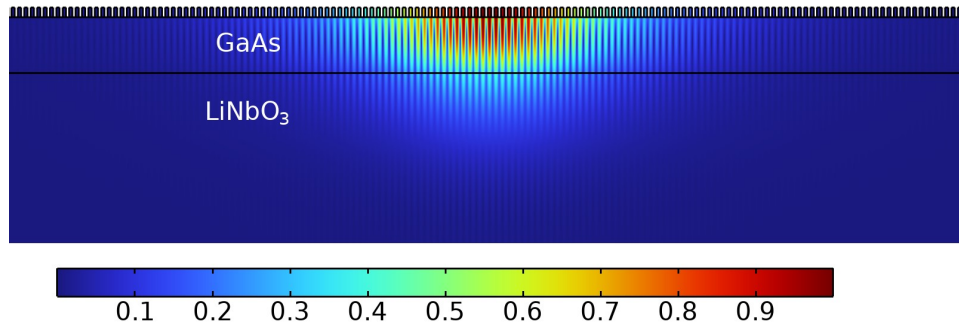
(a) Modal Displacement
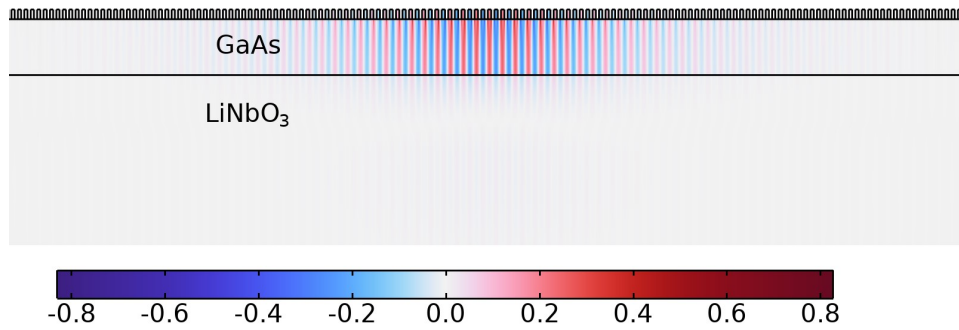
(b) Volumetric Strain

Figure 4.14: Displacement and volumetric strain of the fundamental SAW mode.

significantly different parameters were found for the Gen-2 SAW-2DM devices which incorporated an unpatterned spacer region of length $L_c = 10.0\Lambda$, shown in 4.12c-4.12d.

4.2.3   Displacement and Strain Profiles

Figure 4.14a shows the displacement mode profile and Figure 4.13 a line plot of the ϵ_{11} strain component or in-plane tensile strain along the cavity direction and its Fourier transform, showing the spatial and spatial frequency distribution of the hybridized GaAs-LiNbO$_3$ SAW resonance. This strain distribution was evaluated at the interface between the LiNbO$_3$ substrate and GaAs epilayer.

Plotting in units of the inverse SAW resonance wavelength, which is lithographically defined in the SAW cavity, the SAW resonance lies between the k-space or inverse wavelength lines that correspond to Rayleigh SAWs propagating in single-material $LiNbO_3$ and GaAs with the same resonance frequency. If the resonance were closer to the $LiNbO_3$ Rayleigh SAW line, this would indicate that the resonant mode has its energy predominantly concentrated in the $LiNbO_3$ substrate and not in the GaAs epilayer, as would be the case for the limit of a very thin layer of GaAs approaching a bare $LiNbO_3$ substrate. On the other extreme, if the resonance were close to the GaAs sound cone boundary, this would indicate the mode has concentrated its energy in the GaAs epilayer and has minimal energy in the substrate. One consequence of this condition would be the wavelength and the electromechanical efficiency of SAWs generated via IDTs on this heterostructure will be significantly different than those of a bare $LiNbO_3$ substrate.

The design showed in Figure 4.14b has a resonance which is about midway between the two lines, if not slightly biased towards the GaAs line. This is a result of the appreciable thickness of the QD epilayer relative to the SAW wavelength: 270 nm / 800 nm $\approx \Lambda_3$. Due to the significant wavelength mismatch between SAWs in the designed $GaAs/LiNbO_3$ heterostructure and bare $LiNbO_3$, there will be a significant reflection launching SAWs from an IDT patterned on bare $LiNbO_3$ into the heterostructure. Regardless, launching SAWs into a SAW phononic crystal cavity was expected to generate significant reflections, and so the issue of wavelength mismatch was not addressed in this design. In future iterations of this heterostructure, it may be possible to reduce the GaAs epilayer thickness to maintain a SAW wavelength more similar to $LiNbO_3$, or to maintain a high electromechanical efficiency to drive SAWs directly on the GaAs epilayer, using an IDT located within the SAW cavity.

Another observation to note of the resonance lineshape in Figure 4.14b is that it has a finite k-space distribution, indicating some periodicity in the strain distribution which

does not follow the periodicity of the SAW mirror phononic crystal structure. This spread in periodicity occurs fundamentally because the SAW cavity mode has a finite spatial distribution, and in general for any localized cavity mode, the spread in real and frequency space of the strain distribution is related by the Fourier transform [130]. While SAW cavity modes could in principle be made quite compact by introducing a small gap between two strong Bragg mirrors, this approach results in large SAW scattering into the substrate, because the cavity mode's frequency space distribution extends into the sound cone of the SAW substrate, which couples energy from the SAW mode to unguided bulk modes. This loss to bulk modes can be reduced by separating two phononic crystal mirrors by a large distance much greater than the SAW wavelength, thereby reducing the fraction of the SAW resonant mode's energy which interacts with the mirrors, but at the cost of much greater device size and reduced optomechanical coupling. It has been shown that the optimally minimal spread in both spatial and frequency space for a cavity mode exists with a Gaussian envelope function modulating the spatial and frequency space cavity distributions [278]. For the Gen-2 devices, the graded taper from the mirror period to a longer period towards the center of the cavity creates an approximately quadratic profile for the mirror strength, which supports a Gaussian envelope for the SAW mode.

Figure 4.14 shows the displacement and volumetric strain distributions for a hybrid GaAs-LiNbO$_3$ SAW mode with a fundamental resonance at $f = 4.01$ GHz. The cavity is oriented with the horizontal axis lying along the crystalline X-axis of LiNbO$_3$ and $\langle 110 \rangle$ axis in GaAs. The X-axis of LiNbO$_3$ is the preferred direction for maximum electromechanical coupling K^2, and the high-symmetry $\langle 110 \rangle$ axis of GaAs is the orientation of the samples used in this study.

Figure 4.15 shows the nonzero strain components $\epsilon_{11}, \epsilon_{33}$ and the optomechanical coupling, g_0 for the fundamental resonance as a function of the depth into the device from the center of the optimized Gen-2 SAW-QD device. The optomechanical coupling
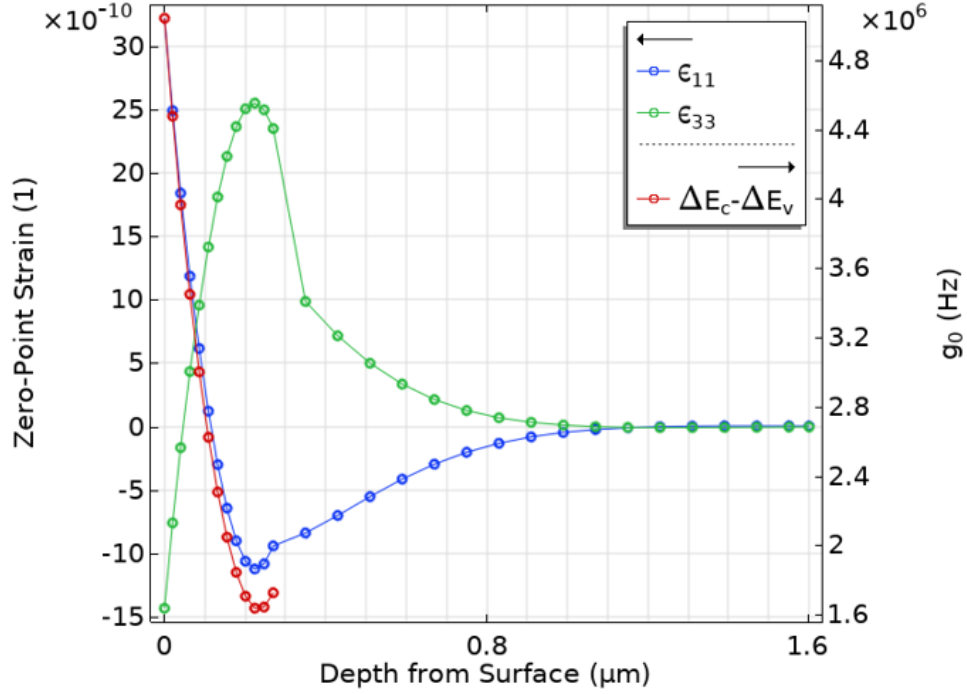
Figure 4.15: Simulated strain profile z-cut of the Gen-2 SAW-QD device.

rate was calculated using Pikus-Bir theory [163], where the electrons and holes of a semiconductor couple to strain via the deformation potential of the host material. The optomechanical coupling, g_0 is then equivalent to the difference in energy splitting ΔE between the conduction and valence band energy levels of GaAs, $g_0 = \Delta E_c - \Delta E_v$. For the conduction band, $\Delta E_c = a_c(\epsilon_{xx} + \epsilon_{yy} + \epsilon_{zz})$, where a_c is the conduction band deformation potential, $\epsilon_{xx} = \epsilon_{11}$ is the tensile strain x-component, ϵ_{yy} is the tensile strain y-component, which is zero for Rayleigh SAWs, and $\epsilon_{zz} = \epsilon_{33}$ is the tensile strain z-component. The strain-induced modulation of the valence band can be expressed as $\Delta E_v = \epsilon_{xx}(a_v + b/2) + \epsilon_{zz}(a_v - b)$, where a_v is the hydrostatic valence band deformation potential, and b is the shear deformation potential, using the deformation parameters for GaAs [163, 194]. The red curve and right axis in Figure 4.15 shows the energy splitting calculated from the above expressions as a function of depth into the GaAs epilayer of

99

thickness 0.27 μm and the strain components $\epsilon_{11} = \epsilon_{xx}$ and $\epsilon_{33} = \epsilon_{zz}$, which are shown in green and blue and are normalized to their amplitudes for the zero-point strain field, as shown on the left axis. The strain values calculated by the simulation are normalized by the square root of the ratio of the zero-point energy to the simulated mode energy:

$$\alpha_{corr} = \sqrt{\frac{E_{ZP}}{E_{sim}}} = \sqrt{\frac{\frac{h\nu}{2}}{W_s + W_k}}$$

To calculate a 3D mode energy from a simulation of a 2D cross-section, the SAW mode was assumed to have an effective in-plane thickness $t_{eff} = 2\Lambda$, consistent with results for focusing SAW cavities in GaAs [60]. At the position of the QDs in the Gen-2 design $\approx$ 200 nm from the surface, the coupling reaches a local minimum because of the antiphased ϵ_{xx} and ϵ_{zz} components, which are consistent with the elliptical motion of Rayleigh SAWs [203].

4.2.4   Focusing SAW Anisotropy Correction Factor

For the Gen-2 devices, developing focusing SAW cavities was important to reduce the SAW mode volume while preserving a high quality factor. Focusing IDTs [156, 213] and SAW cavities [164, 214, 313, 204, 60] show focusing down to $\approx \Lambda$ beam waists, concentrating the SAW mode to near the diffraction limit. One of the main challenges of SAW focusing is acoustic diffraction, which occurs in any crystalline material and requires corrections to the IDT and mirror curvature to focus SAWs to a single focal point. SAW device elements need to follow the angular profile of the Rayleigh SAW group velocity [204].

The following procedure to calculate the anisotropy-corrected curvature of the focusing IDT and SAW cavity corrugations of the Gen-2 devices follows closely that of Ref. [60]. The group velocity profile was extracted separately for the free-space, IDT electrode, and mirror corrugation regions as described below. This group velocity was then

used to define an angle-dependent correction factor, $C(\theta) = v_g(\theta)/v_g(0)$, applied to each IDT electrode and mirror corrugation for their respective velocity surfaces, which are shown below. This correction factor adjusts the shape of the electrodes to focus SAWs radially to a common point.

The group velocity is defined as the gradient in k-space of the temporal angular frequency, $\omega(\vec{k})$ [11]; in the Cartesian $k_x k_y$ plane, it can be decomposed into k_x and k_y components, which are themselves parameterized functions of the k-space polar angle, ϕ, defined with respect to the SAW cavity axis, which is aligned with the LiNbO$_3$ crystalline X-axis and $\langle 110 \rangle$ direction in GaAs:

$$\vec{v_g}(\phi) = \nabla_{\vec{k}} \, \omega(\vec{k}) = \hat{k}_x v_{g,\,x}(\phi) + \hat{k}_y v_{g,\,y}(\phi) \tag{4.3}$$

Meanwhile, $\omega(\vec{k})$ is a function of both k and the polar angle, ϕ, or alternatively the phase velocity, $v_p(\phi)$:

$$\omega(\vec{k}) = \omega(k, \phi) = v_p(\phi)k \tag{4.4}$$

Like with the group velocity, the wavevector $\vec{k}$ can be parameterized into Cartesian k_x and k_y components using the trigonometric functions sine and cosine:

$$\vec{k} = k\langle \cos\phi, \sin\phi \rangle \rightarrow k_x \equiv k\cos\phi,\ k_y \equiv k\sin\phi \tag{4.5}$$

The k_x and k_y components of group velocity in Equation 4.3. Since $\omega(\vec{k})$ will now be solved for, expressed in the polar coordinates (k, ϕ). To avoid confusion with taking partial derivatives in different coordinate systems, the gradient has to be evaluated using polar coordinates; then, the components can be converted to Cartesian coordinates.

$$\nabla_{\vec{k}} \, \omega(k, \phi) = \frac{\partial \omega}{\partial k} \hat{k} + \frac{1}{k} \frac{\partial \omega}{\partial \phi} \hat{\phi} \tag{4.6}$$

Equation 4.6 can be solved for in parts. From Equation 4.4, the partial derivative $\frac{\partial \omega}{\partial k}$ is just the phase velocity, $v_p(\phi)$; and $\frac{\partial \omega}{\partial \phi}$ is the product of k and the radial derivative of

the phase velocity, $v_p'(\phi)$.

$$\nabla_{\vec{k}}\,\omega(k,\phi) = v_p(\phi)\,\hat{k} + v_p'(\phi)\,\hat{\phi}$$

$$= v_p(\phi)\big[\cos{(\phi)}\hat{k}_x + \sin{(\phi)}\hat{k}_y\big] + v_p'(\phi)\big[-\sin{(\phi)}\hat{k}_x + \cos{(\phi)}\hat{k}_y\big] \qquad (4.7)$$

$$= [v_p(\phi)\cos{(\phi)} - v_p'(\phi)\sin{(\phi)}]\hat{k}_x + [v_p(\phi)\sin{(\phi)} + v_p'(\phi)\cos{(\phi)}]\hat{k}_y$$

From the last line of the above:

$$\boxed{\begin{aligned} v_{g,x}(\phi) &= v_p(\phi)\cos\phi - v_p'(\phi)\sin\phi \\ v_{g,y}(\phi) &= v_p(\phi)\sin\phi + v_p'(\phi)\cos\phi \end{aligned}} \qquad (4.8)$$

With the Cartesian components of the group velocity parameterized in terms of the k-space angle ϕ, the next step is to find the radial component of the group velocity at an arbitrary geometric or real-space angle θ. For acoustically anisotropic materials, the group velocity $\vec{v}_g(\phi)$ is not in general parallel to the radial direction $\hat{k}$ at an angle ϕ, unlike the phase velocity $\vec{v}_p(\phi)$, which is parallel to $\vec{k}$ and therefore the radial direction. This means that SAW focusing IDT electrodes and cavity mirror corrugations with arcs defined by $v_g(\phi)$ alone would not focus all of the SAW energy to the center of the cavity. This would result in a spread in the focus of the SAW mode along the x-direction over a length determined by the degree of anisotropy of the LiNbO$_3$ substrate or GaAs/LiNbO$_3$ heterostructure.

Instead, the k-space angle, ϕ can be used as a tuning parameter to align $\vec{v}_g(\phi)$ to be parallel to the radial direction $\hat{k}$ at the geometric angle of interest θ. This is done by solving for ϕ as a solution of the equation $\tan\theta = v_{g,y}(\phi)/v_{g,x}(\phi)$. The resulting function $\phi(\theta)$ is used as the input for the group velocity components $\{v_{g,x}, v_{g,y}\}$, which are in turn used to compute the radial component of the group velocity:

$$v_{g,r}(\theta) = v_{g,x}[\phi(\theta)]\cos(\theta) + v_{g,y}[\phi(\theta)]\sin(\theta) \qquad (4.9)$$

Finally, the velocity anisotropy correction factor for the SAW mirror and IDT structures is $C(\theta) = v_{g,r}(\theta)/v_{g,r}(0)$.

Figure 4.16 shows the phase and group velocity profiles obtained from the above analysis. The group and phase velocity profiles coincide where the angular derivative of the phase velocity approaches zero at $\theta = \{0, \pm 90°\}$. The velocity profiles of the IDT and mirror structures differ from those of the free-space structure because of the mechanical and electrical loading at the surface, which tends to decrease the wave velocity [11].

The phase velocity $v_p(\phi)$ was simulated using a finite-element simulation in COMSOL Multiphysics, using the model shown in Figure 4.16d. An example simulation model of the IDT structure is shown in d. The models each have a substrate thickness of 5 Λ, periodic boundary conditions applied to the geometry x and $-x$ faces, shown in red, and continuity boundary conditions applied to the geometry y and $-y$ faces, shown in blue. The IDT structure has a width in the x direction equal to the IDT wavelength, Λ_{IDT}, whereas the mirror model has a width of $\Lambda_{mirror}/2$ because the increased periodicity if this structure allows a smaller periodic unit cell to be simulated; similarly, the free-space model a small simulation domain width of $\Lambda_{f-s}/10$ because of its continuous translation symmetry. A rotated coordinate system was used to initially align the SAW materials as follows. The geometry x axis was aligned with the crystalline X-axis in LiNbO$_3$ and the $\langle 110 \rangle$ direction in GaAs, the latter for the Gen-2 QD devices. The geometry z axis was aligned with the 128°-Y crystalline cut of the LiNbO$_3$ sample and the GaAs [001] plane. Solid mechanics and electrostatics modules were then coupled using the piezoelectric effect, with material parameters given in Appendix B. The eigenfrequencies of the structures were calculated, and the corresponding wave velocities were computed as the product of the wavelengths defined by the simulation domains and the returned eigenfrequencies f. These velocity data were then fitted to a Fourier series expansion, with a cutoff of 10 coefficients for each of the phase velocity and its angular derivative:

$$v_p(\phi) = a_0 + \sum_{n=1}^{\infty} a_n \sin n\phi + b_n \cos n\phi$$

$$v_p'(\phi) = \sum_{n=1}^{\infty} n \left(a_n \cos n\phi - b_n \sin n\phi \right)$$
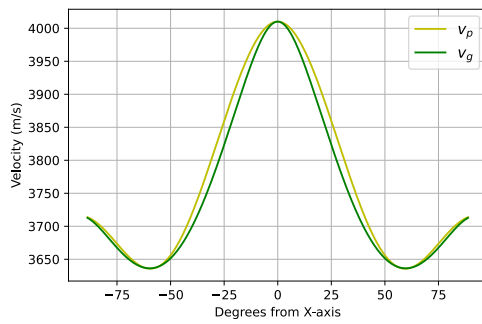
(a) Free-Space
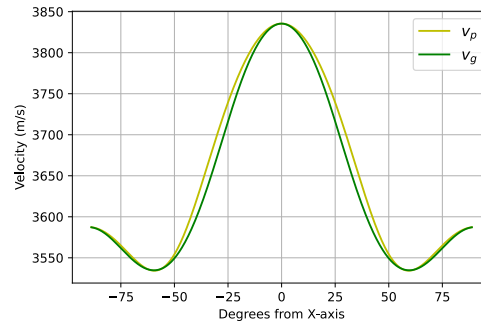
(b) IDT
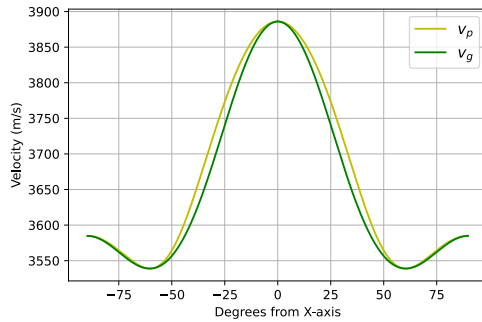
(c) Mirror
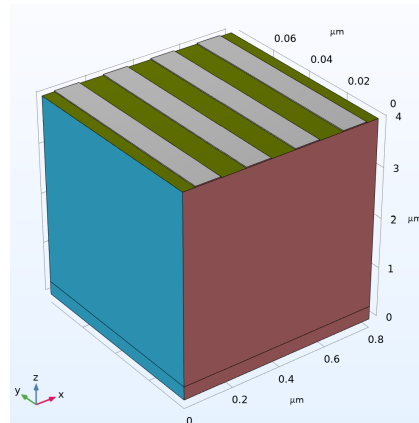
(d) IDT Model

Figure 4.16: SAW group and phase velocities for 128° Y-X cut $LiNbO_3$ at cryogenic temperatures ($T \lessgtr 10K$) varying the direction of propagation from the crystalline X-axis. a Velocity for free space. b Velocity profile for IDTs with 20 nm NbN. c Velocity profile for mirrors with an etch depth corresponding to 5 % of the acoustic wavelength. d 3D model of the IDT structure.

Chapter 5

Sample Fabrication

5.1 Process for Gen-1 Devices

The Gen-1 devices for the data shown in Chapters 6 and 7 were produced in the same fabrication run. The design parameters of these devices are shown in Table 4.2. Figure 5.1 shows a schematic illustration of the Gen-1 SAW-QD and 2DM device fabrication process.

In this process, a blanket layer of NbN is deposited using the optimized recipe described in Section 5.1.1. A NbN thickness of 20 nm was decided as a tradeoff between excessively thick or thin films. Too thick of a NbN film would result in mass loading [203], especially given the much higher density of NbN (8.470 g/cm^3) relative to the common SAW metal Al (2.799 g/cm^3). This mass loading can lead to spurious reflections within the IDT and mirrors [243]. On the other extreme, depositing too thin of a NbN film can compromise the film's superconductivity due to the proximity effect as well as surface oxides and interfacial layers [260, 57], which is particularly significant at higher IDT excitation powers, as observed in Chapter 6.

The NbN thin film is then patterned to form the IDT and resonator mirror electrodes
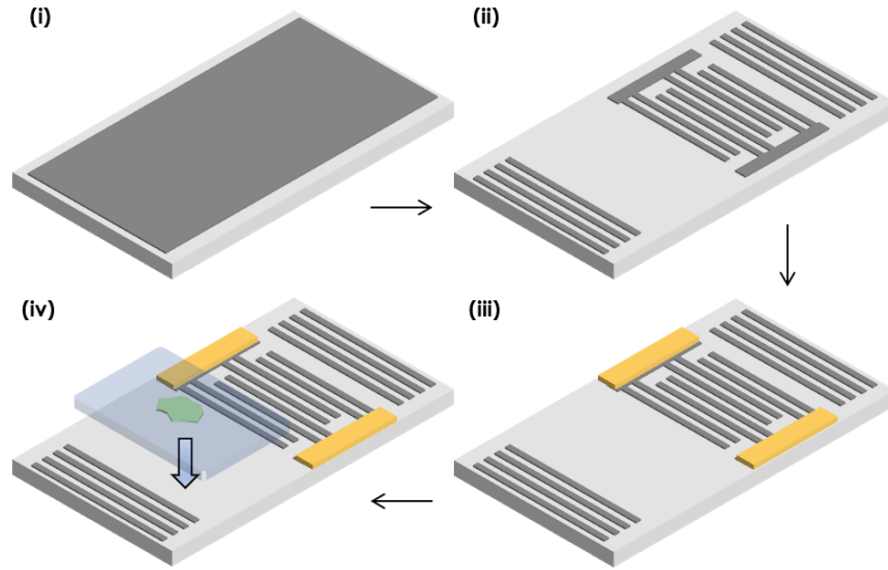
Figure 5.1: Gen-1 SAW device process flow: (i) NbN sputter deposition, (ii) optical lithography and etch, (iii) contact pad metallization lift-off, (iv) epitaxial liftoff of QD epilayer or Van der Waals transfer of a 2DM sample.

using a resist mask patterned optical lithography. The lithography was performed using a deep-UV stepper tool (ASML 5500). One challenge with lithography with LiNbO$_3$ is that because the material is both pyroelectric and piezoelectric, any thermal gradient across the thickness of the wafer when the wafer is laid onto a hot plate or removed from a hot plate can create a significant strain gradient, which was found to cause the wafer to shatter when removed from hot plates even at relatively low bake temperatures $\approx 80°$ C. To avoid introducing significant thermal gradients to the wafer, the wafer was placed on a hot plate which was held at 60° C, then the temperature was gradually ramped up to the desired bake temperature, the bake was performed for the desired time, and the temperature was finally ramped down to 60° C, where it could be safely removed from the hot plate.

After photolithography, the NbN thin film was etched using an ICP-RIE tool and with the following etch parameters: 0.4 Pa chamber pressure, 144 sccm CF_4 and 9 sccm nitrogen gas flows, 850 W ICP source power, 35 W forward bias power. ICP-RIE processing with CF_4 gas as a precursor fluorinates the photoresist sidewalls and forms a residue, leading to "stringers" which can be difficult to remove after etching. In Figure 5.2a, the NbN etch resulted in "Teflon"-like strings of photoresist which delaminated from the NbN electrodes. This leftover photoresist was efficiently removed using an O_2 plasma asher and with organic solvents, avoiding acetone immediately after the NbN etch, because acetone appears to react with the residue and makes the resist residue exceedingly difficult to remove.

The SAW devices were then completed by creating electrical contacts to the IDTs with a Ti/Au thin film via a metallization liftoff process using optical lithography. The liftoff lithography was initially attempted with the deep-UV stepper tool, but it was moved to a direct-laser-write lithography tool (Heidelberg MLA150). The lithography was moved to a direct-write tool because the 4-inch $LiNbO_3$ substrates on which the SAW devices were fabricated experienced significant thermal expansion and contraction from the photolithography bakes, which were large enough that the stepper tool could not compensate for the changes in the wafer dimensions between lithography layers. As a result, only the first layer of the SAW devices could be patterned using the stepper tool. The Ti (10 nm)/Au (90 nm) contacts were shown to be sufficiently thick to enable Au wire bonding without delamination of the contacts. After completing the SAW resonator fabrication, the devices were cingulated using a dicing saw, and the QD and 2DM samples were transferred. For the SAW-QD devices, the QD samples are self-assembled In(Ga)As quantum dots, which are transferred onto the LN substrate by the Yablonovitch epitaxial liftoff process [321] using a patterned layer of Pd as an adhesion promoter. For the Gen-1 2DM devices, monolayer WSe_2 flakes were identified by optical contrast under
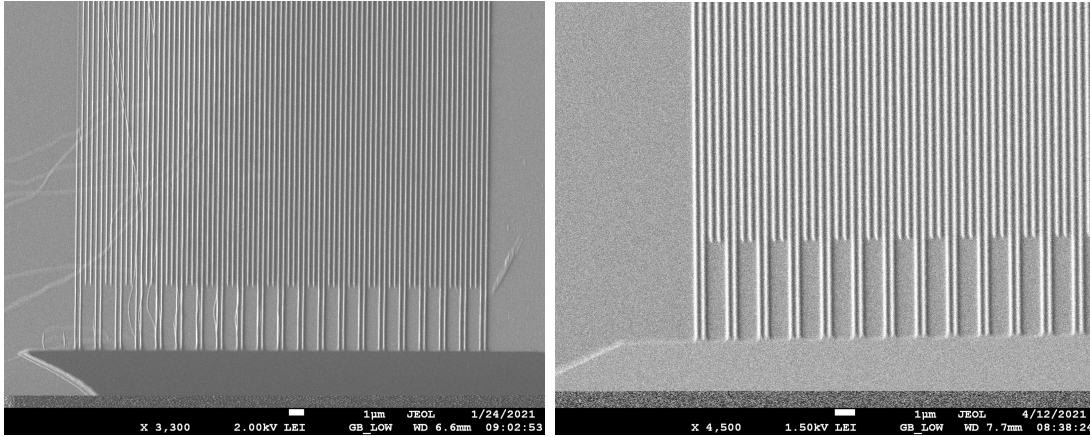
(a) Photoresist "stringers"   (b) Stringers removed with O_2 Ash

Figure 5.2: Development of a NbN etch process. a NbN electrodes with photoresist "stringers" left after etching. b Adding an O_2 photoresist step immediately after CF_4 etching and avoiding using acetone after etching removed the photoresist.

a microscope following mechanical exfoliation, then they were transferred onto SAW resonators using an all-dry transfer method.

5.1.1   Process Development of NbN Thin Films

A NbN sputter deposition process was developed for high-quality superconducting thin films for the SAW-QD and SAW-2DM projects. The main parameter used to judge the quality of the films was the superconducting critical temperature, T_c, defined as the temperature at one-half of the difference from the superconducting state to the normal metal state. Other measurements including stress [59], optical constants from ellipsometry [188], and thin-film resistivity [51] have been used by others, but T_c was chosen as the main parameter to optimize to ensure that the SAW devices are operating at temperatures well below T_c even with some uncertainty in the true sample temperature. For high-quality superconducting thin films, the Nb sputter target needs to have a very high

Parameter	Old Recipe	Optimized Recipe
N_2 Flow (sccm)	2.00	4.00
Ar Flow (sccm)	48.25	30.00
Pressure (mT)	5.00	2.00
Rotation (rpm)	5.00	20.00
DC Power (W)	150	250
RF Bias (V)	110	0
Gun Tilt (a.u.)	7.00	9.00

Table 5.1: Deposition parameters of the starting and optimized NbN recipes.

purity. ASTM released a standard which sets the limits for the background contaminants [270], facilitating the sourcing of sufficiently pure Nb sputter targets. After ordering a Nb target from a vendor matching the specifications of the ASTM standard for Type 5 Nb, the T_c of the subsequent NbN films deposited increased by about 3 K, from around 8.3 K for 200 nm films to 11-12 K for films of similar thicknesses. The other factors which contributed to the improvement in T_c were the following: increasing the N_2 flow rate and reducing the Ar flow rate to improve the stoichiometry of the deposited film; decreasing the chamber pressure to the minimum repeatable value to increase the mean free path, improving film deposition rate and growth morphology [58]; removing the substrate RF bias, which could introduce contaminants present on the substrate holder; and adjusting the gun tilt angle, which can affect the film uniformity. After depositing thin films of NbN on silicon chips with 300 nm SiO2 previously deposited as an insulating amorphous layer, the samples were cleaved using a scribe and mounted in a four-point probe setup, which was installed in a cryogen-free dilution refrigerator (Quantum Design PPMS DynaCool) for a DC resistivity measurement, repeating the resistivity measurement as the sample

was gradually cooled from slightly above to below T_c. Using the parameters in 5.1, an $\approx$ 400 nm film with $T_c = 14.09$ K was measured using this method, with a resistivity curve shown in red in Figure 5.3 as compared to the resistivity curve of a NbN film deposited using the starting recipe parameters.

After optimizing the film T_c, the superconducting critical current, I_c was characterized using wire test structures defined via photolithography and ICP-RIE etching, using the recipe developed in Table 5.1. These test structures were designed to isolate the current transport through μm-scale NbN wires, with wire widths varying from 1 to 10 μm. Gold contacts were deposited using photolithography and a Ti/Au liftoff method. In the first attempt of making these test structures, these contacts were deposited above the NbN, similar to the processing for the Gen-1 and Gen-2 SAW devices. For this DC measurement, however, there was significant non-Ohmic behavior (non-linear I-V curve) of the wire structures, even at low temperatures below T_c, necessitating a change to the fabrication process. The order of the two metal patternings were reversed, depositing the contacts before depositing and patterning the NbN, and this yielded the expected Ohmic behavior of the wire structures. It is possible that oxidation of the NbN surface after deposition and before deposition of the contact metals could be the cause of the non-Ohmic behavior. With the samples shown in Figure 5.3c, an I_c curve shown in Figure 5.3d yielded a superconducting critical current density of 1.2 MA/cm^2, within the same order of magnitude of the state of the art [57].
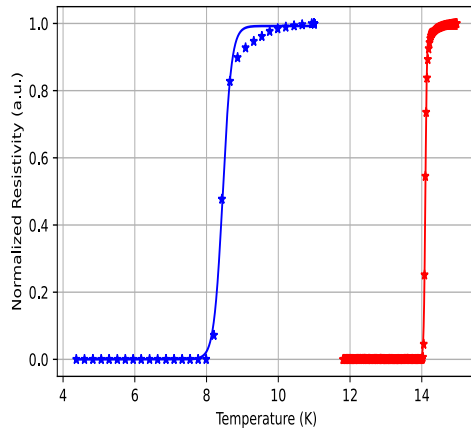
(a) Tc measurement
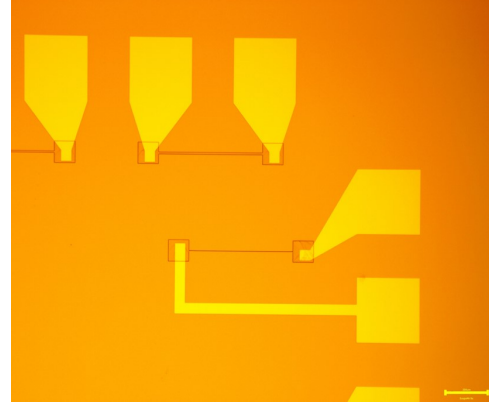
(b) NbN wires
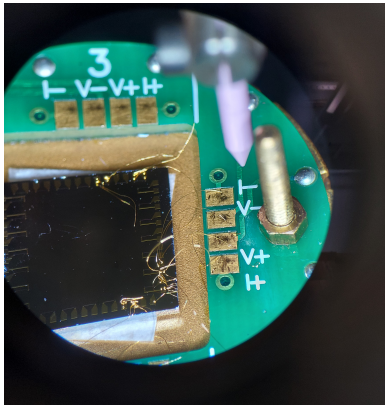
(c) Ic sample setup
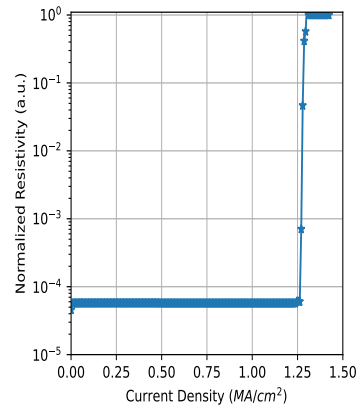
(d) Ic measurement

Figure 5.3: a Superconducting critical temperature T_c characterization for ($\gtrapprox$ 200 nm) NbN films deposited on silicon with the original recipe (blue) and the optimized recipe (red). b Microscope image of fabricated NbN microbridge test structures. c NbN microbridge samples wire bonded to a 2-point probe measurement contact assembly for characterization inside a dilution refrigerator. d Measurement of superconducting critical current density, J_c.

5.2   Process for Gen-2 QD Devices

In contrast to the Gen-1 SAW-QD devices, where QD epilayers were integrated on LiNbO$_3$ after SAW device fabrication, the Gen-2 devices were designed to incorporate a QD epilayer from the start of device fabrication, which enables large (several mm^2) arrays of devices to be fabricated in the same fabrication run. A simplified process flow diagram is shown in Figure 5.4. After bonding a GaAs epilayer grown on a GaAs substrate to LiNbO$_3$, the GaAs substrate is removed using a wet etch solution of NH$_4$OH:H$_2$O$_2$. When the wet etch reaches the etch stop layer of Al$_{0.92}$Ga$_{0.08}$As, the wet etch is halted, because the AlGaAs surface oxidizes readily into Al$_2$O$_3$, which is insoluble in the wet etch solution [201]. The etch stop layer is subsequently removed in a buffered HF solution, exposing the GaAs epilayer. This epilayer is then patterned to form the outlines of the SAW cavities, shown in Figure 5.5b for a set of test structures for the Gen-2 SAW-QD fabrication process. Next, the IDTs are patterned as will be described in Subsection 5.2.2, and finally, the SAW cavities are patterned as described in Subsection 5.2.3.

The process test structures shown in Figure 5.5 were used to ensure that the entire Gen-2 SAW-QD fabrication process could be carried out on a QD sample bonded to LiNbO$_3$. This sample did include a thin 8 nm layer of AlO$_x$ depsited using an ALD deposition tool to help the bond to LiNb$_3$. Subsequent work bonding GaAs to SiC and single-crystalline diamond showed that this amorphous AlO$_x$ layer is unnecessary for direct bonding. After bonding, the sample was annealed at 150 ° C for 12 hours in ambient air to improve the bond strength. Per the analysis in 5.2.1, this anneal may have been too high of a temperature for full-thickness GaAs. In subsequent work, mechanical substrate thinning with a polishing tool (Allied Multiprep polisher) was found to be an effective method to reduce the bonded sample thickness to $< 200 \ \mu m$, where the sample was able to withstand annealing at elevated temperatures.

1. GaAs-LiNbO$_3$ Bonding

3. Pattern IDTs

LiNbO$_3$

GaAs

AlGaAs

2. Substrate Removal

4. Pattern SAW Cavities

NbN

Ti/Au
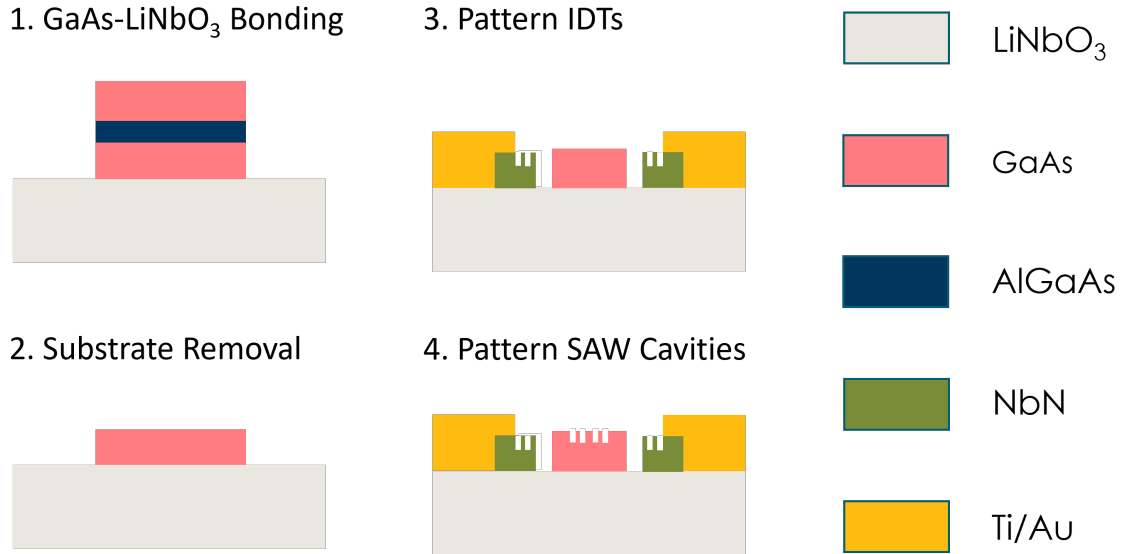
Figure 5.4: Gen-2 SAW-QD simplified process flow.

During the GaAs substrate removal wet etch, pieces of the sample began chipping off after approximately 600 μm of the 625 μm substrate had been etched away. By the end of the substrate removal process, less than one-quarter of the bonded epilayer remained, which could be because of the 150 °C anneal with the full thickness substrate, as discussed above. However, there were several other possible explanations. Firstly, there appeared to be some non-uniform etching of the GaAs substrate across the bonded sample. This was particularly noticeable on one corner, where there was a stripe of residual III-V material (composition unknown) which was deposited from the MBE backing wafer, which had been reused after a previous growth. The sample was also kept in the more aggressive of the two substrate removal solutions (10:1 ammonia:peroxide solution ratio versus the 30:1 solution) for longer than necessary, which likely etched away part of the etch stop and etched away part of the sample.

The portion of the sample which remained after GaAs substrate and AlGaAs etch stop removal stayed intact for the remainder of the fabrication process. Figure 5.5b shows
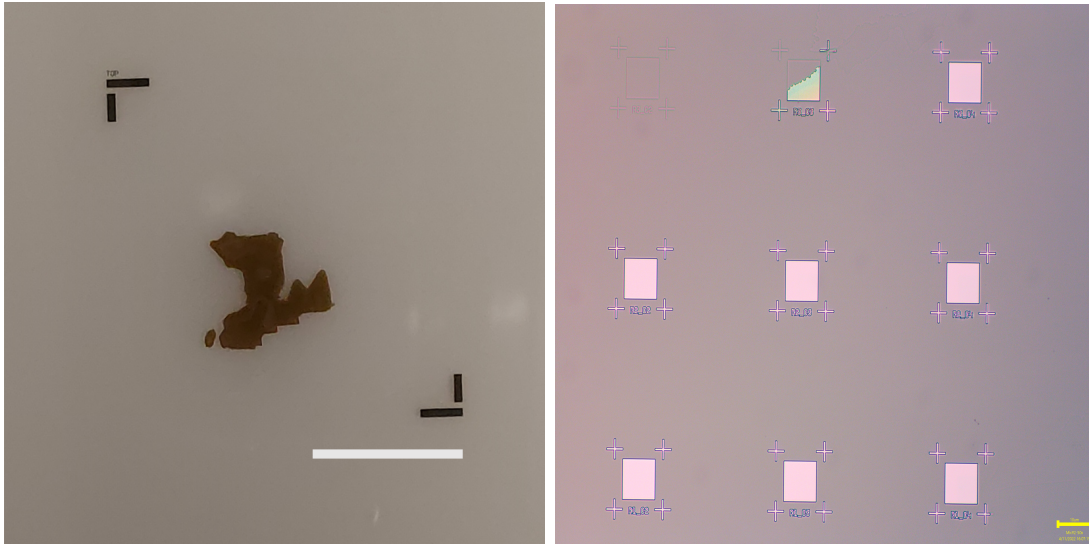
(a) Bonded epilayer

(b) GaAs Islands
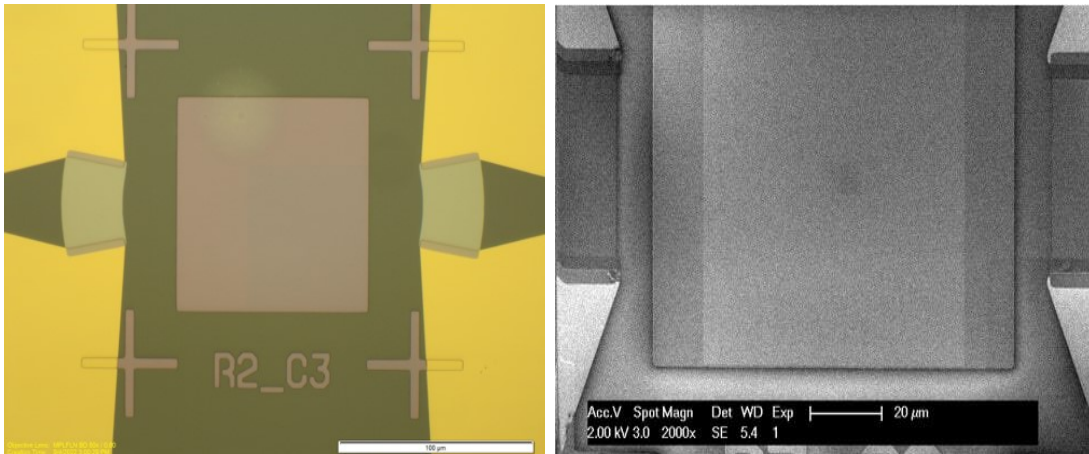
(c) IDT fabrication

(d) Completed device

Figure 5.5: a Remaining bonded material after the test structures epilayer substrate and etch stop removal steps. Scale bar: 5 mm. b Patterned islands of GaAs on LiNbO$_3$. c Sample device after the IDT outline and contact metal liftoff steps. d Completed test structures device.

the patterning of the GaAs epilayer into a grid of isolated $100 \times 100 \ \mu m^2$ "islands" forming the outlines of SAW cavities, which left 25 islands across the sample. Following

(a) CTE mismatch

(b) Interfacial energy density
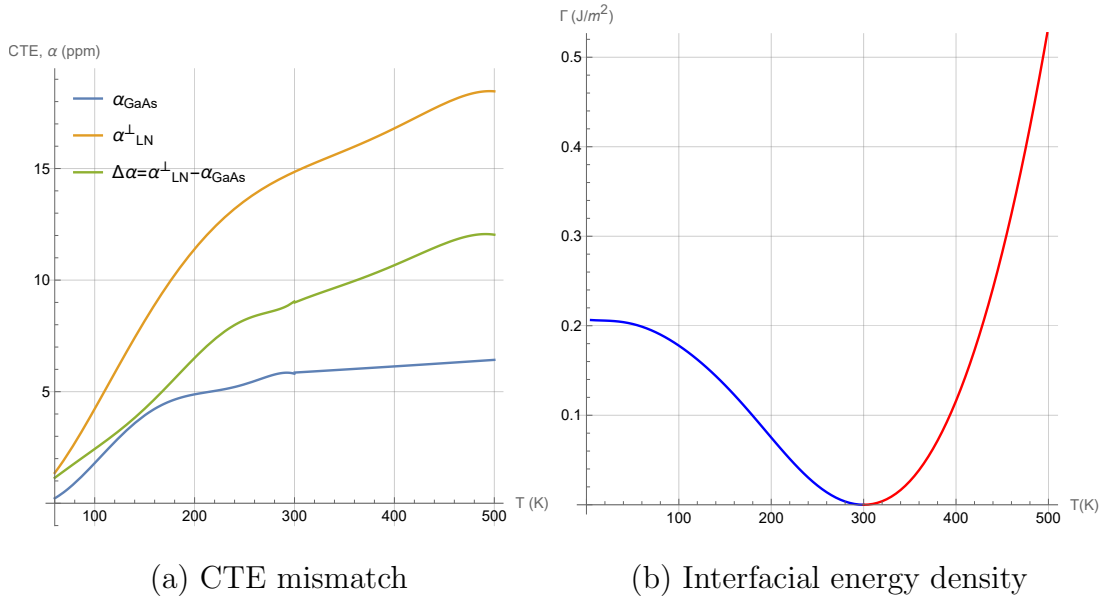
Figure 5.6: Mismatch in the coefficient of thermal expansion and the interfacial energy density for a direct bond between 1 μm of GaAs and a $LiNbO_3$ substrate.

IDT fabrication, as shown in Figure 5.5c, the GaAs wet etch for the SAW cavities was repeated three times across three subsets of the sample's GaAs islands to perform a rough sweep of the etch depth for SAW cavities.

5.2.1 Process Development of GaAs-LiNbO3 Direct Bonding

The most critical step in the Gen-2 SAW-QD fabrication process is creating a stable bond between the GaAs epilayer and the $LiNbO_3$ substrate. Several options for room-temperature bonding of dissimilar substrates exist. While the epitaxial liftoff bonding process used for the Gen-1 devices has been shown to work up to the wafer scale [197], at the time of device fabrication, employ ambient-pressure, plasma-assisted direct chip-to-wafer bonding was employed [53]. This method had the most expertise and infrastructure already in place within the UCSB Nanofabrication Facility to achieve several mm^2 area of QD epilayer bonded to $LiNbO_3$.

116

The process for the direct bonding method used here involves cleaning the two samples, in this case a 1 cm^2 GaAs chip and a 4" LiNbO$_3$ wafer, to eliminate particle contamination, and then exposing them to an oxygen plasma activation tool (EVG 810), which makes the surfaces hydrophilic, adding hydroxyl groups to the surfaces which then attract water vapor via hydrogen intermolecular bonding. When the two surfaces of the bonding samples are later placed into contact, hydrogen bonding between the water molecules on each sample immediately creates a bond between the samples [53]. If the bonded sample is left at room temperature for long enough, and preferably annealed at an elevated temperature, the water diffuses out from the bonding interface to the edges of the bonded area and evaporates, where then the hydroxyl groups from either surface of the bond can form strong covalent oxygen-oxygen bonds [226].

Successfully bonding GaAs directly to LiNbO$_3$ is challenging because of the large difference in the thermal expansion coefficient (CTE). For the X and Y crystalline axes in LiNbO$_3$, the CTE is 14.8 $\times 10^{-6}$ at room temperature, whereas in GaAs the CTE is 5.9 $\times 10^{-6}$. Figure 5.6a shows the CTE mismatch between these two materials, $\delta\alpha$ over the range of T = 60 K to 500 K. The GaAs CTE data is sourced from Ref. [198] and [93], and the LiNbO$_3$ data from Ref. [18] and [35].

Because the GaAs epilayer is present throughout the Gen-2 SAW-QD fabrication process, it is important to examine the thermal stress on the bonded GaAs thin film across the elevated temperature range in device fabrication. Likewise, there is a thermally-induced strain on the GaAs-LiNbO$_3$ bonding interface when cooling down a completed device to cryogenic temperatures. Both heating and cooling could result in bond delamination and cracking if the interface strain energy induced by the CTE mismatch overcomes the bond strength. Using the elastic properties of the GaAs film, the stress energy at the bonding interface can be calculated as a function of the temperature difference (assuming bonding at T = 300 K) and the CTE mismatch as a function of temperature. Figure 5.6b shows

the strain energy density at the interface between a 1 μm thick GaAs film direct bonded to LiNbO$_3$. Note that the thickness of the GaAs film of 1 μm is chosen arbitrarily to help compare the interfacial strain energy versus the bond energy for different thicknesses of GaAs thin films, since the interfacial strain energy is directly proportional to the GaAs thickness. For a full-thickness GaAs substrate ($\approx 625\ \mu m$), the strain energy density is nearly three orders of magnitude higher than is shown in the plot. In comparison, the typical bond strength between direct bonded silicon oxide surfaces is between 50-200 mJ/m%2 [16]. While the bond strength for the GaAs-LiNbO$_3$ bonds was not measured, it is assumed to be near the lower end of the range of typical silicon oxide-oxide bond strengths, since neither the oxide-oxide or GaAs-LiNbO$_3$ pairs of surfaces is crystalline at the bond interface. This is because GaAs has a native oxide, which even if stripped in an HF solution, it will regrow when exposed to an O$_2$ plasma in the plasma activation step used in this work; LiNbO$_3$ has been shown to create a $\approx$ 2 nm thick amorphous interface layer when bonded with glass [320]. Interfacial strain energy densities $\ggg$ 1 J/m^2 at elevated temperatures are too high for GaAs-LiNbO$_3$ direct bonds [120], which prevents high-temperature annealing steps to strengthen the bond until after the GaAs substrate is removed. After the GaAs substrate and AlGaAs etch stop removal steps, however, the interface strain energy density decreases to a value lower than the assumed bond strength. This is an encouraging result, as it suggests that direct GaAs-LiNbO$_3$ bonds are possible in principle, particularly for the thinner Gen-2 SAW-QD GaAs sample thickness of 270 nm.

Three main factors determine whether two surfaces are sufficiently smooth enough for bonding: particle contamination and surface defects, surface roughness, and surface planarity. Both particle contamination and surface defects separate the opposing bonding surfaces, preventing bonding not just at the location of the particles, but often over much larger areas: a particle with a diameter of 0.5 μm between two 4 inch silicon wafers with a
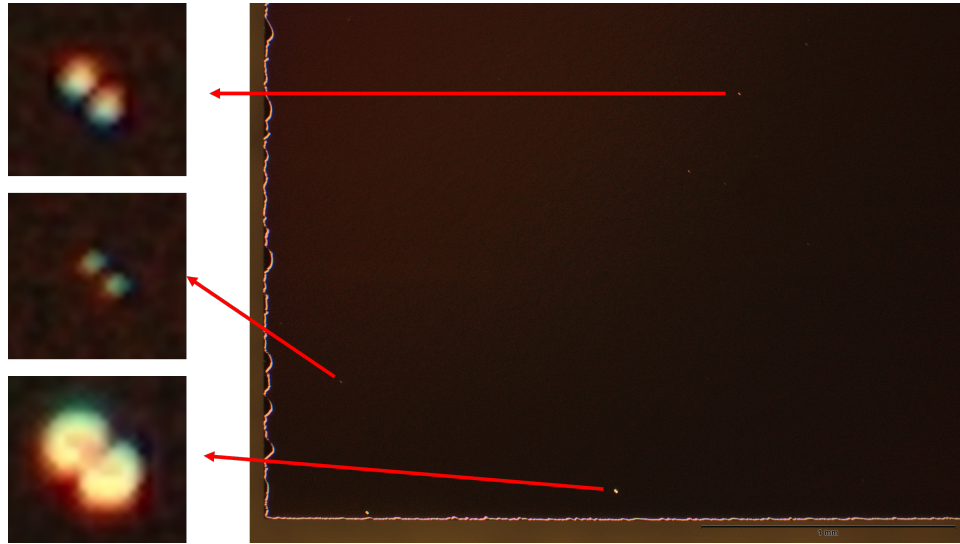
Figure 5.7: Microscope image of a cleaned GaAs surface showing an acceptable density of oval defects for direct bonding of GaAs to LiNbO$_3$. This sample was successfully bonded and is the GaAs source material for the devices shown in Figure 5.5.

thickness of 525 μm can lead to an unbonded area with a diameter of 1 cm [53]. Cleaning samples for particles will be discussed in more detail below. In addition to particles, growing III/V materials often introduces surface defects from large particles of gallium or other species occasionally being ejected by the reactor onto the growth material, which is then grown over with epitaxial material and can grow in lateral size if more material is deposited. Surface defects can also limit bonding areas, though anecdotally from experience in the Moody Group and others, these defects tend to not inhibit bonding as much as particles, perhaps because these surface defects separate the bonding surfaces by a lesser distance. Figure 5.7 shows a representative Namarski/DIC mode microscopy image of a corner of a GaAs sample with a measured oval defect density ≈ 200 cm^{-2}. The oval defects are all observed to have a similar orientation and consist of two lobes separated by a small gap.

Similar to particles, surface roughness of the bonding samples can limit the true

119
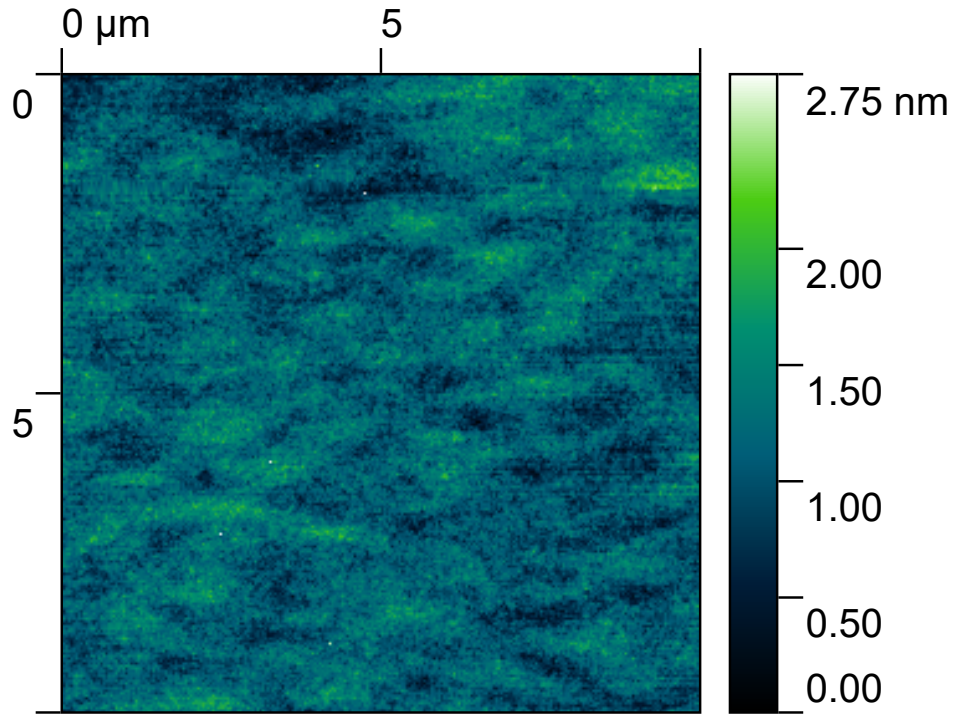
Figure 5.8: 10 x 10 μm^2 AFM profile of MBE-grown GaAs.

contacted surface area when the bonding surfaces are brought into contact. The RMS surface roughness, S_q acceptable for direct bonding is commonly stated to be below 0.5 nm [226, 53, 86]. AFM can be used to characterize surface roughness, which is especially important when exploring different cleaning or activation treatments to a sample. Figure 5.8 shows a representative AFM profile of a GaAs sample with a surface roughness of 271.7 pm, well within the acceptable range for direct bonding. The white spots on the figure could be metallic or organic contamination, though they may also be scanning artifacts because they are exceedingly small, measuring one pixel in length (roughly 40 nm).

Lastly, surface planarity or flatness is important to consider for direct bonding, since the curvature of a sample can cause it to debond. The flatness is quantified using a parameter known as the total thickness variation, which is the difference between the

Straight down, onto the center of the chip

5-10 X Past the edge of the chip, perpendicular to edge

~ 80 % of length

Slight twisting motion
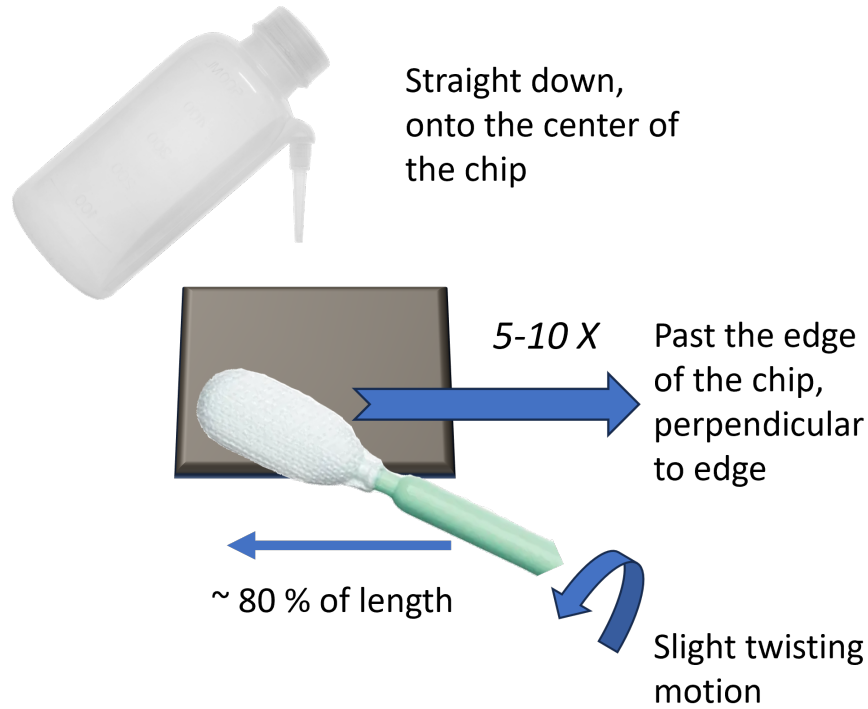
Figure 5.9: Cartoon of the cleaning procedure.

highest and lowest elevation on a sample, assuming the bottom face is lying completely flat. As long as the two samples have low enough surface roughness and are sufficiently clean, total thickness variations of a few μm over a full four-inch wafer are tolerable for silicon-silicon bonds [226]. A good "rule of thumb" metric for III/V bonding is that a total thickness variation on the order of ≈ 10s of nm over a length of 100s of μm or more is acceptable, which scales to a few μm total thickness variation over a four-inch wafer, consistent with that of typical commercially available 0.5 mm thickness silicon wafers [53].

Cleaning a sample sufficiently well for bonding requires careful sample handling and acute attention to detail, and it is often an iterative process involving repeated rounds of

cleaning and sample microscope inspection. A mockup cartoon of the cleaning procedure used for the Gen-2 SAW-QD process is shown in Figure 5.9. The full process traveler is detailed in C. The sample is placed on a non-shedding clean room wipe held above a crystallizing dish with a custom perforated PTFE basket, shown in C. A wash bottle with three drops of tergitol solution diluted in DI water is used to wet the surface of the sample while a cleanroom swab is applied to the sample and gently slided across the surface, using a slight twisting motion to attempt to remove particles from the surface. After swabbing with one flat face of the swab across one side of the sample for 5-10 times, the swab can be flipped over to the opposite face and the process repeated. Afterwards, the sample is rotated 90 degrees, the process is repeated for the next side, and the swabbing is repeated for all four sides of the rectangular sample.

5.2.2   Process Development of IDTs

The IDTs of the Gen-2 SAW-QD devices were designed with an electrode structure supporting unidirectional emission (FEUDTs) and to operate at 4.0 GHz. The electrode feature size of $\Lambda/12 = 84.5$ nm required the development of a high-resolution electron beam lithography (EBL) process. To minimize the EBL write time, the IDTs were fabricated in two process steps. First, the outlines of the IDT electrode area were patterned with photolithography using a negative-tone photoresist, then etched using the recipe in Section 5.1 to remove the NbN thin film except where the IDTs were to be subsequently patterned. Next, the inverse of the electrode pattern was written using a positive-tone EBL resist, to clear the gaps between the electrodes as well as the NbN to the right and left of the IDT left over from the IDT outline patterning.

For the second step of IDT fabrication, an IDT EBL process was developed on NbN-on-LiNbO$_3$ using a high resolution EBL resist called CSAR, which is similar to the more

(a) Underdeveloped CSAR

(b) Incorrect line width

(c) Lost pattern at edges

(d) Final process, from device
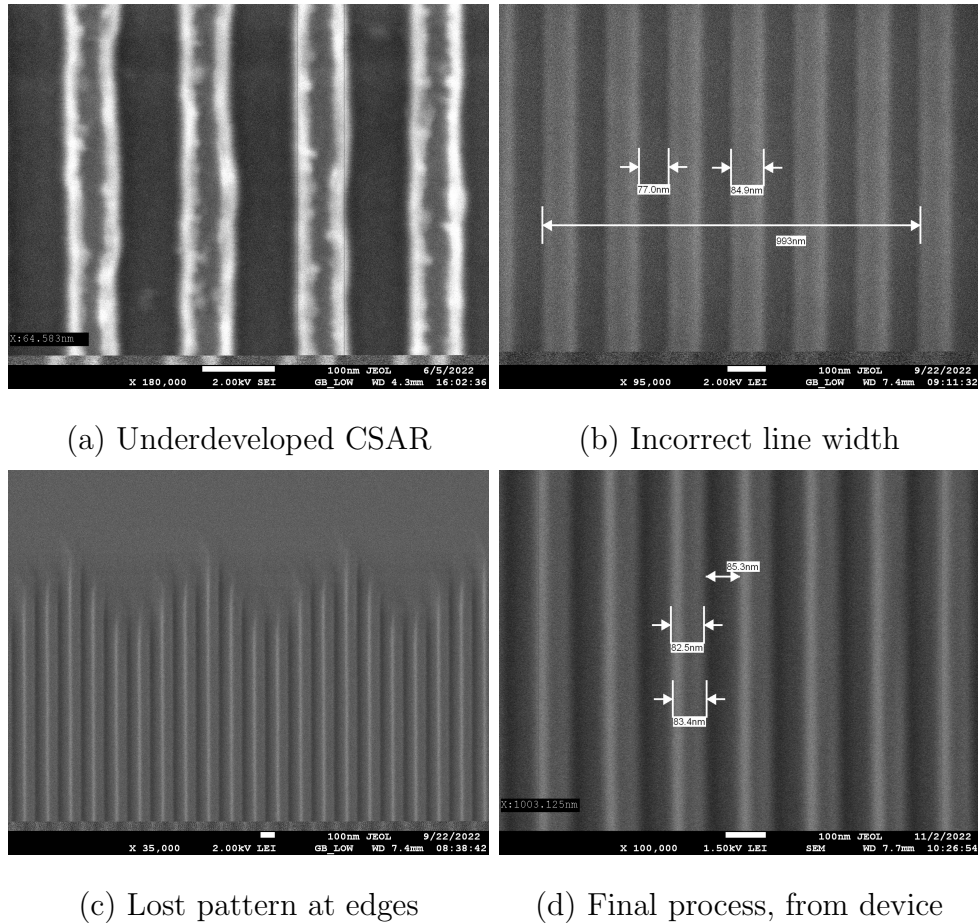
Figure 5.10: a Initial run of CSAR dose/pattern bias calibration showing lines in CSAR (lighter gray) with residue indicating insufficient resist develop time. b Subsequent run showing too narrow of etched lines, indicating an incorrect exposure dose or pattern process bias. c SEM of the top of a prototype FEUDT structure showing the pattern was lost (resist not cleared) at the edges of the pattern, necessitating proximity correction. d IDT electrodes with the correct dose and pattern bias selected, taken from a device on the Gen-2 test structures chip.

common ZEP resists and features excellent dry etch resistance. To optimize the EBL process, both the optimal EBL base dose for the IDT electrodes and a pattern width bias correction had to be found within the same array of test structures. An initial wide

sweep of the EBL dose was used to find the correct ballpark dose value, then a finer sweep was performed to find the optimal dose and pattern bias.

During the first several runs of the dose array tests, SEM and AFM characterization were performed after the EBL and etching steps, due to the difficulty in successfully imaging $LiNbO_3$ with charging effects. Initial fabrication runs showed the patterned lines in NbN had an irregular pattern, which did not improve with finer dose sweeps. Indeed, the subsequent fine dose arrays were difficult to use for any quantitative judgements on dose or pattern bias, given that the line widths of the NbN electrodes were not uniform and adjacent structures looked similar to each other. After some difficulty pinpointing the cause of this nonuniformity, SEM images were taken after the EBL development step and before the etch step so that the CSAR resist pattern could be imaged. The result in Figure 5.10a shows the irregular pattern in the NbN electrodes was transferred from the CSAR resist, which appears to have some leftover residue from the develop step. Concluding that the CSAR was underdeveloped, and the develop time was increased by 20 seconds, which yielded much more uniform structures in the following EBL runs, as seen in Figure 5.10b-5.10d.

After another run of dose and pattern bias arrays, after which the optimal dose of 200 $\mu C/cm^2$ and pattern bias of -15 nm were found, the IDT process was used in a device, as shown in Figure 5.10d. The lines closely match the predicted widths based on the data from the previous dose array and process bias run.

5.2.3   Process Development of GaAs Wet Etch

The Gen-2 SAW-QD cavities require a GaAs etch process to etch a depth of approximately 38 nm with a resolution of 8 nm, as discussed in section 4.2. The GaAs etch process should also be repeatable, with multiple fabrication runs producing similar etch

depths, and both the etched surface roughness as well as the line edge roughness of the cavity corrugations should be as low as possible to reach a high internal quality factor.

A wet etch approach was selected because it was believed to be a simpler etch method to develop over dry etching. While ICP-RIE dry etching can be operated with lower power to decrease the etch rate, due to the complexity of achieving the correct balance of surface passivating and etching gases [297] and bias power, and because the requirements for the SAW cavity etch aspect ratio and sidewall angle are not demanding for the Gen-2 devices, a wet etch is a simpler and perfectly acceptable approach. The literature for wet etching of GaAs commonly uses a citric acid/peroxide mixture, which has been shown to be highly selective to GaAs over AlGaAs [201, 140]. The most important parameters for these room-temperature, mixed-solution etch experiments are the concentration of etchants in the solution and the volume ratio of the citric acid to the hydrogen peroxide base etchant.

The etch was used with a low citric acid/peroxide volume ratio of approximately 0.4:1 of citric acid to peroxide to limit the etch rate. To calibrate an etch time for this etch, first, process test structures were first fabricated using optical lithography for ease of testing; samples were then etched for 1, 2 and 5 minutes; the samples were stripped of photoresist; and the etch depths were measured using AFM as shown in 5.11a. After determining a ballpark etch rate, a subsequent set of test structures using the same EBL resist and feature sizes as the Gen-2 SAW-QD cavities were fabricated, then multiple samples were etched and measured using AFM. The AFM profile results of two such etch tests are shown in Figure 5.12b and 5.12b, etched for 5 and 20 minutes, respectively. As a check, samples with both EBL resist and photoresist were immersed in the etch solution for 5 minutes, and using ellipsometry, the resists did not have any measurable etch rate in the etch solution.

It was important to use the same resist and feature sizes for the etch tests as for the

real devices, because the first etch attempts caused significant delamination of the resist lines, as seen in Figure 5.11b. Adding an adhesion promoter and adjusting the resist bake parameters did not resolve the issue; instead, what was effective was sputter-depositing a very thin ($\ll 1$ nm) layer of titanium before spinning on the resist. Titanium has been shown to be an effective adhesion layer for very long and thin EBL features [173]. Interestingly, as opposed to works in the literature, the titanium adhesion layer used for this work was less than one monolayer thick, and did not lead to a noticeable increase in surface conductivity using an electrical four-point probe measurement. To be cautious for the SAW-QD devices, an optical lithography step was added to pattern openings in a photoresist layer to deposit titanium where the GaAs was to be etched; then, the resist was stripped and the EBL resist was spun for the GaAs etch. Surprisingly, exposure to wet solvents did not seem to have reduced the effectiveness of the titanium adhesion layer.

After calibrating the wet etch, three different EBL and GaAs etch runs were performed to pattern SAW cavities, which could be tested to determine the optimal etch depth for the SAW resonator quality factor. Unfortunately, the etch showed significant variability on the sample, with some attempts at etching not showing any appreciable etching over several minutes, as characterized by AFM before and after the etch. In one of the cases where no etching occurred, an O_2 ashing step for 10 seconds was performed, and a subsequent etch immediately after ashing showed an enhanced etch rate ≈ 400 % of the calibrated value. One hypothesis for why the etch may not succeed is that for some reason, the resist is not completely clearing from the EBL-exposed lines, and there is enough resist to prevent the etching solution from reaching the GaAs. This effect appeared in an etch calibration sample with PMMA resist, as well, and the O_2 ashing step was integrated into the process traveler. However, in subsequent etches after the ashing step, the Gen-2 test structure sample etched much faster than in any of the calibration samples. Two

attempts using the Gen-2 test structures sample showed ≈ 60 % or more increase in the etch rate compared to the calibrated rate of 10 nm per minute with the same resist and feature sizes (Figure 5.11a). The most significant difference between the two samples is that the Gen-2 process test structures sample is composed of MBE-grown GaAs, whereas the etch calibration test structures were from full-substrate GaAs wafers grown with the Czochralski method. It is plausible that the difference in material quality could lead to noticeable differences in the etch rate. Further study using similar MBE grown samples will need to be performed to calibrate the etch rate for MBE-grown GaAs samples.

5.3   Process for G2 2DM Devices

Figure 5.13 shows a simplified process flow used for the fabrication of the Gen-2 SAW-2DM devices. Initially, the process used a combination of direct-write optical and electron-beam lithography, but the direct-write optical lithography tool caused large misalignments $\approx 1~\mu m$ between successive device layers, which were not tolerable for this design. For this reason, the process was moved completely to EBL, which resolved the issue with an alignment accuracy $\approx$ 100-200 nm. First, alignment marks were patterned using EBL in a positive-tone PMMA and PMMA copolymer resist liftoff process, depositing a Ti (5 nm)/Au (100 nm) layer via electron-beam evaporation deposition. These alignment marks ensured the correct orientation of the SAW devices with respect to the crystalline X axis of $LiNbO_3$. The alignment marks were aligned with respect to the wafer flat of $LiNbO_3$; after liftoff of the alignment marks, the wafer was cleaved into large chips to reduce the thermal loading on the hot plate used for the $LiNbO_3$ wet etch. Next, a 150 nm SiO_2 hard mask was deposited using room-temperature sputter deposition and patterned using EBL in a positive-tone CSAR process and ICP-RIE etching, using a CHF_3 precursor and an O_2 ash immediately after etching to remove fluorinated resist residue.

After removing the resist, the LiNbO$_3$ substrate was then etched to form the SAW cavity mirrors with a wet etch consisting of heated ammonia and hydrogen peroxide. The SiO$_2$ hard mask was then stripped using a buffered HF solution, and a thin film of 20 nm of NbN was deposited and patterned using EBL in a negative-tone maN resist process and ICP-RIE etching with the same recipe as for the Gen-1 devices. Finally, contacts to the IDT devices were patterned using EBL in a positive-tone PMMA and copolymer liftoff process, depositing a Ti (5 nm)/Au (100 nm) layer via electron-beam evaporation deposition.

5.3.1   Process Development of LiNbO3 Wet Etch

The SAW cavity corrugations were defined using a mixture of 30 % weight ratio NH$_4$OH, 30 % weight ratio H$_2$O$_2$, and DI water in a 2:2:1 volume ratio, following the recipe used in Ref. [333] to realize high-Q photonic structures in thin-film LiNbO$_3$. This ammonia and peroxide mixture was found to have an extremely high selectivity to LiNbO$_3$ over the SiO$_2$ hard mask [333]. The solution temperature was found to have a dramatic effect on the LiNbO$_3$ etch rate, with an increase from $\approx$ 1 nm/min. at $\approx$ 83 °C to $>$ 5 nm/min. at 87 ° C. A temperature probe was inserted into the beaker of solution and used to regulate the sample temperature with a PI controller integrated within the hot plate. However, realizing a stable sample temperature proved difficult after inserting a sample, which often caused the solution to decrease by a few degrees, then to be heated more aggressively by the hot plate, which sometimes caused the temperature to overshoot and approach $\approx$ 86-87 ° C over a timescale of $\approx$ 5-10 minutes. AFM step measurements of the etched samples were taken at regular intervals to chart the progress of the etch. AFM profiles of the etched samples are shown in Figure 5.14 for both 2 GHz and 700 MHz devices on the same chip.

(a) Etch Rate Calibration

(b) Delaminated Resist

(c) Short Etch
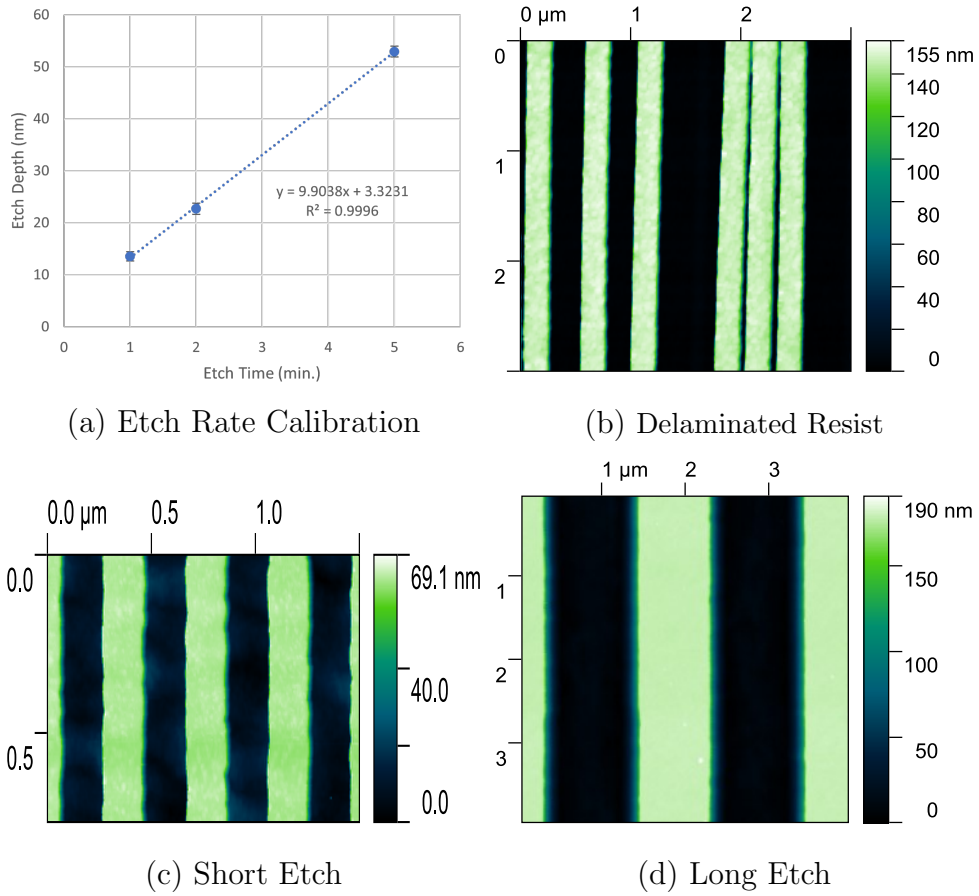
(d) Long Etch

Figure 5.11: a Rates of initial test structures patterned with optical lithography. b Delamination of EBL resist with etching for 30 seconds in a citric/peroxide 0.4:1 mixture. c AFM profile of "short" etch of 5 minutes. d AFM profile of "long" etch of 20 minutes.
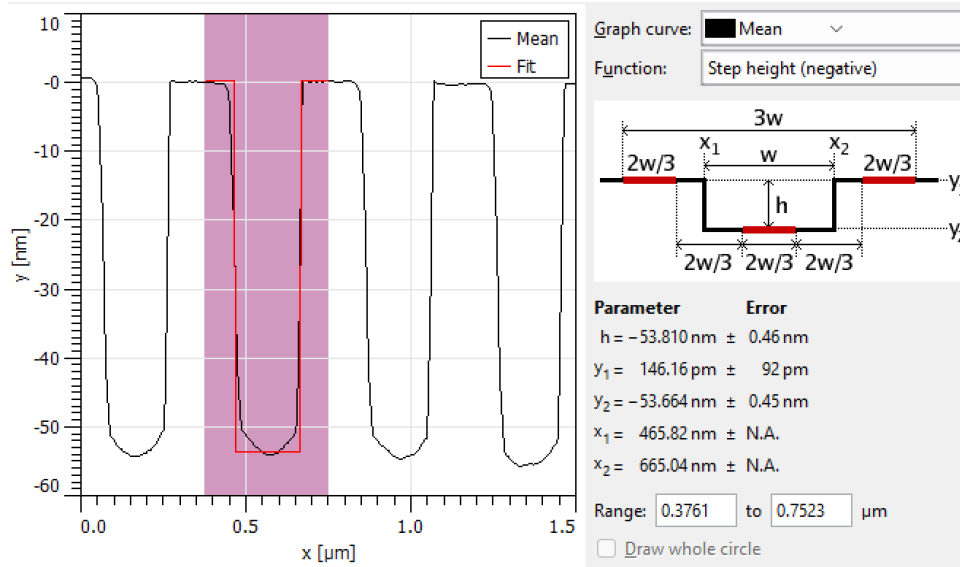
(a) Short Etch 1D Profile
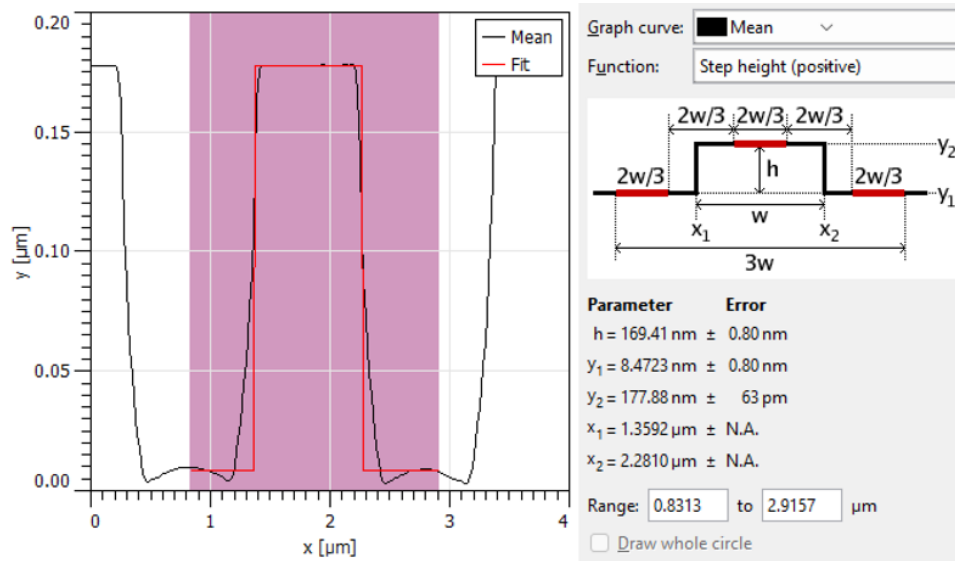
(b) Long Etch 1D Profile

Figure 5.12:

a 1D line average of profile in Figure 5.11 c. b Line average of profile in Figure 5.11 d.

1. Alignment marks

2. SiO2 hard mask dep.

3. Hard mask patterning

4. LiNbO3 patterning

5. NbN patterning

6. Contacts patterning
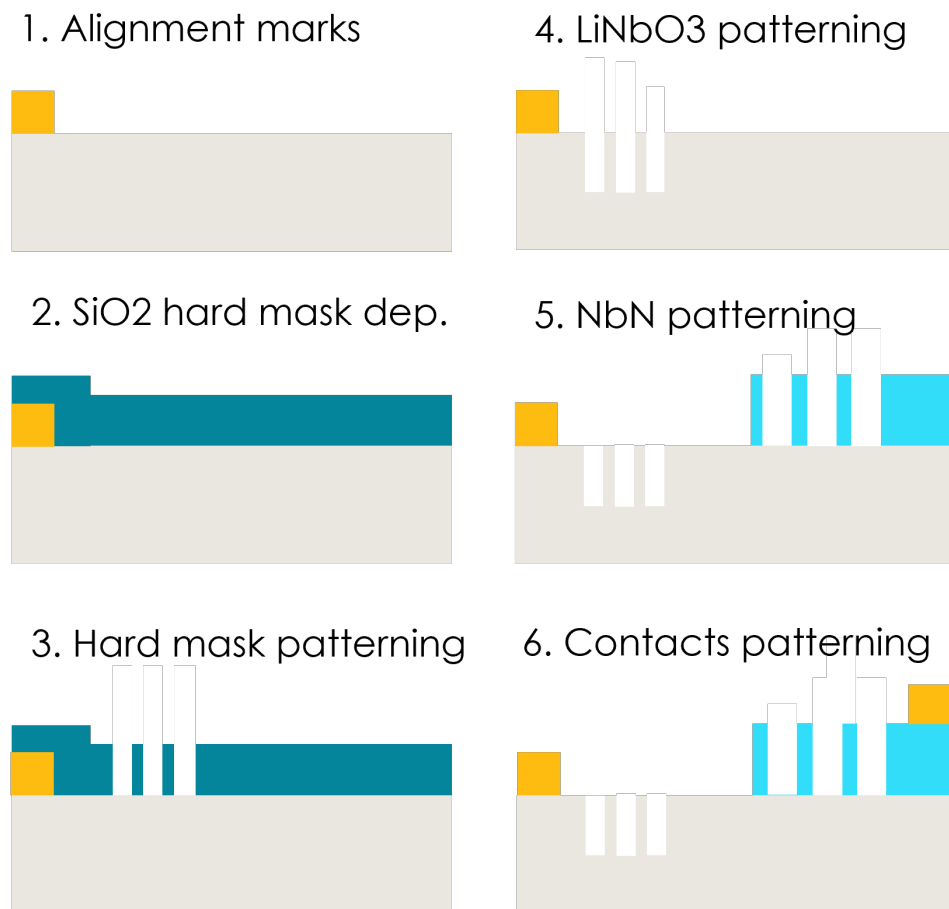
Figure 5.13: Simplified process flow diagram for the Gen-2 2DM-SAW devices.
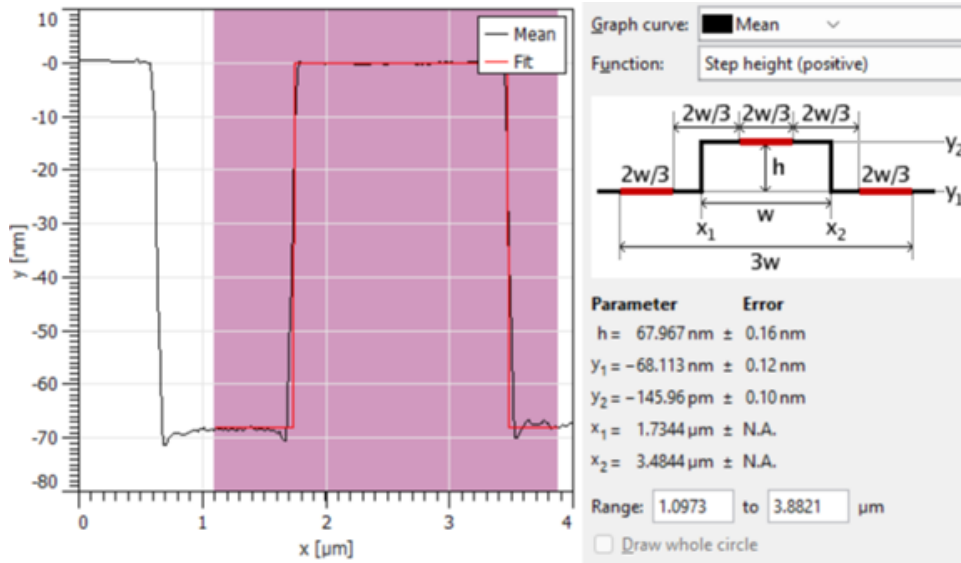
(a) 700 MHz
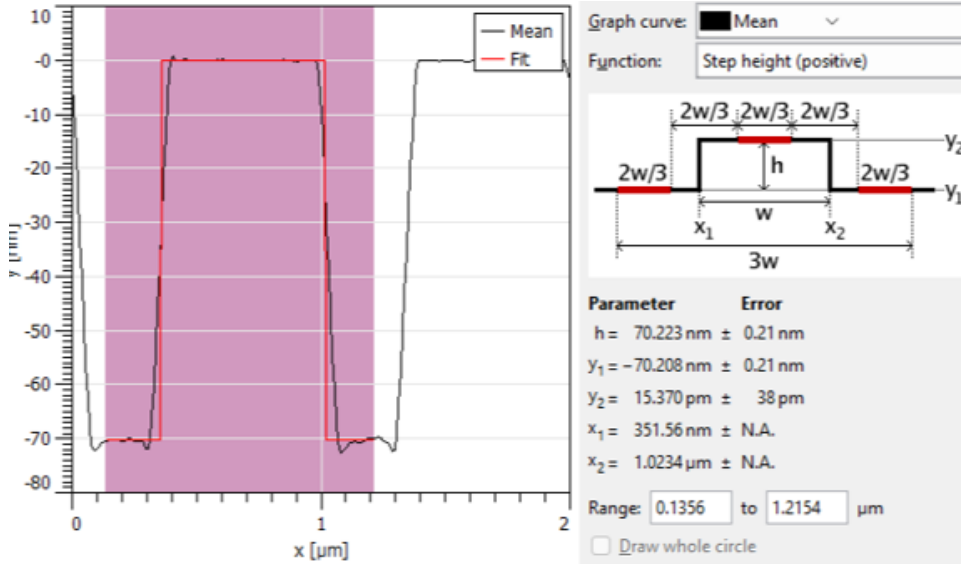
(b) 2 GHz

Figure 5.14: AFM profiles with step fits for the Gen-2 SAW-2DM devices.

Chapter 6

SAW Resonators Integrated with Quantum Dots

The following is adapted from Michelle Lienhart, Michael Choquer, Emeline Nysten *et al.*, "Heterogeneous integration of superconducting thin films and epitaxial semiconductor heterostructures with lithium niobate" in J. Phys. D: Appl. Phys. vol. 56, art. no. 365105, 2023.

6.1 Introduction

Lithium niobate ($LiNbO_3$) is a key material in the interconnected fields of nonlinear optics and acoustics due to its strong optical nonlinearity (e.g. $\chi^{(2)}$, $r_{33} = 3 \times 10^{-11} \, \mathrm{m\,V^{-1}}$) and piezoelectricity (e.g. $d_{22} = 21 \, \mathrm{pC\,N^{-1}}$) [305, 332, 61]. $LiNbO_3$'s strong electro- and acousto-optical effects can be harnessed in quantum integrated photonic circuits [63, 299]. This unique combination of properties renders $LiNbO_3$ a versatile host to synergistically combine various nonlinear photonic elements. Despite these advantages, $LiNbO_3$ does not host optical emitters, which are required for many photonics

applications. To overcome this shortcoming, several approaches are the focus of current research, including doping with rare earth ions [21, 127], direct growth [228] or transfer of 2D semiconductors [159, 256, 221], as well as heterogeneous integration of epitaxial semiconductors [211, 2].

Piezoelectrically generated SAWs are one method for integrating $LiNbO_3$ with optically active quantum emitters, as discussed in Chapter 3. For quantum applications, SAW devices have to be further improved by mitigating loss channels. These include Ohmic heating in conducting electrodes of finite electrical conductivity. To alleviate these losses, SAW devices can be fabricated using superconducting electrode materials. For example, aluminum (Al) electrodes have been employed in SAW resonators of high quality factors $Q \approx 10^5$ [175, 180, 6] proving the feasibility of this strategy. However, superconducting operation of such devices is limited to temperatures below aluminum's critical temperature $T_c \approx 1.2\,\text{K}$. Such low temperatures are not strictly necessary for quantum control schemes of optically active solid-state two-level systems like semiconductor quantum dots (QDs) or defect centers. These QDs exhibit low decoherence already at moderate temperatures $T \geq 4\,K$, which are accessible with conventional ^{4}He cryostats. This low decoherence was impressively demonstrated by the implementation of all-optical coherent control schemes [83, 23]. These experiments are conducted under significantly relaxed conditions, i.e., higher operation temperatures compared to superconducting Al quantum systems. Thus, materials with moderately high T_c would mark a significant advantage for hybrid SAW-QD devices. An additional challenge for integrating single quantum emitters with hybrid phononic quantum technologies remains the enhancement of the interaction strength between QDs and SAW phonons [194, 311, 316, 124] and at the same time mitigating the aforementioned losses due to Ohmic heating by employing superconducting electrodes. The first has motivated the development of hybrid systems consisting of strong piezoelectric SAW substrates with heterogeneously integrated III-V

compound semiconductors [241, 242, 97]. Heterogeneously integrated SAW devices are an extremely active field of current research, and recently large-scale radio frequency acoustoelectric devices have been realized [104, 103] This versatile approach is naturally suited to realize hybrid QD-SAW devices with transferred epitaxially grown QD layers [230, 211, 212]. For the latter, nitride-based superconductors are a leading material platform in the moderate temperature range because these materials exhibit much higher critical temperatures compared to Al. For example, niobium nitride (NbN) exhibits its superconducting transition at $T_\mathrm{c} \approx 16\,\mathrm{K}$ and is a well established material for superconducting single-photon detectors (SSPDs) [239, 328, 330, 49, 57]. SSPDs made from NbN and related compounds have been successfully demonstrated on a variety of substrates, including the materials used in this work: $LiNbO_3$ [279, 55, 248, 167] and GaAs [87, 67]. NbN and NbTiN single-photon detectors on $LiNbO_3$-on-insulator waveguides have been demonstrated with system detection efficiencies of $46\,\%$ and $27\,\%$, respectively [248, 167].

Here, a scalable two-stage heterointegration process of III-V epitaxial QD heterostructures and superconducting electrodes on $LiNbO_3$ is developed. In this process, the fabrication technologies for NbN SSPDs, epitaxial lift-off, and bonding of III-V heterostructures are co-integrated. The full functionality of the fabricated devices is validated by verifying and quantifying two key performance metrics: (i) the superconducting transition of the electrodes and (ii) the optomechanical and acoustoelectric control of the QDs and simultaneous superconducting operation of the SAW electrodes.

6.2   Sample design and fabrication

The two-stage heterointegration process is implemented on 128° Y-rotated $LiNbO_3$, a common piezoelectric substrate for SAW resonator filters and delay lines with high

135
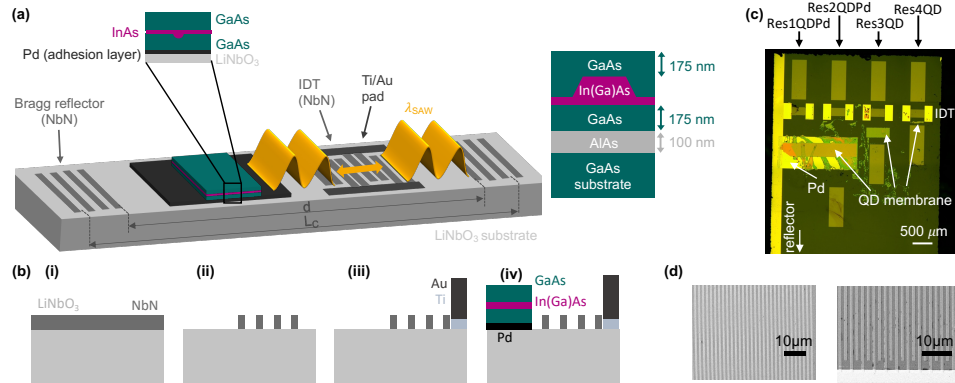
Figure 6.1: **Device fabrication** – (a) Schematic of the hybrid device. (b) Heterogeneous integration process flow: (i) NbN sputter deposition, (ii) optical lithography and etch, (iii) contact pad metallization lift-off, (iv) transfer of epitaxial III-V semiconductor heterostructure. (c) Optical microscope image of four devices of different cavity lengths with In(Ga)As QD heterostructure membranes heterointegrated.

(d) Scanning electron microscope images of the reflectors (left) and the IDT (right).

electromechanical coupling $K^2 = 5.4\%$ and phase velocity of $c_0 = 3978\,\mathrm{m\,s^{-1}}$ at room temperature along the X-direction [203]. The prototype device is shown in Figure 6.1 (a). It is a one-port SAW-resonator aligned along the X-direction with NbN superconducting electrodes and an In(Ga)As QD heterostructure. In essence, two Bragg reflectors separated by a distance d form a SAW resonator with an effective cavity length L_c. An interdigital transducer (IDT) is positioned in close proximity to one of the reflectors for SAW generation. This asymmetric configuration allows for heterointegation of large area semiconductor films. The electrodes of the Bragg reflectors and the IDT are made from NbN. The IDT electrodes are contacted by normal conducting pads. This configuration is adopted from previous work [212] employing normal conducting electrodes which provides the reference for benchmarking the performance of the advanced design developed here. The process flow diagram for sample fabrication is schematically shown in Figure

6.1(b). Steps (i) - (iii) are the first heterointegration stage in which the SAW component is realized. It follows a top-down route starting with a continuous thin film and, thus, is fully scalable to the wafer-scale. In step (i) a uniform 20 nm thick film of NbN is deposited directly on a 100 mm diameter $LiNbO_3$ substrate using reactive DC magnetron sputtering. The NbN deposition parameters are as follows: 2 mT chamber pressure, 30 sccm argon and 4 sccm nitrogen gas flows, 250 V DC bias voltage. To generate high-quality superconducting NbN films with high T_c, an RRR superconducting-grade Nb sputter target was used[270]. In step (ii) this film is subsequentially patterned using optical lithography and inductively coupled plasma reactive ion etching with CF_4 chemistry. The corresponding ICP etch parameters are the following: 0.4 Pa chamber pressure, 144 sccm CF_4 and 9 sccm nitrogen gas flows, 850 W source power, 35 W bias power. The SAW resonators are finalized in step (iii) when pads composed of Ti (10 nm)/Au (90 nm) are defined by a lift-off process to contact the NbN electrodes of the IDT. The second heterointegration stage is step (iv) during which the semiconductor membrane is transferred onto the $LiNbO_3$ using epitaxial lift-off and transfer [321, 211]. The heterostructure used is shown in the right part of Figure 6.1 (a). It is grown by molecular beam epitaxy on a semi-insulating (001) GaAs substrate starting with a 100 nm thick AlAs sacrificial layer. The active part of the heterostructure consists of a 250 nm thick GaAs layer with a single layer of In(Ga)As at its center. This active part is removed from the growth substrate by selectively etching the AlAs sacrificial layer using hydrofluoric acid (HF) and then transferred onto the $LiNbO_3$.

In contrast to previous work [211, 212], two types of devices are studied in this chapter. For the first type, shown in Fig. 6.1 (a), analogous to the previous design [212], a 50 nm thick palladium (Pd) adhesion layer on top of a 5 nm thick titanium (Ti) layer defined via a lift-off process creates a strong and rigid metallurgic bond between $LiNbO_3$ and the semiconductor. This layer also serves to shunt the piezoelectric fields,

suppressing acoustoelectric charge carrier dynamics. For the second type, no Ti/Pd is used and consequently the interface between $LiNbO_3$ and the semiconductor is no longer an equipotential plane. Thus, the piezoelectric potential induced by the SAW at the $LiNbO_3$ surface extends into the semiconductor[309]. This allows the verification of piezo-optomechanical coupling comprising dynamic control of the QD energy levels and electric field driven ultrafast carrier dynamics [254, 145, 267] to regulate the charge state of the QD [253, 312]. The one-port SAW resonators were designed for a SAW wavelength $\lambda_0 = 10.0\,\mu m$ corresponding to a nominal SAW frequency of $f_0 \simeq 400\,MHz$. These resonators had four different mirror spacings $d = \{440, 220, 110, 60\} \times \lambda_0$ as shown in Fig. 6.1(c). The effective cavity length is given by $L = d + 2 \times L_p$, where d is the above spacing between the Bragg reflectors and $L_p = w/r_s$ is the mirror penetration depth for of a single Bragg reflector. For the electrode width used, $w = \lambda_0/4 = 2.5\,\mu m$ and single-electrode reflectivity $r_s \approx 0.02$ [212, 179, 203], this equation yields $L_p \approx 130\,\mu m$. Figure 6.1 (c) and (d) show optical and scanning electron microscope images of the final devices. Figure 6.1 (c) shows that Res1QDPd and Res2QDPd contain QD membranes attached via a Pd adhesion layer, whereas the Pd layer is absent for Res3QD and Res4QD. Table 6.1 gives an overview of the different resonator designs (nominal SAW frequency f_0, nominal SAW wavelength λ_0, mirror spacing d, QD membrane, and Pd adhesion layer). Figure 6.1 (d) shows high resolution images of the Bragg reflector (left) and the IDT (right) demonstrating successful pattern transfer into the NbN.

6.3   Characterization Techniques

After completing the two-step heterointegration process, the sample was affixed to a custom made sample mount and wire bonded to a PCB. All measurements were performed with the sample placed inside a variable temperature closed-cycle optical cryostat with

radio frequency (RF) signal lines. A vector network analyzer (VNA) was employed for RF analysis, determining the S_{11} scattering parameter under various RF power levels (Prf). To study the piezo-optomechanical response of individual QDs, a blend of time-integrated and time-resolved photoluminescence (PL) spectroscopy was used [308]. A RF signal generator provided excitation of the SAW resonator via the IDT. An oscilloscope, synced to the timing of the excitation laser and connected via a directional bridge to the device under test (DUT), was used to maintain consistency between optical and RF electrical data [212].

All of the optical excitation used a continuous wave diode laser at $\lambda = 833 nm$, focused by a microscope objective (NA = 0.81) with a moderate optical pumping density ($P_{optical} = 191\,Wcm^{-2}$), which ensured that there was a preferential excitation of single excitons and a negligible amount of biexciton emission. The QD emission was collected by the same microscope objective as for excitation, then spatially dispersed using a 0.7 m grating monochromator. Optical detection involved cooled CCD detectors for time-integrated multi-channel analysis and a single photon avalanche diode (SPAD) for single-channel time-resolved detection with a timing resolution $< 50\,ps$, synchronized with the electrical signal applied to the IDT [144].

6.4   Electrical Characterization

First, the electrical functionality of the fabricated device is verified within the superconducting phase of NbN and determine the permissible ranges of the key operational parameters: sample temperature (T) and the RF electrical power (Prf) applied to the IDT. Figure 6.2 presents a comprehensive dataset and its analysis for resonator **Res0** prior to transferring the QD heterostructure. The nominal design frequency was $f_0 = 300$ MHz, accompanied by a designated mirror distance of d1 = 340 $\lambda_0 = 4522\,\mu m$,
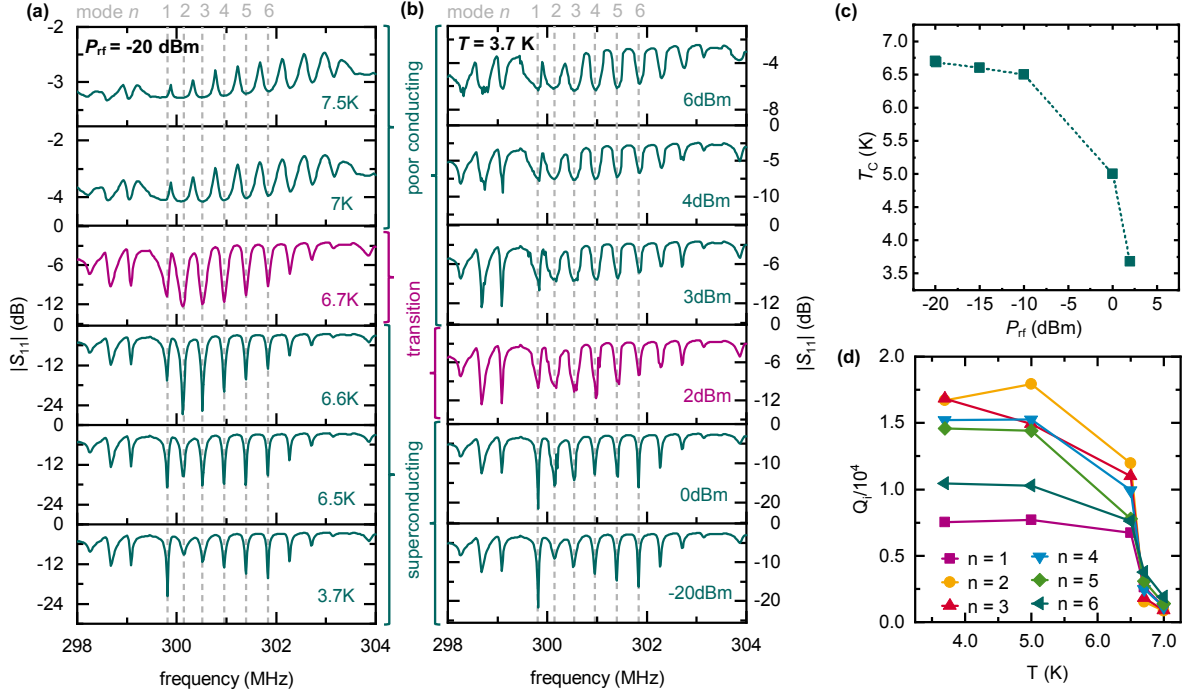
Figure 6.2: **Electrical Characterization** – Microwave S_{11} parameter electromechanical characterization of the device **Res0**.

where $\lambda_0 = 13.3\,\mu m$. A relatively low RF power of $P_{\rm RF} = -20\,{\rm dBm}$ is applied to the device, and the $S_1 1$ scattering parameter is recorded across various applied electrical frequencies at different sample temperatures within the cryostat. These findings are graphically depicted in 6.2 (a), with the temperature increasing from the lower to upper spectra. The spectrum recorded at the baseline temperature of T = 3.7 K exhibits distinctly resolved minima in the reflected RF power at the resonance frequencies of the cavity modes (indicated by vertical dashed lines). The determined free spectral range (FSR) is FSR = $(410 \pm 40)\,{\rm kHz}$, which is equivalent to an effective resonator length of $L_{\rm c} = (4866 \pm 568)\,\mu{\rm m}$, in good agreement with the nominal lithographically defined cavity length of $d = 4522\,\mu{\rm m}$. The measured S_{11} can be fitted using

$$S_{11}(f) = \frac{(Q_{{\rm e},n} - Q_{{\rm i},n})/Q_{{\rm e},n} + 2iQ_{{\rm i},n}(f - f_n)/f}{(Q_{{\rm e},n} + Q_{{\rm i},n})/Q_{{\rm e},n} + 2iQ_{{\rm i},n}(f - f_n)/f} \tag{6.1}$$

140

Device name	Res0	Res1QDPd	Res2QDPd	Res2QD	Res3QD	Res4QD
f_0 (MHz)	300	400	400	400	400	400
λ_0 (µm)	13.3	10.0	10.0	10.0	10.0	10.0
d (λ_0)	340	440	220	220	110	60
d (µm)	4522	4400	2200	2200	1100	600
QD membrane	no	yes	yes	yes	yes	yes
Pd layer	no	yes	yes	no	no	no

Table 6.1: Overview of the different resonator designs, where f_0 nominal SAW frequency, λ_0 is the SAW wavelength as defined lithographically, d is the mirror spacing defined lithographically, and the bottom two rows indicate the presence or absence of a QD membrane and a Pd adhesion layer.

with $Q_{i,n}$ and $Q_{e,n}$ being the internal and external Q factors of mode n at frequency f_n [179]. At the base temperature of the cryostat, the obtained values range from $7000 \leq Q_{i,n} \leq 17000$, indicating a threefold enhancement compared to identical resonator devices equipped with normal conducting Ti/Al electrodes [212].

As T increases, the transition from superconductivity to normal conductivity is observed to occur at $T_c = 6.7\,\mathrm{K}$ (purple spectrum). For temperatures above T_c, there is a characteristic change of the spectrum with the emergence of peaks (instead of dips) that are shifted in frequency compared to the modes in the superconducting state (dashed lines). This behavior is expected for loss-dominated resonators, which is the case for NbN thin films above T_c. Its conductivity is at least one order of magnitude lower than commonly used normal conducting metals like aluminum [89, 303, 203]. In Figure 6.2 (b) analogous S_{11} spectra with the temperature held constant are shown at $T = 3.7\,\mathrm{K}$ and the electrical power applied to the IDT increasing from the bottom to the top. As P_{RF}

increases from $P_{\mathrm{RF}} = -20\,\mathrm{dBm}$, there is a clear change of the spectrum at $P_{\mathrm{RF}} = +2\,\mathrm{dBm}$ (purple). This change is markedly different to the abrupt change in Figure 6.2 (a) between $T_c = 6.7\,\mathrm{K}$ and $T = 7\,\mathrm{K}$. Here, the dips at the resonator mode frequencies broaden continuously and evolve in a spectrum similar to the normal conducting state at the highest power level $P_{\mathrm{RF}} = +6\,\mathrm{dBm}$. This continuous broadening cannot be explained by a change of the global sample temperature, but instead indicates a local breakdown of superconductivity in a subset of the electrodes. Since the cavity mode frequencies (vertical grey lines) remain constant, this implies that superconductivity is initially preserved in the Bragg mirrors' electrodes. Breakdown occurs locally in the IDT electrodes, where the driving RF electrical signals drives a current. The corresponding local increase of the current density above the critical value breaks superconductivity. This occurs first at the cavity resonance where the highest current densities are reached. With increasing P_{RF}, the critical current density is reached off-resonance giving rise to the observed apparent broadening. At the highest P_{RF}, superconductivity breaks down over the entire range of frequencies. Ohmic heating in this normal conducting state raises the global sample temperature above T_c, retaining a spectrum similar to that observed in Figure 6.2 (a).

To further corroborate this interpretation, the observed T_c as a function of P_{RF} is analyzed, plotted in Figure 6.2 (a). These data show that an increase of P_{RF} leads to a decrease of the measured T_c. At this point, it is important to keep in mind that an increase of P_{RF} corresponds to an increase of the current density. Thus the data in 6.2 (a) corresponds to an effective phase boundary of a superconductor in the current-temperature parameter space. Finally, $Q_{\mathrm{i},n}$ is analyzed as a function of T obtained from a best fit of Equation 7.1 to the data in Figure 6.2 (a). The obtained values for modes $n = 1, 2, \ldots 6$ are plotted for temperatures $3.7 \leq T \leq 7\,\mathrm{K}$ in Figure 6.2 (d). The data clearly show that high $Q_{\mathrm{i},n}$ is in fact preserved for all modes up to T_c when superconductivity breaks down. To summarize, the performed electrical characterization

proves superconducting operation with high internal $Q_{i,n} > 17000$. The derived effective phase boundary defines the parameter space for the operation of the studied device. For all experiments shown in the remainder of this article, the effective phase boundary was first pinpointed to ensure superconducting operation in the optical experiments.

6.5   Piezo-optomechanical characterization

In the second phase of the heterointegrated device characterization, the piezo-optomechanical interaction is investigated between the SAW resonator and the QDs in the heterointegrated device. The optomechanical coupling between single QDs and phononic modes is probed by measuring the optical emission as a function of the applied RF parameters. In all these experiments, the electrodes are in the superconducting state. Thus the *combined* superconducting operation and SAW control of single QDs is validated. In the following, the design frequency of the investigated devices is $f_0 \approx$ 400 MHz. In Sections 6.5.1 and 6.5.2, the resonator Res2QDPd resonator is used with the QD heterostructure transferred onto a Pd adhesion layer in its center. The Pd shunts the electric field induced by the SAW [230, 211]. Accordingly, Stark-effect modulation, which becomes dominant at high SAW amplitudes [309] and acoustoelectric charge state regulation [298, 253] are effectively suppressed and can be neglected in the following. In Section 6.5.3 a Res2QD resonator is used where a QD heterostructure is directly transferred onto the LiNbO$_3$ without a Pd adhesion layer. In this case, the piezoelectic fields can induce spatio-temporal carrier dynamics and thus regulate the charge state of the QD.
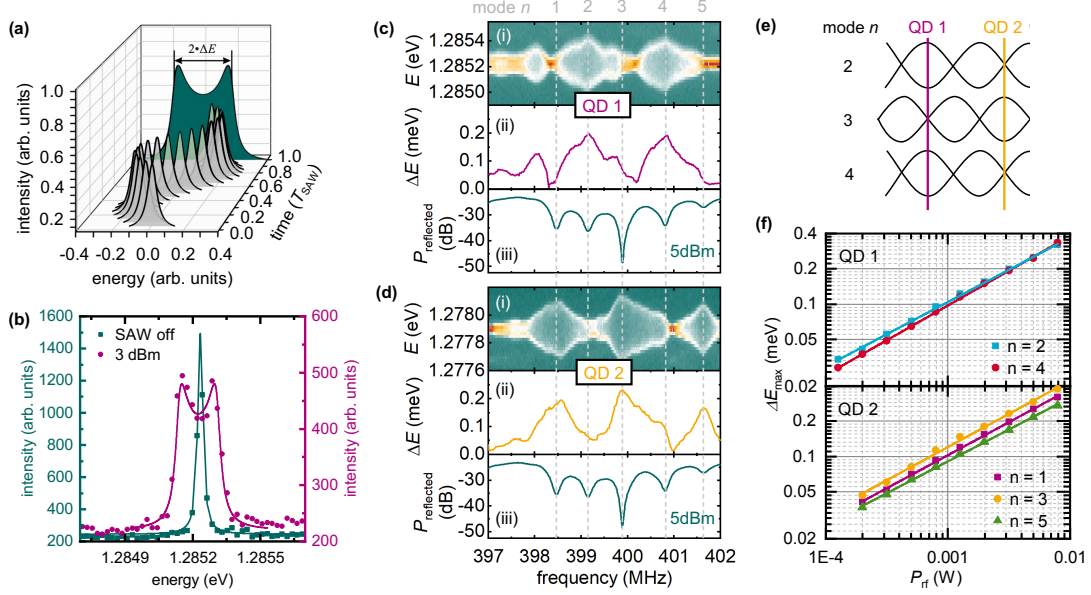
Figure 6.3: **Piezo-optomechanical characterization** – (a) Schematic of dynamic modulation of Lorentzian emission line giving rise to the time-integrated spectrum given by (6.2). (b) Emission line of a single QD (data points) without a SAW applied (green) and with a SAW applied (purple) with best fits of Equation 6.2 (solid lines). (c) and (d) PL spectrum (i), extracted ΔE (ii) and reflected electrical RF power (iii) recorded from QD 1 and QD 2, respectively. (e) Schematic of site-selective coupling of QD 1 and QD 2. (f) ΔE for different phononic modes as function of P_{RF} of QD 1 (top) and QD 2 (bottom).

6.5.1 Time-integrated optomechanical characterization

The optomechanical response of a single QD is first measured by time and phase averaged PL spectroscopy. As schematically shown in Figure 6.3 (a), the detected line shape is a time-average of the sinusoidally modulated Lorentzian QD emission line [309, 310] given by

$$I(E) = I_0 + f_{\mathrm{RF}} \cdot \frac{2A}{\pi} \cdot \int_0^{\frac{1}{f_{\mathrm{RF}}}} \frac{\omega}{4(E - (E_0 + \Delta E \cdot \sin(2\pi f_{\mathrm{RF}} \cdot t)))^2 + \omega^2} \, \mathrm{d}t \; . \qquad (6.2)$$

In this expression, I_0 denotes a time-independent intensity offset, E_0 the center energy, A the amplitude, ω the width of the Lorentzian emission peak, and ΔE the optomechanical modulation amplitude. Figure 6.3(a) schematically shows the sinusoidal modulation of the Lorentzian emission line of a single QD (gray) and the resulting time-integrated emission spectrum (green) with its optomechanical tuning amplitude labeled as $2\Delta E$. Figure 6.3(b) shows the measured time-integrated emission spectra of a exemplary QD (data points) and a best fit of Equation 6.2 (solid line). Without a SAW applied (green), the expected Lorentzian line is faithfully detected. When strained by a SAW ($P_{\mathrm{RF}} = 3\,\mathrm{dBm}$, $f_{\mathrm{RF}} = 399.62\,\mathrm{MHz}$, purple), the characteristic lineshape given by Equation 6.2 is observed.

Next, the optomechanical coupling of QDs to the SAW resonator modes is confirmed. By applying $P_{\mathrm{RF}} = 5\,\mathrm{dBm}$ to the IDT, a continuous-wave SAW field is generated within the resonator which is modulating the emission of the QDs, in which the resonator was verified to be in the superconducting state. Then, f_{RF} is scanned from 397 to 402 MHz. Two QDs are selected, QD 1 and QD 2, which are separated by $\approx 1.5 \times \lambda_0$ along the axis of the resonator. The results of the performed characterization experiments are shown for QD 1 and QD 2 in Figure 6.3(c) and (d), respectively. The upper panels (i) show the time-integrated PL intensity as a function of electrical f_{RF} (horizontal axes) applied to the IDT and photon energy (vertical axes). The lower panels (iii) show the simultaneously recorded reflected RF power to identify the involved SAW modes f_n of mode index (n) of the hybrid SAW resonator. These are labelled and marked by the vertical dashed lines. The center panels (ii) show $\Delta E(f_{\mathrm{RF}})$ of the two QDs extracted from the experimental data by fitting Equation 6.2. These data clearly prove the anticipated site and frequency

selective coupling of the embedded QDs and the phononic modes. QD 1 in Figure 6.3 (c) shows strong optomechanical response ΔE and, thus, strong optomechanical coupling when f_{RF} is in resonance with an even index mode $n = 2, 4$. Conversely, this coupling is suppressed for odd index models $n = 1, 3, 5$. The optomechanical coupling is inverted for QD 2 in Figure 6.3 (d), which exhibits strong and weak coupling for $n = 1, 3, 5$ and $n = 2, 4$, respectively. These observations are in agreement with the QD 1 being at the antinodes of the $n = 2, 4$ modes and QD 2 being at those of the $n = 1, 3, 5$ modes as shown schematically in Figure 6.3 (e) [212].

In a third step, the dependence of the optomechanical modulation ΔE on the applied RF power is studied. The applied power, P_{RF} is increased from $P_{RF} = -9\,\mathrm{dBm}$ in steps of $2\,\mathrm{dB}$ to $+9\,\mathrm{dBm}$ and record the resulting ΔE of QD 1 and QD 2. In this range of P_{RF}, the device is in the superconducting state, which was confirmed by the simultaneously measured electrical power reflected from the device. This measured range is $3\,\mathrm{dB}$ larger than that of the $300\,\mathrm{MHz}$ device shown in 6.2. The extracted ΔE of QD 1 and QD 2 are plotted as a function of P_{RF} in the upper and lower panel of Figure 6.3(f), respectively. These data are presented for all modes to which the respective QDs couple. Moreover, the data is plotted in double-logarithmic representation to identify the power law dependence $\Delta E \propto P_{RF}^m$ and the underlying coupling mechanism. QD 1 exhibits a power law dependence with an average slope $m_{QD1} = 0.57 \pm 0.01$ and QD 2 with $m_{QD2} = 0.55 \pm 0.01$. The amplitude of the SAW, $u_z \propto \sqrt{P_{RF}}$, and $\Delta E \propto u_z$. Hence, a slope of $m \sim 0.5$ is a characteristic fingerprint for deformation potential coupling being the dominant mechanism [308]. It is noted that the small increase compared to the ideal value of $m = 0.5$ may arise from a weak nonlinearity as observed for similar hybrid devices with normal conducting electrodes [212]. Moreover, the extracted slope excludes Stark effect modulation for which $m = 1$ is expected [309].
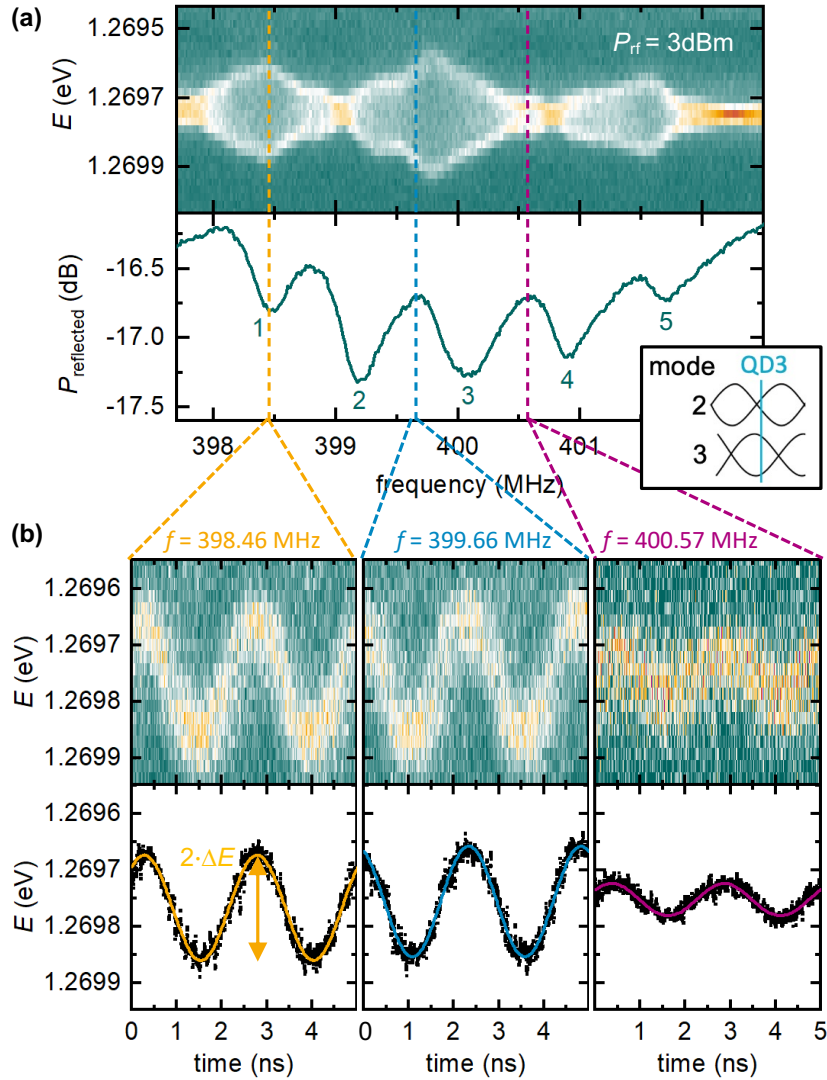
Figure 6.4: **Time-resolved dynamic modulation** – (a) Time integrated PL spectrum of QD 3 and reflected RF power. The inset shows the position of QD with respect to the $n = 2$ and $n = 3$ modes. (b) Time-dependent PL spectra (top) for three selected f_{RF} marked in (a) and extracted spectral modulations (bottom).

6.5.2 Time-resolved optomechanical characterization

Next, time-correlated single-photon counting is performed to resolve the SAW-driven dynamics of QD 3 directly in the time domain. This type of characterization allows

direct observation of the temporal shift of the QD emission line, which was not addressed in the previous work on hybrid QD-SAW resontors with normal conducting electrodes [212]. In the following, $P_{RF} = 3\,$dBm is fixed. Before conducting these time-resolved measurements, the time-integrated emission of QD 3 is studied as in the previous section to determine the position of the selected QD in the SAW cavity field. Figure 6.4(a) shows the time-integrated emission spectrum of QD 3 (top panel) and the simultaneously measured reflected RF power (bottom panel) as a function of f_{RF}. From these data, it is concluded that QD 3 couples strongly to odd modes and only weakly to even modes. The derived relative position of QD 3 within the SAW cavity field is shown schematically as an inset of Figure 6.4(a). In addition and in agreement with the data shown in Figure 6.3 and [212], a pronounced optical response can be found in the frequency range between the $n = 2$ and $n = 3$ modes. The time-resolved analysis of the dynamically strained QD 3 is performed for three characteristic frequencies f_{RF} marked by different colored lines in Figure 6.4 (a). $f_1 = 398.46\,$MHz corresponds to the resonance of mode $n = 1$. $f_{23} = 399.66\,$MHz and $f_{34} = 400.57\,$MHz are chosen in between the $n = 2/n = 3$ and $n = 3/n = 4$ modes, respectively. At these frequencies, QD 3 shows strong (f_{23}) and weak (f_{34}) modulations. The top panels of Figure 6.4 (b) present plots of the temporal modulation of the QD emission line at the three selected frequencies in false color representation. In all three cases, a clear sinusoidal modulation is observed in the time domain. Furthermore, the period of these modulations correspond to that set by the applied RF. The bottom panels of Figure 6.4 (b) show the peak positions (black) as a function of time extracted from these data by best fits of a Lorentzian line for each time stamp. By fitting the obtained data with a sine function (solid orange, blue, and purple lines) the modulation frequencies of QD 3 are extracted to be $f_{QD,1} = 398.45 \pm 2.77\,$MHz, $f_{QD,23} = 399.66 \pm 2.75\,$MHz, and $f_{QD,34} = 400.45 \pm 1.27\,$MHz. These values agree well with the electrical RF. Thus, these data prove that in this sample the QD is predominantly modulated at
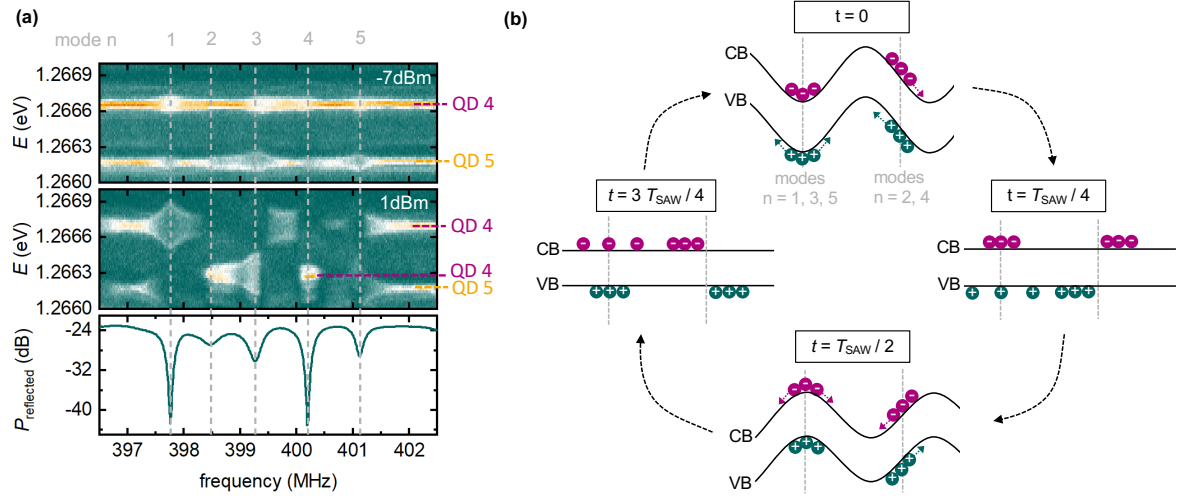
Figure 6.5: **Acoustoelectric charge state regulation** – (a) PL spectra as function of f_{RF} at $P_{RF} = -7\,\text{dBm}$ (top) and $P_{RF} = +1\,\text{dBm}$ (center) showing the emission of QD 4 and QD 5 and simultaneously measured reflected RF power (bottom). (b) Schematic SAW-induced bandstructure modulation in the device and the resulting acoustoelectric electron (purple) and hole (green) dynamics for one full acoustic cycle. Dashed lines mark the position of QD 4 when even and odd index modes are excited.

the SAW excitation frequency, regardless of its location in the phononic mode spectrum. These findings furthermore clearly indicate that no dominant wave mixing processes occur in the SAW resonator and that the dominant coupling mechanism is deformation potential coupling.

6.5.3   Acoustoelectric charge state control

Finally, acoustoelectric control of the charge states of single QDs is demonstrated on this hybrid platform. To this end, resonator Res2QD is studied with a nominal SAW frequency of $f_0 = 400\,\text{MHz}$ with a mirror spacing d $= 220\,\lambda_0$ and a QD heterostructure directly transferred onto the LiNbO$_3$ without a Pd adhesion layer. Again, the design

frequency is $f_0 = 400\,\text{MHz}$ as confirmed by the SAW mode spectrum plotted in the lower panel of Figure 6.5 (a). The upper panel of Figure 6.5 (a) shows the emission spectrum of two QDs, QD 4 and QD 5 (plotted in false-color representation as a function f_{RF}). These data are recorded at relatively low RF power of $P_{\text{RF}} = -7\,\text{dBm}$ at which strain coupling is dominant [309, 312]. Thus, both emission lines QD 4 at $E = 1266.66\,\text{meV}$ and QD 5 at $E_5 = 1266.17\,\text{meV}$ show the expected broadening when f_{RF} is tuned into resonance with modes of odd ($n = 1, 3, 5$) index, while no significant coupling is observed for modes of even index ($n = 2, 4$). Thus, it is concluded that both QDs are at the antinodes (nodes) of the strain field of odd (even) index modes. This observation proves mode-selective *strain* coupling of the QD to the SAW even with a relatively weak van der Waals bond between the semiconductor and LiNbO$_3$ substrate, compared to the rigid metalurgical bond for the devices with the Pd adhesion layer. Next, the RF power is increased to $P_{\text{RF}} = +1\,\text{dBm}$ and plot the recorded emission spectra in the same range of photon energies and f_{RF} in false-color representation in the center panel of Figure 6.5 (a). These data exhibit a completely different behaviour than those of samples with a Pd adhesion layer [cf. Figures 6.3 and 6.4, and references [211, 212]] arising from the combination of strain tuning and acoustoelectrically driven carrier dynamics by the SAW. In this device without the Pd adhesion layer, no highly-conductive metal shortens the piezoelectric fields induced by the SAW on the LiNbO$_3$-GaAs interface. Thus, the electric field extends into the semiconductor. This field efficiently ionizes the photogenerated excitons and induces spatio-temporal charge carrier dynamics (STCDs) [88, 254, 145]. The induced dynamics regulate the charge state of the QDs on timescales of the SAW and lead to correlated suppression and emergence of different emission lines [298, 253]. In contrast to other previous work, these dynamics are observed within a SAW resonator, and no freely propagating SAWs were employed.

In the following analysis, the emission from QD 4 is analyzed, for which different

emission lines can be clearly identified. In order to understand the experimental findings, it must be kept in mind that the analyzed device is a SAW resonator, in contrast to devices with propagating SAWs studied previously in the literature. In this resonator, the nodes of the phononic modes' standing wave pattern are stationary. To understand the experimental findings, the time-dependent strain and electric field at the position of QD 4 for a given mode index n is studied. As shown above, QD 4 is located at the antinodes of odd index ($n = 1, 3, 5$) modes and at nodes of of even index ($n = 2, 4$) modes. For X-propagating SAWs on 128° Y-rotated $LiNbO_3$, the volume dilatation inducing the optomechanical modulation and the electric potential are in phase and simultaneously tune the emission line and regulate the occupancy state. Figure 6.5 (b) schematically depicts the dynamic evolution of the bandstructure modulation at four distinct times during the acoustic cycle. At $t = 0$, the amplitude of piezoelectric potential of the SAW is maximum. Thus, the corresponding sinusoidal modulation is superimposed giving rise to the well established type-II band-edge modulation [237]. At $t = T_{SAW}/2$, the situation is reversed and positions of maxima and minima are exchanged. At $t = T_{SAW}/4$ and $t = 3T_{SAW}/4$, destructive interference of the SAW fields occurs and leads to an unperturbed flat bandstructure. In these schematics, the vertical dashed lines indicate the position of QD 4 in this bandstructure when odd index ($n = 1, 3, 5$) modes or even index ($n = 2, 4$) modes are excited.

For $n = 2, 4$, QD 4 is at the node of the electric potential modulation. Thus, the resulting gradient and hence amplitude of its electric field is maximum. This leads to an efficient dissociation of excitons and pronounced STCDs as shown in the schematics of Figure 6.5 (b). In the experimental data, a strong suppression of the emission line is observed for the weakly modulated case at $E = 1266.66\,meV$ and a new emission line at $E = 1266.28\,meV$. This switching is a characteristic fingerprint of acoustically regulated carrier injection driven by STCDs. For $n = 1, 3, 5$, QD 4 is at the antinode of the electric

potential modulation. Thus, the gradient and electric field vanishes and the STCDs are dominated by redistribution processes of electrons and holes from their unstable points (and position of the QD) to regions of maximum electric field. These processes are indicated in the schematics of Fig. 6.5 (b) and are slow compared to field-driven drift. This leads to marked changes in the carrier injection dynamics into QD 4 which favors the preferential generation of different occupancy states and resulting emission lines for different n. For $n = 1$, the occupancy state corresponding to the $E = 1266.66\,\mathrm{meV}$ line is preferentially generated, while for $n = 3$, that of the $E = 1266.28\,\mathrm{meV}$ line. For $n = 5$, both lines are almost completely suppressed which points towards efficient carrier depletion at the position of the QD 4. When tuning f_{RF}, a characteristic and reproducible switching pattern is observed. This observation unambiguously proves that the direct coupling of QD heterostructure to the LiNbO$_3$ substrate leads to pronounced STCDs and charge state regulation which can be efficiently suppressed by a thin metallic layer shunting the electric fields. Note that detailed modelling at the level possible for propagating SAWs [253, 312] is not possible for the devices studied here. As shown for the piezo-optomechanical response the complex mode pattern of the resonator comprises contributions of propagating and stationary waves. The observed switching hampers the faithful disentanglement of these contributions, which would be required to perform numerical simulations of the STCDs.

6.6   Conclusion

In summary, a two-step heterointegration process of a hybrid SAW-resonator device comprising superconducting electrodes and an epitaxial semiconductor heterostructure on a LiNbO$_3$ substrate is developed and implemented. This fabrication process can be reproduced at the wafer-scale by building on recent breakthroughs in this field. Firstly, the

transfer of millimeter-sized and few 100 nm-thick semiconductor heterostructure membranes can be realized at the wafer-scale through wafer bonding techniques [104, 103, 48]. Secondly, superconducting thin films are sputter-deposited and patterned in a subtractive process, which is in principle also directly scalable. The functionality of the fabricated devices was validated by characterizing the parameter space for superconducting operation of the SAW component. In these first experiments, the superconducting to normal conducting transition of the NbN electrodes was monitored as a function of temperature and applied electrical RF power. The achieved internal quality factor $Q_i \approx 17000$ marks a three-fold improvement to previously studied similar devices using normal conducting electrodes [212]. After transfer of the III-V semiconductor, the combined superconducting operation of the SAW device and piezo-optomechancial control of the embedded QDs was verified. In a series of experiments, mode-selective coupling of the QDs, time-modulation of the QD emission line, and acoustically regulated carrier injection are verified. The latter observation provides direct evidence of spectral tuning of the QD by dynamic strain and simultaneous acoustoelectric regulation of the QD's occupancy state for the first time in a SAW resonator.

This two-step heterointegration opens directions for advanced piezo-optomechanical quantum devices. First, the superconducting SAW resonators are fabricated with the same processes used for NbN single-photon detectors [167], enabling future SAW devices to be integrated with superconducting single-photon detectors during a single fabrication step. Second, the performance of these resonators can be deliberately enhanced to small mode volume ($V \approx \lambda^3$), higher Q-factor, and high frequency (> 1 GHz) operation [262]. These devices then harness the large K^2 of LiNbO$_3$ and strong optomechanical coupling of III-V semiconductor QDs [194, 311, 316]. These may ultimately enable coherent optomechanical control in the sideband regime [124, 106]. Third, the process can be extended to additional heterointegration steps for example adding defect quantum

153

emitters providing spin qubits serving as quantum memories [177, 95, 275, 208].

Chapter 7

Surface Acoustic Wave Cavity Optomechanics with Atomically Thin h-BN and WSe$_2$ Single-Photon Emitters

The following has been adapted from Sahil D. Patel, Kamyar Parto, Michael Choquer et al., "Surface Acoustic Wave Cavity Optomechanics with Atomically Thin h-BN and WSe$_2$ Single-Photon Emitters," PRX Quantum, vol. 5, no. 1, p. 010330, Feb. 2024.

7.1   Introduction

The recent discovery of single-photon emitters (SPE)s in 2D materials [15, 137], such as WSe$_2$ [269, 110, 44, 148, 285] and hexagonal boron nitride [288, 131], provides an opportunity to further enhance the coupling to SAWs while simplifying the device and fabrication complexity. 2D SPEs, which originate from crystalline defects in the host

material, exhibit high optical extraction efficiency and brightness with detection rates up
to 25 MHz [100, 170, 331], indistinguishable [82] and near transform-limited linewidths
[65], high single-photon purity, unique spin-valley phenomena [249, 78, 272], high working
temperatures [288, 171, 220], and site selective engineering [34, 217, 81, 219]. The layered
structure of 2D materials arising from van der Waals forces ensures that the defects are
two-dimensional and are able to function at surfaces, devoid from any surface states,
allowing for strong proximity interaction with their surrounding environment.

This strong proximity interaction, in addition to the site specific fabrication and
relaxed lattice-matching requirements, make 2D SPEs an ideal two-level system to be
integrated with optomechanical resonators. Proximity effects allow for efficient defor-
mation potential coupling, as illustrated in Fig. 7.3(a) and 7.3(b), while the ability to
deterministically transfer 2D monolayers onto nearly any surface allows for nanoscale
precision in positioning of a single SPE within optomechanical resonators [219]. Indeed,
modulation of few-layer hBN SPEs with propagating SAWs has resulted in large deforma-
tion potential coupling [159]; however, to date, integration of 2D SPEs with high-quality
SAW resonators, a critical step for exploring the potential of 2D materials for quantum
optomechanics, has not yet been explored.

In this work, the resonance frequency of SPEs in monolayer WSe$_2$ and multi-layer
hBN integrated with a LiNbO$_3$ SAW resonator driven by superconducting electronics are
parametrically modulated, and a study is performed of the coupling mechanisms, strain
susceptibility, and potential for acoustic quantum-regime operation. This work demon-
strates cavity phonon-SPE coupling with deformation potential coupling of at least 35
meV/% for WSe$_2$ and 12.5 meV/% for hBN, which is larger than or comparable to
alternative SPE host materials [52]. The dynamics of the SPE-SAW cavity system are
measured through time-resolved, stroboscopic, and steady-state photoluminescence spec-
troscopy. By sweeping the SAW frequency and the cavity phonon occupation, exquisite

control is demonstrated over the local strain environment. It is shown that when driven on resonance, the SAW modulates and mixes the emission from exciton fine-structure transitions that have been attributed to anisotropic exchange [110] and intervalley symmetry breaking in the presence of defects [165], providing a dynamical on-chip control knob for mixing of the WSe_2 SPE doublets. These results establish a new experimental platform that combines cavity optomechanics with 2D material quantum optics, paving the way for efficient and high-speed manipulation of 2D quantum emitters for single-photon switching, tuning and stabilization, and entangled photon-pair generation.

7.2   Sample Fabrication and Characterization

7.2.1   Sample Fabrication

One-port SAW resonators were fabricated on bulk $LiNbO_3$ using a combination of NbN sputtering and optical lithography to define superconducting Bragg reflectors and interdigital transducers (IDTs), as detailed in Chapter 5 Section 5.1. The particular device used in this work, **Res1WSe** has parameters detailed in 4.3. After SAW device fabrication, monolayer WSe_2 and plasma annealed hBN flakes [137] were identified using mechanical exfoliation and high-contrast optical imaging. Monolayers were then integrated within the SAW resonator using an all-dry transfer method [41]. After the device fabrication was completed, the samples were attached to an OFHC copper mount that holds both the sample and PCB, and the devices were wire-bonded prior to the experiments.
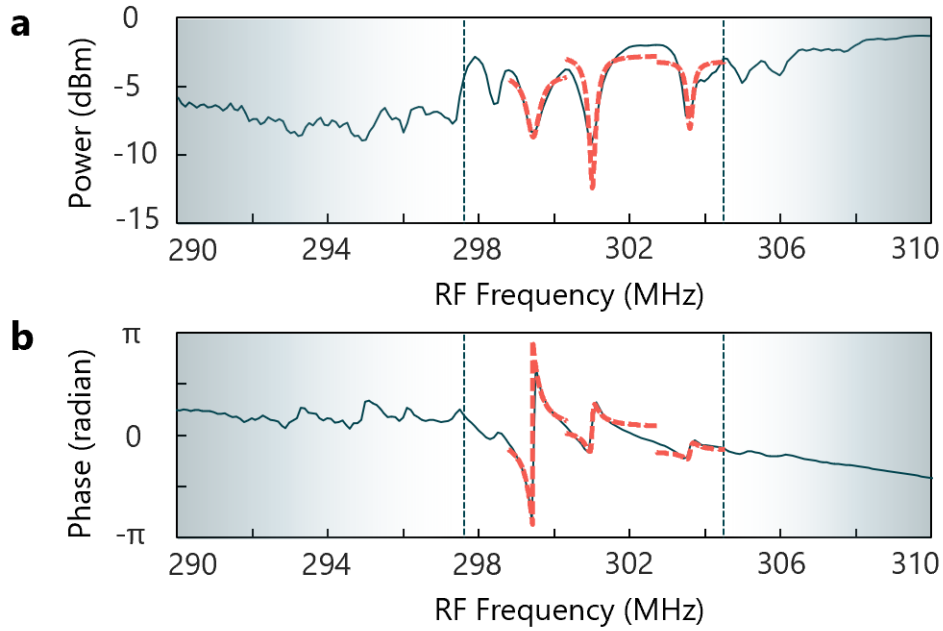
Figure 7.1: Resonance quality factor fits. **(a)** Cavity reflection spectrum magnitude, $|S_{11}|$, showing modes centered around 300 MHz. Vertical dashed lines and gradient areas represent the Bragg mirror band edges. Fits to each $|S_{11}|$ mode is denoted in a dashed red line. **(b)** Corresponding phase data for the cavity reflection spectrum is shown. The corresponding phase fit to each $|S_{11}|$ mode fit are denoted by dashed red lines. Data also reproduced in Figure 4.2d

7.2.2   Sample Electromechanical Characterization

The microwave S_{11} scattering parameter was measured at 4.4 K to ascertain the intrinsic quality factor, Q_i, and external quality factor, Q_e, of the SAW resonator. The output from a vector network analyzer (VNA) was sent to the single port of the SAW resonator IDT. The reflected signal from the resonator was sent back to the VNA, and the magnitude and phase of S_{11} were measured as a function of RF frequency at 4.4 K. Figs. 7.1(a) and 7.1(b) show representative results from this measurement. Dips in the $|S_{11}|$ spectrum within the bandwidth of the SAW resonator mirrors ($\sim 298 - 304$

f_{SAW} [MHz]	298.425	299.425	300.975	303.561
Q_i	1,300	3,000	1,600	1,700
Q_e	5,900	800	2,300	6,000

Table 7.1: Intrinsic (Q_i) and external (Q_e) quality factors for each of the SAW resonator modes.

MHz) are indicative of the different SAW resonator modes. By simultaneously fitting the magnitude and phase at each resonance frequency to Eqn. 7.1, both Q_i and Q_e are extracted for each resonance. These fits to both the magnitude and phase of S_{11} are shown in Table 7.1 and reveal that the cavity is in the undercoupled regime with an average intrinsic quality factor of 1900 and extrinsic quality factor of 3700 after the flake transfer, which are similar to loaded quality factors of SAWs integrated with III-V QDs [212]. Electromechanical measurements of the S_{11} parameter for the cavity alone yield internal quality factors on the order of 12,000 and external quality factors of 7,000, which are limited by the loss due to the mirrors.

$$S_{11}(f) = \frac{(Q_{e,n} - Q_{i,n})/Q_{e,n} + 2iQ_{i,n}(f - f_n)/f}{(Q_{e,n} + Q_{i,n})/Q_{e,n} + 2iQ_{i,n}(f - f_n)/f} \tag{7.1}$$

7.2.3 Sample Photoluminescence Spectroscopy Setup

A schematic of the steady-state PL spectroscopy used in the below experiments is illustrated in Fig. 7.2(a). A 532 nm continuous-wave laser source was used for both the steady-state and stroboscopic photoluminescence (PL) measurements. A dichroic mirror at 540 nm is used to separate the optical excitation and collection paths. An additional 600 nm long-pass optical filter is used to further extinguish the excitation laser in the collection path. An infinity-corrected 0.55 NA objective with 13 mm working

159
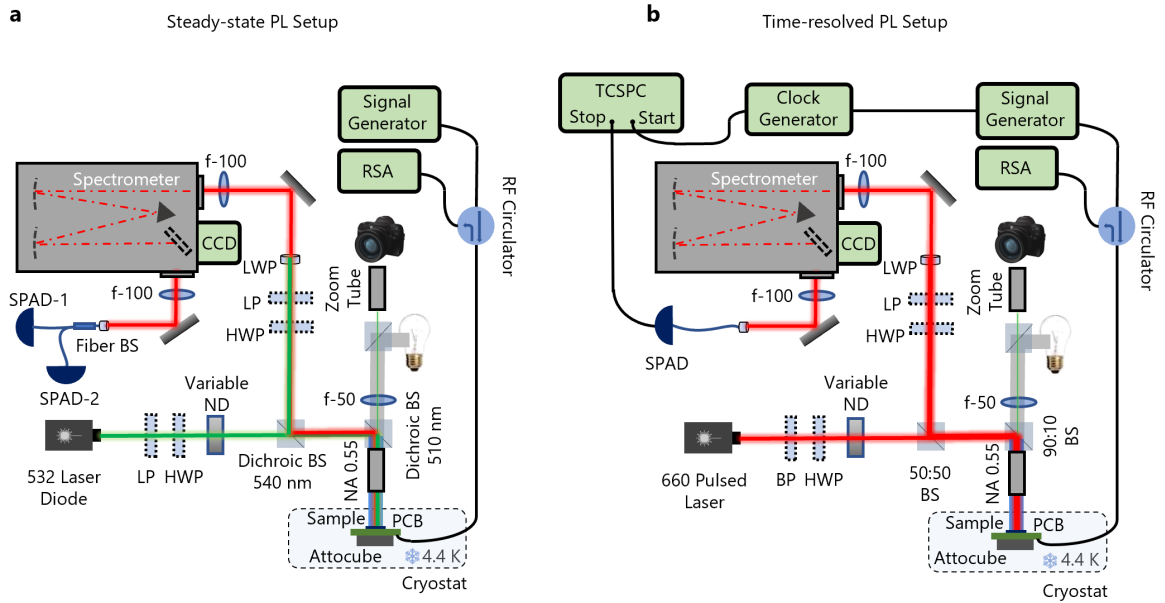
Figure 7.2: **PL spectroscopy setup (a)** The steady-state PL setup is shown. Components illustrate capability for imaging on the CCD and second-order auto-correlation measurements. **(b)** The PL setup for time-resolved spectroscopy, mainly stroboscopic measurement, is illustrated.

distance is used for spectroscopy. Samples were placed on a customized radio-frequency (RF) PCB sample carrier for microwave connection and were cooled to 4.4 K inside a Montana S200 cryostation. Optical spectra were acquired using a Princeton instruments HRS-500 with 300/1200/1800 groove/mm gratings and a thermo-electrically cooled Pixis silicon CCD. Second-order autocorrelation measurements with continuous-wave optical excitation were performed by utilizing the spectrometer as a monochromator to filter the emission from individual emitters. The optical signals were then collected in a multimode fiber beamsplitter connected to two single-photon avalanche detectors (Excelitas SCPM-AQRH-13-FC). Swabian time-tagging electronics were used for photon counting.

Time-resolved photoluminescence measurements were performed using a 660 nm, 80

MHz repetition rate pulsed laser source and single-photon counting. For stroboscopic measurements, the internal oscillator of the RF signal generator for driving the SAW IDT was connected to an external clock generator for synchronization between the SAW and detected photons. The external clock provided a pulsed signal with f$_{RF}$/30 to the start channel of the photon counting module. The emitter photoluminescence detected after the monochromator with the single-photon detector was connected to the stop channel, and a histogram of start-stop times was constructed as the spectrometer grating was scanned across the modulated SPE resonances. A schematic of the time-resolved PL spectroscopy is illustrated in Fig. 7.2(b).

7.3   Cavity optomechanics with WSe$_2$ & hBN SPEs

WSe$_2$ and hBN SPEs are identified using steady-state photoluminescence (PL) spectroscopy. SPEs in WSe$_2$ and hBN appear as spatially localized and spectrally sharp peaks in the PL spectra, as illustrated by the narrow filled peaks in Fig. 7.3(c) and 7.3(e). The lineshapes are instrument-response limited with a resolution of $\sim 200\ \mu$eV. Emission of single photons is verified by the anti-bunching dip at zero time delay in the second-order autocorrelation function shown in Figs. 7.3(c) and 7.3(f) for WSe$_2$ and hBN, respectively as detailed above in Section 7.2.3.

After identifying the SPE and SAW cavity resonances, the SAW drive frequency applied to the IDT for each device was fixed at the location of each cavity resonance, and the PL measurement was repeated. When driving the SAW on resonance, a standing surface acoustic wave is formed inside of the cavity. Depending on the position of the SPE relative to the node and anti-node of the standing wave, the SPE experiences dynamic compressive and tensile strain from the SAW (Fig. 7.3(a)). Through deformation potential coupling, the strain modulates the local bandgap of the material, resulting in a
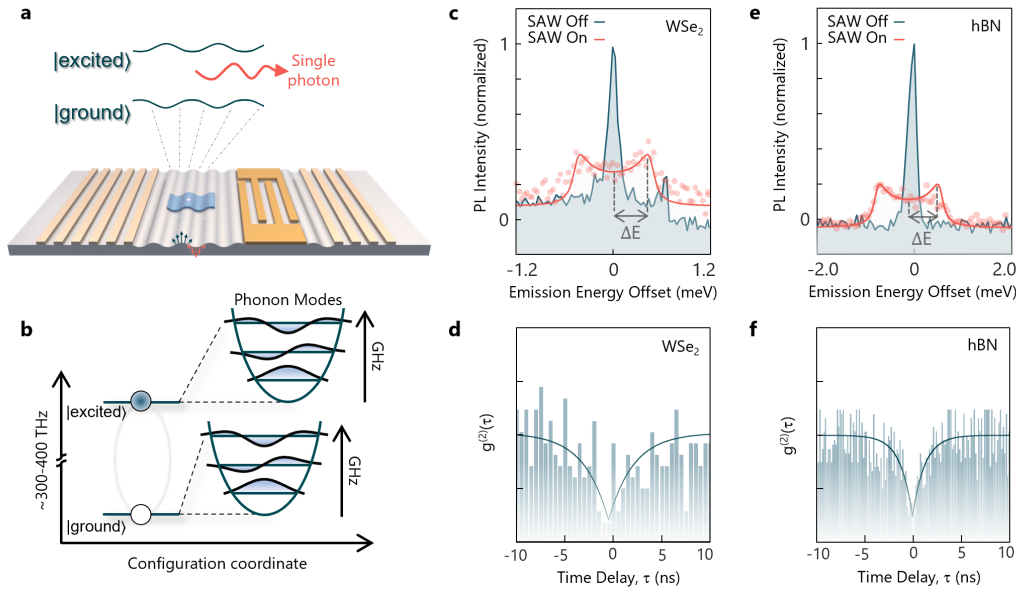
Figure 7.3: **LiNbO$_3$ SAW integration with 2D based single photon emitters.** **(a)** Schematic illustration of a 2D material hosting a single-photon emitter modulated in a surface acoustic wave cavity. The sketch denotes the modulation of the ground and excited state of the emitter over time. The out-of-plane strain vector is indicated by the arrows on the surface of the substrate. **(b)** Franck-Condon representation of the interaction between cavity phonons and the emitter. Both ground and excited state are coupled to phonon modes with energies significantly lower than the optical transition energy. **(c)** Representative photoluminescence (PL) spectra of SPEs in the WSe$_2$ monolayer measured at 4.4 K when driven on and off resonance with a resonator cavity mode at 303.6 MHz. **(d)** The second-order auto-correlation function of a WSe$_2$ emitter demonstrating photon anti-bunching.**(e)** Representative PL spectra of an SPE in hBN measured at 4.4 K when driven on and off resonance with a resonator cavity mode at 398 MHz. **(f)** The second-order auto-correlation function demonstrating photon anti-bunching for a thermally activated hBN SPE.

temporally varying energy shift of the SPE at the frequency of the SAW mode. Within the Franck-Condon framework, as illustrated in Fig. 7.3(b), both the ground state and the excited state of the emitters interact with the phonon vibrational modes with an intensity determined by Huang-Rhys factor. A surface acoustic wave cavity mode can be treated similar to a bulk phonon in this description. On resonance, the cavity mode interacts strongly with the ground and excited state of the emitter and imprints its signature on the photoluminescence spectrum. In the side-band resolved regime where the frequency of the resonant cavity phonon is larger than the linewidth of the emitter (typ-

ically in the gigahertz range), the PL spectra would consists of a series of replicas of the zero-phonon line (ZPL) spaced by the frequency of the resonance cavity phonon mode. In the present study, the opposite case is true, where the linewidth of the emitter is larger than the cavity phonon frequency. This slow modulation timescale compared to the emission merges the phonon replicas, which appear as a double-peak structure. The PL signals are fit to a Lorentzian function modulated by a sinusoidal interaction in the time domain given by:

$$I(E) = I_0 + f_{RF} \frac{2A}{\pi} \int_0^{1/f_{RF}} \frac{\omega}{4(E - (E_0 + \xi))^2 + \omega^2} \, dt \qquad (7.2)$$

Where I_0 is an offset, A is the amplitude, E_0 is the center energy, ω is the width of the Lorentzian emission peak, ξ is $\Delta E \sin(2\pi f_{RF} t)$, and ΔE is the optomechanical modulation amplitude of the SPE, which can be extracted. PL signals shown in Fig. 7.3(c) and 7.3(e) show data fitted to Eqn. 7.2. The ΔE versus P_{RF} scaling shown in Fig. 7.6 is obtained similarly.

Fig. 7.3(c) and Fig. 7.3(e) show representative modulated spectra from a WSe$_2$ and hBN emitters when the SAW cavity is driven on resonance (shown for different drive powers due to differences in deformation potential coupling efficiency as described below). The narrow Lorentzian lineshape of the SPEs is split into a double-peak structure with a peak-to-peak separation of $2\Delta E = 0.92$ meV for WSe$_2$ and $2\Delta E = 1.75$ meV for hBN. This double-peak structure is a clear signature of SPE-SAW coupling, consistent with previous observations from III-V QDs [61] and SiC vacancy centers [313] coupled to surface acoustic waves cavities. The PL signals were fit to a Lorentzian function modulated by a sinusoidal interaction in the time domain to extract the modulation energy ΔE [179]. These temporal simulations are carried out in MATLAB. In the classical

regime, the spectral response of the system at any given time can be denoted as:

$$\Omega(t) = \frac{\Gamma}{1 + \frac{(\omega - \omega_\circ - \Delta E sin(2\pi f_{RF}))^2}{\Gamma^2}} \tag{7.3}$$

where Γ and $\omega_\circ$ are the radiative decay rate and the frequency of the emitter and ΔE and f_{RF} are the amplitude of the SAW modulation and frequency of the SAW. The monochromator is modeled as a square pulse in frequency space as $U(\omega_l) - U(\omega_h)$ where ω_l and ω_h are the low-pass and high-pass corner frequencies of an ideal bandpass filter. While performing the stroboscopic measurment, the counts on the single photon detector would follow $\Omega(t)(U(\omega_l) - U(\omega_h))$. The fit to the data is calculated using this expression for an emitter with a lifetime of 2 ns, a non-radiatively broadened linewidth of 2 meV, and an ideal bandpass filter with a bandwidth of 3 meV where the filter is set on the high energy wing of the spectral response.

Next, the evolution of the PL spectrum as a function of the SAW cavity frequency at a constant power (4 dBm for WSe$_2$ and 11 dBm for hBN) was measured. The maximum modulation of the PL lineshape occurs at the SAW cavity resonant frequencies for both hBN and WSe$_2$. In WSe$_2$, as seen in Figs. 7.4(a) and 7.4(b), the three resonances at 299.4 MHz, 301.0 MHz, and 303.6 MHz are associated with clear splitting, distinctly different from when driving the SAW cavity off-resonance. Interestingly, this emitter shows a non-zero splitting between 299.0-301.5 MHz, which may be attributed to mode mixing between the neighboring cavity resonances due to the SPE being spatially located somewhere between a node and anti-node for this frequency range as similarly reported for QDs; the non-zero splitting may also be due to nonlinear effects such as acoustic wave mixing [212]. The characteristic spectral jitter in Fig. 7.4(a) arises from charge noise due to non-resonant excitation [15]. Note that among the WSe$_2$ emitters

164
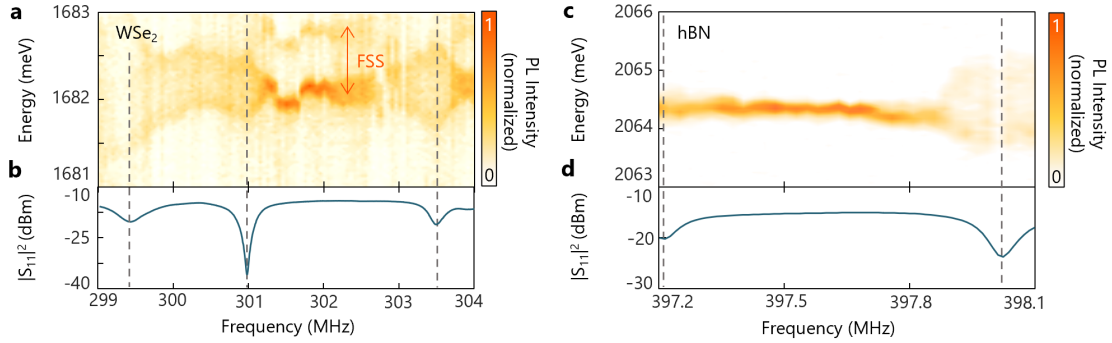
Figure 7.4: **Microwave frequency-dependent energy splitting of a WSe$_2$ and hBN single-photon emitter obtained from 4.4 K photoluminescence modulation spectroscopy. (a)** Representative WSe$_2$ emitter resonance modulation as a function of applied frequency to the SAW cavity. The spectral jumps are due to spectral jitter that appear at slow measurement timescales often observed under non-resonant excitation of WSe$_2$ emitters. **(b)** SAW cavity reflection spectrum for the WSe$_2$ device. **(c)** The hBN single-photon emission modulation as function of applied frequency to the SAW cavity. In general, hBN emitters demonstrate higher spectral stability compared to WSe$_2$. **(d)** SAW cavity reflection spectrum for the hBN device.

.

that were measured, only those that exhibited linewidths below 1 meV without applied SAW modulation exhibited a measurable splitting. Among these emitters, nearly 75% exhibited coupling to at least one of the cavity modes (Fig. 7.4(b)), a result which is not surprising given that the positions of the SPEs with respect to node/anti-node of the cavity is randomly distributed in these devices. Notably, the SPE in Fig. 7.4(a) consists of a doublet with a fine-structure splitting on the order of 700 μeV, which has been previously attributed to anisotropic strain [110] and intervalley excitonic mixing in WSe$_2$ [165, 42, 220]. Interestingly, both peaks of the doublet exhibit the same splitting as a function of frequency, and given the extent of the modulation, the two peaks can overlap and mix at the position of the cavity resonances. This mixing has implications for photon-state engineering and entanglement as discussed below.

The trend is similar in hBN as seen in the modulated spectral map in Fig. 7.4(c). Clear splitting is observed for both cavity resonances at 398.0 MHz and 397.2 MHz, while
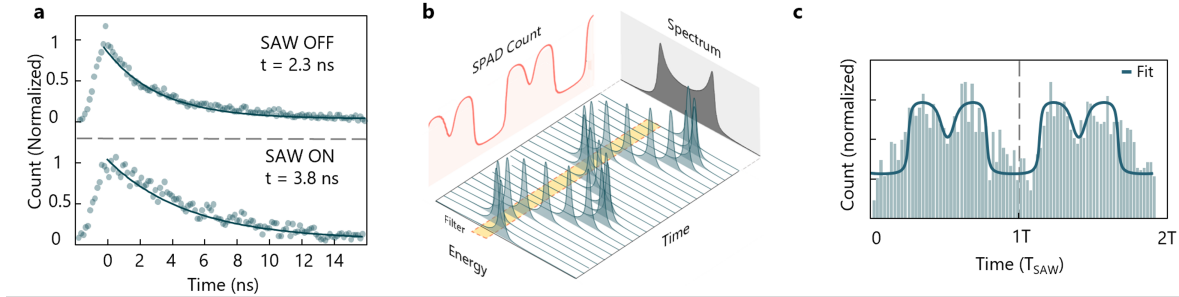
Figure 7.5: **Time-resolved and stroboscopic photoluminescence measurements. (a)** Time-resolved photoluminescence of a WSe$_2$ emitter with the SAW off (top panel) and SAW on (bottom panel). A recombination lifetime > 2 ns is observed in both cases, ruling out any non-radiative, electrodynamic charging, or thermal dissipation mechanisms for the observed modulated signals. **(b)** Conceptual illustration of the stroboscopic measurement. A monochromator is used to filter out a portion of the modulated signal. The filtered photons are sent to a single photon avalanche diode (SPAD) and their arrival with respect to the SAW drive signal, which modulates the SPE frequency, is recorded. This allows unravelling of the temporal dynamics of the SPE modulation at nanosecond time scales (dark green peaks), which is otherwise inaccessible due to the slow time-scale of steady-state PL measurement (dark gray time-averaged spectrum, which is a projection along the time-axis). **(c)** Results from the stroboscopic measurement (points) with a fit from a Monte Carlo simulation (solid line). Based on the center of the bandpass optical filter, both f$_{RF}$ and a 2f$_{RF}$ components are observed as expected.

the emitter linewidth remains instrument-response limited when the cavity is driven off resonance. Notably, these hBN emitters exhibit less jitter compared to WSe$_2$. Among the hBN emitters identified in these devices, only 10% of them exhibit SAW-induced splitting, which is a considerably lower yield than WSe$_2$; however, given that the hBN flakes are multi-layer, it is expected that the coupling strength of the SAW to the emitter would be proportional to the proximity of the defect to the surface of the lithium niobate. This is especially the case in vdW materials where the in-plane compressive or tensile stress transfers weakly in the c-axis direction due to weak out-of-plane interactions as evidenced by the extremely low c-axis thermal conductivity of 2D materials [128].

7.4   Stroboscopic measurements and deformation

potential coupling

While it is clear that the SPEs are modulated by the SAWs, to rule out alternative explanations, such as induced non-radiative decay or local heating, time-resolved and stroboscopic PL measurements are performed to map out the SAW dynamics. In the following, the analysis is restricted to the WSe$_2$ SPE devices, but similar arguments apply to hBN SPE devices as well. First, Fig. 7.5(a) shows the time-resolved PL dynamics of the WSe$_2$ emitter from Fig. 7.3 with (P_{RF} = 6 dBm) and without power applied to the SAW IDT. In both cases, the SPE recombination lifetime is longer than $\sim$ 2 ns, ruling out any new non-radiative recombination or thermal processes that could lead to faster recombination and broadening of the linewidth in the steady-state PL spectrum. Next, stroboscopic measurements are performed in which the arrival time of the emitted photons with respect to the phase of the applied SAW waveform is measured through single-photon counting and binning. The emission was spectrally filtered using a monochromator to isolate photons near the wings of the modulated steady-state PL spectrum (Fig. 7.5(b)). Results from this measurement are shown by the histogram in Fig. 7.5 (c), which demonstrates clear modulation of the emission waveform at the fundamental SAW frequency of f_{RF}. An additional frequency component at $2f_{RF}$ is observed due to the limited resolution of the used monochromator with respect to the total linewidth of the modulated emitter. A fit of the data using a Monte Carlo-like simulation of a modulated emitter overlapped with a non-ideal bandpass filter is shown as the solid line in Fig. 7.5(c) as shown in Section 7.2.3.

Next, experiments are performed measuring ΔE as a function of the applied power to the IDT for both WSe$_2$ and hBN emitters. A plot of the observed energy splitting, $2\Delta E$, as a function of the square root of the applied IDT power (P_{RF}) is shown in Fig.

167
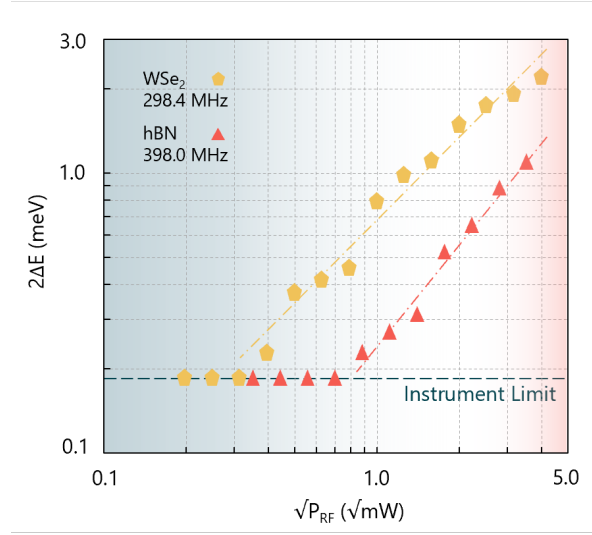
Figure 7.6: **Power dependence of the emitter lineshape splitting demonstrating deformation potential coupling.** ΔE is shown as a function of applied power to the SAW IDT. Data for the WSe_2 (hBN) emitter coupled to a 298.4 MHz (398 MHz) SAW cavity resonance is shown in yellow (red). Fits to the power-dependent splitting for the WSe_2 and hBN emitters yield slopes of 0.976 meV/$\sqrt{mW}$ and 1.199 meV/$\sqrt{mW}$ respectively, indicating deformation potential coupling.

7.6. The splitting $2\Delta E$ for WSe_2 and hBN is extracted at each applied power and fit as discussed in Section 7.3 for the resonant cavity modes at 298.4 MHz and 398 MHz, respectively. From Fig. 7.6, it is clear that ΔE increases monotonically with the power. On a double-logarithmic scale, it is observed that $\Delta E \propto \sqrt{P_{RF}}$ with a slope of 0.976 meV/$\sqrt{mW}$ for WSe_2 and 1.199 meV/$\sqrt{mW}$ for hBN. This linear splitting behavior is consistent with deformation potential coupling as the physical mechanism between the SAW and SPE that gives rise to the energy modulation [230]. The linear fit of the power dependence allows us to rule out any additional contributions, such as Stark-induced electric field coupling, as having a negligible effect on the SPE splitting and modulation, since this would scale as $\Delta E \propto P_{RF}$ [230].

To extract the deformation potential coupling efficiency, a finite element simulation
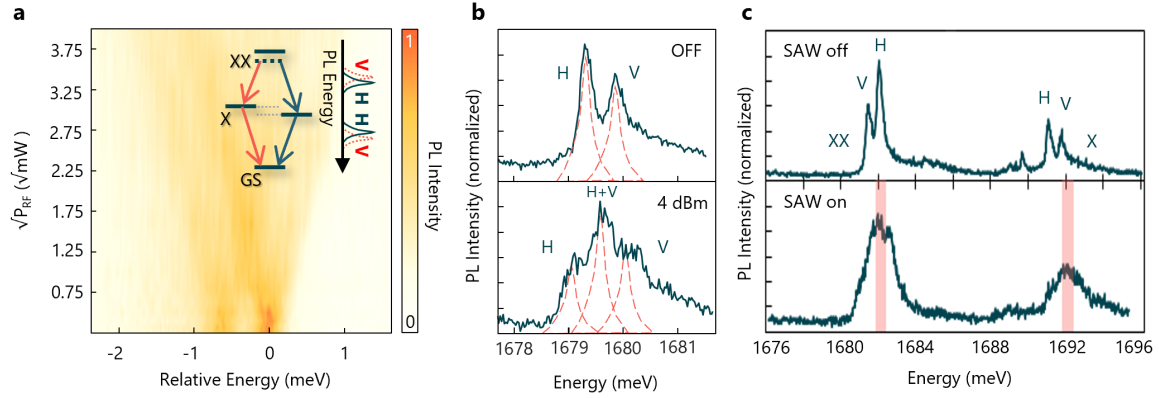
Figure 7.7: **Deformation potential coupling and fine-structure mixing of the exciton-biexciton radiative cascade in monolayer WSe$_2$.** **(a)** Contour map showing the increase in ΔE with applied IDT power to a SAW cavity mode at 298.4 MHz. Inset demonstrates a conceptual illustration of biexciton-exciton radiative cascade from WSe$_2$ emitters with non-zero fine-structure splitting. GS, X, and XX denote the ground-state, exciton, and biexciton states. **(b)** Fine-structure splitting of a representative single-photon emitter in WSe$_2$ with horizontally (H) and vertically (V) polarized transitions split into a doublet separated by 0.7 meV. Bottom panel demonstrates mixing of the single-photon emitter's fine-structure states when injecting phonons into the SAW mode at 299.4 MHz. The characteristic double-peak spectrum of SAW-modulated SPEs is observed for both the H and V transitions, which results in a single three-fold Lorentzian in which the central peak arises from mixing of the H and V transitions. **(c)** Mixing of the emission from fine-structure states of the exciton-biexciton-like cascade in WSe$_2$ upon SAW modulation. The top panel shows the emission spectrum for no applied SAW power with the characteristic set of doublets corresponding to the exciton-like (X) and biexciton-like (XX) transitions. The bottom panel shows the spectrum from the same emitter with SAW modulation. The doublets merge as demonstrated in **(b)**, and the highlighted region demonstrates the energies at which the fine-structure splitting is erased by mixing both the H and V photons..

is used to extract the tensile strain component along the propagation axis of the cavity at various applied powers to the IDT. A strain of 0.012% at 0 dBm applied power is determined for the 300 MHz resonator **Res1WSe** with a cavity length L = 2600 μm: see Table 4.3 for the cavity parameters and subsection 4.1.2 for the simulation details. Assuming that the strain in the SAW fully transfers to the WSe$_2$ flake, this results in at least ~35 meV/1% frequency shift for WSe$_2$ SPEs; this is a lower bound for the sensitivity of the emitter, given that the van der Waals interaction between the monolayer and LiNbO$_3$ surface could potentially reduce the full transfer of the strain to the SPE.

169

Previously reported measurements of the static energy shift versus strain applied to SPEs leads to an average value of 20 meV/1% shift (up to 120 meV/1% maximum) for WSe$_2$ emitters. These values are within the same order of magnitude as the extracted coupling efficiency, which suggests the strain at the LiNbO$_3$ surface is efficiently transferred to the WSe$_2$ monolayer. Similarly for hBN, 0.125 meV splitting is measured at 0 dBm of applied power, leading to 12.5 meV/1% deformation potential coupling for hBN, which is in line with previous estimates from static strain tuning of hBN red single photon emitters [193].

7.5 Dynamic modulation of SPE exciton-biexciton-like features

After confirming the deformation potential coupling as the microscopic nature of the SPE modulation for both WSe$_2$ and hBN, a unique feature is studied that arises in WSe$_2$ SPEs due to the inter-valley crystal symmetry breaking in the presence of the defects. The zero-phonon line of SPEs in WSe$_2$ typically exhibits a doublet with energy splitting of ~ 0.7 meV, as shown in Fig. 7.7(a) and 7.7(b). The doublet is thought to arise from asymmetry in the confining potential, which hybridizes the spin and valley states. This hybridization leads to splitting of the SPE transition into orthogonal linearly polarized transitions shown as H and V [165, 42, 220]. Similar fine-structure splitting effects have been observed in other SPE platforms, most notably III-V QDs [22, 258, 250]. In some cases, such as the deterministic generation of linearly polarized photons, fine-structure splitting can be advantageous [300, 91], while in others, such as generation of entangled-photon pairs via the biexciton-exciton radiative cascade, the fine-structure splitting can be detrimental by reducing the entanglement fidelity [121, 273]. Despite observations of

the radiative biexciton-exciton cascade in monolayer WSe_2 observed here and in prior works [109, 220], the non-zero fine-structure splitting has prevented any measurements of polarization entanglement with 2D materials.

SAW control of the single-photon emission is a unique, on-chip mechanism to manipulate the fine-structure splitting features. As shown in Fig. 7.7(a) and 7.7(b), the excitonic peak with its associated polarization can be split into two peaks with an energy spacing tuned by the applied SAW IDT power. In a specific range of powers, the H and V transitions overlap, resulting in a steady-state PL spectrum consisting of three Lorentzians for which the side peaks are vertically and horizontally polarized and the central peak becomes a mixture of the two polarizations. By aligning an optical band-pass filter to the central peak, the collected photons are reminiscent of an atomic-like emitter without fine structure, and the SAW modulation may serve as a mechanism to erase the fine structure altogether, although at a cost of reduced brightness. The SAW-mediated fine-structure mixing may find immediate applications for entangled-photon pair generation from WSe_2 SPEs through the radiative biexciton cascade, whereby the emission of a photon from the biexciton-to-exciton transition leads to a second photon emitted from the exciton-to-ground state transition (inset to Fig. 7.7(a)). Indeed, for many SPEs, exciton-biexciton transitions are observed with fine-structure split doublets, as shown in the top panel of Fig. 7.7(c). When turning on the SAW drive power at 299.4 MHz, the deformation potential mixes the transitions in the central regions highlighted in the bottom panel of Fig. 7.7(c).

The underlying mechanism of the fine-structure mixing still remains an interesting open question worth future investigation. Two potential mechanisms can be envisioned to cause the mixing. First, similar to Fig. 7.3a, due to oscillating compressive and tensile strain, the bandgap of WSe_2 oscillates at the SAW frequency, causing the atomic-level transitions to renormalize and oscillate as well. In this picture, the atomistic descrip-

tion of the two-level system that is responsible for the fine-structure splitting remains relatively the same, and the two fine-structure peaks oscillate in-phase with one another. This mechanism would only appear to have their fine-structure splitting removed on the central peak due to the slow time-scale of the steady-state PL measurements. For the second possible mechanism, the single-particle wavefunctions of the ground and excited states become compressed and elongated across the strain axis, which also causes the fine-structure transition energies to oscillate. Here, however, the fundamental mechanism of the oscillation is not bandgap renormalization, but instead strain-induced modification to the atomic morphology of the defect. In this case, similar to control of the fine-structure splitting via strain in III-V QDs [259], the compressive and tensile strain can restore the system symmetry associated with the exchange interaction, eliminating the fine structure altogether. In the former case, the central Lorentzian appearing in the PL spectra would become a mixed state of H and V polarized light on slow timescales relative to the inverse of the fine-structure splitting. In the latter case, the central Lorentzian is a coherent en-tangled state. These two scenarios, on a slow time-scale of steady state PL, lead to the same spectral response, and given that their polarimetric density matrices are identical, they cannot be distinguished from each other with polarization state tomography. It is plausible that both mechanisms, each acting with different strengths, are simultaneously occurring.

7.6   Discussion

To compare the potential of single photon emitters in 2D materials for optomechan-ical applications, a holistic approach is required. As evidenced by these experiments, WSe_2 emitters show a higher sensitivity to deformation potential coupling than hBN. This is expected given that the ratio of the photon energy to the bandgap for WSe_2 is

considerably lower than that for hBN. Hence to first order, the transition in WSe$_2$ is more sensitive to small modulations of the bandgap. Additionally, WSe$_2$ emitters are hypothesized to arise from an interplay between the defects and strain, where a valley symmetry breaking defect located at an strained region comes into resonance with the dark exciton energy in WSe$_2$ and becomes a viable pathway for the radiative recombination of the dark exciton as single photon light[165, 220]. Given the crucial role of strain in the microscopic origin of WSe$_2$ emitters, these emitters are also expected to exhibit a higher deformation potential coupling. This in fact has also been observed in other studies, where on average, higher deformation potential coupling for WSe$_2$ emitters has been measured compared to hBN; however, this appears to be the first work which compares the deformation potential coupling on the same platform, and using the same methods, which allows us to further corroborate this conclusion [43, 152, 122]. Lastly, SPEs in WSe$_2$ are known to exist in the monolayer and bilayer form of WSe$_2$, whereas in hBN, high-quality SPEs appear in multilayer forms of hBN. Given the overall low c-axis thermal conductivity in 2D materials, it is expected that strain transfer to monolayer or bilayer materials would exceed that of multilayer flakes and allow us to observe higher deformation potential coupling in monolayer WSe$_2$; however, larger deformation potential coupling only translates to larger vacuum optomechanical coupling g_0, and for optomechanical applications, factors such as brightness, purity, linewidth, and indistinguishibility are also crucial factors that require attention in order to engineer coherent quantum mechanical systems using 2D material hosts. The purity and brightness of hBN and WSe$_2$ SPEs are relatively on par with each other; however, as also apparent from these results, hBN SPEs demonstrate higher stability and lower frequency jitter. In hBN, while the deformation potential coupling is weaker than in WSe$_2$ by a factor of 4, Fourier-limited SPE emission from hBN red emitters have been observed with linewidths as low as 25 MHz [65] and the generation of indistinguishable photons [82], whereas the

smallest linewidths observed in WSe_2 emitters appears to be   2.5 GHz [153]. This implies that reaching a sideband-resolved regime and coherent photon-phonon interactions in hBN may be more feasible in the near future using higher frequency SAW cavities and resonant excitation schemes. In addition to this, reports of possible spin ground states in hBN could make hBN SPEs a more suitable platform for quantum optomechanics that include photons, phonons, and spins. While the current iteration of the SPE-SAW resonator is in the initial stage of development with the resonator operating in a fully classical regime, the next generation of devices require reducing the mode volume and increasing the operation frequency to the gigahertz range to reach the sideband resolved regime. This would allow for coherent quantum phenomena to be observed, such optical sideband pumping to herald the generation of single cavity phonons [124], photon-phonon entangled states, and acoustically driven Rabi oscillations [313].

7.7   Conclusion

In summary, acoustic control of single-photon emitters in monolayer WSe_2 and multilayer hBN integrated with $LiNbO_3$ surface acoustic wave resonators is demonstrated through electro-mechanical and opto-mechanical spectroscopy. The observed single-photon emitter modulation is consistent with deformation potential coupling through strain with sensitivity of at least 35 meV/% for WSe_2, and 12.5 meV/% for hBN. A near-term application of classical control of 2D material emitters is demonstrated through SAW-mediated single-photon frequency modulation and high-speed fine-structure manipulation, which may open the door for demonstrations of entangled-photon pair generation from 2D materials. Integrating 2D materials with gigahertz-frequency SAW resonators in the future could enable future demonstrations in the quantum regime of sideband-resolved excitation and detection, quantum transduction, and photon-phonon entanglement.

174

Chapter 8

Future Directions and Outlook

There are several potential directions in SAW design in addition to the ones explored in this thesis. As mentioned in 2, SAW devices incorporating two-dimensional phononic crystals [324] may alleviate the diffraction losses associated with SAW Fabry-Perot resonators, which is persistent even with focusing devices [124] and materials engineering of the SAW substrate [76]. An alternative to phononic crystals may be SAW waveguiding [154, 192], where either dielectric strips or even etched wedges or ridges may be used to define a waveguide structure, supporting Rayleigh-like SAW waves with lateral confinement to approximately a free-space SAW wavelength. These structures may circumvent etching the SAW substrate, in particular $LiNbO_3$ for which it is difficult to control the etch and achieve vertical sidewalls.

Multiple near-term pursuits are on the horizon for SAWs coupled to various optically active artificial atoms and spins. First, utilizing the full planar mode area of SAWs to couple to multiple solid-state spins could increase the sensitivity of an optomechanical sensing scheme, where typically nanobeams are used [149]. Second, examining the time and polarization-resolved photoluminescence of the single photons from WSe_2 emitters coupling to SAWs could elucidate the mechanism of fine-structure mixing observed in 7.

In addition, there is room for additional study on the mechanism of the acoustoelectric charge transport by SAWs observed in 6 using time-resolved photoluminescence, perhaps with applications in occupancy state control for pulsed single photon sources.

In addition to the optically-active systems explored in this review, the study of SAWs coupled to electrically-active quantum emitters is rapidly evolving. Several milestone experiments have been demonstrated within the last five years, including SAW Fock-state generation[247], strong multimode interactions and squeezing[202, 6], an acoustic analogue of Young's double-slit experiment[264], as well as quantum state transfer and remote entanglement[25]. Large capacitive and inductive couplings ≈10 MHz are realized by appreciable spatial overlaps between the SAW mode and qubit, which may be coupled to SAWs via an IDT [202, 247] or integrated within the SAW mirrors [6]. The large couplings enabled these systems to reach Stage 3 in Table 3.1. Electrostatic QDs are another electrically active system that couples to SAWs; such systems were investigated theoretically in Ref. [251] and recently demonstrated coherent SAW spin control and transport[125].

Strong coherent interactions can be engineered in both electromechanical and optomechanical SAW-artificial atom hybrid systems, suggesting the potential to integrate SAWs with both optically and electrically-active quantum emitters in a complete electro-optomechanical system. Such a hybrid system would enable the study of interactions between microwave quantum systems and single optical photons mediated through SAW mechanics. One can envision coupling microwave-frequency qubits and single photon emitters through their mutual interactions with SAWs, providing a path towards microwave-optical entanglement and microwave-to-optical state transfer[251]. Hybrid and heterogenously-integrated heterostructures offer more control knobs to tailor the material properties of the photonic, acoustic, and microwave degrees of freedom, allowing confinement of the photonic and phononic modes within the same device [184]. The platform-agnostic cou-

pling of many quantum emitters to SAWs via strain, electric and magnetic fields enables many possible approaches to realizing complex microwave-SAW-optical hybrid quantum systems.

Appendix A

SAW Simulations with COMSOL

A.1   COMSOL and Livelink for MATLAB

To design complex structures in COMSOL and analyze data, it is helpful to have a scripting interface to control COMSOL. COMSOL does have a native application builder utility, but it also provides an interface to MATLAB, which greatly enhances its functionality for post-processing and data visualization. In this interface, MATLAB programs can be written to build and edit a COMSOL model, run a simulation using the COMSOL engine, and then extract the data from COMSOL and process it within MATLAB.

A brief overview of writing a script using COMSOL Livelink for MATLAB is given below. The full instructions are given in the COMSOL documentation. First, Livelink for MATLAB is opened from the Windows Start Menu, which opens an instance of MATLAB and a connection to the COMSOL server. Next, the Livelink for MATLAB functions are imported from two `import` statements: `import com.comsol.model.*` and `import com.comsol.model.util.*`. MATLAB variables can then be assigned to the COMSOL model object, and a model Component node and the default nodes for the component can then be assigned: definitions, geometry, materials, meshing, physics,

multiphysics, as well as study, and results can each be created and assigned to a variable with a corresponding `create()` statement. Using MATLAB variables to store other COMSOL nodes, including `parameters` and `selections`, also simplifies the syntax of editing the attributes of these objects. Geometry, meshing, physics, study, results, and other categories objects can then be created and manipulated using calls to the respective model objects. The interface is similar to Java, with `set()` and `get()` methods used to change the attributes of COMSOL nodes.

To build a Livelink for MATLAB script from scratch, often it is easier to start with an existing COMSOL model created using the desktop GUI, and then save the file as a MATLAB file, which automatically generates a script using the Livelink for MATLAB syntax. The code generated from this save feature can often be made more readable by assigning variables to the COMSOL node objects. Afterwards, the script can be run to generate a COMSOL model object in MATLAB, which can also be opened with the COMSOL desktop application by using imported function `mphlaunch()`.

```matlab
% Calculate_Bandstructure.m
% Define material stack and thickness parameters
% example material stack structure 'mat_stack':
mat_stack = struct('mat', {'ln-128yx', 'gaas'}, 't_norm', {4, 0.25});
w_norm = 0.25; % normalized width (wavelengths)
d_norm = 0.05; % normalized depth (wavelengths)

k_range = linspace(0, 1, 100); % percent of k=1 (the Brillouin zone edge)
% number of eigenfrequency values for the solver to return at each k-point
num_eigs = 3;
% matrix to hold the returned eigenfrequencies
eigenfreqs = zeros(num_eigs, length(k_range));

% Make the unit cell model defined in make_unitcell_model() (see separate documentation)
model = make_unitcell_model(mat_stack, d_norm, w_norm);

% Disable bottom fixed boundary for low-k range,
```

179

```matlab
% otherwise the Lamb eigenfrequencies are artificially shifted up > 0 at k = 0
model.component('comp').physics('solid').feature('fix1').active(false);


% Set 'neigs' to a constant number for exporting data easier
model.study('std1').feature('eig').set('neigs', num_eigs);


% Plot the returned eigenfrequencies versus the k-range specified
figure
hold on
for i = 1 : length(k_range)
    model.param.set('k', [num2str(k_range(i)) '* 2 * pi/1 [m]']);
    model.sol('sol1').runAll;
    eigenfreqs(:, i) = mphglobal(model, 'solid.freq')';
    plot([k_range(i)], real(eigenfreqs(:,i)), 'k*');
end


% Save the data
% avoids warning/possible error if MATLAB tries saving the model file
clear('model');
clear('ans');
save('bandstructure_data_corr2p.mat');
```

```matlab
% Calculate_Eff_Velocity.m
% Extract the effective Rayleigh velocity for a SAW wave in
% a given material stack, with the option of adding periodic corrugations
% which shifts the effective velocity relative to a free surface
% - Inputs:
%   * 'wavelength': (float | int) [um] acoustic wavelength
%   * 'mats': (Cell array of str) names of materials used in get_mechanical_consts()
%   * 't': (array of float | int) thicknesses of materials
%   * 'd': (float | int) [um] depth of corrugation etch
%   * 'w': (float | int) [um] width of corrugation etch
%   * 'plot_modes' (bool) whether to plot strain profiles of modes found (useful for a sanity check)
% - Returns:
%   * v_eff: effective velocity for normalized-length heterostructure.
%       Can divide by either frequency or wavelength to get the complementary
%       variable for SAW cavity simulations
%   * taper_delta: same parameter as in 2D cavity simulation, should be >~ 0.02
```

```matlab
%               to be a physically realizable, "good" cavity (Q > 1e3)
%   * en_ratio: energy participation ratio of Rayleigh modes, should be ~ 0.9-1 for
%          true Rayleigh modes, otherwise likely bulk waves or higher-order
%          SAW waves (Sezawa modes)
function [v_eff, taper_delta, en_ratio] = ...
        get_eff_velocity(wavelength, mats, t, d, w, plot_modes)

model = make_unitcell_model(wavelength, mats, t, d, w);
% mphlaunch(model) % view model file


model.sol('sol1').runAll;
eigenfreqs = mphglobal(model, 'solid.freq')';


v_eff = sum(real(eigenfreqs(1:2))) / 2 * wavelength * 1e-6; % m/s
taper_delta = real(eigenfreqs(2))/v_eff*wavelength*1e-6 - 1; % use in the 2D cavity script


% find the energy contained within the top layer: useful for determining
% whether the modes found are SAWs or bulk waves. Can also plot the modes
% (make a plot group, like in "Bilayer_2D_Cavity_Mech_Eigenfrequency.m")
total_en = mphint2(model, {'solid.Wh', 'solid.Wk + solid.Ws + es.Wav'}, ...
                   'surface', 'selection', 'all');
surface_en = mphint2(model, {'solid.Wh', 'solid.Wk + solid.Ws + es.Wav'}, ...
                   'surface', 'selection', 'dom_surf');
en_ratio = surface_en ./ total_en;
en_ratio = en_ratio(1:2); % first two modes should be the Rayleigh modes


if plot_modes
    mech_pg = model.result.create('pg1', 'PlotGroup2D');
    mech_pg.set('data', 'dset1');
    mech_pg.set('showlegends', false);
    mech_pg.label('Strain (solid)');


    mech_disp = mech_pg.create('surf1', 'Surface');
    mech_disp.set('expr', {'solid.evol'});
    mech_disp.set('colortable', 'RainbowLight');


    figure(1)
    mech_pg.set('looplevel', 1);
    mech_pg.run;
```

```matlab
    mphplot(model, 'pg1');

    axis square

    axis([-wavelength / 4, wavelength / 4, sum(t) - wavelength, sum(t)])


    figure(2)

    mech_pg.set('looplevel', 2);

    mech_pg.run;

    mphplot(model, 'pg1');

    axis square

    axis([-wavelength / 4, wavelength / 4, sum(t) - wavelength, sum(t)])


end
```

```matlab
% make_unitcell_model()

% Helper function to set up the COMSOL model for periodic material heterostructures

% supporting SAWs

function model = make_unitcell_model(wavelength, mats, t, d, w)


if sum(t) < wavelength

    ME = MException('make_unitcell_model:materialStackThicknessError', ...

                        'Sum of material thicknesses less than parameter _wavelength_');

    throw(ME);

end


import com.comsol.model.*

import com.comsol.model.util.*


% blank COMSOL model and attributes

model = ModelUtil.create('Model');

comp = model.modelNode.create('comp', true);

selections = comp.selection;

geometry = comp.geom.create('geom', 2); % 2D geometry

geometry.lengthUnit('um');

physics = comp.physics;


lmats = length(mats);

rect_tags = cell(1, lmats);

t_curr = 0; % um
```

```matlab
parameters = model.param;

parameters.set('wavelength', [num2str(wavelength) '[um]']);

parameters.set('a', 'wavelength / 2');

parameters.set('k', 'pi / a');

parameters.set('d', [num2str(d) '[um]']);

parameters.set('w', [num2str(w) '[um]']);

%parameters.set('d_qd', [num2str(d_qd) '[um]']);

parameters.set('t_total', [num2str(sum(t)) '[um]']);

parameters.set('t_sub', [num2str(t(1)) '[um]']);



%% Geometry and material import

for i = 1 : lmats

    mat = get_mechanical_consts(mats{i});

    mat.feature = set_mech_material(model, mat);


    % create a "cumulative selection" for the current block, to

    % use for placing the material

    rect_sel = geometry.selection.create(['csel' num2str(i)], ...

        'CumulativeSelection');

    rect_sel.label(['rectsel_' num2str(i)]);


    % add the current layer (substrate, overlayer)

    rect = geometry.create(['r' num2str(i)],'Rectangle');

    rect.set('base', 'center');

    rect.set('size', {'a', [num2str(t(i)) '[um]']});

    rect.set('pos', {'0', [num2str(t_curr + t(i) / 2) '[um]']});


    rect_tags{i} = ['r' num2str(i)];

    rect.set('contributeto', ['csel' num2str(i)]);

    mat.feature.selection.named(['geom_csel' num2str(i) '_dom']);

    t_curr = t_curr + t(i);


    if i == lmats && d ~= 0

        % line segment for "top" distinguishing surface and bulk waves

        ls = geometry.create('ls_top', 'LineSegment');

        ls.set('specify1', 'coord');

        ls.set('coord1', {'-a / 2', 't_total - wavelength - 1e-4'});
```

```matlab
        ls.set('specify2','coord');

        ls.set('coord2', {'a / 2', 't_total - wavelength + 1e-4'});

        ls.label('surface-bulk boundary');


        % add an etch into the center of the structure
        etch = geometry.create(['r' num2str(i+1)],'Rectangle');

        etch.set('size', {'w', 'd'});

        etch.set('base','center');

        etch.set('pos', {'0', 't_total - d / 2'});


        difference_etch = geometry.create('mirror etch','Difference');

        difference_etch.selection('input').set(rect_tags);

        difference_etch.selection('input2').set(['r' num2str(i+1)]);
    end
end


geometry.run;


%% Selections
% edges for the mesh in the PML regions
side_l = selections.create('side_l','Box');

side_l.set('condition','inside');

side_l.set('entitydim', 1);

side_l.set('xmin','-a/2 - 1e-4');

side_l.set('xmax','-a/2 + 1e-4');


side_r = selections.duplicate('side_r','side_l');

side_r.set('xmin','a/2 - 1e-4');

side_r.set('xmax','a/2 + 1e-4');


sides = selections.create('sides_lr','Union');

sides.set('entitydim', 1);

sides.set('input', {'side_l', 'side_r'});


% bottom for fixed-constraint solid mechanics boundary condition
side_b = selections.create('side_btm','Box');

side_b.set('condition','inside');

side_b.set('entitydim', 1);

side_b.set('ymin','- 1e-4');
```

```matlab
side_b.set('ymax','1e-4');


% arbitrary "top" domain for determining whether a mode is a surface or bulk wave
surface_sel = selections.create('dom_surf','Box');
surface_sel.set('entitydim', 2);
surface_sel.set('condition','inside');
surface_sel.set('ymin', '-1e-5');
surface_sel.set('ymax', 't_total + 1e-5');


% top surface for get_ksquared(): short tangential electric field for determining piezo coupling
top_sel = selections.create('top_surface', 'Box');
top_sel.set('entitydim', 1);
top_sel.set('condition','inside');
top_sel.set('ymin', 't_total - 1e-5');
top_sel.set('ymax', 't_total + 1e-5');


%% Mesh
mesh = model.mesh.create('mesh','geom');
mesh.label('Mesh');
mesh.feature('size').set('hmax', 'wavelength/16'); %


free_tri = mesh.create('freetri','FreeTri');
free_tri.selection.remaining();


mesh.run;


%% Physics
solid_mech = physics.create('solid','SolidMechanics','geom');
% piezoelectric material in material XZ-plane system automatically for 2D sims
solid_mech.create('pzm1','PiezoelectricMaterialModel');
solid_mech.feature('pzm1').selection.all;


floquet_bound_sm = solid_mech.create('pc1','PeriodicCondition', 1);
floquet_bound_sm.selection.named('sides_lr');
floquet_bound_sm.set('PeriodicType','Floquet');
floquet_bound_sm.set('kFloquet', {'k', '0', '0'});


% removes Rayleigh mode with displacement at bottom of structure
fixed_cnst = solid_mech.create('fix1','Fixed', 1);
```

185

```
fixed_cnst.selection.named('side_btm');


electrostatics = physics.create('es','Electrostatics','geom');

electrostatics.create('ccnp1','ChargeConservationPiezo');

electrostatics.feature('ccnp1').selection.all;


floquet_bound_es = electrostatics.create('pc1','PeriodicCondition', 1);

floquet_bound_es.selection.named('sides_lr');

floquet_bound_es.set('PeriodicType','Floquet');

floquet_bound_es.set('kFloquet', {'k', '0', '0'});


piezo_effect = comp.multiphysics.create('pze1','PiezoelectricEffect', ...
                                   'geom', 2);

piezo_effect.set('Solid_physics','solid');

piezo_effect.set('Electrostatics_physics','es');


%% Study and solver settings
study1 = model.study.create('std1');

solution = model.sol.create('sol1');

solution.study('std1');


study_step1 = solution.create('st1','StudyStep');

eigenfrequency = study1.create('eig','Eigenfrequency');

study_step1.set('studystep','eig');

% solutions will coincide with wave speed in m/s
eigenfrequency.set('shift','1 [Hz]');


solution.create('v1','Variables');

solution.feature('v1').set('control','eig');

solution.create('e1','Eigenvalue');

solution.feature('e1').set('control','eig');

solution.attach('std1');
```

```
% get_mechanical_consts()

% Helper function with elastic and piezoelectric material data to be imported into COMSOL


function mat_data = get_mechanical_consts(mat)
```

```matlab
switch mat
    case {'GaAs', 'gaas'} % GaAs, (001)-plane, <110> along local/geometric x coordinate
        mat_data = struct('c', 1e9 * ...
            [[149.6, 26.5, 54.5, 0, 0, 0]; ... % GPa
            [26.5, 149.6, 54.5, 0, 0, 0]; ...
            [54.5, 54.5, 121.6, 0, 0, 0]; ...
            [0, 0, 0, 61.5, 0, 0]; ...
            [0, 0, 0, 0, 61.5, 0]; ...
            [0, 0, 0, 0, 0, 33.5]], ...
             'e', [[0, 0, 0, 0, -0.16, 0]; [0, 0, 0, 0.16, 0, 0]; [-0.16, 0.16, 0, 0, 0, 0]], ...
             'rho', 5332, 'eps', 12.35, 'tag', 'GaAs', 'label', 'GaAs - mK', ...
             'lossfactor', 1.25e-4);


    case {'LiNbO3-128YX', 'ln-128yx'} % 128-degree YX-LN, 0-6 K, Tarumi et al.
        mat_data = ...
            struct('c', 1e9 *...                                    % v_R ~ 3980 m/s
                    [[205.6, 69.59, 57.21, 8.243, 0, 0]; ... % Pa
                    [ 69.59, 195.39, 85.38, 7.517, 0, 0]; ...
                    [ 57.21, 85.38, 219.2, 7.237, 0, 0]; ...
                    [ 8.243, 7.517, 7.237, 77.48, 0, 0]; ...
                    [ 0, 0, 0, 0, 58.90, -4.032]; ...
                    [ 0, 0, 0, 0, -4.032, 77.40]], ... % C/m^2
                    'e', [[ 0, 0, 0, 0, 4.0652, 0.3843]; ... % C/m^2
                    [-1.2965, 4.5102, -0.9358, 0.2837, 0, 0]; ...
                    [1.9139, -1.8676, 2.8693, 0.745, 0, 0]], ...
                    'rho', 4613, ... % kg/m^3
                    'eps', [[39.5, 0, 0]; [ 0, 33.5, -7.67]; [ 0, -7.67, 29.7]], ...
                    'tag', 'LiNbO3_128_YX', 'label', 'Lithium Niobate - 128-degree YX', ...
                    'lossfactor', 1.25e-4);


    case {'Nb', 'nb'} % Niobium/Niobium nitride, assumed (001)-plane
        c11 = 25.34; % GPa, Carroll '65
        c12 = 133.6; % GPa, Carroll '65
        c44 = 30.9; % GPa, Carroll '65
        mat_data = struct('c', 1e9 * ...
            [[c11, c12, c12, 0, 0, 0]; ... % GPa
            [c12, c11, c12, 0, 0, 0]; ...
            [c12, c12, c11, 0, 0, 0]; ...
            [0, 0, 0, c44, 0, 0]; ...
```

```
                [0, 0, 0, 0, c44, 0]; ...
                [0, 0, 0, 0, 0, c44]], ...
                 'e', zeros(3,6), 'rho', 8561, 'eps', 1e5, 'tag', 'Nb', 'label', 'Nb - 4.2 K', ...
                 'lossfactor', 0);


    end


end



%% set_mech_material()
% Helper function for importing material properties for the Structural Mechanics Module


function [matrl] = set_mech_material(model, mat, print_import)


import com.comsol.model.*
import com.comsol.model.util.*


if nargin < 8
    print_import = false;
end


if print_import
    disp(['Adding material "' name '"...'])
end


matrl = model.material.create(mat.tag, 'Common');
matrl.propertyGroup('def').set('lossfactor', mat.lossfactor);
stress_charge = matrl.propertyGroup.create('StressCharge', 'Stress-charge form');
matrl.label(mat.label);


stress_charge.set('cE', cellstr(string(reshape(mat.c,1,36))));
stress_charge.set('eES', cellstr(string(reshape(mat.e, 1, 18))));
stress_charge.set('density', [num2str(mat.rho) '[kg/m^3]']);


if size(mat.eps, 1) == 1 % presume a scalar
    stress_charge.set('epsilonrS', num2str(mat.eps));
else                     % presume a 3-by-3 matrix
    stress_charge.set('epsilonrS', cellstr(string(reshape(mat.eps, 1, 9))));
```

```
end


end
```

Appendix B

Material Constants

In the SAW simulations, the elastic constants of the 128°-Y cut LiNbO$_3$ substrate and $\langle 110 \rangle -$ orientation, (001) cut GaAs epilayer were computed from the available data for these materials at low temperatures (T < 10 K) [[280, 37]] by rotating the elastic stiffness, piezoelectric coupling, and electrical permittivity matrices using the Bond rotation matrices [[30, 11]].

LiNbO$_3$ has trigonal *3m* symmetry, with the following stiffness, piezoelectric, and dielectric matrices and density from Ref. [[280]]:

$$
c =
\begin{bmatrix}
205.6 & 56.9 & 69.9 & 8.0 & 0 & 0 \\
\cdot & 205.6 & 69.9 & -8.0 & 0 & 0 \\
\cdot & \cdot & 234.2 & 0 & 0 & 0 \\
\cdot & \cdot & \cdot & 62.0 & 0 & 0 \\
\cdot & \cdot & \cdot & \cdot & 62.0 & 8.0 \\
\cdot & \cdot & \cdot & \cdot & \cdot & 72.2
\end{bmatrix}
\text{GPa}
$$

$$
e = \begin{bmatrix} 0 & 0 & 0 & 0 & 3.44 & -2.20 \\ -2.20 & 2.20 & 0 & 3.44 & 0 & 0 \\ 0.71 & 0.71 & 2.28 & 0 & 0 & 0 \end{bmatrix} \mathrm{C\,m^{-2}}
$$

$$
\epsilon = \begin{bmatrix} 85.2 & 0 & 0 \\ \cdot & 85.2 & 0 \\ \cdot & \cdot & 44.3 \end{bmatrix}
$$

$$
\rho = 4632\,\mathrm{kg/m^3}
$$

Gallium arsenide has cubic $\bar{4}3m$ symmetry, with the following material constants for the stiffness matrix [[37]], piezoelectric matrix [[9]], dielectric matrix [[274]], and density [[1]]:

$$
c = \begin{bmatrix} 121.7 & 54.6 & 54.6 & 0 & 0 & 0 \\ \cdot & 121.7 & 54.6 & 0 & 0 & 0 \\ \cdot & \cdot & 121.7 & 0 & 0 & 0 \\ \cdot & \cdot & \cdot & 61.6 & 0 & 0 \\ \cdot & \cdot & \cdot & \cdot & 61.6 & 0 \\ \cdot & \cdot & \cdot & \cdot & \cdot & 61.6 \end{bmatrix} GPa
$$

$$
e = \begin{bmatrix} 0 & 0 & 0 & 0 & 3.44 & -2.20 \\ -2.20 & 2.20 & 0 & 3.44 & 0 & 0 \\ 0.71 & 0.71 & 2.28 & 0 & 0 & 0 \end{bmatrix} \mathrm{C\,m^{-2}}
$$

$$
\epsilon = \begin{bmatrix} 85.2 & 0 & 0 \\ \cdot & 85.2 & 0 \\ \cdot & \cdot & 44.3 \end{bmatrix}
$$

$$
\rho = 5332\,\mathrm{kg/m^3}
$$

The form of the Bond matrices for a general rotation using the angle cosines a_{ij} defined in Ref. [[218]] is the following:

Vector rotation matrix:

$$a = \begin{bmatrix} a_{xx} & a_{xy} & a_{xz} \\ a_{yx} & a_{yy} & a_{yz} \\ a_{zx} & a_{zy} & a_{zz} \end{bmatrix}$$

Stiffness matrix rotation matrix:

$$M = \begin{bmatrix} a_{xx}^2 & a_{xy}^2 & a_{xz}^2 & 2a_{xy}a_{xz} & 2a_{xz}a_{xx} & 2a_{xx}a_{xy} \\ a_{yx}^2 & a_{yy}^2 & a_{yz}^2 & 2a_{yy}a_{yz} & 2a_{yz}a_{yx} & 2a_{yx}a_{yy} \\ a_{zx}^2 & a_{zy}^2 & a_{zz}^2 & 2a_{zy}a_{zz} & 2a_{zz}a_{zx} & 2a_{zx}a_{zy} \\ a_{yx}a_{zx} & a_{yy}a_{zy} & a_{yz}a_{zz} & a_{yy}a_{zz}+a_{yz}a_{zy} & a_{yx}a_{zz}+a_{yz}a_{zx} & a_{yy}a_{zx}+a_{yx}a_{zy} \\ a_{zx}a_{xx} & a_{zy}a_{xy} & a_{zz}a_{xz} & a_{xy}a_{zz}+a_{xz}a_{zy} & a_{xz}a_{zx}+a_{xx}a_{zz} & a_{xx}a_{zy}+a_{xy}a_{zx} \\ a_{xx}a_{yx} & a_{xy}a_{yy} & a_{xz}a_{yz} & a_{xy}a_{yz}+a_{xz}a_{yy} & a_{xz}a_{yx}+a_{xx}a_{yz} & a_{xx}a_{yy}+a_{xy}a_{yx} \end{bmatrix}$$

The rotation rules for the stiffness matrix, the piezoelectric coupling matrix and the dielectric constant are the following [[11]]:

$$c_f = M \cdot c_i \cdot M^T \tag{B.1}$$

$$e_f = a \cdot e_i \cdot M^{-1} \tag{B.2}$$

$$\epsilon_f = a \cdot \epsilon \cdot a^T \tag{B.3}$$

To coincide with $128-YX$ LiNbO$_3$, the material constants above for LiNbO$_3$ have to be rotated by -38 ° counterclockwise from the +X axis; this figure of -38 ° is a result of the 1978 IEEE standard as explained in this tutorial page from COMSOL. This rotation is calculated first by taking the cosines of the resulting rotation for the a_{ij} components, then assembling matrices a and M and following the transformation rules B.3. Using the

above rotation matrices, the following are the elastic and permittivity matrices used as input in the FEM simulations:

$$c_{LN} = \begin{bmatrix} 205.6 & 69.59 & 57.21 & 8.243 & 0 & 0 \\ \cdot & 195.4 & 85.38 & 7.517 & 0 & 0 \\ \cdot & \cdot & 219.2 & 7.237 & 0 & 0 \\ \cdot & \cdot & \cdot & 77.48 & 0 & 0 \\ \cdot & \cdot & \cdot & \cdot & 58.90 & -4.032 \\ \cdot & \cdot & \cdot & \cdot & \cdot & 77.40 \end{bmatrix} \text{GPa}$$

$$e_{LN} = \begin{bmatrix} 0 & 0 & 0 & 0 & 4.065 & 0.3843 \\ -1.297 & 4.510 & -0.9358 & 0.2837 & 0 & 0 \\ 1.914 & -1.868 & 2.869 & 0.745 & 0 & 0 \end{bmatrix} \text{C\,m}^{-2}$$

$$\epsilon_{LN} = \begin{bmatrix} 39.5 & 0 & 0 \\ \cdot & 33.5 & -7.47 \\ \cdot & \cdot & 29.7 \end{bmatrix}$$

Similarly, the material constants for GaAs have to be rotated by 45 ° clockwise about the material Z axis, yielding the following matrices:

$$c_{GaAs} = \begin{bmatrix} 149.6 & 26.5 & 54.5 & 0 & 0 & 0 \\ \cdot & 149.6 & 54.5 & 0 & 0 & 0 \\ \cdot & \cdot & 121.6 & 0 & 0 & 0 \\ \cdot & \cdot & \cdot & 61.5 & 0 & 0 \\ \cdot & \cdot & \cdot & \cdot & 61.5 & 0 \\ \cdot & \cdot & \cdot & \cdot & \cdot & 33.5 \end{bmatrix} \text{GPa}$$

$$e_{GaAs} = \begin{bmatrix} 0 & 0 & 0 & 0 & -0.16 & 0 \\ 0 & 0 & 0 & 0.16 & 0 & 0 \\ -0.16 & 0.16 & 0 & 0 & 0 & 0 \end{bmatrix} \mathrm{C\,m^{-2}}$$

$$\epsilon_{GaAs} = \begin{bmatrix} 12.35 & 0 & 0 \\ \cdot & 12.35 & 0 \\ \cdot & \cdot & 12.35 \end{bmatrix}$$

Appendix C

Fabrication Processes

C.1 Gen-2 SAW-QD Bonding Cleaning Procedure and Basket

1. Solvent bench preparation

   (a) Prepare bottles of acetone, IPA, DI water (if using: see below), and a bottle of 3 drops of Tergitol mixed in DI water, shaken to mix evenly.

   (b) Wipe down any liquid, wipe down working surfaces w/IPA, and put out a stack of several fresh wipes for sample drying.

   (c) Set the N2 gun air pressure to 25-30 psi.

   (d) Rinse the tergitol soaking beaker and sample holding beakers with IPA (2-3 cycles), then wipe dry.

   (e) Fill soak beaker 1/3 full with Tergitol solution and drop in half a pack of TX-710 swabs (sample size < 12 mm: otherwise use larger swabs).

   (f) Set up basket on sample holding beaker, cleaning with wipe and IPA, then cut 1/4 of a non-shedding wipe and lay inside, spraying vertically with an N2 gun for particles.

2. Swab clean

Note : before any solvents are applied, swab following the procedure below 1-2X through, substituting DI water for any solvents and inspecting for large numbers of particles (cannot remove all of them, but want to remove most before dissolving the photoresist).

Note : Use only ceramic tweezers for sample handling, since metal tweezers may generate particles when handling the sample. It is best to keep the tweezers isolated in their own case, and wipe off the tweezers with an IPA-soaked wipe and drying with N2 before handling a sample.

(a) Place the sample on the non-shedding wipe and basket by first sliding one inside face of the tweezers underneath the sample in its holder, then tilting the sample holder upwards, allowing more of the tweezers to slip underneath the sample, then picking up the sample and carefully transferring to the wipe.

(b) Spray the sample with acetone (10 s), then IPA (10 s), spraying as completely vertically as possible.

(c) Grab a swab using your right hand and bring it towards the sample, tilting it so that the swab is ~ 20 degrees inclined from sample and oriented such that the raised ridge running along the perimeter of the foam tip is parallel to and will not make contact with the sample.

(d) Start spraying Tergitol directly above the sample with your left hand, keeping the spray as vertical as possible. Continue to do so until finished swabbing.

(e) Make contact with the sample about 80 % of the sample length from the right edge, then very gently slide the swab towards the right edge and slightly twist the swab counter-clockwise while moving past the right edge, avoiding contacting the corners or the top and bottom edges of the sample.

(f) Repeat for 5-10 swabs, then rotate the swab 180 degrees to the other side and repeat.

(g) Replace the used swab with a new one, rotate the sample 90 degrees using the basket, and repeat the above for all four edges of the sample.

(h) When finished swabbing, clean off the Tergitol by spraying the sample with IPA (10 s), then slide one side of a pair of wide ceramic tweezers underneath the sample, balancing the sample from its bottom face, then lift and transfer to the dry stack of wipes set out earlier for sample drying.

(i) Blow dry with the N2 gun, holding the N2 gun as vertically as possible above the sample. For samples smaller than $\sim 12 \times 12$ mm^2, tweezers are needed for holding the sample firmly to prevent the sample from being blown away.

(j) Slide one side of the tweezers underneath the sample, then lift and transfer to a chip container, tilting the container to place the sample, then carefully sliding the tweezers out from underneath the sample, taking care not to touch the top face of the sample against the edges of the container.

3. Sample inspection

(a) First, set up the sample under the microscope and adjust focus while imaging with the bright-field "normal" mode on the edge of the sample, making sure to focus on the front face. This is more challenging with transparent substrates, but it can help to look at the edge or corner and adjust the focus until it is obvious which face is coming into focus.

(b) Switch to Namarski/DIC mode, adjusting the polarizer to go through the transition where the surface appears nearly black, then back off slightly from the darkest setting to have some light from the surface for examining surface texture.

(c) Inspect the surface for particles and growth defects, moving first along the edges of the sample, then towards the center. Make a mental note of which edges or corners have more particles, paying particular attention to particles with irregular shapes and clusters of particles, which may occur from contamination during the drying step.

(d) Growth defects are typically isolated show a double-lobed structure as shown in Figure 5.7, but can also occur in patches.

(e) If there are any scratches $\gtrsim 50$ μm across the sample, likely near the edges from tweezer handling, discard the sample and start with a new one.

(f) If any larger particles with jagged, defined features (as opposed to dust particles, which tend to have rounded features) persist after multiple rounds of cleaning, these may be flakes of sample generated from chipping while handling and may be exceptionally difficult to remove. Either use more physical pressure while swabbing in the area around the particle (taking care not to scratch the surface, particularly for III/V material), or replace the sample with a new one.

197

4. Repeat Steps 2-3 until the sample is free of particles, usually within 2-4 rounds of cleaning. Isolated particles which persist after 3 cleaning cycles may be tolerable if close to the edge of the sample ($\lessapprox 100~\mu m$)
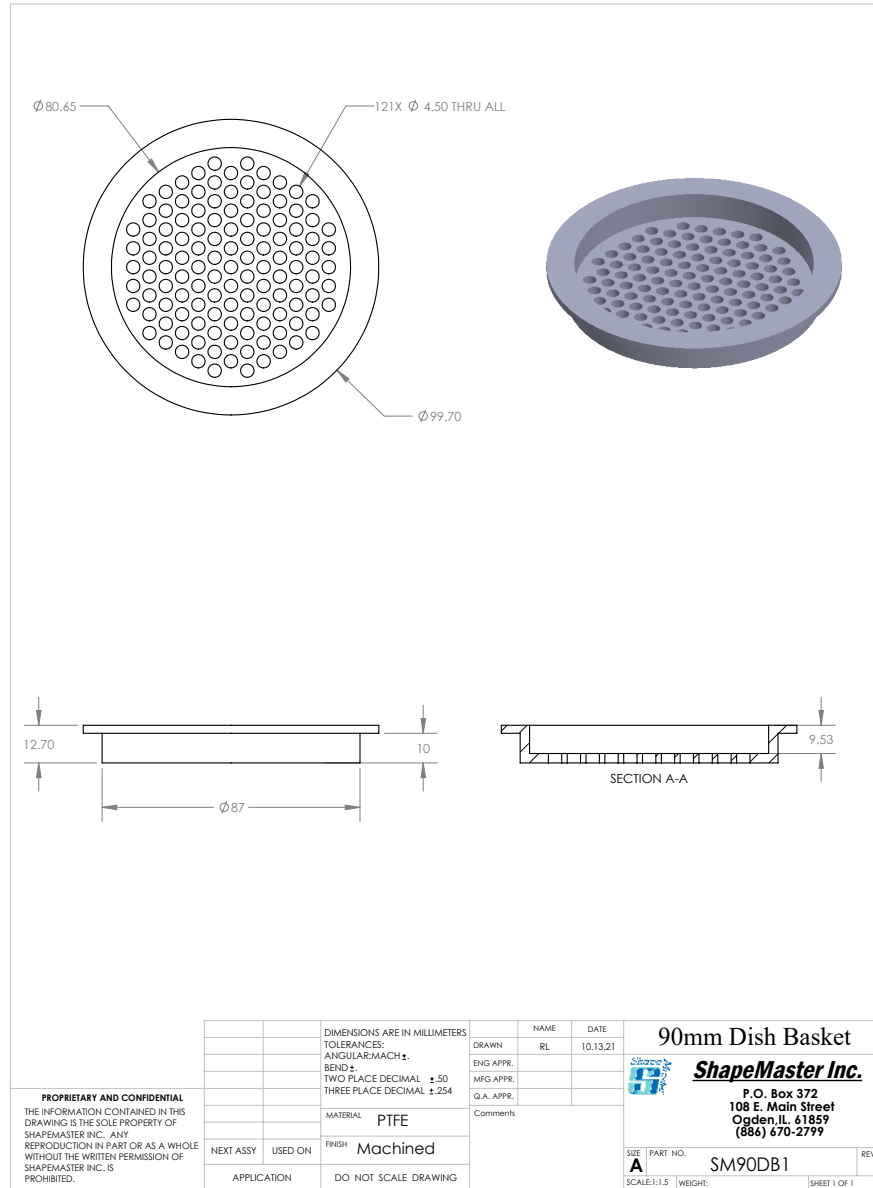
Figure C.1: Custom-made basket for holding chip-scale samples while cleaning for direct bonding.

Nomenclature

AFM   Atomic Force Microscopy

ALD   Atomic Layer Deposition

CCD   Charge coupled device

CTE   Coefficient of Thermal Expansion

DBR   Distributed Bragg Reflector

DIC   Differential Interference Contrast

DUT   Device under test

FEM   Finite Element Method

FEUDT Floating Electrode Unidirectional Transducer

IPA   Isopropyl Alcohol

MBE   Molecular Beam Epitaxy

PCB   Printed circuit board

PML   Perfectly Matched Layer

RF   Radio frequency

SPE   Single-photon emitter

STCD Spatio-temporal charge carrier dynamics

ZPL   Zero-phonon line

Bibliography

[1] Sadao Adachi. "GaAs, AlAs, and AlxGa1−xAs: Material parameters for use in research and device applications". In: *Journal of Applied Physics* 58.3 (Aug. 1985), R1–R29. ISSN: 0021-8979. DOI: `10.1063/1.336070`.

[2] Shahriar Aghaeimeibodi et al. "Integration of quantum dots with lithium niobate photonics". In: *Appl. Phys. Lett.* 113.22 (2018), p. 221102. DOI: `10.1063/1.5054865`. (Visited on 02/26/2021).

[3] Igor Aharonovich, Dirk Englund, and Milos Toth. "Solid-state single-photon emitters". In: *Nat. Photonics* 10.10 (Oct. 2016), pp. 631–641. DOI: `10.1038/nphoton.2016.186`.

[4] A. Albrecht et al. "Coupling of nitrogen vacancy centres in nanodiamonds by means of phonons". In: *New J. Phys.* 15.8 (Aug. 2013), p. 083014. DOI: `10.1088/1367-2630/15/8/083014`.

[5] Gustav Andersson, Maria K. Ekström, and Per Delsing. "Electromagnetically Induced Acoustic Transparency with a Superconducting Circuit". In: *Phys. Rev. Lett.* 124.24 (June 2020), p. 240402. DOI: `10.1103/PhysRevLett.124.240402`.

[6] Gustav Andersson et al. "Squeezing and Multimode Entanglement of Surface Acoustic Wave Phonons". In: *PRX Quantum* 3.1 (Jan. 2022), p. 010312. DOI: `10.1103/PRXQuantum.3.010312`.

[7] Reed W Andrews et al. "Bidirectional and efficient conversion between microwave and optical light". In: *Nature physics* 10.4 (2014), pp. 321–326.

[8] Thomas Aref et al. "Quantum acoustics with surface acoustic waves". In: *Superconducting devices in quantum optics*. Springer, 2016, pp. 217–244.

[9] G. Arlt and P. Quadflieg. "Piezoelectricity in iii-v compounds with a phenomenological analysis of the piezoelectric effect". In: *physica status solidi (b)* 25.1 (1968), pp. 323–330. DOI: https://doi.org/10.1002/pssb.19680250131.

[10] Markus Aspelmeyer, Tobias J. Kippenberg, and Florian Marquardt. "Cavity optomechanics". In: *Rev. Mod. Phys.* 86.4 (), pp. 1391–1452. DOI: 10.1103/RevModPhys.86.1391.

[11] B. A Auld. *Acoustic fields and waves in solids. Vol. 1-2*. Wiley, 1973.

[12] David Awschalom et al. "Development of Quantum Interconnects (QuICs) for Next-Generation Information Technologies". In: *PRX Quantum* 2 (1 Feb. 2021), p. 017002. DOI: 10.1103/PRXQuantum.2.017002.

[13] David D. Awschalom et al. "Quantum technologies with optically interfaced solid-state spins". In: *Nat. Photonics* 12 (Sept. 2018), pp. 516–527. DOI: 10.1038/s41566-018-0232-2.

[14] Vollrath M Axt, M Herbst, and Tilmann Kuhn. "Coherent control of phonon quantum beats". In: *Superlattices Microstruct.* 26.2 (Aug. 1999), pp. 117–128. DOI: 10.1006/spmi.1999.0765.

[15] Shaimaa I Azzam, Kamyar Parto, and Galan Moody. "Prospects and challenges of quantum emitters in 2D materials". In: *Appl. Phys. Lett.* 118.24 (June 2021), p. 240502. DOI: 10.1063/5.0054116.

[16] Yu Bai et al. "Fabrication of GaAs-on-Insulator via Low Temperature Wafer Bonding and Sacrificial Etching of Ge by XeF $_2$". en. In: *Journal of The Electrochemical Society* 159.2 (2011), H183–H190. ISSN: 0013-4651, 1945-7111. DOI: 10.1149/2.070202jes. URL: https://iopscience.iop.org/article/10.1149/2.070202jes (visited on 05/08/2024).

[17] Gopalakrishnan Balasubramanian et al. "Nanoscale imaging magnetometry with diamond spins under ambient conditions". In: *Nature* 455.7213 (Oct. 2008), pp. 648–651. DOI: 10.1038/nature07278.

[18] Stanley S. Ballard, Stephen E. Brown, and James Steve Browder. "Measurements of the thermal expansion of six optical materials, from room temperature to 250°C". en. In: *Applied Optics* 17.7 (Apr. 1978), p. 1152. ISSN: 0003-6935, 1539-4522. DOI: 10.1364/AO.17.001152. URL: https://opg.optica.org/abstract.cfm?URI=ao-17-7-1152 (visited on 04/29/2024).

[19] Michael S. J. Barson et al. "Nanomechanical Sensing Using Spins in Diamond". In: *Nano Lett.* 17.3 (Feb. 2017), pp. 1496–1503. DOI: 10.1021/acs.nanolett.6b04544.

[20] H. P. Bartling et al. "Coherence and entanglement of inherently long-lived spin pairs in diamond". In: *arXiv: 2103.07961* (Mar. 2021). DOI: 10.48550/ARXIV.2103.07961.

[21] I. Baumann et al. "Erbium incorporation in LiNbO3 by diffusion-doping". In: *Appl. Phys. A* 64.1 (1996), pp. 33–44. DOI: 10.1007/s003390050441.

[22] M Bayer et al. "Fine structure of neutral and charged excitons in self-assembled In (Ga) As/(Al) GaAs quantum dots". In: *Physical Review B* 65.19 (2002), p. 195315.

[23] Jonas Nils Becker et al. "Ultrafast all-optical coherent control of single silicon vacancy colour centres in diamond". In: *Nat. Commun.* 7.1 (2016), p. 13512. DOI: `10.1038/ncomms13512`.

[24] D. L. T. Bell and R. C. M. Li. "Surface-acoustic-wave resonators". In: *Proc. IEEE* 64.5 (May 1976), pp. 711–721. DOI: `10.1109/PROC.1976.10200`.

[25] A. Bienfait et al. "Phonon-mediated quantum state transfer and remote qubit entanglement". In: *Science* 364.6438 (Apr. 2019), pp. 368–371. DOI: `10.1126/science.aaw8415`.

[26] A. Bienfait et al. "Quantum Erasure Using Entangled Surface Acoustic Phonons". In: *Phys. Rev. X* 10.2 (June 2020), p. 021055. DOI: `10.1103/PhysRevX.10.021055`.

[27] Sam G. Bishop et al. "Room-Temperature Quantum Emitter in Aluminum Nitride". In: *ACS Photonics* 7.7 (July 2020), pp. 1636–1641. DOI: `10.1021/acsphotonics.0c00528`.

[28] M. Block et al. "Optically Enhanced Electric Field Sensing Using Nitrogen-Vacancy Ensembles". In: *Phys. Rev. Applied* 16 (2 Aug. 2021), p. 024024. DOI: `10.1103/PhysRevApplied.16.024024`.

[29] Aleksey N. Bolgar et al. "Quantum Regime of a Two-Dimensional Phonon Cavity". In: *Phys. Rev. Lett.* 120.22 (May 2018), p. 223603. DOI: `10.1103/PhysRevLett.120.223603`.

[30] Walter L. Bond. "The mathematics of the physical properties of crystals". In: *The Bell System Technical Journal* 22.1 (Jan. 1943). Conference Name: The Bell System Technical Journal, pp. 1–72. ISSN: 0005-8580. DOI: `10.1002/j.1538-7305.1943.tb01304.x`.

[31]   Romain Bourrellier et al. "Bright UV Single Photon Emission at Point Defects in h-BN". In: *Nano Lett.* 16.7 (July 2016), pp. 4317–4321. DOI: `10.1021/acs.nanolett.6b01368`.

[32]   Carlo Bradac et al. "Optical Nanoscale Thermometry: From Fundamental Mechanisms to Emerging Practical Applications". In: *Adv. Opt. Mater.* 8.15 (May 2020), p. 2000183. DOI: `10.1002/adom.202000183`.

[33]   Conor Bradley et al. "A Ten-Qubit Solid-State Spin Register with Quantum Memory up to One Minute". In: *Phys. Rev. X* 9.3 (Sept. 2019), p. 031045. DOI: `10.1103/PhysRevX.9.031045`.

[34]   Artur Branny et al. "Deterministic strain-induced arrays of quantum emitters in a two-dimensional semiconductor". In: *Nature communications* 8.1 (2017), p. 15053.

[35]   James Steve Browder and Stanley S. Ballard. "Thermal expansion data for eight optical materials from 60 K to 300 K". en. In: *Applied Optics* 16.12 (Dec. 1977), p. 3214. ISSN: 0003-6935, 1539-4522. DOI: `10.1364/AO.16.003214`. URL: `https://opg.optica.org/abstract.cfm?URI=ao-16-12-3214` (visited on 04/29/2024).

[36]   Dominik D. Bühler et al. "On-chip piezo-optomechanical dynamic single photon routing and rotation of a photonic qubit". In: *arXiv: 2202.10173* (Feb. 2022). DOI: `10.48550/arXiv.2202.10173`.

[37]   Y. A. Burenkov et al. "Temperature dependences of the elastic constants of gallium arsenide". In: *Soviet Physics of the Solid State* 15 (1973), pp. 1175–1177.

[38]   T. P. Cameron and W. D. Hunt. "Reflection characteristics of obliquely incident surface acoustic waves from groove and aluminum gratings on {100}-cut gallium arsenide". In: *J. Appl. Phys.* 84.4 (Aug. 1998), pp. 2212–2218. DOI: `10.1063/1.368285`.

[39]   Alexander Carmele and Stephan Reitzenstein. "Non-Markovian features in semiconductor quantum optics: quantifying the role of phonons in experiment and theory". In: *Nanophotonics* 8.5 (Apr. 2019), pp. 655–683. DOI: `10.1515/nanoph-2018-0222`.

[40]   Samuel G. Carter et al. "Tunable Coupling of a Double Quantum Dot Spin System to a Mechanical Resonator". In: *Nano Letters* 19.9 (2019), pp. 6166–6172. DOI: `10.1021/acs.nanolett.9b02207`.

[41]   Andres Castellanos-Gomez et al. "Deterministic transfer of two-dimensional materials by all-dry viscoelastic stamping". In: *2D Materials* 1.1 (2014), p. 011002.

[42]   Chitraleema Chakraborty et al. "Electrical manipulation of the fine-structure splitting of WSe 2 quantum emitters". In: *Physical Review B* 99.4 (2019), p. 045308.

[43]   Chitraleema Chakraborty et al. "Strain tuning of the emission axis of quantum emitters in an atomically thin semiconductor". In: *Optica* 7.6 (2020), pp. 580–585.

[44]   Chitraleema Chakraborty et al. "Voltage-controlled quantum light from an atomically thin semiconductor". In: *Nat. Nanotechnol.* 10.6 (June 2015), pp. 507–511. DOI: `10.1038/nnano.2015.79`.

[45]   Jasper Chan et al. "Optimized optomechanical crystal cavity with acoustic radiation shield". In: *Applied Physics Letters* 101.8 (Aug. 2012), p. 081115. ISSN: 0003-6951. DOI: `10.1063/1.4747726`.

[46]   Abhiroop Chellu et al. "GaAs surface passivation for InAs/GaAs quantum dot based nanophotonic devices". In: *Nanotechnology* 32.13 (Jan. 2021). Publisher: IOP Publishing, p. 130001. ISSN: 0957-4484. DOI: `10.1088/1361-6528/abd0b4`. URL: `https://doi.org/10.1088/1361-6528/abd0b4` (visited on 06/28/2022).

207

[47] Yu-Yuan Chen et al. "Manipulation of magnetic systems by quantized surface acoustic wave via piezomagnetic effect". In: (Apr. 2024). URL: http://arxiv.org/abs/2404.09423.

[48] Cheng-Wei Cheng et al. "Epitaxial lift-off process for gallium arsenide substrate reuse and flexible electronics". In: *Nature Communications* 4.1 (2013), p. 1577. DOI: 10.1038/ncomms2583. URL: https://doi.org/10.1038/ncomms2583.

[49] Risheng Cheng et al. "Epitaxial niobium nitride superconducting nanowire single-photon detectors". In: *Appl. Phys. Lett.* 117.13 (2020), p. 132601. DOI: 10.1063/5.0018818.

[50] V. W. L. Chin, T. L. Tansley, and T. Osotchan. "Electron mobilities in gallium, indium, and aluminum nitrides". In: *Journal of Applied Physics* 75.11 (1994), pp. 7365–7372. DOI: 10.1063/1.356650.

[51] S. P. Chockalingam et al. "Superconducting properties and Hall effect of epitaxial NbN thin films". In: *Phys. Rev. B* 77 (21 June 2008), p. 214503. DOI: 10.1103/PhysRevB.77.214503. URL: https://link.aps.org/doi/10.1103/PhysRevB.77.214503.

[52] Michael Choquer et al. "Quantum Control of Optically Active Artificial Atoms With Surface Acoustic Waves". In: *IEEE Transactions on Quantum Engineering* 3 (2022), pp. 1–17. DOI: 10.1109/TQE.2022.3204928.

[53] S.H. Christiansen, R. Singh, and U. Gosele. "Wafer Direct Bonding: From Advanced Substrate Engineering to Future Applications in Micro/Nanoelectronics". en. In: *Proceedings of the IEEE* 94.12 (Dec. 2006), pp. 2060–2106. ISSN: 0018-9219, 1558-2256. DOI: 10.1109/JPROC.2006.886026. URL: http://ieeexplore.ieee.org/document/4077250/ (visited on 05/08/2024).

[54] A. A. Clerk et al. "Hybrid quantum systems with circuit quantum electrodynamics". In: *Nat. Phys.* 16.3 (Mar. 2020), pp. 257–267. DOI: `10.1038/s41567-020-0797-9`.

[55] M. Colangelo et al. In: *Conf. on Lasers and Electro-Optics* (2020), SM4O.4. DOI: `10.1364/CLEO_SI.2020.SM4O.4`.

[56] Jacob P. Covey, Harald Weinfurter, and Hannes Bernien. "Quantum networks with neutral atom processing nodes". In: *npj Quantum Information* 9.1 (Sept. 2023), p. 90. ISSN: 2056-6387. DOI: `10.1038/s41534-023-00759-9`. URL: `https://doi.org/10.1038/s41534-023-00759-9`.

[57] Nicholas Cucciniello et al. "Superconducting niobium nitride: a perspective from processing, microstructure, and superconducting property for single photon detectors". In: *Journal of Physics: Condensed Matter* 34.37 (July 2022). Publisher: IOP Publishing. ISSN: 0953-8984. DOI: `10.1088/1361-648X/ac7dd6`. URL: `https://doi.org/10.1088/1361-648x/ac7dd6` (visited on 07/29/2022).

[58] Andrew Dane. *Reactive DC Magnetron Sputtering of Ultrathin Superconducting Niobium Nitride Films*. Massachusetts Institute of Technology, 2015.

[59] M. David Henry et al. "Stress dependent oxidation of sputtered niobium and effects on superconductivity". en. In: *Journal of Applied Physics* 115.8 (Feb. 2014), p. 083903. ISSN: 0021-8979, 1089-7550. DOI: `10.1063/1.4866554`. URL: `https://pubs.aip.org/aip/jap/article/373537` (visited on 05/01/2023).

[60] Ryan A. DeCrescent et al. "Large Single-Phonon Optomechanical Coupling Between Quantum Dots and Tightly Confined Surface Acoustic Waves in the Quantum Regime". In: *Phys. Rev. Appl.* 18 (3 Sept. 2022), p. 034067. DOI: `10.1103/PhysRevApplied.18.034067`.

[61] Per Delsing et al. "The 2019 surface acoustic waves roadmap". In: *J. Phys. D: Appl. Phys* 52.35 (Aug. 2019), p. 353001. DOI: `10.1088/1361-6463/ab1b04`.

[62] Yu Deshui and Frank Vollmer. "Active optomechanics". English. In: *Communications Physics* 5.1 (2022). Place: London, United States Publisher: Nature Publishing Group. DOI: `http://dx.doi.org/10.1038/s42005-022-00841-2`. URL: `https://www.proquest.com/docview/2640734120/abstract/AD9F0F759667448CPQ/1` (visited on 03/30/2022).

[63] Boris Desiatov et al. "Ultra-low-loss integrated visible photonics using thin-film lithium niobate". In: *Optica* 6.3 (Mar. 2019), pp. 380–384. DOI: `10.1364/OPTICA.6.000380`. (Visited on 10/27/2021).

[64] Ivan H. Deutsch. "Harnessing the Power of the Second Quantum Revolution". In: *PRX Quantum* 1 (2 Nov. 2020), p. 020101. DOI: `10.1103/PRXQuantum.1.020101`. URL: `https://link.aps.org/doi/10.1103/PRXQuantum.1.020101`.

[65] A Dietrich et al. "Solid-state single photon source with Fourier transform limited lines at room temperature". In: *Physical Review B* 101.8 (2020), p. 081401.

[66] A. Dietrich et al. "Observation of Fourier transform limited lines in hexagonal boron nitride". In: *Phys. Rev. B* 98.8 (Aug. 2018), p. 081414. DOI: `10.1103/PhysRevB.98.081414`.

[67] Giulia Enrica Digeronimo et al. "Integration of Single-Photon Sources and Detectors on GaAs". In: *Photonics* 3.4 (2016). DOI: `10.3390/photonics3040055`.

[68] M. W. Doherty et al. "The negatively charged nitrogen-vacancy centre in diamond: the electronic solution". In: *New J. Phys.* 13.2 (Feb. 2011), p. 025019. DOI: `10.1088/1367-2630/13/2/025019`.

[69]   Marcus W. Doherty, Chunhui Rita Du, and Gregory D. Fuchs. "Quantum science and technology based on color centers with accessible spin". In: *J. Appl. Phys.* 131.1 (Jan. 2022), p. 010401. DOI: `10.1063/5.0082219`.

[70]   F. Dolde et al. "Electric-field sensing using single diamond spins". In: *Nat. Phys.* 7.6 (June 2011), pp. 459–463. DOI: `10.1038/nphys1969`.

[71]   Florian Dolde et al. "Nanoscale Detection of a Single Fundamental Charge in Ambient Conditions Using the NV$^-$ Center in Diamond". In: *Phys. Rev. Lett.* 112 (9 Mar. 2014), p. 097603. DOI: `10.1103/PhysRevLett.112.097603`.

[72]   É. Dumur et al. "Unidirectional distributed acoustic reflection transducers for quantum applications". In: *Appl. Phys. Lett.* 114 (22 June 2019), p. 223501. DOI: `10.1063/1.5099095`.

[73]   Łukasz Dusanowski et al. "Near-Unity Indistinguishability Single Photon Source for Large-Scale Integrated Quantum Optics". In: *Physical Review Letters* 122.17 (May 2019). Publisher: American Physical Society, p. 173602. DOI: `10.1103/PhysRevLett.122.173602`. (Visited on 12/18/2020).

[74]   M. K. Ekström et al. "Towards phonon routing: controlling propagating acoustic waves in the quantum regime". In: *New J. Phys.* 21.12 (Dec. 2019), p. 123013. DOI: `10.1088/1367-2630/ab5ca5`.

[75]   Maria K. Ekström et al. "Surface acoustic wave unidirectional transducers for quantum applications". In: *Appl. Phys. Lett.* 110.7 (Feb. 2017), p. 073105. DOI: `10.1063/1.4975803`.

[76]   A. L. Emser et al. "Minimally diffracting quartz for ultra-low temperature surface acoustic wave resonators". In: *Applied Physics Letters* 121.22 (Nov. 2022), p. 224001. ISSN: 0003-6951. DOI: `10.1063/5.0125122`.

[77] Simon J. Evered et al. "High-fidelity parallel entangling gates on a neutral-atom quantum computer". In: *Nature* 622.7982 (Oct. 2023), pp. 268–272. ISSN: 1476-4687. DOI: 10.1038/s41586-023-06481-y. URL: https://doi.org/10.1038/s41586-023-06481-y.

[78] Annemarie L Exarhos et al. "Magnetic-field-dependent quantum emission in hexagonal boron nitride at room temperature". In: *Nature communications* 10.1 (2019), pp. 1–8.

[79] Abram L. Falk et al. "Electrically and Mechanically Tunable Electron Spins in Silicon Carbide Color Centers". In: *Phys. Rev. Lett.* 112.18 (May 2014), p. 187601. DOI: 10.1103/PhysRevLett.112.187601.

[80] Linran Fan et al. "Superconducting cavity electro-optics: A platform for coherent photon conversion between superconducting and photonic circuits". In: *Science Advances* 4.8 (Aug. 2018), eaar4994. ISSN: 2375-2548. DOI: 10.1126/sciadv.aar4994. (Visited on 05/12/2021).

[81] Clarisse Fournier et al. "Position-controlled quantum emitters with reproducible emission wavelength in hexagonal boron nitride". In: *Nature Communications* 12 (2021), p. 3779.

[82] Clarisse Fournier et al. "Two-photon interference from a quantum emitter in hexagonal boron nitride". In: *arXiv preprint arXiv:2210.05590* (2022).

[83] F. Fras et al. "Multi-wave coherent control of a solid-state single emitter". In: *Nat. Photon.* 10.3 (2016), pp. 155–158. DOI: 10.1038/nphoton.2016.2.

[84] Sulei Fu et al. "High-Frequency Surface Acoustic Wave Devices Based on ZnO/SiC Layered Structure". In: *IEEE Electron Device Lett.* 40.1 (Jan. 2019), pp. 103–106. DOI: 10.1109/LED.2018.2881467.

[85] Satoshi Fujii et al. "Low propagation loss in a one-port SAW resonator fabricated on single-crystal diamond for super-high-frequency applications". In: *IEEE transactions on ultrasonics, ferroelectrics, and frequency control* 60.5 (May 2013), pp. 986–992. DOI: 10.1109/TUFFC.2013.2656.

[86] Shoya Fukumoto et al. "Heterogeneous direct bonding of diamond and semiconductor substrates using NH_3 /H_2O_2 cleaning". en. In: *Applied Physics Letters* 117.20 (Nov. 2020), p. 201601. ISSN: 0003-6951, 1077-3118. DOI: 10.1063/5.0026348. URL: http://aip.scitation.org/doi/10.1063/5.0026348 (visited on 10/14/2022).

[87] A. Gaggero et al. "Nanowire superconducting single-photon detectors on GaAs for integrated quantum photonic applications". In: *Appl. Phys. Lett.* 97.15 (2010), p. 151108. DOI: 10.1063/1.3496457.

[88] A. García-Cristóbal et al. "Spatiotemporal carrier dynamics in quantum wells under surface acoustic waves". In: *Phys. Rev. B* 69 (May 2004), p. 205301. DOI: 10.1103/PhysRevB.69.205301.

[89] J. R. Gavaler et al. "Very High Critical Current and Field Characteristics of Niobium Nitride Thin Films". In: *Journal of Applied Physics* 42.1 (1971), pp. 54–57. DOI: 10.1063/1.1659649.

[90] J R Gell et al. "Modulation of single quantum dot energy levels by a surface-acoustic-wave". In: *Appl. Phys. Lett.* 93.8 (Aug. 2008), p. 81115. DOI: 10.1063/1.2976135.

[91] Stefan Gerhardt et al. "Polarization-dependent light-matter coupling and highly indistinguishable resonant fluorescence photons from quantum dot-micropillar cavities with elliptical cross section". In: *Physical Review B* 100.11 (2019), p. 115305.

[92] Roy J Glauber. "Coherent and incoherent states of the radiation field". In: *Phys. Rev.* 131.6 (Sept. 1963), p. 2766. DOI: `10.1103/PhysRev.131.2766`.

[93] V. M. Glazov and A. S. Pashinkin. "Thermal expansion and heat capacity of GaAs and InAs". en. In: *Inorganic Materials* 36.3 (Mar. 2000), pp. 225–231. ISSN: 0020-1685, 1608-3172. DOI: `10.1007/BF02757926`. URL: `http://link.springer.com/10.1007/BF02757926` (visited on 05/08/2024).

[94] D. Andrew Golter et al. "Coupling a Surface Acoustic Wave to an Electron Spin in Diamond via a Dark State". In: *Phys. Rev. X* 6.4 (Dec. 2016), p. 041060. DOI: `10.1103/PhysRevX.6.041060`.

[95] D. Andrew Golter et al. "Optomechanical Quantum Control of a Nitrogen-Vacancy Center in Diamond". In: *Phys. Rev. Lett.* 116.14 (Apr. 2016), p. 143602. DOI: `10.1103/PhysRevLett.116.143602`.

[96] Maxim Goryachev, Nikita Kostylev, and Michael E. Tobar. "Single-photon level study of microwave properties of lithium niobate at millikelvin temperatures". In: *Phys. Rev. B* 92.6 (Aug. 2015), p. 060406. DOI: `10.1103/PhysRevB.92.060406`.

[97] A. O. Govorov et al. "Nonlinear acoustoelectric transport in a two-dimensional electron system". In: *Phys. Rev. B* 62 (July 2000), pp. 2659–2668. DOI: `10.1103/PhysRevB.62.2659`.

[98] Thomas Grange et al. "Reducing phonon-induced decoherence in solid-state single-photon sources with cavity quantum electrodynamics". In: *Phys. Rev. Lett.* 118.25 (June 2017), p. 253602. DOI: `10.1103/PhysRevLett.118.253602`.

[99] B. L. Green et al. "Neutral Silicon-Vacancy Center in Diamond: Spin Polarization and Lifetimes". In: *Phys. Rev. Lett.* 119 (Aug. 2017), p. 096402. DOI: `10.1103/PhysRevLett.119.096402`.

[100] Gabriele Grosso et al. "Tunable and high-purity room temperature single-photon emission from atomic defects in hexagonal boron nitride". In: *Nat. Commun.* 8.1 (Sept. 2017), p. 705. DOI: `10.1038/s41467-017-00810-2`.

[101] Rachel G. Gruenke et al. "Surface modification and coherence in lithium niobate SAW resonators". In: *Scientific Reports* 14.1 (Mar. 2024), p. 6663. ISSN: 2045-2322. DOI: `10.1038/s41598-024-57168-x`.

[102] M. V. Gustafsson et al. "Propagating phonons coupled to an artificial atom". In: *Science* 346.6206 (Oct. 2014), pp. 207–211. DOI: `10.1126/science.1257219`.

[103] Lisa Hackett et al. "Non-reciprocal acoustoelectric microwave amplifiers with net gain and low noise in continuous operation". In: *Nature Electronics* 6.1 (2023), pp. 76–85. DOI: `10.1038/s41928-022-00908-6`. URL: `https://doi.org/10.1038/s41928-022-00908-6`.

[104] Lisa Hackett et al. "Towards single-chip radiofrequency signal processing via acoustoelectric electron–phonon interactions". In: *Nature Communications* 12.1 (2021), p. 2769. DOI: `10.1038/s41467-021-22935-1`. URL: `https://doi.org/10.1038/s41467-021-22935-1`.

[105] Thilo Hahn et al. "Influence of excited state decay and dephasing on phonon quantum state preparation". In: *Phys. Rev. B* 100.2 (July 2019), p. 024306. DOI: `10.1103/PhysRevB.100.024306`.

[106] Thilo Hahn et al. "Photon scattering from a quantum acoustically modulated two-level system". In: *AVS Quantum Sci.* 4 (Feb. 2022), p. 011403. DOI: `10.1116/5.0077024`.

[107] L.T. Hall et al. "Sensing of Fluctuating Nanoscale Magnetic Fields Using Nitrogen-Vacancy Centers in Diamond". In: *Phys. Rev. Lett.* 103 (Apr. 2009), p. 220802. DOI: 10.1103/PhysRevLett.103.220802.

[108] K. Hashimoto, T. Omori, and M. Yamaguchi. "Design considerations on surface acoustic wave resonators with significant internal reflection in interdigital transducers". In: *IEEE Trans. Ultrason. Ferroelectr. Freq. Control* 51.11 (Nov. 2004), pp. 1394–1403. DOI: 10.1109/TUFFC.2004.1367478.

[109] Yu-Ming He et al. "Cascaded emission of single photons from the biexciton in monolayered WSe_2". In: *Nature Communications* 7.1 (2016), p. 13409.

[110] Yu-Ming He et al. "Single quantum emitters in monolayer semiconductors". In: *Nat. Nanotechnol.* 10.6 (June 2015), pp. 497–502. DOI: 10.1038/nnano.2015.75.

[111] Andreas J. Heinrich et al. "Quantum-coherent nanoscience". In: *Nat. Nanotechnol.* 16.12 (Dec. 2021), pp. 1318–1329. DOI: 10.1038/s41565-021-00994-1.

[112] Sylvain Hermelin et al. "Electrons surfing on a sound wave as a platform for quantum optics with flying electrons". In: *Nature* 477.7365 (Sept. 2011), pp. 435–8. DOI: 10.1038/nature10416.

[113] A Hernández-Mínguez et al. "Anisotropic spin-acoustic resonance in silicon carbide at room temperature". In: *Phys. Rev. Lett.* 125.10 (Sept. 2020), p. 107702. DOI: 10.1103/PhysRevLett.125.107702.

[114] A. Hernández-Mínguez et al. "Acoustically driven photon antibunching in nanowires". In: *Nano Lett.* 12.1 (Jan. 2012), pp. 252–258. DOI: 10.1021/nl203461m.

[115] A. Hernández-Mínguez et al. "Luminescent Defects in a Few-Layer h-BN Film Grown by Molecular Beam Epitaxy". In: *Phys. Rev. Appl.* 10 (4 Oct. 2018), p. 044031. DOI: 10.1103/PhysRevApplied.10.044031.

[116] Alberto Hernández-Mínguez et al. "Acoustically induced coherent spin trapping". In: *Sci. Adv.* 7.44 (Oct. 2021), eabj5030. DOI: `10.1126/sciadv.abj503`.

[117] Jeff T Hill et al. "Coherent optical wavelength conversion via cavity optomechanics". In: *Nature communications* 3.1 (2012), p. 1196.

[118] Kin On Ho et al. "Probing Local Pressure Environment in Anvil Cells with Nitrogen-Vacancy (N-V$^-$) Centers in Diamond". In: *Phys. Rev. Appl.* 13 (2 Feb. 2020), p. 024041. DOI: `10.1103/PhysRevApplied.13.024041`.

[119] Jeffrey Holzgrafe et al. "Cavity electro-optics in thin-film lithium niobate for efficient microwave-to-optical transduction". In: *Optica* 7.12 (Dec. 2020), pp. 1714–1720. ISSN: 2334-2536. DOI: `10.1364/OPTICA.397513`. URL: `https://www.osapublishing.org/optica/abstract.cfm?uri=optica-7-12-1714`.

[120] Rui Huang et al. "Direct bonding of LiNbO3 and GaAs at room temperature by using activated Si atom layer". In: *Vacuum* 216 (2023), p. 112401. ISSN: 0042-207X. DOI: `https://doi.org/10.1016/j.vacuum.2023.112401`. URL: `https://www.sciencedirect.com/science/article/pii/S0042207X23005985`.

[121] AJ Hudson et al. "Coherence of an entangled exciton-photon state". In: *Physical Review Letters* 99.26 (2007), p. 266802.

[122] Oliver Iff et al. "Strain-tunable single photon sources in WS_e2 monolayers". In: *Nano Lett.* 19.10 (Sept. 2019), pp. 6931–6936. DOI: `10.1021/acs.nanolett.9b02221`.

[123] Fernando Iikawa et al. "Acoustically modulated optical emission of hexagonal boron nitride layers". In: *Appl. Phys. Lett.* 114.17 (Apr. 2019), p. 171104. DOI: `10.1063/1.5093299`.

[124] Poolad Imany et al. "Quantum phase modulation with acoustic cavities and quantum dots". In: *Optica* 9.5 (May 2022), pp. 501–504. DOI: 10.1364/OPTICA.451418. URL: https://opg.optica.org/optica/abstract.cfm?URI=optica-9-5-501.

[125] Baptiste Jadot et al. "Distant spin entanglement via fast and coherent electron shuttling". In: *Nat. Nanotechnol.* 16.5 (May 2021), pp. 570–575. DOI: 10.1038/s41565-021-00846-y.

[126] Tomasz Jakubczyk et al. "Impact of phonons on dephasing of individual excitons in deterministic quantum dot microlenses". In: *ACS Photonics* 3.12 (2016), pp. 2461–2466. DOI: 10.1021/acsphotonics.6b00707.

[127] Yuechen Jia et al. "Integrated Photonics Based on Rare-Earth Ion-Doped Thin-Film Lithium Niobate". In: *Laser Photon. Rev.* 16.9 (2022), p. 2200059. DOI: https://doi.org/10.1002/lpor.202200059.

[128] Puqing Jiang, Xin Qian, and Ronggui Yang. "Time-domain thermoreflectance (TDTR) measurements of anisotropic thermal conductivity using a variable spot size approach". In: *Review of Scientific Instruments* 88.7 (2017).

[129] Wenbing Jiang et al. "Thin film aluminum nitride surface acoustic wave resonators for quantum acoustodynamics". In: *Applied Physics Letters* 123.2 (July 2023), p. 024002. ISSN: 0003-6951, 1077-3118. DOI: 10.1063/5.0158083.

[130] John D. Joannopoulos et al. *Photonic Crystals: Molding the Flow of Light*. Princeton University Press, 2008.

[131] Nicholas R Jungwirth et al. "Temperature dependence of wavelength selectable zero-phonon emission from single defects in hexagonal boron nitride". In: *Nano letters* 16.10 (2016), pp. 6052–6057.

[132] Udo Christian Kaletta and Christian Wenger. "FEM simulation of Rayleigh waves for CMOS compatible SAW devices based on AlN/SiO$_2$/Si(100)". In: *Ultrasonics* 54.1 (Jan. 2014), pp. 291–295. DOI: 10.1016/j.ultras.2013.04.009.

[133] Yadav P. Kandel et al. "High-impedance surface-acoustic-wave resonators". In: *Phys. Rev. Appl.* 21 (1 Jan. 2024), p. 014010. DOI: 10.1103/PhysRevApplied.21.014010.

[134] B. Kannan et al. "Generating spatially entangled itinerant photons with waveguide quantum electrodynamics". In: *Sci. Adv.* 6.41 (Oct. 2020), eabb8780. DOI: 10.1126/sciadv.abb8780.

[135] K.V. Kepesidis et al. "Phonon cooling and lasing with nitrogen-vacancy centers in diamond". In: *Phys. Rev. B* 88.6 (Aug. 2013), p. 064105. DOI: 10.1103/PhysRevB.88.064105.

[136] G. Khitrova et al. "Vacuum Rabi splitting in semiconductors". In: *Nat. Phys.* 2.2 (Feb. 2006), pp. 81–90. DOI: 10.1038/nphys227.

[137] Mehran Kianinia et al. "Quantum emitters in 2D materials: Emitter engineering, photophysics, and integration in photonic nanostructures". In: *Applied Physics Reviews* 9.1 (2022), p. 011306.

[138] Hyoju Kim et al. "Position and frequency control of strain-induced quantum emitters in WSe$_2$ monolayers". In: *Nano Lett.* 19.10 (Sept. 2019), pp. 7534–7539. DOI: 10.1021/acs.nanolett.9b03421.

[139] Je-Hyung Kim et al. "Hybrid integration methods for on-chip quantum photonics". In: *Optica* 7.4 (Apr. 20, 2020). Publisher: Optical Society of America, pp. 291–308. ISSN: 2334-2536. DOI: 10.1364/OPTICA.384118.

[140] Jong-Hee Kim, Dae Ho Lim, and Gye Mo Yang. "Selective etching of AlGaAs/-GaAs structures using the solutions of citric acid/H2O2 and de-ionized H2O/buffered oxide etch". In: *Journal of Vacuum Science & Technology B: Microelectronics and Nanometer Structures Processing, Measurement, and Phenomena* 16.2 (Mar. 1998). Publisher: American Institute of Physics, pp. 558–560. ISSN: 1071-1023. DOI: 10.1116/1.589862. URL: https://avs.scitation.org/doi/abs/10.1116/1.589862 (visited on 05/18/2020).

[141] Yoonkee Kim et al. "Surface acoustic wave properties of ZnO films on {001}-cut¡ 110¿-propagating GaAs substrates". In: *J. Appl. Phys.* 75.11 (June 1994), pp. 7299–7303. DOI: 10.1063/1.356639.

[142] Yoonkee Kim et al. "ZnO films on {001}-cut ¡110¿-propagating GaAs substrates for surface acoustic wave device applications". In: *IEEE Trans. Ultrason. Ferroelectr. Freq. Control* 42.3 (May 1995), pp. 351–361. DOI: 10.1109/58.384443.

[143] H. J. Kimble. "The quantum internet". In: *Nature* 453.7198 (June 2008), pp. 1023–1030. ISSN: 0028-0836, 1476-4687. DOI: 10.1038/nature07127.

[144] Jörg B. Kinzel et al. "Directional and Dynamic Modulation of the Optical Emission of an Individual GaAs Nanowire Using Surface Acoustic Waves". In: *Nano Letters* 11.4 (2011). PMID: 21355606, pp. 1512–1517. DOI: 10.1021/nl1042775. URL: https://doi.org/10.1021/nl1042775.

[145] Jörg B. Kinzel et al. "The Native Material Limit of Electron and Hole Mobilities in Semiconductor Nanowires". In: *ACS Nano* 10.5 (May 2016), pp. 4942–4953. DOI: 10.1021/acsnano.5b07639.

[146] J Klein et al. "Site-selectively generated photon emitters in monolayer MoS_2 via local helium ion irradiation". In: *Nat. Commun.* 10.2755 (June 2019), pp. 1–8. DOI: 10.1038/s41467-019-10632-z.

[147] M. Koperski, K. Nogajewski, and M. Potemski. "Single photon emitters in boron nitride: More than a supplementary material". In: *Opt. Commun.* 411 (Mar. 2018), pp. 158–165. DOI: `10.1016/j.optcom.2017.10.083`.

[148] M. Koperski et al. "Single photon emitters in exfoliated WSe$_2$ structures". In: *Nat. Nanotechnol.* 10.6 (June 2015), pp. 503–506. DOI: `10.1038/nnano.2015.67`.

[149] Martin Koppenhöfer et al. "Single-Spin Readout and Quantum Sensing Using Optomechanically Induced Transparency". en. In: *Physical Review Letters* 130.9 (Mar. 2023), p. 093603. ISSN: 0031-9007, 1079-7114. DOI: `10.1103/PhysRevLett.130.093603`. (Visited on 04/26/2024).

[150] H. Kraus et al. "Magnetic field and temperature sensing with atomic-scale spin defects in silicon carbide". In: *Sci. Rep.* 4.1 (July 2014), p. 5303. DOI: `10.1038/srep05303`.

[151] Aishwarya Kumar et al. "Quantum-enabled millimetre wave to optical transduction using neutral atoms". In: *Nature* 615.7953 (Mar. 2023), pp. 614–619. ISSN: 1476-4687. DOI: `10.1038/s41586-023-05740-2`. URL: `https://doi.org/10.1038/s41586-023-05740-2`.

[152] S. Kumar, A. Kaczmarczyk, and B. D. Gerardot. "Strain-Induced Spatial and Spectral Isolation of Quantum Emitters in Mono- and Bilayer WSe$_2$". In: *Nano Letters* 15.11 (2015). PMID: 26480237, pp. 7567–7573. DOI: `10.1021/acs.nanolett.5b03312`.

[153] Santosh Kumar et al. "Resonant laser spectroscopy of localized excitons in monolayer WSe 2". In: *Optica* 3.8 (2016), pp. 882–886.

[154] PE Lagasse. "Higher-order finite-element analysis of topographic guides supporting elastic surface waves". In: *The Journal of the Acoustical Society of America* 53.4 (1973), pp. 1116–1122.

[155] J.D. Larson et al. "Modified Butterworth-Van Dyke circuit for FBAR resonators and automated measurement system". In: *2000 IEEE Ultrasonics Symposium. Proceedings. An International Symposium (Cat. No.00CH37121)*. Vol. 1. Oct. 2000, pp. 863–868. DOI: `10.1109/ULTSYM.2000.922679`.

[156] Vincent Laude et al. "Subwavelength focusing of surface acoustic waves generated by an annular interdigital transducer". In: *Appl. Phys. Lett.* 92.9 (Mar. 2008), p. 094104. DOI: `10.1063/1.2891055`.

[157] Nikolai Lauk et al. "Perspectives on quantum transduction". In: *arXiv:1910.04821 [quant-ph]* (Oct. 2019). arXiv: 1910.04821. URL: `http://arxiv.org/abs/1910.04821`.

[158] S Lazić et al. "Dynamic control of the optical emission from GaN/InGaN nanowire quantum dots by surface acoustic waves". In: *AIP Adv.* 5.9 (Sept. 2015), p. 097217. DOI: `10.1063/1.4932147`.

[159] Snežana Lazić et al. "Dynamically tuned non-classical light emission from atomic defects in hexagonal boron nitride". In: *Commun. Phys.* 2.1 (Dec. 2019), p. 113. DOI: `10.1038/s42005-019-0217-6`.

[160] Donghun Lee et al. "Topical review: spins and mechanics in diamond". In: *J. Opt.* 19.3 (Feb. 2017), p. 033001. DOI: `10.1088/2040-8986/aa52cd`.

[161] M-A Lemonde et al. "Phonon networks with silicon-vacancy centers in diamond waveguides". In: *Phys. Rev. Lett.* 120.21 (May 2018), p. 213603. DOI: `10.1103/PhysRevLett.120.213603`.

[162] R C M Li and J A Alusow. "Suppression of bulk-scattering loss at saw-resonator reflectors". In: *Electron. Lett.* 13.19 (Sept. 1977), pp. 580–581. DOI: `10.1049/el:19770414`.

[163] Yuan-Hua Liang et al. "Simultaneous measurement of nanoprobe indentation force and photoluminescence of InGaAs/GaAs quantum dots and its simulation". In: *Physica E: Low-dimensional Systems and Nanostructures* 36.1 (Jan. 2007), pp. 1–11. ISSN: 13869477. DOI: `10.1016/j.physe.2006.06.023`. URL: `https://linkinghub.elsevier.com/retrieve/pii/S1386947706004048` (visited on 05/20/2024).

[164] M. M. de Lima et al. "Focusing of surface-acoustic-wave fields on (100) GaAs surfaces". In: *J. Appl. Phys.* 94.12 (Dec. 2003), p. 7848. DOI: `10.1063/1.1625419`.

[165] Lukas Linhart et al. "Localized intervalley defect excitons as single-photon emitters in WSe_2". In: *Physical review letters* 123.14 (2019), p. 146401.

[166] Gang-Qin Liu et al. "Single-Shot Readout of a Nuclear Spin Weakly Coupled to a Nitrogen-Vacancy Center at Room Temperature". In: *Phys. Rev. Lett.* 118 (15 Apr. 2017), p. 150504. DOI: `10.1103/PhysRevLett.118.150504`.

[167] Emma Lomonte et al. "Single-photon detection and cryogenic reconfigurability in lithium niobate nanophotonic circuits". In: *Nat. Commun.* 12.1 (2021), p. 6847. DOI: `10.1038/s41467-021-27205-8`.

[168] Brahim Lounis and Michel Orrit. "Single-photon sources". In: *Rep. Prog. Phys.* 68.5 (Apr. 2005), pp. 1129–1179. DOI: `10.1088/0034-4885/68/5/r04`.

[169] Daniil M. Lukin et al. "4H-silicon-carbide-on-insulator for integrated quantum and nonlinear photonics". In: *Nat. Photonics* 14.5 (May 2020), pp. 330–334. DOI: `10.1038/s41566-019-0556-6`.

[170] Yue Luo et al. "Deterministic coupling of site-controlled quantum emitters in monolayer WSe₂ to plasmonic nanocavities". In: *Nature Nanotechnology* 13.12 (2018), pp. 1137–1142.

[171] Yue Luo et al. "Single photon emission in WSe₂ up 160 K by quantum yield control". In: *2D Materials* 6.3 (2019), p. 035017.

[172] Thomas Luschmann et al. "Surface acoustic wave resonators on thin film piezoelectric substrates in the quantum regime". In: *Materials for Quantum Technology* 3.2 (June 2023), p. 021001. ISSN: 2633-4356. DOI: `10.1088/2633-4356/acc9f6`. (Visited on 05/18/2023).

[173] D.S. Macintyre et al. "High resolution e-beam lithography using a thin titanium layer to promote resist adhesion". en. In: *Microelectronic Engineering* 83.4-9 (Apr. 2006), pp. 1128–1131. ISSN: 01679317. DOI: `10.1016/j.mee.2006.01.103`. URL: `https://linkinghub.elsevier.com/retrieve/pii/S016793170600061X`.

[174] E R MacQuarrie et al. "Coherent control of a nitrogen-vacancy center spin ensemble with a diamond mechanical resonator". In: *Optica* 2.3 (Mar. 2015), pp. 233–238. DOI: `10.1364/OPTICA.2.000233`.

[175] E. B. Magnusson et al. "Surface acoustic wave devices on bulk ZnO crystals at low temperature". In: *Appl. Phys. Lett.* 106.6 (Feb. 2015), p. 063509. DOI: `10.1063/1.4908248`.

[176] Gerald D Mahan. *Many-particle physics*. Springer Science & Business Media, 2013.

[177] Smarak Maity et al. "Coherent acoustic control of a single silicon vacancy spin in diamond". In: *Nat. Commun.* 11.1 (Jan. 2020), p. 193. DOI: `10.1038/s41467-019-13822-x`.

[178] Smarak Maity et al. "Mechanical Control of a Single Nuclear Spin". In: *Phys. Rev. X* 12 (1 Mar. 2022), p. 011056. DOI: 10.1103/PhysRevX.12.011056.

[179] R. Manenti et al. "Surface acoustic wave resonators in the quantum regime". In: *Phys. Rev. B* 93.4 (Jan. 2016), p. 041411. DOI: 10.1103/PhysRevB.93.041411.

[180] Riccardo Manenti et al. "Circuit quantum acoustodynamics with surface acoustic waves". In: *Nat. Commun.* 8.1 (Oct. 2017), p. 975. DOI: 10.1038/s41467-017-01063-9.

[181] Santanu Manna et al. "Surface passivation and oxide encapsulation to improve optical properties of a single GaAs quantum dot close to the surface". In: *Applied Surface Science* 532 (2020), p. 147360. ISSN: 0169-4332. DOI: https://doi.org/10.1016/j.apsusc.2020.147360. URL: https://www.sciencedirect.com/science/article/pii/S0169433220321176.

[182] L. J. Martínez et al. "Efficient single photon emission from a high-purity hexagonal boron nitride crystal". In: *Phys. Rev. B* 94 (12 Sept. 2016), p. 121405. DOI: 10.1103/PhysRevB.94.121405.

[183] Clemens Matthiesen, Anthony Nickolas Vamivakas, and Mete Atatüre. "Subnatural Linewidth Single Photons from a Quantum Dot". In: *Phys. Rev. Lett.* 108.9 (Feb. 2012), p. 093602. DOI: 10.1103/PhysRevLett.108.093602.

[184] Felix M. Mayor et al. "Gigahertz Phononic Integrated Circuits on Thin-Film Lithium Niobate on Sapphire". In: *Phys. Rev. Appl.* 15.1 (Jan. 2021), p. 014039. DOI: 10.1103/physrevapplied.15.014039.

[185] J. R. Maze et al. "Properties of nitrogen-vacancy centers in diamond: the group theoretic approach". In: *New J. Phys.* 13.2 (Feb. 2011), p. 025025. DOI: 10.1088/1367-2630/13/2/025025.

[186] Timothy P. McKenna et al. "Cryogenic microwave-to-optical conversion using a triply resonant lithium-niobate-on-sapphire transducer". In: *Optica* 7.12 (Dec. 2020), pp. 1737–1745. DOI: 10.1364/OPTICA.397235.

[187] R P G McNeil et al. "On-demand single-electron transfer between distant quantum dots". In: *Nature* 477.7365 (Sept. 2011), pp. 439–42. DOI: 10.1038/nature10444.

[188] Owen Medeiros et al. "Measuring thickness in thin NbN films for superconducting devices". In: *Journal of Vacuum Science & Technology A* 37.4 (May 2019). Publisher: American Vacuum Society, p. 041501. ISSN: 0734-2101. DOI: 10.1116/1.5088061. URL: https://avs.scitation.org/doi/10.1116/1.5088061 (visited on 07/21/2020).

[189] Seán M. Meenehan et al. "Silicon optomechanical crystal resonator at millikelvin temperatures". In: *Phys. Rev. A* 90 (1 July 2014), p. 011803. DOI: 10.1103/PhysRevA.90.011803. URL: https://link.aps.org/doi/10.1103/PhysRevA.90.011803.

[190] Srujan Meesala et al. "Non-classical microwave–optical photon pair generation with a chip-scale transducer". In: *Nature Physics* 20.5 (May 2024), pp. 871–877. ISSN: 1745-2481. DOI: 10.1038/s41567-024-02409-z. URL: https://doi.org/10.1038/s41567-024-02409-z.

[191] Srujan Meesala et al. "Strain engineering of the silicon-vacancy center in diamond". In: *Phys. Rev. B* 97 (May 2018), p. 205444. DOI: 10.1103/PhysRevB.97.205444.

[192] Jiyang MEI and James FRIEND. "A review: controlling the propagation of surface acoustic waves via waveguides for potential use in acoustofluidics". In: *Mechanical Engineering Reviews* 7.1 (2020), pp. 19-00402-19–00402. DOI: 10.1299/mer.19-00402.

[193] Noah Mendelson et al. "Strain-Induced Modification of the Optical Characteristics of Quantum Emitters in Hexagonal Boron Nitride". In: *Advanced Materials* 32.21 (2020), p. 1908316. DOI: https://doi.org/10.1002/adma.201908316.

[194] M Metcalfe et al. "Resolved Sideband Emission of InAs/GaAs Quantum Dots Strained by Surface Acoustic Waves". In: *Phys. Rev. Lett.* 105.3 (July 2010), p. 37401. DOI: 10.1103/PhysRevLett.105.037401.

[195] Steffen Michaelis de Vasconcellos et al. "Single-Photon Emitters in Layered Van der Waals Materials". In: *Phys. Status Solidi B* 259.4 (Jan. 2022), p. 2100566. DOI: https://doi.org/10.1002/pssb.202100566.

[196] 7ia Michl et al. "Robust and Accurate Electric Field Sensing with Solid State Spin Ensembles". In: *Nano Lett.* 19.8 (July 2019), pp. 4904–4910. DOI: 10.1021/acs.nanolett.9b00900.

[197] Eiko Mieda et al. "Wafer-scale layer transfer of GaAs and Ge onto Si wafers using patterned epitaxial lift-off". In: *Japanese Journal of Applied Physics* 54.3 (Feb. 2015), p. 036505. DOI: 10.7567/JJAP.54.036505. URL: https://dx.doi.org/10.7567/JJAP.54.036505.

[198] A.G. Milnes. *Deep Impurities in Semiconductors.* John Wiley and Sons, 1973.

[199] Mohammad Mirhosseini et al. "Superconducting qubit to optical photon transduction". en. In: *Nature* 588.7839 (Dec. 2020). ISSN: 1476-4687. DOI: 10.1038/s41586-020-3038-6. URL: https://www.nature.com/articles/s41586-020-3038-6 (visited on 08/08/2021).

[200] Galan Moody et al. "2022 Roadmap on integrated quantum photonics". In: *J. Phys. Photonics* 4.1 (Jan. 2022), p. 012501. DOI: 10.1088/2515-7647/ac1ef4.

[201] Eun-A Moon, Jong-Lam Lee, and Hyung Mo Yoo. "Selective wet etching of GaAs on AlxGa1−xAs for AlGaAs/InGaAs/AlGaAs pseudomorphic high electron mobility transistor". In: *Journal of Applied Physics* 84.7 (Oct. 1998), pp. 3933–3938. ISSN: 0021-8979. DOI: `10.1063/1.368571`. URL: `https://doi.org/10.1063/1.368571`.

[202] Bradley A. Moores et al. "Cavity Quantum Acoustic Device in the Multimode Strong Coupling Regime". In: *Phys. Rev. Lett.* 120.22 (May 2018), p. 227701. DOI: `10.1103/PhysRevLett.120.227701`.

[203] David Morgan. *Surface acoustic wave filters with applications to electronic communications and Signal Processing*. Elsevier Science, 2007.

[204] Madeleine E. Msall and Paulo V. Santos. "Focusing Surface-Acoustic-Wave Microcavities on GaAs". In: *Phys. Rev. Appl.* 13.1 (Jan. 2020), p. 014037. DOI: `10.1103/PhysRevApplied.13.014037`.

[205] COMSOL Multiphysics. "Introduction to COMSOL multiphysics®". In: *COMSOL Multiphysics, Burlington, MA, accessed Feb* 9 (1998), p. 2018.

[206] H. Nakahata et al. "SAW devices on diamond". In: *1995 IEEE Ultrasonics Symposium. Proceedings. An International Symposium.* Vol. 1. Nov. 1995, pp. 361–370. DOI: `10.1109/ULTSYM.1995.495599`.

[207] Elke Neu et al. "Single photon emission from silicon-vacancy colour centres in chemical vapour deposition nano-diamonds on iridium". In: *New J. Phys.* 13 (Feb. 2011), p. 025012. DOI: `10.1088/1367-2630/13/2/025012`.

[208] Tomáš Neuman et al. "A phononic interface between a superconducting quantum processor and quantum networked spin memories". In: *npj Quantum Inf.* 7.1 (2021), p. 121. DOI: `10.1038/s41534-021-00457-4`.

[209] C. T. Nguyen et al. "An integrated nanophotonic quantum register based on silicon-vacancy spins in diamond". In: *Phys. Rev. B* 100 (16 Oct. 2019), p. 165428. DOI: 10.1103/PhysRevB.100.165428.

[210] Gichang Noh et al. "Stark Tuning of Single-Photon Emitters in Hexagonal Boron Nitride". In: *Nano Lett.* 18.8 (Aug. 2018), pp. 4710–4715. DOI: 10.1021/acs.nanolett.8b01030.

[211] Emeline D S Nysten et al. "Multi-harmonic quantum dot optomechanics in fused LiNbO$_3$-(Al)GaAs hybrids". In: *J. Phys. D: Appl. Phys* 50.43 (Nov. 2017), 43LT01. DOI: 10.1088/1361-6463/aa861a.

[212] Emeline D. S. Nysten, Armando Rastelli, and Hubert J. Krenner. "A hybrid (Al)GaAs-LiNbO3 surface acoustic wave resonator for cavity quantum dot optomechanics". In: *Applied Physics Letters* 117.12 (Sept. 2020), p. 121106. ISSN: 0003-6951. DOI: 10.1063/5.0022542. (Visited on 09/28/2022).

[213] Richard O'Rorke et al. "Slowness curve surface acoustic wave transducers for optimized acoustic streaming". In: *RSC Advances* 10.20 (2020), pp. 11582–11589. ISSN: 2046-2069. DOI: 10.1039/C9RA10452F. URL: http://xlink.rsc.org/?DOI=C9RA10452F (visited on 11/17/2020).

[214] Ayato Okada et al. "Cavity Enhancement of Anti-Stokes Scattering via Optomechanical Coupling with Surface Acoustic Waves". In: *Phys. Rev. Appl.* 10 (2 Aug. 2018), p. 024002. DOI: 10.1103/PhysRevApplied.10.024002.

[215] Jason Orcutt et al. "Engineering electro-optics in SiGe/Si waveguides for quantum transduction". In: *Quantum Science and Technology* 5.3 (May 2020), p. 034006. ISSN: 2058-9565. DOI: 10.1088/2058-9565/ab84c1. URL: https://iopscience.iop.org/article/10.1088/2058-9565/ab84c1 (visited on 05/10/2021).

[216] Oskar Painter, Kartik Srinivasan, and Paul E. Barclay. "Wannier-like equation for the resonant cavity modes of locally perturbed photonic crystals". In: *Phys. Rev. B* 68.3 (July 2003), p. 035214. DOI: 10.1103/PhysRevB.68.035214.

[217] Carmen Palacios-Berraquero et al. "Large-scale quantum-emitter arrays in atomically thin semiconductors". In: *Nature Communications* 8.1 (2017), p. 15093.

[218] Alan Palazzolo. "Formalism for the rotation matrix of rotations about an arbitrary axis". In: *American Journal of Physics* 44.1 (Jan. 1976), pp. 63–67. ISSN: 0002-9505. DOI: 10.1119/1.10140. URL: https://doi.org/10.1119/1.10140.

[219] Kamyar Parto et al. "Cavity-Enhanced 2D Material Quantum Emitters Deterministically Integrated with Silicon Nitride Microresonators". In: *arXiv preprint arXiv:2206.14845* (2022).

[220] Kamyar Parto et al. "Defect and strain engineering of monolayer WSe_2 enables site-controlled single-photon emission up to 150 K". In: *Nature Communications* 12.1 (2021), p. 3585.

[221] Sahil D. Patel et al. "Surface Acoustic Wave Cavity Optomechanics with Atomically Thin h-BN and WSe_2 Single-Photon Emitters". In: *PRX Quantum* 5 (1 Feb. 2024), p. 010330. DOI: 10.1103/PRXQuantum.5.010330. URL: https://link.aps.org/doi/10.1103/PRXQuantum.5.010330.

[222] J. Pedrós et al. "Guided propagation of surface acoustic waves and piezoelectric field enhancement in ZnO/GaAs systems". In: *Journal of Applied Physics* 110.10 (Nov. 15, 2011). Publisher: American Institute of Physics, p. 103501. ISSN: 0021-8979. DOI: 10.1063/1.3660215. (Visited on 07/01/2021).

[223] Ivan Pelant and Jan Valenta. *Luminescence spectroscopy of semiconductors*. OUP Oxford, 2012.

[224] Emanuele Pelucchi et al. "The potential and global outlook of integrated photonics for quantum technologies". In: *Nature Reviews Physics* 4.3 (Mar. 2022), pp. 194–208. ISSN: 2522-5820. DOI: 10.1038/s42254-021-00398-z. URL: https://doi.org/10.1038/s42254-021-00398-z.

[225] Zhiwei Peng et al. "Strain engineering of 2D semiconductors and graphene: from strain fields to band-structure tuning and photonic applications". In: *Light Sci. Appl.* 9.1 (Nov. 2020), p. 190. DOI: 10.1038/s41377-020-00421-5.

[226] A Plößl. "Wafer direct bonding: tailoring adhesion between brittle materials". en. In: *Materials Science and Engineering: R: Reports* 25.1-2 (Mar. 1999), pp. 1–88. ISSN: 0927796X. DOI: 10.1016/S0927-796X(98)00017-5. URL: https://linkinghub.elsevier.com/retrieve/pii/S0927796X98000175 (visited on 04/29/2024).

[227] M. Pompili et al. "Realization of a multinode quantum network of remote solid-state qubits". In: *Science* 372.6539 (Apr. 2021), pp. 259–264. DOI: 10.1126/science.abg1919.

[228] Edwin Preciado et al. "Scalable fabrication of a hybrid field-effect and acousto-electric device by direct growth of monolayer MoS2/LiNbO3". In: *Nat. Commun.* 6.1 (2015), p. 8593. DOI: 10.1038/ncomms9593.

[229] Johann A Preuß et al. "Assembly of large hBN nanocrystal arrays for quantum light emission". In: *2D Mater.* 8.3 (Mar. 2021), p. 035005. DOI: 10.1088/2053-1583/abeca2.

[230] Jens Pustiowski et al. "Independent dynamic acousto-mechanical and electrostatic control of individual quantum dots in a LiNbO$_3$-GaAs hybrid". In: *Appl. Phys. Lett.* 106.1 (Jan. 2015), p. 013107. DOI: 10.1063/1.4905477.

[231] Qimin Quan and Marko Loncar. "Deterministic design of wavelength scale, ultra-high Q photonic crystal nanobeam cavities". In: *Opt. Express* 19.19 (Sept. 2011), pp. 18529–18542. DOI: 10.1364/OE.19.018529. URL: https://opg.optica.org/oe/abstract.cfm?URI=oe-19-19-18529.

[232] Andrey A. Rakhubovsky, Darren W. Moore, and Radim Filip. "Quantum non-Gaussian optomechanics and electromechanics". In: *Progress in Quantum Electronics* 93 (2024), p. 100495. ISSN: 0079-6727. DOI: https://doi.org/10.1016/j.pquantelec.2023.100495. URL: https://www.sciencedirect.com/science/article/pii/S0079672723000447.

[233] Lord Rayleigh. "On Waves Propagated along the Plane Surface of an Elastic Solid". In: *Proc. Lond. Math. Soc.* s1-17.1 (Nov. 1885), pp. 4–11. DOI: 10.1112/plms/s1-17.1.4.

[234] DE Reiter et al. "Generation and dynamics of phononic cat states after optical excitation of a quantum dot". In: *Phys. Rev. B* 84.19 (Nov. 2011), p. 195327. DOI: 10.1103/PhysRevB.84.195327.

[235] Hengjiang Ren et al. "Two-dimensional optomechanical crystal cavity with high quantum cooperativity". In: *Nature Communications* 11.1 (July 2020). ISSN: 2041-1723. DOI: 10.1038/s41467-020-17182-9.

[236] Ralf Riedinger et al. "Non-classical correlations between single photons and phonons from a mechanical oscillator". In: *Nature* 530.7590 (Feb. 2016), pp. 313–316. DOI: 10.1038/nature16536.

[237] C. Rocke et al. "Acoustically Driven Storage of Light in a Quantum Well". In: *Phys. Rev. Lett.* 78 (1997), pp. 4099–4102. DOI: 10.1103/PhysRevLett.78.4099.

[238] L. J. Rogers et al. "Multiple intrinsically identical single-photon emitters in the solid state". In: *Nat. Commun.* 5.1 (Aug. 2014), p. 4739. DOI: 10.1038/ncomms5739.

[239] R Romestain et al. "Fabrication of a superconducting niobium nitride hot electron bolometer for single-photon counting". In: *New J. Phys.* 6.1 (Oct. 2004), p. 129. DOI: 10.1088/1367-2630/6/1/129.

[240] L. Rondin et al. "Magnetometry with nitrogen-vacancy defects in diamond". In: *Rep. Prog. Phys.* 77.5 (May 2014), p. 056503. DOI: 10.1088/0034-4885/77/5/056503.

[241] M. Rotter et al. "Single-chip fused hybrids for acousto-electric and acousto-optic applications". In: *Appl. Phys. Lett.* 70.16 (1997), pp. 2097–2099. DOI: 10.1063/1.118960.

[242] M. Rotter et al. "Voltage controlled SAW velocity in GaAs/LiNbO/sub 3/-hybrids". In: *IEEE Trans. Ultrason. Ferroelectr. Freq. Control* 46.1 (1999), pp. 120–125. DOI: 10.1109/58.741522.

[243] D. Royer and E. Dieulesaint. *Elastic Waves in Solids II: Generation, Acousto-optic Interaction, Applications.* Springer, 1999.

[244] Brian D. Rummel et al. "Exploring electromechanical utility of GaAs interdigitated transducers; using finite-element-method-based parametric analysis and experimental comparison". In: *Journal of Vacuum Science & Technology B* 41.1 (Jan. 2023), p. 013203. ISSN: 2166-2746, 2166-2754. DOI: 10.1116/6.0002169. URL: https://avs.scitation.org/doi/10.1116/6.0002169.

[245] A. H. Safavi-Naeini et al. "Electromagnetically induced transparency and slow light with optomechanics". In: *Nature* 472.7341 (Apr. 2011), pp. 69–73. ISSN: 1476-4687. DOI: 10.1038/nature09933.

[246] Sina Saravi, Thomas Pertsch, and Frank Setzpfandt. "Lithium Niobate on Insulator: An Emerging Platform for Integrated Quantum Photonics". In: *Adv. Opt. Mater.* 9.22 (Sept. 2021), p. 2100789. DOI: 10.1002/adom.202100789.

[247] K. J. Satzinger et al. "Quantum control of surface acoustic-wave phonons". In: *Nature* 563.7733 (Nov. 2018), pp. 661–665. DOI: 10.1038/s41586-018-0719-5.

[248] Ayed Al Sayem et al. "Lithium-niobate-on-insulator waveguide-integrated superconducting nanowire single-photon detectors". In: *Appl. Phys. Lett.* 116.15 (2020), p. 151102. DOI: 10.1063/1.5142852.

[249] John R Schaibley et al. "Valleytronics in 2D materials". In: *Nature Reviews Materials* 1.11 (2016), pp. 1–15.

[250] Christopher F Schuck et al. "Single-photon generation from self-assembled GaAs/InAlAs (111) A quantum dots with ultrasmall fine-structure splitting". In: *Journal of Physics: Photonics* 3.2 (2021), p. 024012.

[251] M. J. A. Schuetz et al. "Universal Quantum Transducers Based on Surface Acoustic Waves". In: *Phys. Rev. X* 5.3 (Sept. 2015), p. 031031. DOI: 10.1103/PhysRevX.5.031031.

[252] Florian J R Schülein et al. "Fourier synthesis of radiofrequency nanomechanical pulses with different shapes". In: *Nat. Nanotechnol.* 10.6 (Apr. 2015), pp. 512–516. DOI: 10.1038/nnano.2015.72.

[253] Florian J. R. Schülein et al. "Acoustically regulated carrier injection into a single optically active quantum dot". In: *Phys. Rev. B* 88.8 (Aug. 2013), p. 085307. DOI: 10.1103/PhysRevB.88.085307.

[254] Florian J. R. Schülein et al. "Surface acoustic wave controlled charge dynamics in a thin InGaAs quantum well". In: *JETP Lett.* 95.11 (2012), pp. 575–580. DOI: 10.1134/s0021364012110082.

[255] Marco Scigliuzzo et al. "Phononic loss in superconducting resonators on piezoelectric substrates". In: *New Journal of Physics* 22.5 (May 2020), p. 053027. DOI: 10.1088/1367-2630/ab8044.

[256] Diego Scolfaro et al. "Acoustically Driven Stark Effect in Transition Metal Dichalcogenide Monolayers". In: *ACS Nano* 15.9 (Sept. 2021), pp. 15371–15380. DOI: 10.1021/acsnano.1c06854.

[257] Marlan O Scully and M Suhail Zubairy. *Quantum optics.* 1999.

[258] R Seguin et al. "Size-dependent fine-structure splitting in self-organized InAs/GaAs quantum dots". In: *Physical review letters* 95.25 (2005), p. 257402.

[259] Stefan Seidl et al. "Effect of uniaxial stress on excitons in a self-assembled quantum dot". In: *Applied Physics Letters* 88.20 (2006), p. 203113.

[260] A. Semenov et al. "Optical and transport properties of ultrathin NbN films and nanostructures". In: *Physical Review B* 80 (Aug. 2009). ISSN: 1098-0121. DOI: 10.1103/PhysRevB.80.054510. URL: http://adsabs.harvard.edu/abs/2009PhRvB..80e4510S.

[261] Pascale Senellart, Glenn Solomon, and Andrew White. "High-performance semiconductor quantum-dot single-photon sources". en. In: *Nature Nanotechnology* 12.11 (Nov. 2017), pp. 1026–1039. ISSN: 1748-3387, 1748-3395. DOI: 10.1038/nnano.2017.218. (Visited on 01/16/2020).

[262] Linbo Shao et al. "Phononic Band Structure Engineering for High-Q Gigahertz Surface Acoustic Wave Resonators on Lithium Niobate". In: *Phys. Rev. Appl.* 12.1 (July 2019), p. 014022. DOI: 10.1103/PhysRevApplied.12.014022.

[263] Jeong Hyun Shim et al. "Multiplexed Sensing of Magnetic Field and Temperature in Real Time Using a Nitrogen-Vacancy Ensemble in Diamond". In: *Phys. Rev. Appl.* 17 (1 Jan. 2022), p. 014009. DOI: 10.1103/PhysRevApplied.17.014009.

[264] L. R. Sletten et al. "Resolving Phonon Fock States in a Multimode Cavity with a Double-Slit Qubit". In: *Phys. Rev. X* 9.2 (June 2019), p. 021056. DOI: 10.1103/PhysRevX.9.021056.

[265] W Richard Smith et al. "Analysis of interdigital surface wave transducers by use of an equivalent circuit model". In: *IEEE Trans. Microw. Theory Tech.* 17.11 (Nov. 1969), pp. 856–864. DOI: 10.1109/TMTT.1969.1127075.

[266] Sameer Sonar et al. *High-Efficiency Low-Noise Optomechanical Crystal Photon-Phonon Transducers.* arXiv:2406.15701 [physics, physics:quant-ph]. June 2024. URL: http://arxiv.org/abs/2406.15701 (visited on 07/11/2024).

[267] Maximilian M. Sonner et al. "Ultrafast electron cycloids driven by the transverse spin of a surface acoustic wave". In: *Sci. Adv.* 7.31 (2021), eabf7414. DOI: 10.1126/sciadv.abf7414.

[268] Shingo Sotoma, Chandra P. Epperla, and Huan-Cheng Chang. "Diamond Nanothermometry". In: *Chem. Nano. Mat.* 4.1 (Oct. 2018), pp. 15–27. DOI: 10.1002/cnma.201700257.

[269] Ajit Srivastava et al. "Optically active quantum dots in monolayer WSe$_2$". In: *Nat. Nanotechnol.* 10.6 (June 2015), pp. 491–496. DOI: 10.1038/nnano.2015.60.

[270] *Standard specification for Niobium and niobium alloy strip, sheet, and plate.* May 2018. URL: https://www.astm.org/b0393-18.html.

[271] S. Steinert et al. "High sensitivity magnetic imaging using an array of spins in diamond". In: *Rev. Sci. Instrum.* 81.4 (Apr. 2010), p. 043705. DOI: 10.1063/1.3385689.

[272] Hannah L Stern et al. "Room-temperature optically detected magnetic resonance of single defects in hexagonal boron nitride". In: *Nature communications* 13.1 (2022), pp. 1–9.

[273] R Mark Stevenson et al. "A semiconductor source of triggered entangled photon pairs". In: *Nature* 439.7073 (2006), pp. 179–182.

[274] Ireneusz Strzalkowski, Sharad Joshi, and C. R. Crowell. "Dielectric constant and its temperature dependence for GaAs, CdTe, and ZnSe". In: *Applied Physics Letters* 28.6 (Mar. 1976), pp. 350–352. ISSN: 0003-6951. DOI: 10.1063/1.88755.

[275] D. D. Sukachev et al. "Silicon-Vacancy Spin Qubit in Diamond: A Quantum Memory Exceeding 10 ms with Single-Shot State Readout". In: *Phys. Rev. Lett.* 119 (22 Nov. 2017), p. 223602. DOI: 10.1103/PhysRevLett.119.223602.

[276] Ben Sussman et al. "Quantum Canada". In: *Quantum Science and Technology* 4.2 (Feb. 2019), p. 020503. ISSN: 2058-9565. DOI: 10.1088/2058-9565/ab029d. URL: https://iopscience.iop.org/article/10.1088/2058-9565/ab029d.

[277] Y. Takagaki et al. "Guided propagation of surface acoustic waves in AlN and GaN films grown on 4H–SiC (0001) substrates". In: *Phys. Rev. B* 66.15 (Oct. 2002), p. 155439. DOI: 10.1103/PhysRevB.66.155439.

[278] Yoshinori Tanaka, Takashi Asano, and Susumu Noda. "Design of Photonic Crystal Nanocavity With Q-Factor of ${{\sim}10^{9}}$". en. In: *Journal of Lightwave Technology* 26.11 (June 2008), pp. 1532–1539. ISSN: 0733-8724. DOI: `10.1109/JLT.2008.923648`. URL: `http://ieeexplore.ieee.org/document/4542944/` (visited on 04/25/2024).

[279] M G Tanner et al. "A superconducting nanowire single photon detector on lithium niobate". In: *Nanotechnology* 23.50 (Nov. 2012), p. 505201. DOI: `10.1088/0957-4484/23/50/505201`.

[280] Ryuichi Tarumi, Tomohiro Matsuhisa, and Yoji Shibutani. "Low Temperature Elastic Constants and Piezoelectric Coefficients of LiNbO3 and LiTaO3: Resonant Ultrasound Spectroscopy Measurement and Lattice Dynamics Analysis". In: *Japanese Journal of Applied Physics* 51.7S (July 2012), 07GA02. DOI: `10.1143/JJAP.51.07GA02`. URL: `https://dx.doi.org/10.1143/JJAP.51.07GA02`.

[281] J. Teissier et al. "Strain Coupling of a Nitrogen-Vacancy Center Spin to a Diamond Mechanical Oscillator". In: *Phys. Rev. Lett.* 113 (2 July 2014), p. 020503. DOI: `10.1103/PhysRevLett.113.020503`. URL: `https://link.aps.org/doi/10.1103/PhysRevLett.113.020503`.

[282] *The National Quantum Initiative Act.* `https://www.congress.gov/115/bills/hr6227/BILLS-115hr6227enr.pdf`. 2018.

[283] V. Tiwari et al. "Radio-frequency stress-induced modulation of CdTe/ZnTe quantum dots". In: *J. Appl. Phys.* 127.23 (June 2020), p. 234303. DOI: `10.1063/5.0011124`.

[284] Natasha Tomm et al. "A bright and fast source of coherent single photons". In: *Nature Nanotechnology* 16.4 (Apr. 2021), pp. 399–403. DOI: `10.1038/s41565-020-00831-x`. (Visited on 01/19/2024).

[285] Philipp Tonndorf et al. "Single-photon emission from localized excitons in an atomically thin semiconductor". In: *Optica* 2.4 (Apr. 2015), pp. 347–352. DOI: 10.1364/OPTICA.2.000347.

[286] Toan Trong Tran et al. "Quantum Emission from Defects in Single-Crystalline Hexagonal Boron Nitride". In: *Phys. Rev. Appl.* 5 (3 Mar. 2016), p. 034005. DOI: 10.1103/PhysRevApplied.5.034005.

[287] Toan Trong Tran et al. "Quantum emission from hexagonal boron nitride monolayers". In: *Nat. Nanotechnol.* 11.1 (Jan. 2016), pp. 37–41. DOI: 10.1038/nnano.2015.242.

[288] Toan Trong Tran et al. "Robust Multicolor Single Photon Emission from Point Defects in Hexagonal Boron Nitride". In: *ACS Nano* 10.8 (July 2016), pp. 7331–7338. DOI: 10.1021/acsnano.6b03602.

[289] Péter Udvarhelyi et al. "Spin-strain interaction in nitrogen-vacancy centers in diamond". In: *Phys. Rev. B* 98.7 (Aug. 2018), p. 075201. DOI: 10.1103/PhysRevB.98.075201.

[290] Ravitej Uppu et al. "Quantum-dot-based deterministic photon–emitter interfaces for scalable photonic quantum technology". In: *Nature Nanotechnology* (Oct. 18, 2021), pp. 1–10. DOI: 10.1038/s41565-021-00965-6.

[291] Alexei Vagov, Vollrath M Axt, and Tilmann Kuhn. "Electron-phonon dynamics in optically excited quantum dots: Exact solution for multiple ultrashort laser pulses". In: *Phys. Rev. B* 66.16 (Oct. 2002), p. 165312. DOI: 10.1103/PhysRevB.66.165312.

[292] Alexei Vagov et al. "Real-time path integrals for quantum dots: Quantum dissipative dynamics with superohmic environment coupling". In: *Phys. Rev. B* 83.9 (Mar. 2011), p. 094303. DOI: 10.1103/PhysRevB.83.094303.

[293] Anne-Marie Valente-Feliciano. "Superconducting RF materials other than bulk niobium: a review". en. In: *Superconductor Science and Technology* 29.11 (Nov. 2016), p. 113002. ISSN: 0953-2048, 1361-6668. DOI: 10.1088/0953-2048/29/11/113002. URL: https://iopscience.iop.org/article/10.1088/0953-2048/29/11/113002 (visited on 05/08/2024).

[294] P. Varshney et al. "Theoretical and experimental analysis of high Q SAW resonator transient response in a wireless sensor interrogation application". In: (July 2012), pp. 1–6. DOI: 10.1109/FCS.2012.6243714.

[295] B. Villa et al. "Surface acoustic wave modulation of a coherently driven quantum dot in a pillar microcavity". In: *Appl. Phys. Lett.* 111.1 (July 2017), p. 011103. DOI: 10.1063/1.4990966.

[296] Anja Vogele et al. "Quantum Dot Optomechanics in Suspended Nanophononic Strings". In: *Adv. Quantum Technol.* 3.2 (Feb. 2020), p. 1900102. DOI: 10.1002/qute.201900102.

[297] Maïté Volatier et al. "Extremely high aspect ratio GaAs and GaAs/AlGaAs nanowaveguides fabricated using chlorine ICP etching with N_2-promoted passivation". en. In: *Nanotechnology* 21.13 (Apr. 2010), p. 134014. ISSN: 0957-4484, 1361-6528. DOI: 10.1088/0957-4484/21/13/134014. URL: https://iopscience.iop.org/article/10.1088/0957-4484/21/13/134014 (visited on 05/10/2024).

[298] S. Völk et al. "Enhanced Sequential Carrier Capture into Individual Quantum Dots and Quantum Posts Controlled by Surface Acoustic Waves". In: *Nano Letters* 10.9 (2010), pp. 3399–3407.

[299] Lei Wan et al. "Highly efficient acousto-optic modulation using nonsuspended thin-film lithium niobate-chalcogenide hybrid waveguides". In: *Light Sci. Appl.* 11.1 (May 2022), p. 145. DOI: 10.1038/s41377-022-00840-6.

[300] Hui Wang et al. "Towards optimal single-photon sources from polarized microcavities". In: *Nature Photonics* 13.11 (2019), pp. 770–775.

[301] Junliang Wang et al. "Coulomb-mediated antibunching of an electron pair surfing on sound". In: *Nature Nanotechnology* 18.7 (July 2023), pp. 721–726. ISSN: 1748-3395. DOI: 10.1038/s41565-023-01368-5. URL: https://doi.org/10.1038/s41565-023-01368-5.

[302] Lei Wang et al. "High performance 33.7 GHz surface acoustic wave nanotransducers based on AlScN/diamond/Si layered structures". In: *Appl. Phys. Lett.* 113.9 (Aug. 2018), p. 093503. DOI: 10.1063/1.5046113.

[303] Zhen Wang et al. "Superconducting properties and crystal structures of single-crystal niobium nitride thin films deposited at ambient substrate temperature". In: *Journal of Applied Physics* 79.10 (1996), pp. 7837–7842. DOI: 10.1063/1.362392.

[304] Shi-Hai Wei et al. "Towards Real-World Quantum Networks: A Review". In: *Laser Photonics Rev.* 16.3 (Jan. 2022), p. 2100219. DOI: 10.1002/lpor.202100219.

[305] R. S. Weis and T. K. Gaylord. "Lithium niobate: Summary of physical properties and crystal structure". In: *Applied Physics A* 37.4 (1985), pp. 191–203. DOI: 10.1007/BF00614817.

[306] Stefan Weis et al. "Optomechanically Induced Transparency". en. In: *Science* 330.6010 (Dec. 2010), pp. 1520–1523. ISSN: 0036-8075, 1095-9203. DOI: 10.1126/science.1195596. URL: https://science.sciencemag.org/content/330/6010/1520 (visited on 07/01/2021).

[307] M. Weiß et al. "Surface acoustic wave regulated single photon emission from a coupled quantum dot-nanocavity system". In: *Appl. Phys. Lett.* 109.3 (July 2016), p. 033105. DOI: `10.1063/1.4959079`.

[308] Matthias Weiß and Hubert J. Krenner. "Interfacing quantum emitters with propagating surface acoustic waves". In: *Journal of Physics D: Applied Physics* 51.37 (Aug. 2018), p. 373001. DOI: `10.1088/1361-6463/aace3c`. URL: `https://dx.doi.org/10.1088/1361-6463/aace3c`.

[309] Matthias Weiß et al. "Dynamic Acoustic Control of Individual Optically Active Quantum Dot-like Emission Centers in Heterostructure Nanowires". In: *Nano Lett.* 14.5 (May 2014), pp. 2256–64. DOI: `10.1021/nl4040434`.

[310] Matthias Weiß et al. "Multiharmonic Frequency-Chirped Transducers for Surface-Acoustic-Wave Optomechanics". In: *Phys. Rev. Appl.* 9.1 (Jan. 2018), p. 014004. DOI: `10.1103/PhysRevApplied.9.014004`.

[311] Matthias Weiß et al. "Optomechanical wave mixing by a single quantum dot". In: *Optica* 8.3 (Mar. 2021), p. 291. DOI: `10.1364/OPTICA.412201`.

[312] Matthias Weiß et al. "Radio frequency occupancy state control of a single nanowire quantum dot". In: *J. Phys. D: Appl. Phys* 47.39 (Oct. 2014), p. 394011. DOI: `10.1088/0022-3727/47/39/394011`.

[313] Samuel J. Whiteley et al. "Spin–phonon interactions in silicon carbide addressed by Gaussian acoustics". In: *Nat. Phys.* 15.5 (May 2019), pp. 490–495. DOI: `10.1038/s41567-019-0420-0`.

[314] Daniel Wigger, Krzysztof Gawarecki, and Paweł Machnikowski. "Remote Phonon Control of Quantum Dots and Other Artificial Atoms". In: *Adv. Quantum Technol.* 4.4 (Apr. 2021), p. 2000128. DOI: `10.1002/qute.202000128`.

[315] Daniel Wigger et al. "Quantum dynamics of optical phonons generated by optical excitation of a quantum dot". In: *J. Comput. Electron.* 15.4 (July 2016), pp. 1158–1169. DOI: 10.1007/s10825-016-0856-8.

[316] Daniel Wigger et al. "Resonance-fluorescence spectral dynamics of an acoustically modulated quantum dot". In: *Phys. Rev. Res.* 3.3 (Aug. 2021), p. 033197. DOI: 10.1103/PhysRevResearch.3.033197.

[317] Andrea Willege. *Explainer: What is quantum technology and what are its benefits?* URL: https://www.weforum.org/agenda/2024/07/explainer-what-is-quantum-technology/.

[318] Thomas Wolf et al. "Subpicotesla Diamond Magnetometry". In: *Phys. Rev. X* 5 (4 Oct. 2015), p. 041001. DOI: 10.1103/PhysRevX.5.041001.

[319] Sean Wu, Ruyen Ro, and Zhi-Xun Lin. "Rayleigh surface acoustic wave modes of (100) ZnO films on (111) diamond". en. In: *Applied Physics Letters* 94.3 (Jan. 2009), p. 032908. ISSN: 0003-6951, 1077-3118. DOI: 10.1063/1.3074370. URL: https://pubs.aip.org/apl/article/94/3/032908/117899/Rayleigh-surface-acoustic-wave-modes-of-100-ZnO (visited on 06/27/2024).

[320] Jikai Xu et al. "Glass-on-LiNbO3 heterostructure formed via a two-step plasma activated low-temperature direct bonding method". en. In: *Applied Surface Science* 459 (Nov. 2018), pp. 621–629. ISSN: 0169-4332. DOI: 10.1016/j.apsusc.2018.08.031. URL: https://www.sciencedirect.com/science/article/pii/S0169433218321500 (visited on 06/24/2021).

[321] E. Yablonovitch et al. "Van der Waals bonding of GaAs epitaxial liftoff films onto arbitrary substrates". In: *Applied Physics Letters* 56.24 (June 1990), pp. 2419–2421. ISSN: 0003-6951. DOI: 10.1063/1.102896. URL: https://doi.org/10.1063/1.102896.

[322] K. Yamanouchi, H. Nakagawa, and H. Odagawa. "GHz-range surface acoustic wave low loss filter at super low temperature". In: *Proceedings of the 1999 Joint Meeting of the European Frequency and Time Forum and the IEEE International Frequency Control Symposium*. Vol. 2. Apr. 1999, pp. 911–914. DOI: `10.1109/FREQ.1999.841453`.

[323] I Yeo et al. "Strain-mediated coupling in a quantum dot-mechanical oscillator hybrid system." In: *Nat. Nanotechnol.* 9.2 (Dec. 2013), pp. 106–110. DOI: `10.1038/nnano.2013.274`.

[324] Didit Yudistira et al. "Non-radiative complete surface acoustic wave bandgap for finite-depth holey phononic crystal in lithium niobate". In: *Appl. Phys. Lett.* 100.6 (Feb. 2012), p. 061912. DOI: `10.1063/1.3684839`.

[325] Emil Zeuthen et al. "Electrooptomechanical Equivalent Circuits for Quantum Transduction". In: *Phys. Rev. Appl.* 10.4 (Oct. 2018), p. 044036. DOI: `10.1103/PhysRevApplied.10.044036`.

[326] Gang Zhang et al. "Material platforms for defect qubits and single-photon emitters". In: *Appl. Phys. Rev.* 7 (Sept. 2020), p. 031308. DOI: `10.1063/5.0006075`.

[327] Jixing Zhang et al. "Diamond Nitrogen-Vacancy Center Magnetometry: Advances and Challenges". In: *arXiv: 2010.10231* (Oct. 2020). DOI: `10.48550/arXiv.2010.10231`.

[328] L. Zhang et al. "Ultra-low dark count rate and high system efficiency single-photon detectors with 50 nm-wide superconducting wires". In: *Appl. Phys. B* 102.4 (Mar. 2011), pp. 867–871. DOI: `10.1007/s00340-010-4234-0`.

[329] Shibin Zhang et al. "Surface Acoustic Wave Devices Using Lithium Niobate on Silicon Carbide". In: *IEEE Transactions on Microwave Theory and Techniques*

68.9 (Sept. 2020), pp. 3653–3666. ISSN: 0018-9480, 1557-9670. DOI: `10.1109/TMTT.2020.3006294`. URL: `https://ieeexplore.ieee.org/document/9139293/` (visited on 06/27/2024).

[330] WeiJun Zhang et al. "NbN superconducting nanowire single photon detector with efficiency over 90% at 1550 nm wavelength operational at compact cryocooler temperature". In: *Sci. China Phys. Mech.* 60.12 (Oct. 2017), p. 120314. DOI: `10.1007/s11433-017-9113-4`.

[331] Huan Zhao et al. "Site-controlled telecom-wavelength single-photon emitters in atomically-thin $MoTe_2$". In: *Nature Communications* 12.1 (2021), p. 6753.

[332] Di Zhu et al. "Integrated photonics on thin-film lithium niobate". In: *Adv. Opt. Photon.* 13.2 (June 2021), pp. 242–352. DOI: `10.1364/AOP.411024`.

[333] Rongjin Zhuang et al. "High-Q Thin-Film Lithium Niobate Microrings Fabricated with Wet Etching". In: *Advanced Materials* 35.3 (2023), p. 2208113. DOI: `https://doi.org/10.1002/adma.202208113`. URL: `https://onlinelibrary.wiley.com/doi/abs/10.1002/adma.202208113`.